

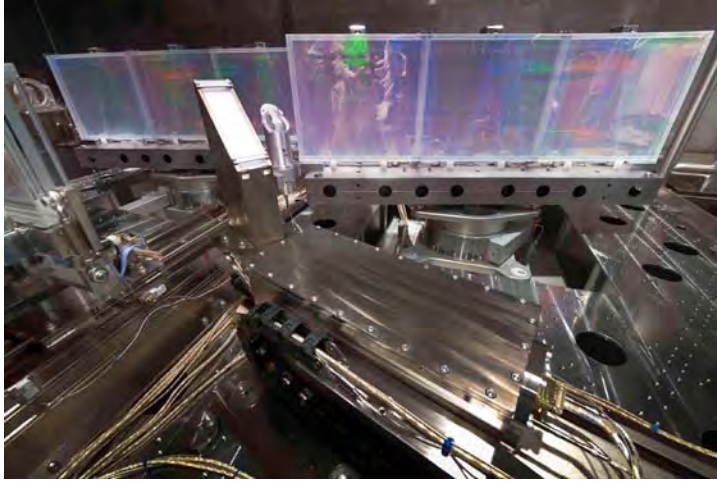
LLE Review

Quarterly Report



About the Cover:

The cover of this issue of the LLE Review features Thanh Nguyen, project team leader for the OMEGA EP grating inspection system (GIS), the subject of this issue's feature article (see p. 165). The photograph shows the author examining the GIS hardware on the upper compressor table of the grating compressor chamber (GCC), which is normally maintained at vacuum. The GIS is a line-scanned, dark-field imaging system that detects damage features *in situ* on the final tiled-grating assembly of the pulse-compression system on OMEGA EP. A portion of the pulse compressor's first tiled-grating assembly can be seen in the mirror's reflection on the right side of the image. The GIS has allowed the Omega EP facility to identify potential damage on critical optics while maintaining the pulse compressor in a vacuum environment—a necessary capability for maximizing the performance and availability of the short-pulse laser system.



The image at the left shows another view of the GIS within the GCC. The GIS is in the foreground, shown extended to one end of its scan range. The enclosure nearest to the viewer is a pressure vessel containing the imaging optics and linear charge-coupled-device array. The periscope assembly and illumination system both extend vertically from the pressure vessel and are oriented to illuminate and view the fourth tiled-grating assembly (TGA4), visible in the background at the left of the image (shown rotated away from its normal use angle). The first tiled grating is on the right side of the image. The GIS projects a vertical line of illumination on TGA4 and images the light scattered from potential damage sites. The system is scanned horizontally to sequentially illuminate and image the entire grating surface, resulting in a 2-D defect map. The development

team faced many unique challenges in designing and operating such a scanning system in a thermally isolated vacuum environment. These are discussed in detail in the article on p. 165.

This report was prepared as an account of work conducted by the Laboratory for Laser Energetics and sponsored by New York State Energy Research and Development Authority, the University of Rochester, the U.S. Department of Energy, and other agencies. Neither the above named sponsors, nor any of their employees, makes any warranty, expressed or implied, or assumes any legal liability or responsibility for the accuracy, completeness, or usefulness of any information, apparatus, product, or process disclosed, or represents that its use would not infringe privately owned rights. Reference herein to any specific commercial product, process, or service by trade name, mark, manufacturer, or otherwise, does not necessarily constitute or imply its endorsement, recommendation, or favoring by

the United States Government or any agency thereof or any other sponsor. Results reported in the LLE Review should not be taken as necessarily final results as they represent active research. The views and opinions of authors expressed herein do not necessarily state or reflect those of any of the above sponsoring entities.

The work described in this volume includes current research at the Laboratory for Laser Energetics, which is supported by New York State Energy Research and Development Authority, the University of Rochester, the U.S. Department of Energy Office of Inertial Confinement Fusion under Cooperative Agreement No. DE-FC52-08NA28302, and other agencies.

Printed in the United States of America

Available from

National Technical Information Services
U.S. Department of Commerce
5285 Port Royal Road
Springfield, VA 22161
www.ntis.gov

For questions or comments, contact Brian E. Kruschwitz, Editor, Laboratory for Laser Energetics, 250 East River Road, Rochester, NY 14623-1299, (585) 273-5104.
www.lle.rochester.edu

LLE Review

Quarterly Report



Contents

In Brief	iii
Grating Inspection System for Large-Scale Multilayer-Dielectric Gratings for High-Energy Laser Systems	165
Scaling Hot-Electron Generation to High-Power, Kilojoule-Class Laser–Solid Interactions	174
Measurement of the Self-Phase Modulation on OMEGA	179
Large-Aperture, Plasma-Assisted Deposition of Inertial Confinement Fusion Laser Coatings	184
Improved On-Shot Focal-Spot Measurement on OMEGA EP Using Phase-Retrieval–Enhanced Wavefront Measurements	192
The Second Omega Laser Facility Users Group Workshop	205
LLE’s Summer High School Research Program	224
FY10 Laser Facility Report	226
National Laser Users’ Facility and External Users’ Programs	229
Publications and Conference Presentations	

In Brief

This volume of the LLE Review, covering July–September 2010, features “Grating Inspection System for Large-Scale Multilayer-Dielectric Gratings for High-Energy Laser Systems” by T. Nguyen, C. Kingsley, J. Bunkenburg, A. Kalb, M. Bedzyk, D. Weiner, T. Walker, and J. R. Marciante. The article (p. 165) reports on the development of a high-resolution inspection system for the detection of laser damage on large-scale (1.41-m \times 0.43-m) multilayer diffraction gratings in the OMEGA EP short-pulse laser system. The grating inspection system (GIS) is fully integrated within the vacuum grating compressor and enables inspections to be carried out while the compressor chamber is under vacuum. Damage is detected by imaging scattered light from damage sites on the grating surface. Features as small as 250 μm can be identified with the system.

Additional highlights of research presented in this issue include the following:

- P. M. Nilson, A. A. Solodov, J. F. Myatt, W. Theobald, P. A. Jaanimagi, L. Gao, C. Stoeckl, R. S. Craxton, J. A. Delettrez, J. D. Zuegel, B. E. Kruschwitz, C. Dorrer, J. H. Kelly, R. Betti, T. C. Sangster, and D. D. Meyerhofer (LLE); K. U. Akli (General Atomics); and P. K. Patel and A. MacKinnon (LLNL) report on the scaling of hot-electron generation to high-power, kilojoule-class laser–solid interactions (p. 174). Thin-foil targets were irradiated with high-power (1- to 210-TW), 10-ps pulses focused to intensities of $I > 10^{18} \text{ W/cm}^2$ and studied with K-photon spectroscopy. Comparing the energy emitted in K photons to target-heating calculations shows a laser-energy-coupling efficiency to hot electrons of $\eta_{L \rightarrow e} = 20 \pm 10\%$. Time-resolved x-ray–emission measurements suggest that laser energy is coupled to hot electrons over the entire duration of the incident laser drive. Comparison of the K-photon emission data to previous data at similar laser intensities shows that $\eta_{L \rightarrow e}$ is independent of laser-pulse duration from $1 \text{ ps} \leq \tau_p \leq 10 \text{ ps}$.
- W. R. Donaldson, J. H. Kelly, and R. E. Bahr (LLE); and D. N. Maywar (Rochester Institute of Technology) present a measurement of the self-phase modulation-induced bandwidth in a 30-kJ–class laser-amplifier chain (p. 179). Self-phase modulation (SPM) in a multikilojoule laser system was detected spectroscopically and correlated with the time derivative of the intensity measured at the output of the system. This correlation provides an empirical relationship that makes it possible to rapidly determine the magnitude of the SPM being generated using measured experimental data. This empirical relationship was verified by modeling the propagation of an optical pulse in the laser amplifier chain to predict both pulse shape and the SPM.
- J. B. Oliver, P. Kupinski, A. L. Rigatti, A. W. Schmid, J. C. Lambropoulos, S. Papernov, A. Kozlov, J. Spaulding, D. Sadowski, Z. Chrzan, and R. D. Hand (LLE); D. R. Gibson and I. Brinkley (Thin Film Solution, Ltd., Scotland); and F. Placido (University of West Scotland, Scotland) describe large-aperture plasma-assisted deposition of ICF laser coatings (p. 184). Plasma-assisted electron-beam evaporation leads to changes in the crystallinity, density, and stresses of thin films. A dual-source plasma system was developed that provides stress control of large-aperture, high-fluence coatings used in vacuum for substrates 1 m in aperture.

- B. E. Kruschwitz, S.-W. Bahk, J. Bromage, D. Irwin, and M. D. Moore present an improved on-shot focal-spot measurement on OMEGA EP using phase-retrieval-enhanced wavefront measurements (p. 192). Target-plane intensities on the short-pulse beamlines of OMEGA EP are characterized on-shot using the focal-spot diagnostic (FSD), an indirect wavefront-based measurement. Phase-retrieval methods are employed using on-shot and off-line far-field measurements to improve the on-shot wavefront measurements and yield more-accurate, repeatable focal-spot predictions. Incorporation of these techniques has resulted in consistently high (>90%) correlation between the FSD focal-spot predictions and direct far-field fluence measurements in the target chamber in low-energy testing.
- R. D. Petrasso (Plasma Science and Fusion Center, MIT) reports on the second Omega Laser Facility Users Group Workshop (28–30 April 2010) on p. 205. LLE hosted more than 115 researchers from 44 universities and laboratories and 9 countries for the second Omega Laser Facility Users Group (OLUG) workshop. The workshop fostered communications among the individual OMEGA users and between users and the facility, including discussions of research results and opportunities and improvements in the Omega and Omega EP laser facilities. An important function of the workshop was to develop a set of recommendations and findings to help set future priorities for the Omega Laser Facility.
- This volume concludes with a summary of LLE’s Summer High School Research Program (p. 224), the FY10 Laser Facility Report (p. 226), and the National Laser Users’ Facility and External Users’ Programs (p. 229).

Brian E. Kruschwitz
Editor

Grating Inspection System for Large-Scale Multilayer-Dielectric Gratings for High-Energy Laser Systems

Introduction

The OMEGA EP Laser System at LLE is a petawatt-class laser system capable of producing high-energy laser pulses with lengths shorter than a picosecond. Short-pulse production is achieved in a pulse compressor composed of large-aperture (meter-scale) multilayer-dielectric diffraction gratings.¹ The pulse compressor consists of four tiled-grating assemblies (TGA's) within a vacuum grating compressor chamber (GCC).² The fourth TGA handles the highest compressed power and is, therefore, most prone to laser-induced damage, requiring frequent inspection. A grating inspection system (GIS) has been developed to provide *in-situ* detection of potential damage features on the fourth TGA without disturbing the vacuum environment or the alignment of the TGA's.

In this article we describe the GIS, which provides high-resolution damage-sensitive imaging of the diffraction grating's optical surface. Selective sensitivity to damage is achieved by using a dark-field imaging system that collects scattered (as opposed to reflected or diffracted) light from the optical surface. This technique is not, in principle, dependent on the diffractive nature of the surface under test and should be applicable to any flat optical surface that causes minimal scattering when in an undamaged state.³

This article will (1) discuss the GIS system with design requirements and constraints; (2) present an alignment method that optimizes performance; (3) discuss the background and thermal issues that arise from using the GIS system in a vacuum environment; (4) present a data-reduction scheme that addresses various unique issues posed by the system; (5) demonstrate measurement results obtained from the GIS during a recent energy ramp campaign; and (6) present conclusions.

System Description

A number of key requirements were imposed on the GIS system design to ensure compatibility with the OMEGA EP pulse compression system:

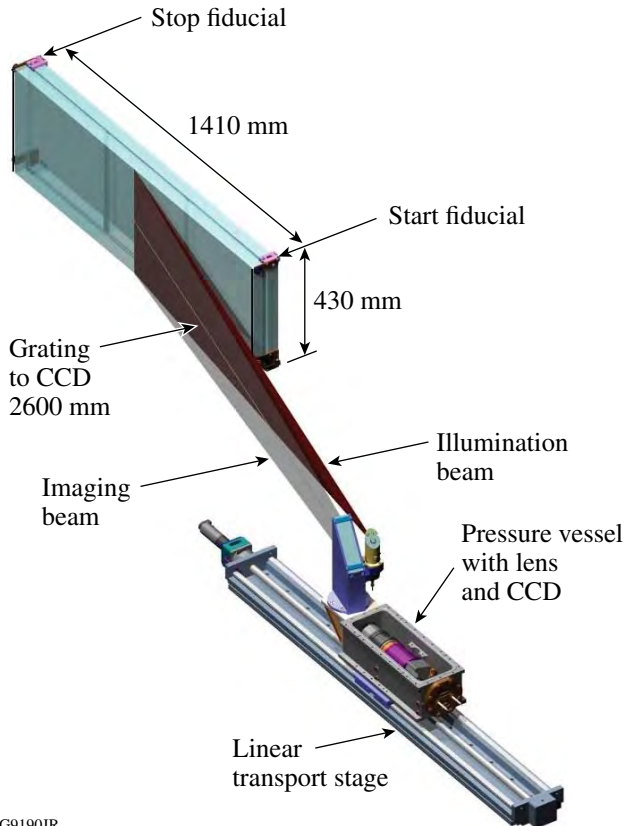
1. The GIS may not enter a volume assigned to any other GCC devices.
2. The GIS must not obstruct shot and alignment beams.
3. GIS heat output must be less than 1 W/h per measurement.
4. All material must be rated as vacuum compatible and satisfy class-100-level cleanliness requirements.
5. GIS must be capable of detecting damage features as small as 250 μm .

To best satisfy these requirements, a linearly scanned, dark-field imaging concept was selected. A scanning system allows one to sample a number of object points greater than the number of pixels on the sensor, which is a significant advantage over other design concepts given the size of the object to be imaged ($\sim 6 \times 10^5 \text{ mm}^2$) and the feature size requirement [see requirement (5) above]^a. In the context of imaging a highly angle dependent surface such as a diffraction grating, a scanning system has the additional advantage that the viewing angle is constant with respect to position along the scan-parallel direction.

The GIS consists of three subsystems: (1) a line-illumination system, (2) a line-imaging system aligned to view the illuminated portion of the grating surface, and (3) a transport mechanism that scans these across the width of the TGA to form a two-dimensional image. Figure 124.1 shows an overview of the system, and Table 124.I outlines the specifications of the as-built system, which satisfies the design requirements.

The illumination system consists of a line generator that projects an elongated Gaussian pattern onto the grating surface.

^aNote that requirement (5) concerns *detection*, not *resolution*. It is invoked here only as an estimator of the required resolution and, in turn, the required number of object plane samples.



G9190JR

A line generator is used rather than a simpler area illumination concept to provide sufficient irradiance in the region imaged by the camera, while requiring only a modest total power. Light is provided by a 1053-nm fiber laser external to the GCC and transported to the line generator via a single-mode, polarization-maintaining fiber. Since both high illumination intensity and a long optical fiber to deliver illumination to the GIS are required, special care was necessary to prevent stimulated Brillouin scattering from destroying the fiber. This was achieved by using a custom fiber-laser source with a relatively short coherence length as compared to commercial products at this wavelength.

As closely as possible, the illumination light matches the polarization (vertical), incidence angle ($\sim 72^\circ$), and wavelength (1053 nm) for which the gratings are designed to exhibit their highest diffraction efficiency. Mechanical restrictions on the location of the GIS within the GCC [see requirement (1) above] preclude, however, an exact match to the desired angle of incidence. As a compromise, an angle of incidence of 78.5°

Figure 124.1

Grating inspection system is shown scanning across a 1.41-m \times 0.43-m tiled-grating assembly. Note that the pressure vessel housing cover is absent in this image for illustrative purposes.

Table 124.I: System parameters.

Imaging System	
Working (object) distance	2.6 m
Viewing angle w.r.t grating surface	76°
Focal length	250 mm
Full field of view	14°
Feature detection	$250 \mu\text{m}$ or larger
Sensor	Dalsa Piranha 2 8192-pixel array, 10 bits/pixel, $7\text{-}\mu\text{m}$ pixel size
Lens	Mamiya KL 4.5/250L-A (Ref. 4)
Illumination	
Wavelength	1053 nm
Angle of incidence	78.5° from surface normal
Power at line generator	180 mW
Line shape on grating surface	Gaussian $1 \times 500 \text{ mm}$ at $1/e^2$
Mechanical	
Alignment fiducial	$250\text{-}\mu\text{m}$ -diam acid-etched wires, coplanar with grating surface
Vacuum-compatible reticulating stage	Straightness = $100 \mu\text{m}$ over 1.5 m, effective drive/encoder resolution = $2 \mu\text{m}$

from the grating surface normal is used. This is close enough to the ideal angle that diffraction efficiency is not significantly affected. Most of the incident light is therefore diffracted, minimizing stray light from reflections in the grating substrate or nearby mechanical components. Light striking a damaged portion of the grating will be diffracted less efficiently, leading to scatter that may be detected by the imaging system.

The imaging system consists of a commercial medium-format photographic lens that images the optic surface to a linear charge-coupled-device (CCD) array camera. The camera captures light from one vertical strip of the optic during each acquisition, building an image as the scanner moves horizontally across the TGA surface. The camera and imaging lens are housed in an airtight case, along with temperature and pressure sensors. This casing preserves atmospheric pressure to facilitate heat dissipation from the camera (see **Mitigation of Thermal and Background Effects**, p. 168) and to prevent contamination of the GCC by outgassing from the camera, lens, or associated electronics. A periscope assembly, external to the airtight case, keeps the camera and imaging lens out of the on-shot and alignment beam envelopes. Figure 124.2 gives an overhead view of the GIS camera and pressure vessel including the periscope and illumination and imaging systems.

The imaging lens provides a reduction from object to image by a factor of 8.9, mapping the $7\text{-}\mu\text{m}$ pixels of the camera to about $62.5\ \mu\text{m}$ in the object plane.⁴ The camera views the grating surface at a shallow angle, however, which spreads the object space footprint of each pixel by a factor of 3.8 in the horizontal direction, covering an area of $62.5 \times 237.5\ \mu\text{m}$ in the plane of the grating surface. The GIS typically acquires

a line of data per $16\ \mu\text{m}$ of travel across the grating surface, which, in combination with the horizontal extent of the pixel footprint in object space, means that every point on the grating surface contributes to the signal in adjacent lines of data in the output image. Acquiring data in this way provides a low-pass effect and strong oversampling, which is an advantage in data reduction for reducing noise and eliminating a particular type of image defect (see **Data Reduction**, p. 169).

The linear transport is parallel to the surface of the grating and offset from it along the scan direction. The placement of the GIS transport was chosen to accommodate existing GCC equipment and satisfied the top-level requirements. Custom drive electronics for the linear transport provide a trigger signal for the camera, which is synchronized to the rotary encoder output from the drive motor. This prevents fluctuations in transport velocity from producing distortions in the image data and ensures that the scale of the image will be highly repeatable.

Installation and Alignment

To maximize the sensitivity of the GIS, the illumination line and the line imaged by the CCD must overlap precisely. Using a high-precision coordinate measuring machine,⁵ the transport stage was aligned to be parallel to the grating surface at the correct distance to yield a nominal viewing angle of 14° relative to the scan direction (76° relative to the grating surface normal). This angle was mandated by the mechanical constraints discussed in the previous section. To facilitate the alignment between illumination and imaging beams, alignment fiducials are installed on the TGA for use with the GIS. The fiducials are $250\text{-}\mu\text{m}$ -diam stainless-steel wire, strung 3 mm from the edge of the grating, parallel to the edge, and copla-

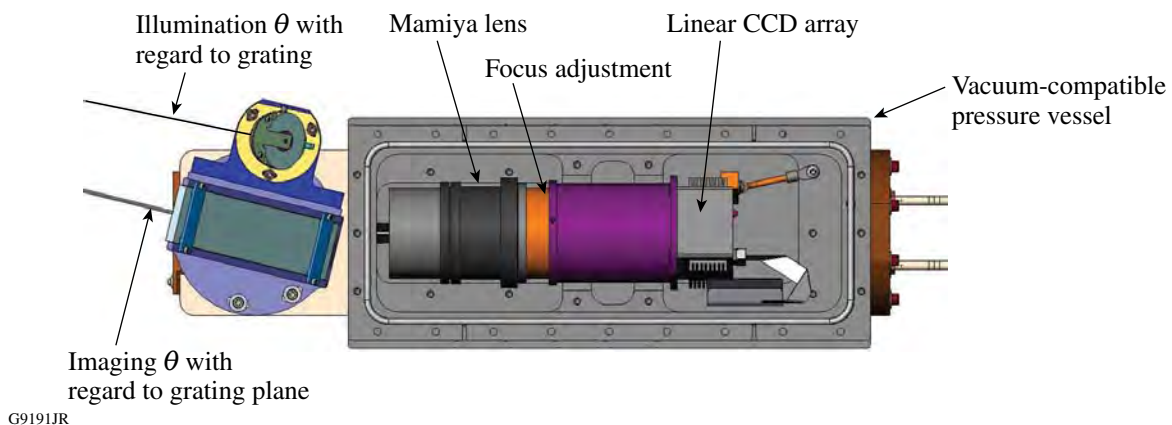


Figure 124.2

An engineering top-view drawing shows the vacuum-compatible pressure vessel housing the major components of the imaging system. This reduces contamination and out-gassing while keeping the camera functioning in air. The separation between illumination and imaging is also indicated.

nar with the grating surface. They are imaged in every GIS scan, providing information on the GIS alignment and focus state and verification that the illumination source is functioning properly. The fiducials also play an important role in the installation and alignment of the GIS, where they serve as a reference for the rotation and pointing of both the camera and the illumination line.

Alignment was achieved using the following procedure: First, the top and bottom of the fiducial wire were illuminated with small “marker” beams from a HeNe laser. With the camera moved to the limit of travel corresponding to the illuminated fiducial, the periscope was tipped and tilted until the HeNe illumination was detected and centered on the CCD. The camera was then rotated to bring both HeNe illuminated portions of the fiducial into view. Next, the 1.053- μm line generator was added and pointed at the fiducial wire. The line had to be rotated to be within the field of view of the linear CCD array, corresponding to a 120- μrad tolerance. Finally, the focus and polarization of the line generator were checked to maximize the return signal and minimize transmitted light through the grating, respectively. These alignment steps had to be iteratively repeated until the desired signal level was achieved.

Mitigation of Thermal and Background Effects

The GIS camera generates a significant quantity of heat whenever it is receiving power and suffers from severely limited thermal dissipation because it operates in a vacuum environment. This creates a number of consequences when operating the instrument: Unnecessary thermal pollution of the GCC by the GIS can impact the optical alignment of the grating compressor, which must be avoided. The CCD temperature can vary strongly over the scan duration of roughly 8 min, which directly influences the dark current background. Finally, the long-term equilibrium temperature of the camera, while energized, is potentially damaging to the CCD.

The pressure vessel housing the camera mitigates these effects to some degree by providing a significant thermal mass in close contact with the camera, while the vessel itself remains in poor contact with the GCC as a whole. Thermal effects, however, must also be minimized procedurally.

A study of the thermal behavior of the GIS was conducted during installation within the vacuum GCC, which was used as a guide in developing a set of usage protocols that mitigate thermal effects. Data were continuously acquired from the GIS camera for roughly 45 min, and the temperature was recorded from an in-camera thermistor. Temperature data were collected

once per 500 lines of image data at a 0.5 °C resolution. A model function was fitted to the data, consisting of a single exponential function rounded to the nearest half-degree. Figure 124.3 shows the raw data and the rounded-fit function, as well as the exponential component of the model, before rounding.

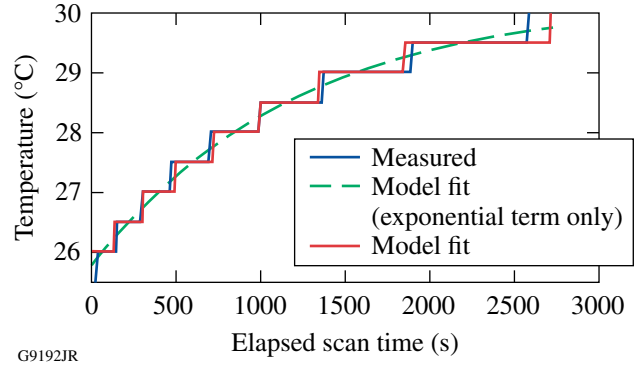


Figure 124.3

Measured temperature, fitted-model data, and the exponential component of the fitted model.

The exponential component of the fitted model is used to estimate the temperature, from which a value is interpolated to correspond with each line of image data. Figure 124.4 shows the background level versus temperature for each line of data from the CCD. This establishes a thermal variation of the background of 2.0 counts/degree.

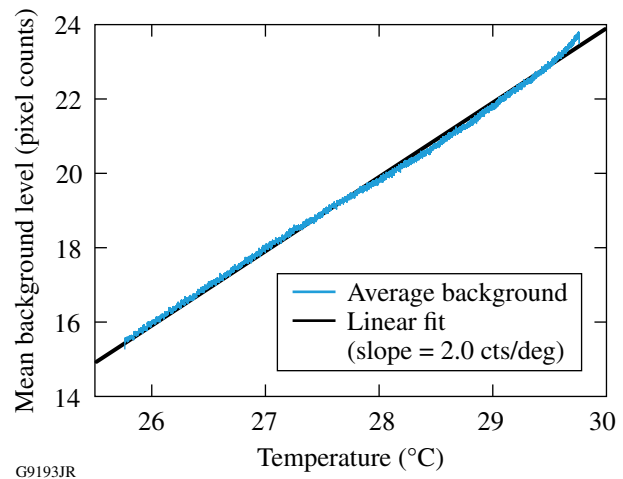


Figure 124.4

Mean background level versus temperature during the thermal study.

Over an 8-min scan, the rise in temperature could be many degrees, which would produce unacceptable variations in background. This is mitigated in GIS operation by a series of operations carried out by the GIS acquisition software. When

a scan is initiated by the user, this software ensures that the camera is at or above 23 °C to reduce the second derivative of the temperature with respect to time. If the camera is below this temperature, it is energized and warmed up before the scan is initiated. Once scanning begins, 500 lines of image data are acquired to provide pre-scan background data. Post-scan background is similarly measured immediately after the scan is concluded. The pre- and post-scan background data are used quite effectively by the GIS data-reduction algorithms to compensate for variation in the background, as described in the next section. The variance in the background will, of course, also increase with temperature; this variation has been undetected in testing, however, and is assumed to be negligible.

Data Reduction

Raw data from the GIS, as from practically all imaging systems, have a number of undesirable characteristics that must be corrected during data reduction to provide the most-accurate possible representation of the surface being inspected. Some characteristics of the GIS data are relatively unique, and their treatment will be described in detail. Double exposures (DE's) are the most notable of these because of their strong impact on image quality if uncorrected. DE errors, as they occur in a scanning system like the GIS, are quite unique and cannot be corrected using basic image-processing techniques, such as smoothing or filtering. The GIS data reduction also performs background subtraction, which is, in principle, a common operation. However, because of the thermally induced background variation over the duration of a GIS scan, this process is carried out in a somewhat unique manner. Finally, the GIS data reduction must correct for the nonuniform illumination level, which varies strongly across the vertical extent of the image as a result of the Gaussian shape of the illumination line.

DE's are caused by a known issue in the trigger logic of the Dalsa Piranha2 camera when running at line rates below 1 kHz. During a DE, the camera fails to respond to a trigger signal,

resulting in a line of data being exposed for two integration periods. DE's are relatively infrequent; it is typical to gather a full scan (roughly 88,000 lines) without a single occurrence. An uncorrected DE would be problematic, however, for later analysis and must be removed. DE's are corrected by inspecting the column sums of a region at the top of the GIS image. The region spans the full image, is 400 pixels tall, and was chosen for its absence of any significant image features (i.e., it is dominated by background). Figure 124.5 identifies this region.

The column sums are divided by a median-filtered copy of themselves, and DE's are identified by points where this ratio exceeds six standard deviations above its mean value. Figure 124.6 displays the column sums and the same data after a median filter. DE reduction in this manner is highly effective because the median filter is ideal for identifying isolated extreme values in the raw data.

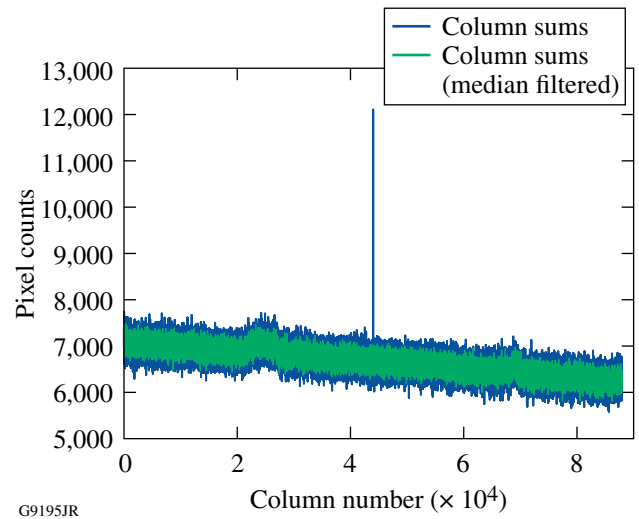


Figure 124.6
Column sums of the image data in the region of interest are shown. A DE is simulated at line 40,000 because real DE's are very infrequent.

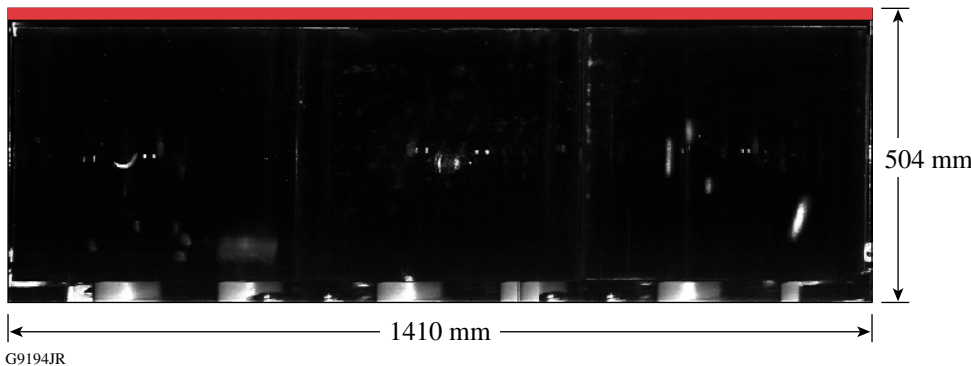


Figure 124.5
A typical GIS image (the region used to detect DE is identified in red).

Once identified, columns affected by a DE are eliminated and replaced with interpolated values from their neighboring columns. This interpolation is justified in this case by the large oversampling in the horizontal (scan) direction. As described in **System Description** (p. 165), the pixel footprint in the plane of the grating has a horizontal extent of roughly $237.5 \mu\text{m}$, while acquisition occurs every $16 \mu\text{m}$. This implies that 93% of the area imaged by each pixel is also imaged in each of the adjacent data lines, making interpolation between adjacent pixels highly reliable.

After correcting DE's in the image data and in the pre- and post-scan background data by the same process, the data reduction corrects for the variable background level. The background values are interpolated linearly across the GIS image from the pre-scan to the post-scan levels, and these interpolated values are subtracted from the image. In effect, this assumes that the background level increases linearly with time as the scan progresses, which of course, it does not. However, because the second derivative of the temperature change versus time has been constrained by the data acquisition process (see **Mitigation of Thermal and Background Effects**, p. 168), the deviation of the background from the linear interpolation is also bounded. Figure 124.7 shows the exponential model for the temperature data, extrapolated to the 7-min period immediately after the camera reaches $23 \text{ }^\circ\text{C}$. The start-to-end linear approximation deviates from the exponential by a maximum of $\sim 0.09 \text{ }^\circ\text{C}$, which translates into a maximum error in the background estimation of roughly 0.18 CCD counts. This subcount departure should be insignificant to further image processing and will be even smaller if the scan begins at a temperature higher than

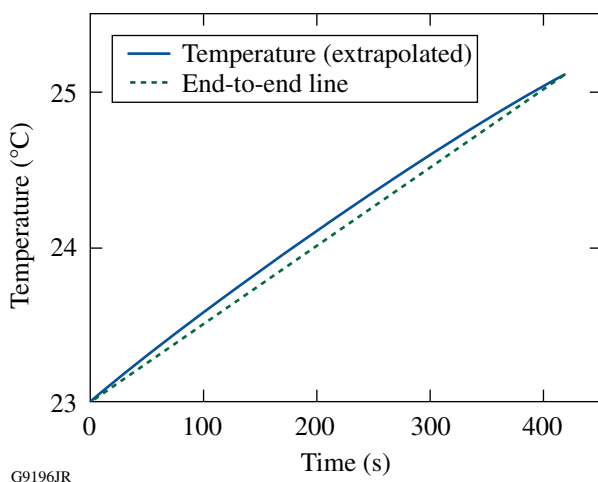


Figure 124.7
Temperature data are shown extrapolated over the travel scan time.

$23 \text{ }^\circ\text{C}$, where the exponential behavior of the temperature is more closely approximated by a line.

Finally, the data reduction corrects for strong variations in signal strength across the vertical extent of the image, such as from illumination nonuniformity. This variation would confound any image analysis based on a fixed binarization threshold. To correct the signal level, an equalization coefficient is applied to the data from each pixel of the CCD array. Equalization coefficients are calculated from a GIS scan of a reference surface, which is collected during installation and maintenance of the GIS. The reference surface is a uniform scattering surface composed of white Delrin.⁶ Note that this measurement includes more than just the Gaussian shape of the illumination. By using measured data from the GIS, rather than a pre-characterization of the illumination profile, this equalization also accounts for variations in photoresponse for each pixel, vignetting in the imaging lens, and other properties of the as-built system.

Figure 124.8 shows the measured equalization coefficient for each pixel in the CCD array, demonstrating that the Gaussian illumination profile clearly dominates other effects. It must be noted that the scattering properties of the reference target and of scattering sites on the optic being imaged are certainly non-Lambertian and likely not identical. It is unclear to what extent this distorts the equalization coefficients, but it is assumed to be negligible. It is also important to understand that equalizing the signal level cannot alter the signal-to-noise ratio, which inevitably varies across the vertical dimension of the image.

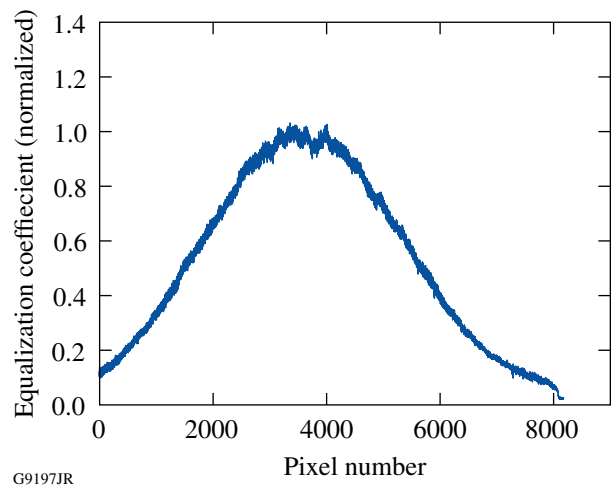


Figure 124.8
Signal equalization coefficients for each pixel in the CCD array.

A 3×3 median filter is applied to the image to suppress noise. Median filtering typically provides good noise suppression without compromising image detail as heavily as, for example, a smoothing filter. A median filter is particularly effective on GIS images at this point because, as discussed above, they are heavily oversampled in the horizontal direction. So, the noise suppression from the median filter comes at the cost of virtually no loss of image structure in the horizontal direction and acceptable loss in the vertical direction.

At this point the anomalies in the GIS data are sufficiently corrected to give an image that represents, as accurately as possible, the scattering sites on the optic under test. The final step in data reduction is to re-scale the GIS image to a standard pixel scale of 16 pixels/mm. This simplifies future processing and measurements and offers an opportunity for further noise suppression. The scale factors for this transformation are determined to sufficient precision by measuring the size of a known feature in a raw GIS image, such as the outline of a grating tile. Raw GIS data have a scale of roughly 61.26 and 16.25 pixels/mm in the horizontal and vertical directions, respectively. The image is re-scaled via bi-cubic interpolation with an anti-aliasing filter.⁷

Results

The GIS allows one to make frequent *in-situ* measurements of the TGA surface. The optics are also inspected visually during semi-annual maintenance periods when the GCC is vented to atmospheric pressure. This visual inspection is the conventionally accepted method for observing morphological change (MC) on optical surfaces and serves as a performance benchmark for the GIS in terms of sensitivity to damage features. Visual inspection also provides a point of comparison for determining whether all MC's that appear under visual inspection are detected by the GIS. Figure 124.9 compares (a) a photograph of a damaged region of a grating taken during visual inspection and (b) the same region as imaged by the GIS.

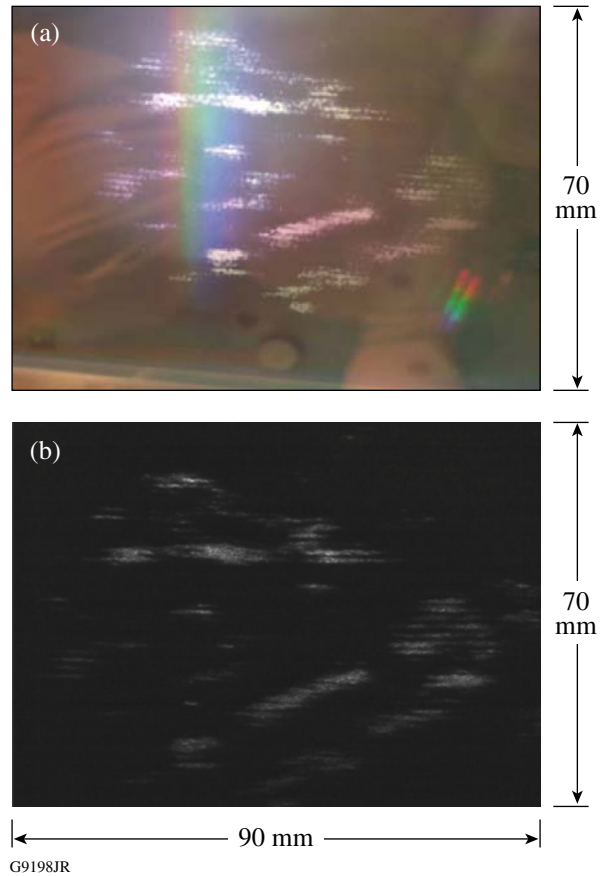


Figure 124.9
 (a) A photograph taken during visual inspection on 19 June 2009 and (b) the same region of the TGA surface imaged by the GIS on 7 September 2009. Clear correlation can be seen between the surface features detected by both methods.

Such correspondence between GIS observations and visual inspections has now been repeatedly supported and represents an important measure of the success of the GIS.

Final output from the GIS is a high-quality, high-resolution image ready to use to identify and analyze damage on the TGA surface. Figure 124.10 shows a typical image. Note that in this

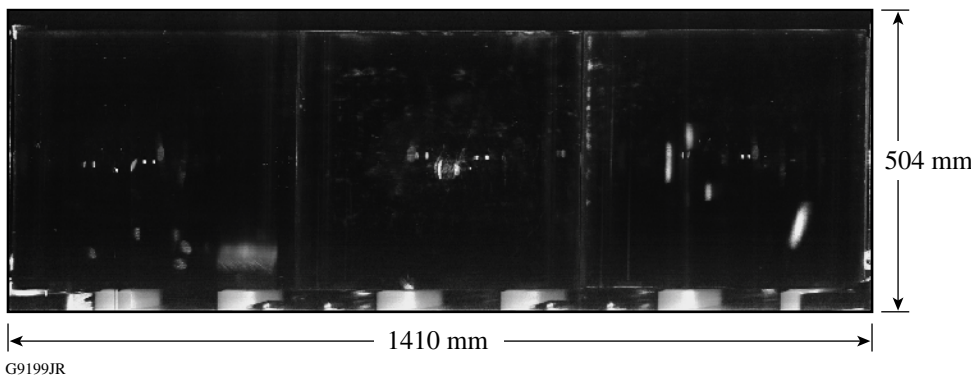


Figure 124.10
 A typical image of a TGA as produced by the GIS. A variety of common non-damage features are visible.

image, and most others presented in this article, the contrast has been significantly adjusted to make details visible to the reader. In their original state, for use in analysis, the dynamic range of the GIS is very large, and much of the interesting structure is present at the lower end of the intensity scale. The TGA was in good condition at the time of the scan in Fig. 124.10, and very little scattering was present from damage or other MC on the optical surface. Therefore, this image is a good illustration of the “background” features in a “pre-damaged” GIS image. In the central region of each grating tile can be observed two pairs of bright circular features, in some cases with another one or two larger oval-shaped features between them. These are inherent to the grating tiles and are not fully understood. They are not visible under human inspection of the gratings. The inter-tile gaps are clearly visible, as well as the fiducial wires at the extreme edges of the image. A number of other optical ghosts are visible, generally appearing as oblong “blemishes.” Some of these ghosts are assumed to be stray-light artifacts, possibly resulting from some part of the TGA mechanical assembly. Finally, along the bottom of the image, one can observe a portion of the TGA mechanical structure. Particularly prominent

here are the six white rectangular features that result from a set of Delrin cylinders on the TGA support structure. Recognizing and measuring these background features are vital to any analysis seeking to identify MC on the grating surface. Clearly, it is necessary to employ techniques that compare a potentially damaged grating to an earlier reference. These analysis methods, however, are beyond the scope of this article.

The GIS has been highly successful in detecting MC attributable to high-energy operation of the OMEGA EP system. Figure 124.11 shows a GIS image gathered after a recent energy-ramp campaign. Even without rigorous analysis, MC is clearly visible in the lower portion of the center tile and the upper-right quadrant of the left tile. The region highlighted by the red box contains the two most-severe MC’s on the grating surface, with severity being judged by the surface area of the MC.

The progression of this damage can be investigated in greater detail. Figure 124.12 shows a sequence of images of this region at full resolution, demonstrating the progression of MC during the energy ramp.

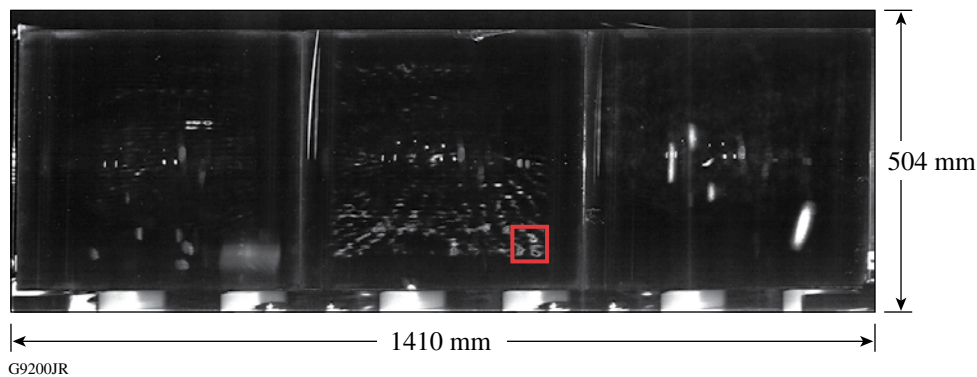


Figure 124.11

GIS image taken after the final shot in the OMEGA EP energy-ramp campaign. Damage-induced scattering is visible in multiple areas. The area outlined in red highlights the two most severely damaged sites in terms of affected area.

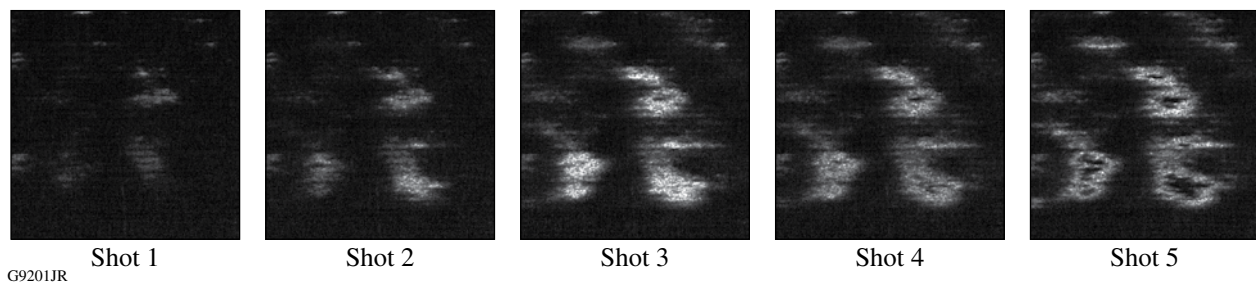


Figure 124.12

A progression of images of a region of the final TGA in the OMEGA EP upper compressor during the energy-ramp campaign. This is the region identified in Fig. 124.11.

It is interesting to note that, as MC's progress, the scattering signal becomes stronger until a point is reached (shot 3) at which the scattering signal is abruptly reduced. This effect becomes visible on shot 4 and is dramatically apparent on shot 5. Subsequent analysis of this and other regions of the grating tile using an atomic force microscope reveal that, in the region where scattering has ceased, the pillars comprising the diffractive surface structure have been completely ejected from the surface.

Conclusion

The grating inspection system has been integrated into the OMEGA EP vacuum grating compression chamber. It operates reliably within the allowed operational window between shots and has successfully demonstrated the ability to detect features in the specified 250- μm scale. Statistical techniques have been applied to GIS observations to establish system fluence limits that minimize the threat of damage to the gratings, while making it possible for OMEGA EP to satisfy its short-pulse mission.⁸ There is great potential for further investigation of the *in-situ* behavior of large-aperture diffraction gratings, and the GIS will continue to play a vital role in this work.

ACKNOWLEDGEMENT

This work was supported by the U.S. Department of Energy Office of Inertial Confinement Fusion under Cooperative Agreement No. DE-FC52-08NA28302, the University of Rochester, and the New York State Energy Research and Development Authority. The support of DOE does not constitute an endorsement by DOE of the views expressed in this article.

Special thanks to LLE software engineers Steve Smith and Mark Wilson and LLE electrical engineer Scott Ingraham for their excellent work and support in developing the GIS image acquisition software and drive electronics. We also extend thanks to system scientist Jie Qiao, optical engineer Damon Diehl (ASE Instrument, Inc.), and LLE engineering director/chief safety officer Dr. D. W. Jacobs-Perkins for their great guidance and support.

REFERENCES

1. T. J. Kessler, J. Bunkenburg, H. Huang, A. Kozlov, and D. D. Meyerhofer, *Opt. Lett.* **29**, 635 (2004).
2. J. Qiao, A. Kalb, M. J. Guardalben, G. King, D. Canning, and J. H. Kelly, *Opt. Express* **15**, 9562 (2007).
3. M. Commandré, in *Laser-Induced Damage in Optical Materials: 2008*, edited by G. J. Exarhos *et al.* (SPIE, Bellingham, WA, 2008), Vol. 7132, p. 713200.
4. This lens is listed as $f/4.5$, EFL = 250 mm. The mechanical requirements of the pressure vessel housing impose, however, a number of noncircular apertures. In practice, this system has different effective apertures in the vertical and horizontal directions and is likely slower, overall, than $f/4.5$.
5. FARO Technologies, Inc., Lake Mary, FL 32746 (<http://www.faro.com>).
6. McMaster Carr Supply, Aurora, OH 44202 (<http://www.mcmaster.com>).
7. See MATLAB 7.8.0.347 documentation for the image resize function in the Image Processing Toolkit.
8. J. Qiao, A. W. Schmid, L. J. Waxer, T. Nguyen, J. Bunkenburg, C. Kingsley, A. Kozlov, and D. Weiner, *Opt. Express* **18**, 10,423 (2010).

Scaling Hot-Electron Generation to High-Power, Kilojoule-Class Laser–Solid Interactions

High-intensity laser–solid interactions ($>10^{18}$ W/cm²) accelerate large numbers of thermal electrons to relativistic energies. These high-energy, MeV-scale electrons are a source of significant energy deposition within plasmas and are used extensively in plasma-based particle acceleration,^{1–3} creation of warm dense matter,⁴ laboratory high-energy astrophysics,⁵ ultrafast γ -ray generation,⁶ and fast-ignition research.^{6,7} Efficient hot-electron generation is of great importance for the energetic feasibility of these applications and has been studied intensively.^{6,8–17}

Previous solid-target experiments showed energy-conversion efficiencies into hot electrons ($\eta_{L\rightarrow e}$) of up to several tens of percent for picosecond or shorter pulses of 1- μ m light and laser intensities from 10^{18} W/cm² $\leq I \leq 10^{20}$ W/cm² (Refs. 6,8–17). With recent developments in laser technology, it is now possible to generate kilojoule-class, $\tau_p = 10$ -ps pulses that can be focused to intensities of $I > 10^{18}$ W/cm² (Ref. 18). Such long-duration, high-intensity laser pulses hold great promise for high-energy applications that require rapid electron-energy deposition over time scales that are short compared to the typical hydrodynamic decompression times of solid and laser-compressed targets.

In fast ignition, laser-compressed deuterium and tritium are rapidly heated and ignited by a high-intensity laser pulse.^{6,7} An intense, multikilojoule, 10- to 20-ps-long laser pulse is required to generate the ignition spark with optimal electron-beam energies and currents for energy deposition within the fuel assembly. Knowledge of the coupling of a high-intensity laser into energetic electrons that heat the fuel, in addition to how this scales to ignition-class lasers, is critical to understanding spark generation and fast ignition.

Hot-electron generation in this regime is only partially understood, however, particularly at high laser energies ($E_L > 1000$ J) and long laser-pulse durations ($\tau_p \sim 10$ ps), where no previous data exist because of the unavailability of suitably high-energy lasers. With increasing laser-pulse duration, a number of processes affect energy coupling to solid targets,

including pre-plasma formation,^{19,20} electron transport,²¹ hole boring,²² and laser-driven shock formation.²³ Understanding these effects on energy coupling is crucial for scaling hot-electron generation to long-pulse, high-intensity lasers. Definitive measurements of the effect of laser-pulse duration on $\eta_{L\rightarrow e}$ are reported in this article.

X-ray spectroscopic measurements of hot-electron generation in high-intensity laser–solid interactions show that the conversion efficiency is independent of laser-pulse duration. Thin-foil targets have been heated with hot electrons generated by $\tau_p = 10$ -ps pulses focused to intensities of $I > 10^{18}$ W/cm², and $\eta_{L\rightarrow e}$ has been inferred with K-photon spectroscopy. Comparing the energy emitted in K photons to target-heating calculations shows an energy-coupling efficiency to hot electrons of $\eta_{L\rightarrow e} \sim 20\%$ with laser powers from $1 \text{ TW} \leq P_L \leq 210 \text{ TW}$. These are the first experiments to study hot-electron generation with intense, $\tau_p = 10$ -ps pulses at such high laser powers. Time-resolved x-ray emission measurements suggest that hot electrons are generated over the entire duration of the incident laser drive. The K-photon emission data are compared to other published data at similar laser intensities, showing for the first time that $\eta_{L\rightarrow e}$ is independent of laser-pulse duration from $1 \text{ ps} \leq \tau_p \leq 10 \text{ ps}$.

The experiments were carried out using LLE’s Multi-Tera-watt (MTW)^{24,25} and Omega EP¹⁸ Laser Facilities. For these experiments, the MTW laser delivered an energy of $E_L = 10$ J in a $\tau_p = 10$ -ps pulse at a wavelength of $\lambda_L = 1.054 \mu\text{m}$. The laser pulse was focused by an $f/3$, off-axis parabolic mirror at normal incidence to the target with an $R_{80} = 5 \mu\text{m}$, where R_{80} is the spot radius containing 80% of the laser energy, providing a laser intensity of $I = 1 \times 10^{18}$ W/cm². OMEGA EP delivered higher laser energies from $300 \text{ J} \leq E_L \leq 2100 \text{ J}$ in a $\tau_p = 10$ -ps pulse at a wavelength of $\lambda_L = 1.054 \mu\text{m}$. An $f/2$, off-axis parabolic mirror focused the laser pulse at either 45° or normal incidence to the target with an $R_{80} = 25 \mu\text{m}$, providing laser intensities of up to $I \sim 10^{19}$ W/cm². The targets were Cu foils with dimensions that were varied between $600 \times 600 \times 50 \mu\text{m}^3$ and $75 \times 75 \times 3 \mu\text{m}^3$, mounted on a 17- μ m-thick silicon-carbide stalk.

Pre-plasma expansion prior to intense laser irradiation affects the energy coupling to solid targets,^{19,20} particularly at high laser energies, and is caused by low laser contrast. For these OMEGA EP shots, fast-diode measurements indicate that the laser pedestal typically reaches 6×10^{-7} of the peak laser power and contains 10^{-4} of the total laser-pulse energy. For the experiments reported here, the energy contained in the pedestal varied from $40 \text{ mJ} \leq E_{\text{ped}} \leq 210 \text{ mJ}$. Over this energy range, calculations made using the 1-D radiation hydrodynamic code *LILAC*²⁶ indicate that the pre-plasma extends up to 5 to $10 \mu\text{m}$ between the critical- and the solid-density plasma.

The main diagnostic for measuring K-photon emission from the target was an absolutely calibrated, single-photon-counting x-ray spectrometer based on an SI-800 x-ray charge-coupled device.²⁷ A combination of heavy shielding and collimation, and a large target-to-spectrometer distance, reduces the number of Cu K-photon hits that are detected, satisfying the single-photon-counting regime, while reducing the hard x-ray flux. Cu filters that transmit Cu K_{α} and K_{β} photons below the filter K edge further optimize the signal to background of the measured spectrum. A graphite (HOPG) crystal spectrometer provided a complementary measurement of the K-photon yield.²⁸ The radiation emission time was measured using an ultrafast x-ray streak camera with a temporal resolution of about 2 ps (Ref. 29).

Typical K-photon spectra obtained in the experiment are shown in Fig. 124.13. Figure 124.13(a) shows a time-integrated x-ray emission spectrum from a $500 \times 500 \times 20\text{-}\mu\text{m}^3$ Cu target irradiated with an $E_L = 1000\text{-J}$, $\tau_p = 10\text{-ps}$ pulse. Figure 124.13(b) shows an x-ray emission spectrum from a $75 \times 75 \times 5\text{-}\mu\text{m}^3$ Cu target irradiated with the same laser conditions.

The emission spectra show peaks at 8.05 keV and 8.91 keV, where the Cu plasma emits K_{α} and K_{β} inner-shell radiation. As hot electrons move through the target, the atomic electrons in the $1s$ shell of copper ions are ejected by electrons with energies 2 to $3\times$ the copper K-shell ionization potential (~ 20 to 25 keV). During de-excitation, the system relaxes to a lower-energy state, with $2p \rightarrow 1s$ and $3p \rightarrow 1s$ transitions generating K_{α} and K_{β} photons. The emission lines are fit to Gaussian line shapes with a full width at half maximum (FWHM) of 220 eV. The emission spectra contain the thermal He_{α} and Ly_{α} ionic-line emission that is generated from hot surface plasma on the laser-irradiated side of the target.

The main observation from these measurements is the suppressed K-photon yield from the reduced-mass target.

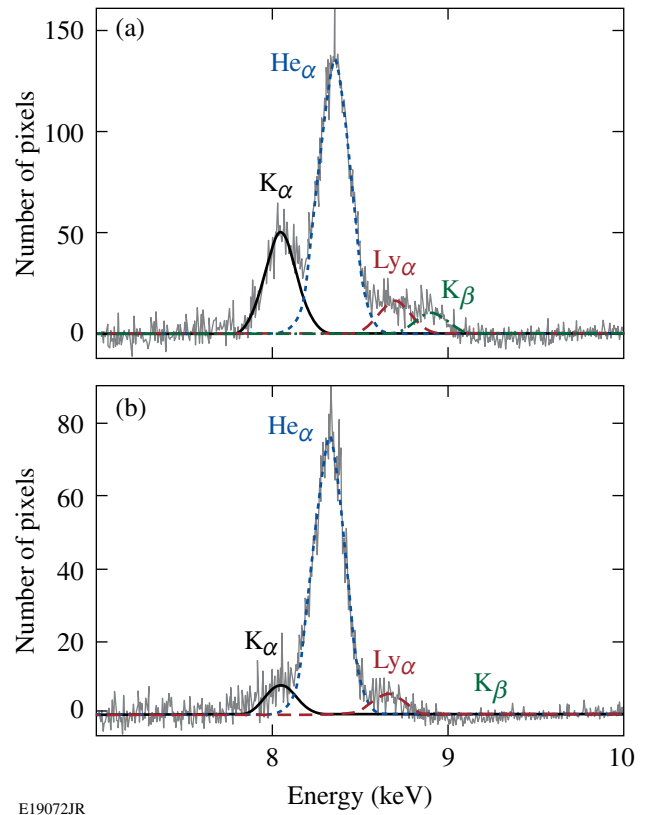


Figure 124.13 Comparison of K-photon emission spectra from (a) $500 \times 500 \times 20\text{-}\mu\text{m}^3$ and (b) $75 \times 75 \times 5\text{-}\mu\text{m}^3$ Cu targets irradiated with $E_L = 1000\text{-J}$, $\tau_p = 10\text{-ps}$ laser pulses.

The $75 \times 75 \times 5\text{-}\mu\text{m}^3$ Cu target generates no K_{β} radiation and has a dramatically suppressed K_{α} yield compared to the larger-volume target. The suppressed K-photon yield suggests higher-energy-density conditions and high thermal-electron temperatures in the reduced-mass target. This is expected for these high-energy interaction conditions.^{15–17,30}

The method for calculating $\eta_{L \rightarrow e}$ involves comparing K-photon emission from reduced-mass targets to target-heating calculations and was described previously in Ref. 16. It relies on a significant fraction of the laser-generated hot electrons being trapped by the target potential that develops because of the charge separation that occurs between the hot escaping electrons and the relatively immobile ions.¹² This effect has been studied theoretically¹⁶ and confirmed experimentally.^{15,17,30} The collisional range of MeV electrons in cold, solid-density copper is several hundred microns and is much greater than the target thickness used in the experiment (up to tens of microns). Hot electrons recirculate (reflux) throughout the target, efficiently transferring energy to the target material

until they range out. Capacitance model calculations indicate that hot-electron refluxing efficiencies in these targets reach >90%, making K-photon spectroscopy measurements of the contained hot electrons highly representative of $\eta_{L \rightarrow e}$.

Time-resolved x-ray emission measurements support the electron-refluxing interpretation for $\tau_p = 10$ -ps pulses. Figure 124.14 shows the radiation time history for a $100 \times 100 \times 10$ - μm^3 Cu target irradiated with an $E_L = 1000$ -J, $\tau_p = 10$ -ps pulse. The ultrafast x-ray streak camera was filtered as shown in Fig. 124.14 (inset), providing sensitivity to bremsstrahlung, inner-shell radiation, and thermal ionic-line emission.

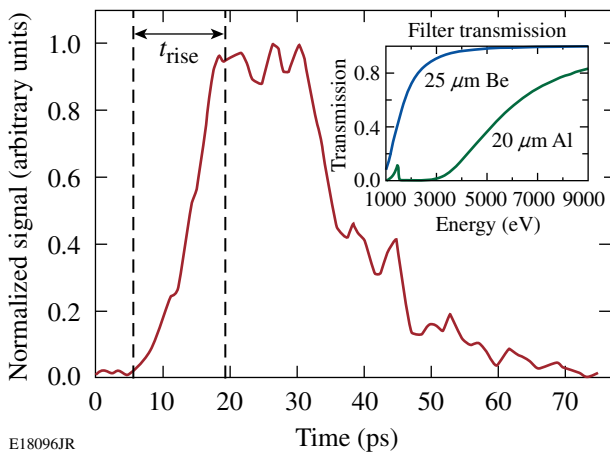


Figure 124.14
Time-resolved x-ray emission from a $100 \times 100 \times 10$ - μm^3 Cu target ($E_L = 1000$ J, $\tau_p = 10$ ps). The transmission functions for the x-ray streak-camera filters are shown (inset).

An increase in radiation emission correlated with the laser-pulse duration, implying an increasing hot-electron number density within the target over this period. This occurs because hot electrons reflux, suggesting constant laser-energy coupling to hot electrons over the entire duration of the incident laser drive. After the laser pulse ends, a radiation afterglow persists for around 20 ps (FWHM) and is likely a combination of inner-shell radiation and thermal radiation, emitted in response to the electron-energy deposition within the target. Thermal radiation persists until the hot electrons thermalize and target decompression dominates.

The absolute K-photon yield generated during the recirculation phase is sensitive to the time-varying number density of hot electrons within the target and target heating. The target-charging process governs the number of hot electrons contained

within the target, while target heating is caused mainly by electron–electron collisional energy deposition from the hot electrons. The ionization state of the target depends on collisions between bound and free conduction electrons. Once the thermal electron temperature inside the target exceeds a few hundred electron volts, the Cu M shell is depleted by thermal ionization, suppressing the plasma’s ability to generate K_β photons. Several hundreds of electron volts are required to deplete the Cu L shell. Time-integrated K-photon emission measurements quantify the target heating, making it possible for $\eta_{L \rightarrow e}$ to be inferred by comparison to target-heating calculations, which are used to predict the ratio of K_β to K_α (K_β/K_α) for a given hot-electron conversion efficiency.

The data show that suppression of the K-photon yield is governed by target energy density. Figure 124.15 shows the experimentally measured values for (K_β/K_α) from reduced-mass targets plotted as a function of the ratio of the laser energy to the target volume (in units of J/mm^3). The data obtained with 10-ps pulses (blue data points) are compared to previously published data with 1-ps pulses (black data points).¹⁷ The measured values for K_β/K_α are normalized to those measured from Cu foils when target heating is negligible ($K_\beta/K_\alpha \sim 0.14$).

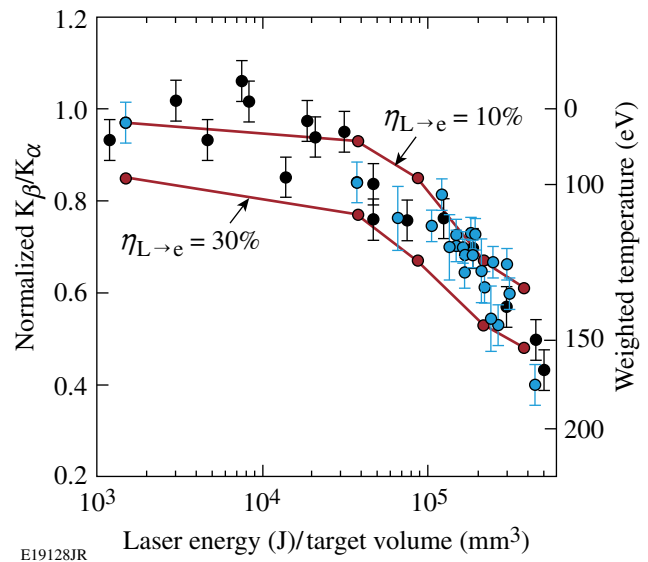


Figure 124.15
Experimental K_β/K_α data [normalized to the cold-material value (left axis)] and inferred bulk-electron temperature (right axis) as a function of laser energy (J)/target volume (mm^3). Data for 10-ps pulses (blue) and 1-ps pulses (black reproduced from Ref. 17); target-heating calculations for $\eta_{L \rightarrow e} = 10\%$ and 30%.

A reduction in the K_β/K_α ratio is observed with increasing laser energy and decreasing target volume. At the lowest target-energy densities studied ($\sim 1.5 \times 10^3 \text{ J/mm}^3$), laser-generated hot electrons interact with cold target material. When the target energy density is increased to greater than $1 \times 10^5 \text{ J/mm}^3$, target heating and thermal ionization suppress K_β/K_α . For target energy densities of $\sim 5 \times 10^5 \text{ J/mm}^3$, K_β/K_α is suppressed to $40 \pm 4\%$ of the cold-material value.

The experimental trend in K_β/K_α with $\tau_p = 10$ -ps pulses is in excellent agreement with previous studies that were performed at significantly lower, joule-class laser energies and picosecond-pulse durations.¹⁷ The same rate of change in K_β/K_α is observed with increasing energy density, independent of laser-pulse duration from $1 \text{ ps} \leq \tau_p \leq 10 \text{ ps}$. For the parameter space studied, variations in laser spot size, laser intensity, laser prepulse, and angle of incidence do not alter this observation. Scaled for laser energy and target mass, the results from these experiments suggest that the same fraction of laser energy is transferred into K-photon-generating hot electrons, independent of laser-pulse duration.

This interpretation is supported by two-dimensional, cylindrically symmetric target-heating calculations using the implicit-hybrid particle-in-cell code *LSP*.³¹ Self-generated fields are included in the model and are calculated self-consistently. Target charging and heating in the calculations were produced by a hot-electron population that had an exponential energy distribution, with a temperature of up to several hundred keV, as defined by the ponderomotive scaling²² and the range of experimental laser irradiation conditions. Spatial and temporal heating variations are accounted for when determining K-photon emission, with the emission probability calculated using the local temperature at the time of emission. The Thomas-Fermi equation-of-state model used was appropriate for the range of temperatures achieved in this experiment.

The calculated values for K_β/K_α as a function of increasing energy density are shown in Fig. 124.15. Calculations were performed assuming $\eta_{L \rightarrow e} = 10\%$ and 30% . The target-heating model predicts suppression in K_β/K_α very similar to that observed in the experiment. The thermal electron temperature inferred from the model for different target interactions is shown in Fig. 124.15 (right axis). This temperature represents a measure of the degree of target heating by hot-electron energy deposition and is weighted by the K-photon emission rate. Weighted thermal electron temperatures approaching several hundred electron volts are achieved in the smallest-mass tar-

gets. Regions of the target that do not emit K photons could reach higher thermal temperatures.

Strong reduction of K_β/K_α in the calculations support the interpretation that in hot Cu-foil targets, thermal ionization causes K-photon suppression with hot-electron refluxing being the dominant energy transfer mechanism. An energy-coupling efficiency to hot electrons of $\eta_{L \rightarrow e} = 20 \pm 10\%$ reproduces the majority of the experimental $\tau_p = 10$ -ps data. This range of $\eta_{L \rightarrow e}$ is in good agreement with previous $\tau_p = 1$ -ps studies at similar laser intensities.^{16,17}

Calculations indicate that around 5% of the hot-electron energy is ohmically dissipated in the high-temperature, low-resistivity plasma. The calculations do not account for fast-proton acceleration by sheath fields at the target surface, with previous measurements indicating 1% to 2% energy-transfer efficiencies to protons.^{32,33} The inferred value for $\eta_{L \rightarrow e}$ therefore represents a lower bound on the energy-conversion efficiency into hot electrons that is required to generate the experimentally observed K-photon emission.

In summary, thin-foil targets have been heated with hot electrons generated by a $\tau_p = 10$ -ps pulse at focused intensities of $I > 10^{18} \text{ W/cm}^2$. K-photon spectroscopy and target-heating calculations show an energy-coupling efficiency into hot electrons of $\eta_{L \rightarrow e} \sim 20\%$ with laser powers from $1 \text{ TW} \leq P_L \leq 210 \text{ TW}$. These measurements are in excellent agreement with previous $\tau_p = 1$ -ps data at similar laser intensities, demonstrating that the energy-conversion efficiency into hot electrons is independent of laser-pulse duration from $1 \text{ ps} \leq \tau_p \leq 10 \text{ ps}$. Ultrafast x-ray streak camera measurements suggest that laser energy is coupled into hot electrons over the entire duration of the incident laser drive. These results are important for the understanding of hot-electron generation in long-pulse, high-intensity laser-solid interactions, such as those found in fast-ignition and high-brightness x-ray-generation experiments.

ACKNOWLEDGMENT

This work was supported by the U.S. Department of Energy Office of Inertial Confinement Fusion under Cooperative Agreement Nos. DE-FC52-08NA28302 and DE-FC02-04ER54789, the University of Rochester, and the New York State Energy Research and Development Authority. The support of DOE does not constitute an endorsement by DOE of the views expressed in this article.

REFERENCES

1. M. I. K. Santala *et al.*, Phys. Rev. Lett. **84**, 1459 (2000).
2. E. L. Clark *et al.*, Phys. Rev. Lett. **84**, 670 (2000).

3. R. A. Snavely, M. H. Key, S. P. Hatchett, T. E. Cowan, M. Roth, T. W. Phillips, M. A. Stoyer, E. A. Henry, T. C. Sangster, M. S. Singh, S. C. Wilks, A. MacKinnon, A. Offenberger, D. M. Pennington, K. Yasuike, A. B. Langdon, B. F. Lasinski, J. Johnson, M. D. Perry, and E. M. Campbell, *Phys. Rev. Lett.* **85**, 2945 (2000).
4. P. K. Patel *et al.*, *Phys. Rev. Lett.* **91**, 125004 (2003).
5. B. A. Remington *et al.*, *Science* **284**, 1488 (1999).
6. M. H. Key, M. D. Cable, T. E. Cowan, K. G. Estabrook, B. A. Hammel, S. P. Hatchett, E. A. Henry, D. E. Hinkel, J. D. Kilkenny, J. A. Koch, W. L. Kruer, A. B. Langdon, B. F. Lasinski, R. W. Lee, B. J. MacGowan, A. MacKinnon, J. D. Moody, M. J. Moran, A. A. Offenberger, D. M. Pennington, M. D. Perry, T. J. Phillips, T. C. Sangster, M. S. Singh, M. A. Stoyer, M. Tabak, G. L. Tietbohl, M. Tsukamoto, K. Wharton, and S. C. Wilks, *Phys. Plasmas* **5**, 1966 (1998).
7. M. Tabak *et al.*, *Phys. Plasmas* **1**, 1626 (1994).
8. D. F. Price *et al.*, *Phys. Rev. Lett.* **75**, 252 (1995).
9. H. Chen, B. Soom, B. Yaakobi, S. Uchida, and D. D. Meyerhofer, *Phys. Rev. Lett.* **70**, 3431 (1993).
10. K. B. Wharton *et al.*, *Phys. Rev. Lett.* **81**, 822 (1998).
11. K. Yasuike *et al.*, *Rev. Sci. Instrum.* **72**, 1236 (2001).
12. S. P. Hatchett, C. G. Brown, T. E. Cowan, E. A. Henry, J. S. Johnson, M. H. Key, J. A. Koch, A. B. Langdon, B. F. Lasinski, R. W. Lee, A. J. MacKinnon, D. M. Pennington, M. D. Perry, T. W. Phillips, M. Roth, T. C. Sangster, M. S. Singh, R. A. Snavely, M. A. Stoyer, S. C. Wilks, and K. Yasuike, *Phys. Plasmas* **7**, 2076 (2000).
13. F. N. Beg *et al.*, *Phys. Plasmas* **4**, 447 (1997).
14. Y. Ping *et al.*, *Phys. Rev. Lett.* **100**, 085004 (2008).
15. W. Theobald, K. Akli, R. Clarke, J. Delettrez, R. R. Freeman, S. Glenzer, J. Green, G. Gregori, R. Heathcote, N. Izumi, J. A. King, J. A. Koch, J. Kuba, K. Lancaster, A. J. MacKinnon, M. Key, C. Mileham, J. Myatt, D. Neely, P. A. Norreys, H.-S. Park, J. Pasley, P. Patel, S. P. Regan, H. Sawada, R. Shepherd, R. Snavely, R. B. Stephens, C. Stoeckl, M. Storm, B. Zhang, and T. C. Sangster, *Phys. Plasmas* **13**, 043102 (2006).
16. J. Myatt, W. Theobald, J. A. Delettrez, C. Stoeckl, M. Storm, T. C. Sangster, A. V. Maximov, and R. W. Short, *Phys. Plasmas* **14**, 056301 (2007).
17. P. M. Nilson, W. Theobald, J. F. Myatt, C. Stoeckl, M. Storm, J. D. Zuegel, R. Betti, D. D. Meyerhofer, and T. C. Sangster, *Phys. Rev. E* **79**, 016406 (2009).
18. L. J. Waxer, D. N. Maywar, J. H. Kelly, T. J. Kessler, B. E. Kruschwitz, S. J. Loucks, R. L. McCrory, D. D. Meyerhofer, S. F. B. Morse, C. Stoeckl, and J. D. Zuegel, *Opt. Photonics News* **16**, 30 (2005).
19. A. G. MacPhee *et al.*, *Phys. Rev. Lett.* **104**, 055002 (2010).
20. F. Perez *et al.*, *Phys. Rev. Lett.* **104**, 085001 (2010).
21. A. J. Kemp, Y. Sentoku, and M. Tabak, *Phys. Rev. Lett.* **101**, 075004 (2008).
22. S. C. Wilks *et al.*, *Phys. Rev. Lett.* **69**, 1383 (1992).
23. K. U. Akli, S. B. Hansen, A. J. Kemp, R. R. Freeman, F. N. Beg, D. C. Clark, S. D. Chen, D. Hey, S. P. Hatchett, K. Highbarger, E. Giraldez, J. S. Green, G. Gregori, K. L. Lancaster, T. Ma, A. J. MacKinnon, P. Norreys, N. Patel, J. Pasley, C. Shearer, R. B. Stephens, C. Stoeckl, M. Storm, W. Theobald, L. D. Van Woerkom, R. Weber, and M. H. Key, *Phys. Rev. Lett.* **100**, 165002 (2008).
24. V. Bagnoud, I. A. Begishev, M. J. Guardalben, J. Puth, and J. D. Zuegel, *Opt. Lett.* **30**, 1843 (2005).
25. V. Bagnoud, J. D. Zuegel, N. Forget, and C. Le Blanc, *Opt. Express* **15**, 5504 (2007).
26. J. Delettrez, R. Epstein, M. C. Richardson, P. A. Jaanimagi, and B. L. Henke, *Phys. Rev. A* **36**, 3926 (1987).
27. C. Stoeckl, W. Theobald, T. C. Sangster, M. H. Key, P. Patel, B. B. Zhang, R. Clarke, S. Karsch, and P. Norreys, *Rev. Sci. Instrum.* **75**, 3705 (2004).
28. A. Pak *et al.*, *Rev. Sci. Instrum.* **75**, 3747 (2004).
29. C. Stoeckl, W. Theobald, P. A. Jaanimagi, P. Nilson, M. Storm, J. A. Delettrez, R. Epstein, T. C. Sangster, D. Hey, A. J. MacKinnon, H.-S. Park, P. K. Patel, R. Shepherd, J. Green, K. L. Lancaster, and P. A. Norreys, *Bull. Am. Phys. Soc.* **52**, 67 (2007).
30. S. D. Baton *et al.*, *High Energy Density Phys.* **3**, 358 (2007).
31. D. R. Welch *et al.*, *Phys. Plasmas* **13**, 063105 (2006).
32. L. Robson *et al.*, *Nat. Phys.* **3**, 58 (2007).
33. J. Fuchs *et al.*, *Nat. Phys.* **2**, 48 (2006).

Measurement of the Self-Phase Modulation on OMEGA

Introduction

The safe operation of a multikilojoule-class laser system requires that the accumulated nonlinear phase remain low enough to avoid beam filamentation and resulting damage to the laser-amplifier glass. A rule of thumb for infrared lasers is to keep the so-called ΔB -integral below 2 radians,¹ where the B -integral is given by

$$B(t) = \frac{2\pi}{\lambda} \int_0^L \gamma(z) \times I(z,t) \times dz \quad (1)$$

for a wavelength λ , optical path length L , nonlinear coefficient γ , and intensity $I(z,t)$, which equals the power divided by the area $P(z,t)/A(z)$. While ΔB , which is calculated per stage, where a stage is defined as all of the components between sequential spatial filters, is of most interest, a potentially more easily measured quantity is the ΣB of the system or the sum of B -integral through all stages of the system.² The protocols for safe operation become particularly important on a system like LLE's OMEGA laser. The OMEGA Laser System consists of 60 beamlines with nine amplification stages employing Nd:phosphate glass (LHG8). Each beamline typically produces about 800 J of infrared energy ($\lambda_{IR} = 1053$ nm) in a 1-ns super-Gaussian pulse. This energy is converted to the UV ($\lambda_{UV} = 351$ nm) by frequency tripling in KDP crystals with approximately 60% conversion efficiency. The temporal pulse shape is adjusted from shot to shot as specified by the principal investigator. Some of these pulse shapes have rapid changes in intensity that can increase the self-phase modulation (SPM) beyond acceptable limits.

Before any of these pulse shapes is propagated down the system, a computer code that incorporates the Frantz–Nodvik model of light propagation in a laser amplifier chain³ simulates the pulse through the system. These simulations have been extensively tested with respect to the temporal pulse shape. The code also predicts the SPM experienced by the pulse due to the B -integral. By introducing an imaging spectrometer at the output of the laser system, it is possible for the first time

to directly compare the model's prediction of the ΣB -integral with a shift in the laser frequency.

The change in instantaneous frequency, $\Delta\nu$, of the pulse caused by SPM is given by⁴

$$\Delta\nu(t) = -\frac{1}{2\pi} \frac{dB(t)}{dt} = -\frac{1}{\lambda} \int_0^L \frac{\gamma(z)}{A(z)} \times \frac{dP(z,t)}{dt} \times dz. \quad (2)$$

Therefore, the instantaneous change in the optical frequency is proportional to the time derivative of the B -integral. If the temporal pulse shape is assumed to be independent of z , the derivative of intensity can be removed from the integrand in Eq. (2) and the instantaneous frequency is simply proportional to dP/dt . This assumption is not valid in most laser amplifier systems. Typically a low-energy pulse injected at the front end of the system is continuously amplified as it propagates. On OMEGA, a single laser pulse feeds all 60 beamlines. The intensity increases as the beam passes through an amplifier stage and then decreases as the beam is split to feed subsequent amplifier stages. The pulse shape, injected at the input of the system, is typically a monotonically increasing temporal ramp. The leading edge of this ramp is preferentially amplified relative to the trailing edge because of the gain–saturation dynamics of the glass amplifiers. Depending on the exact shape of the input pulse, the output pulse shape can be a rising ramp, a super-Gaussian flattop, or a falling ramp. For the purposes of this article, only Gaussian and flattop pulses will be considered. The correct way to handle all these pulse shapes is to calculate $\Delta\nu(z)$ at every point in the laser-amplifier chain and produce an integrated frequency shift for the entire system. This ability is incorporated in the laser system model mentioned above.

Based on temporal and spatial measurements that can be made on the system, we have verified the predictions of the model both in terms of pulse shape and ΣB -integral. Additionally, we have demonstrated that $\Delta\nu$ is approximately proportional to dP/dt as measured in the UV at the output of the laser chain. This relationship is the basis of an empirical analysis

that assumes that the intensity is independent of z . Although this empirical analysis is less accurate than the full-system model, it has the advantage of being available immediately after a shot has been taken, as opposed to more than 1 h for a full simulation. Therefore, this relationship provides a real-time diagnostic that can immediately determine if the laser system is being operated safely. The agreement between the empirical model and the measurements is sufficient for a “go/no-go” decision in terms of shot operations.

The primary modeling tool used here—the *RAINBOW* code—calculates energy transport in solid-state laser systems and uses ray tracing to propagate a pulse through all components of a laser chain. Laser amplifiers are modeled by numerically solving the Frantz–Nodvik³ equations as modified by Avizonis and Grotbeck⁵ on a time-resolved basis for one or more locations in the aperture of the laser. Arbitrary spatial and temporal pulse shapes may be input, allowing for detailed predictions of the spatial and temporal shapes of the laser output. Gain saturation is modeled using a variant of the two-ion model⁶ derived from fits to gain-saturation data.⁷ Disk- and rod-geometry gain elements are modeled. Passive losses are input for each component. Frequency conversion to the third harmonic uses intensity look-up tables from *MIXER* code⁸ calculations.

RAINBOW accurately tracks the accumulated phase retardation of each temporal element of each ray (the “ B ” integral) and includes a phenomenological model of spatial-filter transmission.⁹ Using the determined SPM, it calculates the output pulse spectrum by a Fourier transformation.

Measurement

The temporal pulse shape is measured at both the input and output of the system. After an initial temporal pulse-shaping system, the infrared pulse shape is measured with either an 18-GHz InGaAs photodiode¹⁰ or a streak camera with an S-1 photocathode. The IR measurements are used as the input to the model. At the output of the system, the intensity as a function of time is measured for each of the 60 beamlines on OMEGA with a set of six streak cameras that have a 50-ps temporal resolution.¹¹ Figure 124.16 shows a measured IR pulse shape at the input of the system (scaled to match the peak UV power), a predicted UV pulse shape at the end of the system, and a measured UV output pulse. The excellent agreement between the model and the measurement provides an experimental verification of the model. In addition, an imaging spectrometer measures the UV spectra of all 60 beams with a 2.5-pm (7.6-GHz) resolution.¹² These two sets of measurements can be

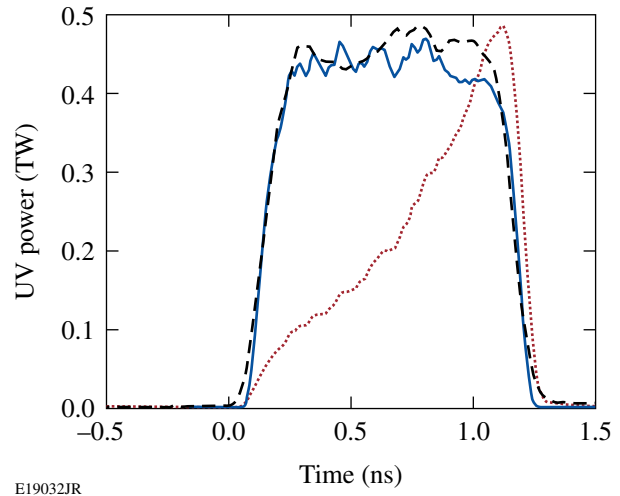


Figure 124.16

The temporal UV pulse shape at the output of the system as measured by the streak cameras (dashed black curve) matches the predicted pulse shape (solid blue curve) derived from the rescaled input IR pulse (dotted red curve).

combined to demonstrate a linear relationship between dP/dt and the frequency shift caused by SPM.

When relatively benign pulse shapes are propagated on the OMEGA Laser System, such as a 200-J, 2-ns square pulse, only negligible amounts of additional bandwidth are generated. Any observed broadening represents the instrument response function of the spectrometer with a full width, $\Delta\nu$, at 1/20th of the peak of 20 GHz. In contrast, the most-pronounced frequency shifts occur when the amplifier chains generate 40 J of UV energy in a 100-ps FWHM asymmetric Gaussian pulse given approximately by

$$P(t) = P_0 \times e^{-[(t-t_0)/\tau]^2}, \quad (3)$$

where $\tau = 49$ ps if $t < t_0$ and $\tau = 80$ ps if $t \geq t_0$. In this case dP/dt is non-negligible (>1 GW/ps) for most of the duration of the pulse, so most of the energy is shifted out of the narrow bandwidth defined by the instrument response function. Figure 124.17 shows the spectra from three different laser shots. The dashed green curve from a 63-J, 3-ns square pulse essentially represents the instrument-response function. The solid blue curve, from the 100-ps pulse described above, shows significant spectral broadening.

Similar shifts occur with 1-ns square pulses that rise to the same intensity as the 100-ps pulses with approximately the same rise time. For the 1-ns square pulses, however, most of the pulse energy remains within a narrow spectral bandwidth defined by a monochromatic seed laser because dP/dt

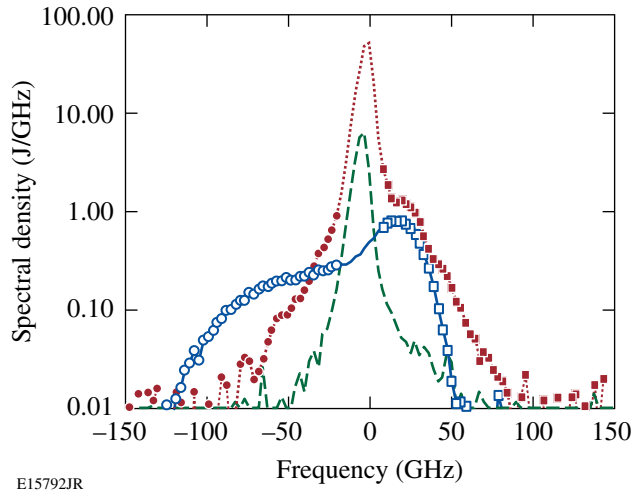


Figure 124.17

The UV spectrum at the output of the system for a 1-ns, 556-J square pulse (dotted red curve), a 100-ps, 48-J pulse (solid blue curve), and a 3-ns, 63-J square pulse (dashed green curve). The squares represent spectral components that have been frequency upshifted; the circles and dots have been downshifted. The 3-ns pulse does not undergo SPM.

is approximately zero (<1 GW/ps) over much of the pulse. The 100-ps pulses produce frequencies that are shifted by as much as 50 GHz from the laser carrier frequency. The integrated effective red and blue spectral shifts for each beamline can be determined from the spectral measurements. From Eq. (2), it can be shown that the rising edge of a pulse ($dP/dt > 0$) gives rise to a red shift ($\Delta\nu < 0$) and the falling edge ($dP/dt < 0$) generates a blue shift ($\Delta\nu > 0$). An effective $\langle dP/dt \rangle$ for the rising edge of the UV pulse is determined by computing a normalized, weighted integral of the time derivative of the power from the 10% to the 80% points on the rising edge:

$$\left\langle \frac{dP_{UV}}{dt} \right\rangle_{\text{rise}} = \frac{\int_{0.1 P_{\max}}^{0.8 P_{\max}} \frac{dP_{UV}(t)}{dt} \times P_{UV} \times dt}{\int_{0.1 P_{\max}}^{0.8 P_{\max}} P_{UV} \times dt}. \quad (4)$$

A similar equation can be generated for the falling edge.

Just as the temporal pulse shape can be divided into rising and falling edges, the UV spectra can be divided into red and blue components by determining where energy has been shifted to lower or higher frequencies. To calculate the frequency-shifted spectra, the instrument response function was scaled to represent the same energy as was measured for

each beamline. The scaled waveform $S_{\text{resp}}(\nu)$ was subtracted from the measured waveform $S_{\text{meas}}(\nu)$:

$$S_{\Delta}(\nu) = [S_{\text{meas}}(\nu) - S_{\text{resp}}(\nu)]. \quad (5)$$

Anywhere the result is positive represents frequency-shifted energy. Negative numbers represent energy that remained at the center-line frequency of the laser, ν_0 . An average, downshifted frequency $\langle \nu_- \rangle$ is defined in a manner similar to $\langle dP/dt \rangle_{\text{rise}}$:

$$\langle \nu_- \rangle = \frac{\int_{-\infty}^{\nu_0} \nu \times S'_{\Delta}(\nu) \times d\nu}{\int_{-\infty}^{\nu_0} S'_{\Delta}(\nu) \times d\nu}, \quad (6)$$

where $S'_{\Delta} = S_{\Delta}$, if $S_{\Delta} > 0$, and $S'_{\Delta} = 0$, if $S_{\Delta} < 0$. In analogy with the temporal pulse shape, an average upshifted frequency $\langle \nu_+ \rangle$ can be similarly defined. The spectral and temporal measurements were combined by pairing $\langle dP/dt \rangle_{\text{rise}}$ with $\langle \nu_- \rangle$ and $\langle dP/dt \rangle_{\text{fall}}$ with $\langle \nu_+ \rangle$. This pairing follows the premise that the rising edge generates red shifts and the falling edge generates blue shifts. When the spectral shifts, recorded for both 1-ns and 100-ps pulses, are plotted versus $\langle dP/dt \rangle$, we find a linear relationship with a slope of -7.8 GHz-ns/TW as shown in Fig. 124.18. As expected, the intercept is approximately zero, which indicates that there is no frequency shift when the intensity is constant. If the amplifier system was characterized by constant power, area, and uniform optical material properties, the slope of the fit in Fig. 124.18 would be directly proportional

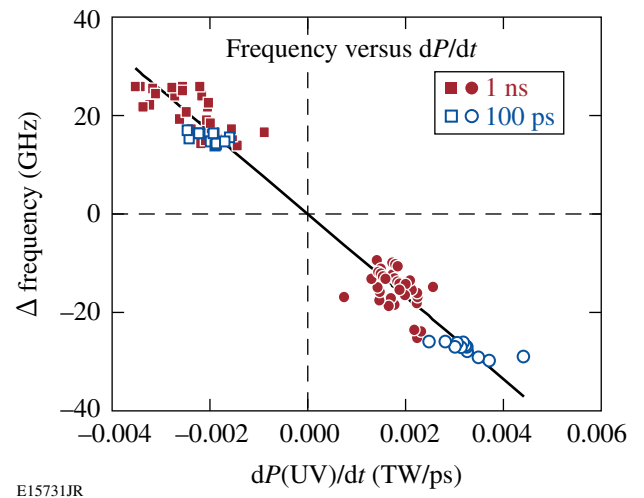


Figure 124.18

Combined plot of $\langle \nu_- \rangle$ versus $\langle dP_{\text{rise}}/dt \rangle$ and $\langle \nu_+ \rangle$ versus $\langle dP_{\text{fall}}/dt \rangle$. Data were acquired for both 100-ps double-Gaussian pulses and 1-ns super-Gaussian pulses.

to the nonlinear coefficient of the material, γ . The evolving temporal pulse shape in the amplifier chain implies, however, that the slope represents an effective aggregate value. The fact that there is a linear relationship that extends over different pulse shapes, beamlines, and beam energies is indicative of the reproducibility of the laser system configuration. The utility of the slope lies in the reconstruction of the spectrum from the temporal pulse shape and the extraction of the ΣB -integral from the measured spectrum.

The slope relates the average frequency shift to the average dP/dt . If the relation holds in detail, the same slope relates the instantaneous frequency to the instantaneous dP/dt . The quantity dP/dt was therefore calculated for every time interval dt in the temporal waveform and mapped, via the fitted slope, to a frequency shift. For the simulated curve, dP/dt was derived from the UV power calculated at the end of the amplifier chain by the system model based on the measured IR input pulse. The energy associated with that frequency shift is given by $P(t)dt$. For comparison with the measured spectrum, this energy is distributed over all frequencies using the instrument response function centered at the instantaneous frequency. Finally, the full spectrum is computed by summing the contributions of all time intervals. The result (Fig. 124.19) shows a comparison of the calculated spectra using this technique as derived from the temporal pulse shape (red curve with diamonds) with the directly measured spectra (black curve with \times 's) and the spec-

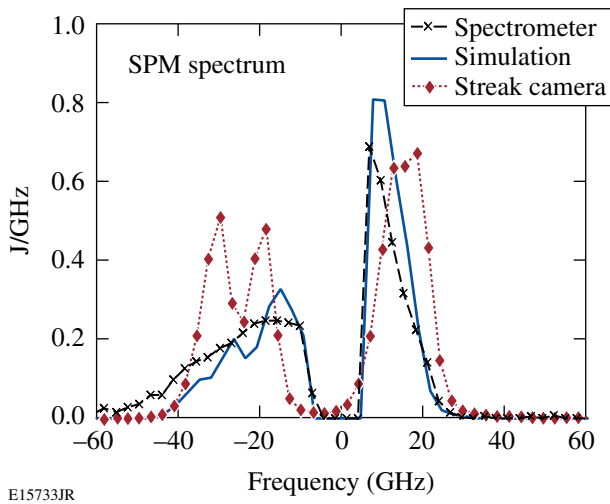


Figure 124.19

A comparison of the frequency-shifted spectra derived from the spectrometer (black curve with \times) with that derived from dP/dt as measured by the streak camera (red curve with diamonds) and predicted by the system model (solid blue curve). Frequencies within the resolution bandwidth of the spectrometer have been removed to highlight the shifted frequencies.

trum predicted for the full-system model (solid blue curve). In all three curves, the frequency components with spectral shifts less than ± 6 GHz, corresponding to the spectrometer resolution, have been removed to highlight the SPM-induced frequencies. The agreement is remarkably good despite violating the assumption about the constancy of the intensity throughout the system.

There is even better agreement between the model-generated spectrum and the measured spectrum. To achieve this agreement, the measured IR pulse shape at the input of the system had to be deconvolved with the 20-ps impulse response of the streak camera used to measure the pulse shape. This deconvolved pulse shape was applied to the laser system model to generate the predicted spectrum. The fact that deconvolution was necessary to match the measured spectrum indicates the high sensitivity of the spectroscopic measurement.

The IR and UV streak cameras and the UV spectrometer have been permanently installed on the system and are monitored on every shot. To further verify the model, a UV streak camera coupled to a spectrometer was temporarily installed to measure the time-resolved spectrum of the UV beam.¹³ The centroid of the UV spectrum increases by approximately 0.2 \AA from the nominal 3510.1 \AA on the rising edge and decreases by 0.1 \AA on the falling edge. The UV power history had a double Gaussian shape with a faster rising edge and slower falling edge as indicated by the dotted red curve in Fig. 124.20. The experimentally measured spectral shifts (black \times 's) closely

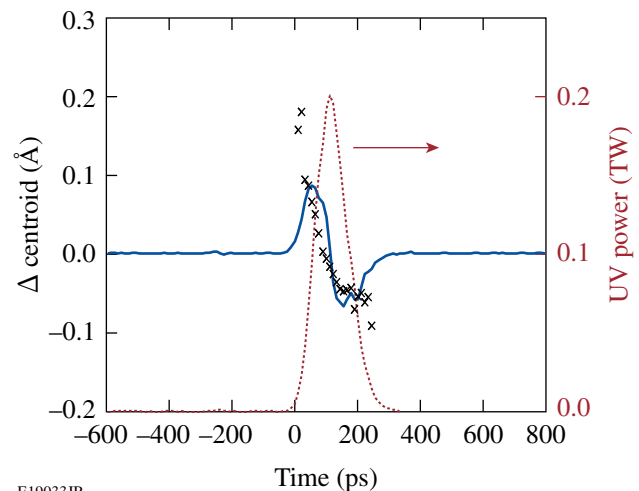


Figure 124.20

The time-resolved centroid of the UV spectrum (black \times 's) matches the derivative of the UV scaled by the constant 32 \AA ps/TW (solid blue curve). The UV temporal shape is overlaid in red (dotted)

match the scaled temporal derivative of the UV power (solid blue curve). This verifies the temporal associations assumed in compiling Fig. 124.18.

These measurements help ensure the safety of the laser system. A scenario for safe operation of the laser system would be as follows: The IR pulse shape is measured at the input of the system, and the instrument temporal response is deconvolved to produce a high-bandwidth estimate of the input shape. This input pulse shape is processed by the model to determine if the pulse shape can be safely propagated through the system. The laser system is then fired and the spectrum is acquired. The measured SPM spectrum can then be converted into a ΣB -integral number to verify the pre-shot prediction.

Conclusion

We have, for the first time, demonstrated the ability to directly monitor the contribution of SPM to the spectrum at the output on a multikilojoule laser system. We have also demonstrated for the first time, to our knowledge, a direct measurement of the important laser parameter ΣB . This provides a real-time diagnostic that can be used to ensure safe operation of the system. This is particularly important as more-complex pulse shapes employing multiple pickets (i.e., 100-ps pulses preceding longer shaped pulses)¹⁴ are deployed on the system.

ACKNOWLEDGMENT

This work was supported by the U.S. Department of Energy Office of Inertial Confinement Fusion under Cooperative Agreement No. DE-FC52-08NA28302, the University of Rochester, and the New York State Energy Research and Development Authority. The support of DOE does not constitute an endorsement by DOE of the views expressed in this article.

REFERENCES

1. D. C. Brown, in *High-Peak-Power Nd:Glass Laser Systems*, edited by D. L. MacAdam, Springer Series in Optical Sciences (Springer-Verlag, New York, 1981), Vol. 25, Chap. 7, Sec. 7.4, p. 214.
2. Common usage of the term “ B ”-integral: ΔB is always the B -integral accumulated between laser stages, usually defined as pinhole-to-pinhole. ΔB determines the damage threat from small-spatial-scale self-focusing and should never exceed 2 rad. ΣB refers to the total B -integral through the entire laser system from oscillator to target. It usually is a determining factor for the focal-spot size. It regulates the growth of the highest-frequency ripple that can make it through all of the pinholes. When used alone, B can refer to either ΔB or ΣB and is used when no distinction is necessary.
3. L. M. Frantz and J. S. Nodvik, *J. Appl. Phys.* **34**, 2346 (1963).
4. Y. R. Shen, *The Principles of Nonlinear Optics* (Wiley, New York, 1984), p. 242.
5. P. V. Avizonis and R. L. Grotbeck, *J. Appl. Phys.* **37**, 687 (1966).
6. C. Bibeau, “Evaluation of the $^4I_{11/2}$ Terminal Level Lifetime for Several Neodymium-Doped Laser Crystals and Glasses,” Ph.D. thesis, Lawrence Livermore National Laboratory, 1995.
7. S. M. Yarema and D. Milam, *IEEE J. Quantum Electron.* **QE-18**, 1941 (1982).
8. R. S. Craxton, *IEEE J. Quantum Electron.* **QE-17**, 1771 (1981).
9. J. Trenholme *et al.*, Shiva Nova CP&D Interim Report, Laser Fusion Program, Lawrence Livermore National Laboratory, Misc. 107, 2-3-2-324 (1977).
10. J. R. Marciante, W. R. Donaldson, and R. G. Roides, *IEEE Photonics Technol. Lett.* **19**, 1344 (2007).
11. W. R. Donaldson, R. Boni, R. L. Keck, and P. A. Jaanimagi, *Rev. Sci. Instrum.* **73**, 2606 (2002).
12. W. R. Donaldson, M. Millecchia, and R. Keck, *Rev. Sci. Instrum.* **76**, 073106 (2005).
13. S. P. Regan, D. K. Bradley, A. V. Chirokikh, R. S. Craxton, D. D. Meyerhofer, W. Seka, R. W. Short, A. Simon, R. P. J. Town, B. Yaakobi, J. J. Carroll III, and R. P. Drake, *Phys. Plasmas* **6**, 2072 (1999).
14. V. A. Smalyuk, V. N. Goncharov, K. S. Anderson, R. Betti, R. S. Craxton, J. A. Delettrez, D. D. Meyerhofer, S. P. Regan, and T. C. Sangster, *Phys. Plasmas* **14**, 032702 (2007).

Large-Aperture, Plasma-Assisted Deposition of Inertial Confinement Fusion Laser Coatings

Introduction

As inertial confinement fusion (ICF) laser systems continue to evolve, the need for large-aperture optical coatings suitable for use in vacuum continues to increase.^{1,2} Laser pulses that are temporally compressed to the picosecond scale or shorter must propagate in vacuum because of *B*-integral and self-focusing effects.³ While reducing the oxygen backfill during silica evaporation may make multilayer coatings less tensile, traditional electron-beam-deposited coatings tend to experience tensile stress failures in vacuum environments.⁴ More-energetic techniques such as magnetron sputtering, ion-beam sputtering, and ion-assisted deposition result in films with compressive stresses, but these techniques tend to have difficulties with low laser-damage resistance, high film stresses, and/or scale-up to large apertures.^{2,5,6} It is essential for ICF laser-system components to establish a coating process that is stable, with a low-compressive stress in vacuum, and a high laser-damage resistance, particularly for picosecond-scale pulses.

This effort focuses on the development and implementation of a hafnia/silica coating process for meter-scale optical coatings with a controlled compressive stress and high laser-damage resistance. Establishing a low-magnitude compressive stress in the coating is critical for large optics to avoid tensile stress failures while maintaining the optical surface figure without unacceptably thick, heavy, and expensive substrates. A plasma source utilizing a lanthanum hexaboride cathode (LaB₆) was selected for modification of the film because of its low defect density, smooth resulting film structure, and high plasma current necessary for densification of hafnia.^{7,8} In this article, results using a single plasma source to modify electron-beam-deposited coatings are presented. Deposition conditions were modified to provide controlled film stresses and high laser-damage thresholds under various wavelengths and pulse durations. This work was then adapted to develop and implement a dual-plasma-source system in a 72-in. coating chamber, suitable for processing meter-scale optics. This process has been used to coat a 0.8-m mirror for use in vacuum at 1053 nm with a 10-ps pulse duration on the OMEGA EP Laser System.

Background

Ion-assisted deposition (IAD) and plasma-assisted deposition, or plasma-ion-assisted deposition (PIAD), have been used to create environmentally stable optical coatings, coating processes suitable for use on temperature-sensitive substrates, and more mechanically durable coatings.^{9–12} These processes utilize an ionized gas that is accelerated with a magnetic field toward the substrate surface during the coating process. Some ion sources can operate on O₂ gas alone, while others require the addition of a neutral gas, such as argon.^{7,8,10,13,14}

Using ion and plasma sources to modify a standard electron-beam evaporation process provides a significant benefit by introducing many additional control variables that may be used to influence film properties such as humidity stability, film stress, mechanical durability, and material refractive indices. Evaporation is a low-energy deposition process, leading to porous coatings that adsorb moisture, making the optical thickness of the film, as well as the coating stress, a function of the relative humidity in the use environment.¹² Variables such as beam voltage, current, gas selection, and gas flow, in addition to source location and pointing, can be utilized to alter these film properties by transferring momentum from incident ions to the condensing film, altering the structure, and collapsing the pores present in the coating.¹⁵ The introduction of these variables requires care in determining the appropriate operating conditions for each to achieve the desired film performance without negatively influencing other film characteristics.

The choice of gas used in a plasma or ion process can have a significant impact on the resulting film densification. Ions with greater mass provide a correspondingly greater momentum, resulting in additional influence on the condensing film structure.^{10,16} The deposition of oxide films by evaporation typically requires the addition of oxygen to the vacuum environment, introducing it directly into the chamber, where it is dispersed. By passing the oxygen through an ion or plasma source, the gas is ionized and accelerated, imparting momentum to the oxygen molecules, leading to densification of the growing film

as the oxygen impacts the surface. As greater densification is required, more argon may be used in the plasma to benefit from its greater atomic mass. If a further increase in momentum is required, higher-atomic-mass gases such as krypton or xenon may be used to provide additional ion momentum. As the relative content of oxygen is decreased, however, the film must be carefully evaluated to prevent an increase in optical absorption, leading to a reduced laser-damage threshold.

Plasma or ion-beam current is simply related to the flow of ions, each of which carries a charge equivalent to the charge of an electron. Increased current in a plasma- or ion-assisted process tends to provide greater densification of the coating being deposited without the risk associated with increased absorption, as is the case with increased ion voltage. Since current will influence the film density, it will also play a role in the ultimate stress achieved in the film. In particular, the impact of ions modifies the film porosity and reduces or eliminates the exchange of water vapor, leading to changes in film stress.^{4,15}

The operating voltage of a plasma source determines the energy of an arriving ion at the substrate surface. By increasing the source voltage, higher ion energies and a correspondingly greater densification of the film structure are achieved; however, ions with too high an energy may break atomic bonds in the film, leading to damage of the coating material and the formation of localized absorption sites. Ion voltage may also influence crystalline content in the film since the film structure exhibits characteristics of deposition at a higher temperature with an increased crystallite size; surface roughness and film stress are also modified.¹⁷ Ion beams and plasmas impart energy to the condensing film, causing the displacement of surface atoms and the compaction of the film structure. Using ions to assist the deposition process may lead to energies at the surface equivalent to deposition temperatures in excess of 10^6 K (Ref. 18). This enables one to continuously modify the film structure from a porous, columnar structure realized with electron-beam evaporation to a highly crystalline film in an extremely compressive state resulting from significant ion impingement. This change in film structure is described by structure-zone models with equivalent deposition temperatures.^{19–21} By adjusting the characteristics of the plasma flux and the evaporant conditions, the desired film stress and density may be achieved.

Coating stress is comprised of intrinsic and thermal stresses. The influence of energetic deposition is such that the intrinsic stress becomes significantly more important, able to balance or dominate the thermal stresses present in the film resulting from the differing coefficients of thermal expansion for coating and

substrate materials when depositing at elevated temperatures. The relationship between the film stress and the substrate surface deflection is described by Stoney's equation²²

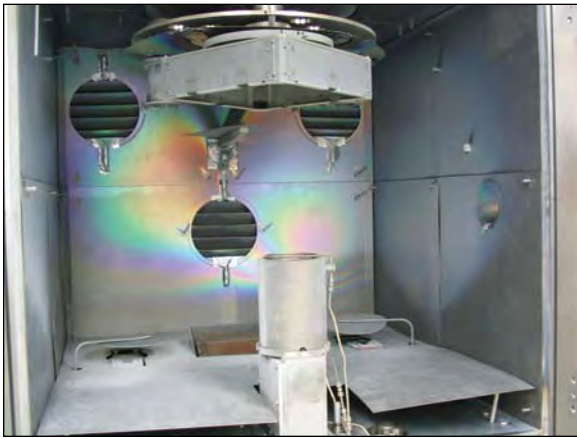
$$\sigma = \frac{E_s t_s^2}{6(1 - \nu_s) t_f R}, \quad (1)$$

where σ is the stress in the film, R is the radius of curvature of the surface, E_s is Young's modulus of the substrate, ν_s is Poisson's ratio for the substrate, and t_f and t_s are the thickness of the film and substrate, respectively. It should be noted that Stoney's equation is an approximation, suitable when $t_f \ll t_s$. Plasma-assisted deposition controls film properties in a way that the deposition process may be tuned for each substrate material with its corresponding thermal stresses by altering the intrinsic stress of the film. The degree of control achievable with a plasma-assisted process will determine the magnitude of the film stress that can be realized and, consequently, the substrate thickness necessary to meet the required surface flatness for an optical component.

The distribution of the ion flux from an ion or plasma source may be modeled much like a deposition source, using a cosine distribution.^{23,24} A primary advantage of plasma sources is that the extraction coil enables one to alter the source flux by changing the strength of the magnetic field in the extractor coil.²⁵ Also, unlike deposition, the influence of the impinging ions is not simply a linear process. To a large extent is a thresholding process, where a minimum ion flux is required to achieve film densification.⁶ The primary goal in this work, however, is the establishment of a low-magnitude compressive-film stress, without the need for complete densification. The source placement and flux-distribution tuning must be performed in such a manner that the film densification and corresponding structure are controlled over the aperture of the substrates.

Experimental Procedure

An initial series of coatings was prepared in a cryo-pumped, 56-in. coating chamber equipped with quartz heater lamps, dual electron-beam guns, multipoint quartz crystal monitoring, and planetary substrate rotation as shown in Fig. 124.21. Granular silicon dioxide was evaporated from a continuously rotating pan, while hafnium metal was deposited in the presence of oxygen from a stationary six-pocket electron-beam gun to form hafnium dioxide. A single Satis PDS plasma source was installed in the chamber at a radius of 15 in. from chamber center to provide a uniform ion flux over the aperture of the substrate.



G9089JR

Figure 124.21

The 56-in. coating chamber with planetary rotation, dual electron-beam guns, and a single Satis PDS plasma source. The plasma source is positioned off-center in the chamber to provide a more-uniform plasma flux over the substrate aperture.

The primary concern with energetically assisting the deposition process for high-peak-power laser applications is that the laser-damage threshold will be compromised, leading to reduced fluence capabilities for the laser.² Hafnia monolayers were deposited on cleaved float glass with an optical thickness of four quarter-waves at 351 nm to form an absentee layer that minimizes the influence of the standing-wave electric field in the film. The cleaved-glass substrate eliminates the effects of substrate fabrication and cleaning processes on laser-damage thresholds.²⁶ The plasma settings for the initial samples were 140 to 180 V/35 A (acceleration voltage/beam current), a nominal 10 sccm of argon gas surrounding the LaB₆ cathode in the plasma source controlled to maintain constant beam current/voltage, and 50 sccm of O₂ gas injected into the plasma using a gas-distribution ring on the top of the source. Chamber pressure was controlled through oxygen backfill to maintain a constant pressure of 4.0×10^{-4} Torr. Laser-damage testing was performed in a standard 1:1 testing configuration at 351 nm at a 0.5-ns pulse duration.²⁷ Finally, x-ray diffraction (XRD) measurements of the hafnia films were collected using a Philips Materials Research diffractometer (MRD) with a CuK α source to evaluate the crystallinity of the hafnia structure. The coated samples were oriented in a near-grazing incidence configuration, with an incident angle $\theta = 2.2^\circ$ and a diffracted angle 2θ incremented in steps of 0.02° , with a 13-s integration time at each position.

The film stress in hafnia monolayers was also evaluated as a function of plasma-assist voltage since this is the primary benefit for large-aperture laser coatings. Hafnia layers with a

140-nm thickness were deposited on 25-mm-diam \times 1-mm-thick BK7 substrates. Surface flatness was measured using a Zygo New View interferometer at controlled relative humidities of 0% and 40%, measuring the uncoated surface of the substrate to avoid the influence of phase effects from the coating. The optics were supported horizontally on a three-point mounting fixture, using equally spaced ball bearings placed at 65% of the radius of the substrate to minimize deflection caused by mounting. The resulting stress in the hafnia films was evaluated as a function of plasma voltage to determine appropriate operating conditions for low-stress coatings.

Development of the plasma-assist process continued with the deposition of multilayer high-reflector coatings using a broad range of deposition conditions, including variations of plasma voltage, current, gas flows, deposition rates, substrate temperature, and chamber pressure. The influence of the deposition conditions on film stress and laser-damage resistance was evaluated to determine optimal deposition conditions. Selected deposition processes were used to deposit high-reflector coatings centered at $\lambda_0 = 1053$ nm on 310-mm-diam \times 14-mm-thick fused-silica substrates for evaluation on an 18-in. Zygo interferometer and a large-aperture laser conditioning station according to National Ignition Facility (NIF) protocol.²⁸

Finally, the plasma-assist process was installed in a 72-in. coating chamber (as shown in Fig. 124.22) utilizing two Thin



G9090JR

Figure 124.22

A Thin Film Solutions Ltd. dual-plasma-source system installed in LLE's 72-in. electron-beam evaporation system. The plasma sources provide a high ion flux over the entire surface of the meter-scale substrates.

Films Solutions Ltd. plasma sources, based on the original Satis PDS source design.^{8,25} Two sources were implemented to ensure adequate plasma flux over the surface of a large optic, given a significantly greater source-to-substrate distance than that in the 56-in. coating chamber, as well as to provide redundancy in the event of a source failure. Custom control software was developed to ramp the source in a series of steps to prevent the poisoning of one source cathode by the operation of the second source. The plasma sources were installed at a radial position of 8.3 in. from chamber center, compromising between maximum ion flux and uniformity. Additional mounting locations were machined in the chamber base plate to provide the ability to tune the flux distribution over the substrate aperture as needed. Uniformity masks were reconfigured to avoid significant impingement of the plasma on the film-correction masks.²³ The sources were operated at 145 V with a beam current of 20 A each, introducing 50 sccm of O₂ during hafnia deposition and 15 sccm of O₂ during silica deposition. Cathode temperatures were kept as low as possible by minimizing the rf power to reduce film defects caused by cathode ejections. Interaction between the sources was determined to be negligible during operation.

Results

Throughout this effort to develop plasma-assisted-deposition processes, the plasma conditions (current, voltage, and gas flows) were modified, as well as chamber conditions (oxygen backfill, deposition rates, and substrate temperature). A qualitative understanding of the influence of each parameter is of primary importance since the process space becomes much larger as the number of process variables is increased. Different chamber configurations will require different operational parameters since the influence of a given plasma voltage, current, and gas flow will be strongly dependent on the source location, distance to the substrate, substrate size, and the substrate motion.

As the use of different gas flows and corresponding chamber pressures was evaluated, one consideration was where to introduce the gas. Oxygen is typically introduced during reactive electron-beam deposition, but the inclusion of a plasma-assist source allows one to introduce some or all of the oxygen through the plasma source. Deposition tests were undertaken with oxygen introduced in the chamber or through the plasma source at different controlled operating pressures. As shown in Fig. 124.23, as the chamber pressure is increased, there is a greater change in optical thickness of the hafnia coating between 0%- and 40%-relative-humidity environments caused by water movement into the pores of the film. By introducing

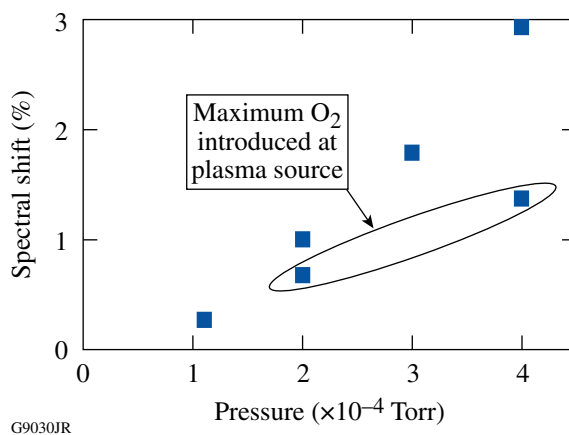


Figure 124.23

Influence of O₂ backfill pressure on the resulting sensitivity of hafnia films to relative humidity. A larger spectral shift between 0% and 40% relative humidity indicates greater film porosity.

the oxygen through the plasma source with all other plasma operating conditions constant, film porosity is reduced 30% to 50%.

It has been found previously that laser-damage thresholds of electron-beam-deposited hafnia improve as the porosity of the film increases.^{29,30} The influence of plasma-assisted deposition on the laser-damage threshold of hafnia coatings was explored for 351-nm light. To minimize the influence of substrate preparation on laser-damage thresholds, coatings were deposited on cleaved float-glass surfaces.²⁶ Laser-damage testing was performed in a standard 1:1 testing configuration at 351 nm at a 0.5-ns pulse duration.³⁰ Laser-damage characterization at 351 nm provides greater sensitivity to changes in film absorption than evaluation at 1053 nm, which tends to be dominated by film defects. These tests demonstrate minimal rate or plasma-voltage influence over the range of parameters tested, as shown in Fig. 124.24. The relatively insignificant change in laser-damage threshold for a plasma voltage in the range of 140 to 180 V indicates the corresponding change in optical absorption of the film must also be negligible. Since the film is deposited with plasma assist, it has a reduced porosity and a correspondingly greater density than a film deposited at the equivalent pressure by electron-beam evaporation. Additionally, the use of plasma assist makes low-porosity deposition no longer necessary to maintain high-laser-damage resistance.^{29,30}

The crystallinity of the hafnia monolayers deposited at 180 V with a 35-A plasma current measured using XRD is shown in Fig. 124.25. The electron-beam-evaporated hafnia exhibits a relatively weak monoclinic crystalline signature, while the crystalline peaks become much more defined as the

ion/evaporant ratio is increased. As the deposition rate of the hafnia is decreased, the relative ion flux is effectively increased and the crystallites grow to approximately 12 nm as calculated using Scherrer's equation.^{30,31} This increase in film crystallinity is equivalent to an increased substrate temperature as described in a structure-zone model.¹⁹⁻²¹ It was determined in a previous study that a reduction in film crystallinity could be correlated with improved laser-damage thresholds for 351-nm light.³⁰ This does not appear to hold true for PIAD films based on the results shown in Figs. 124.24 and 124.25.

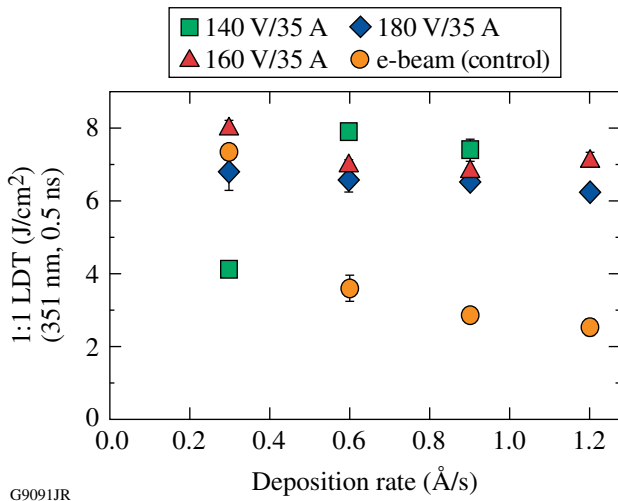


Figure 124.24 Laser-damage thresholds of hafnia deposited with PIAD exhibit minimal deposition-rate dependence, unlike typical electron-beam deposition of hafnia. The control electron-beam coating was deposited with an oxygen backfill pressure of 2×10^{-4} Torr.

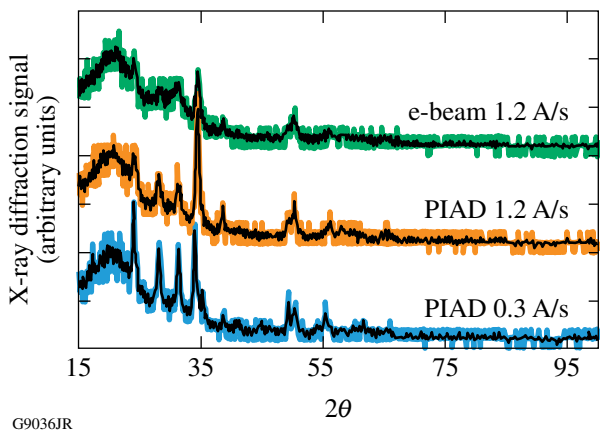


Figure 124.25 X-ray diffraction measurements of hafnia monolayers indicate increasing crystallinity as the plasma/evaporant flux is increased. This may be achieved by increasing the plasma current or decreasing the deposition rate.

The film stress in hafnia monolayers was also evaluated as a function of plasma-assist voltage. Hafnia layers of 140-nm thickness were deposited on 25-mm-diam \times 0.25-mm-thick BK7 substrates. Surface-flatness measurements were performed on a Zygo New View interferometer at relative humidities of 0% and 40%. Using Eq. (1), these measurements were used to calculate the film stress. The resulting stress in the hafnia films is plotted in Fig. 124.26(a) as a function of plasma voltage when operated at 35 A to determine appropriate operating conditions for low-stress coatings. The stress transitioned from a tensile state below 145 V to an increasingly compressive state above this plasma potential. All film stresses for plasma-assisted silica films plotted in Fig. 124.26(b) were found to be compressive, with an increasing compressive stress as the plasma voltage was increased.

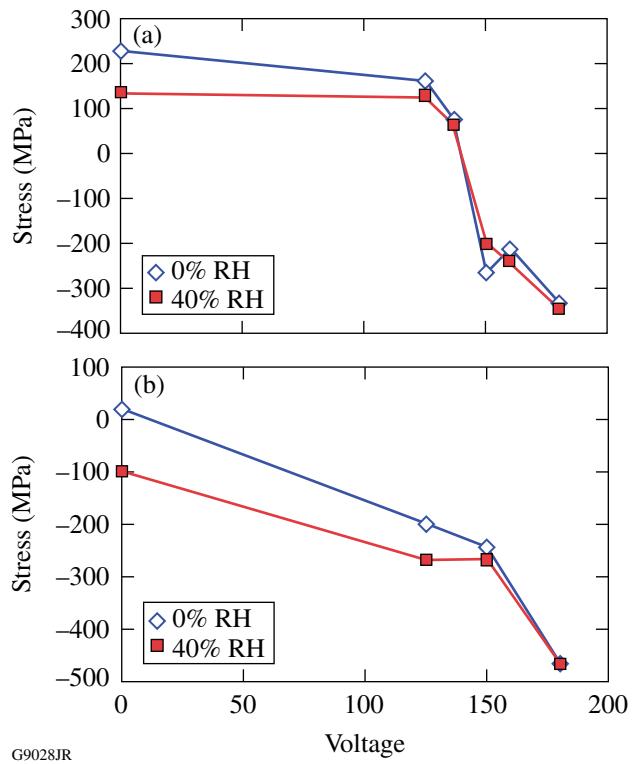
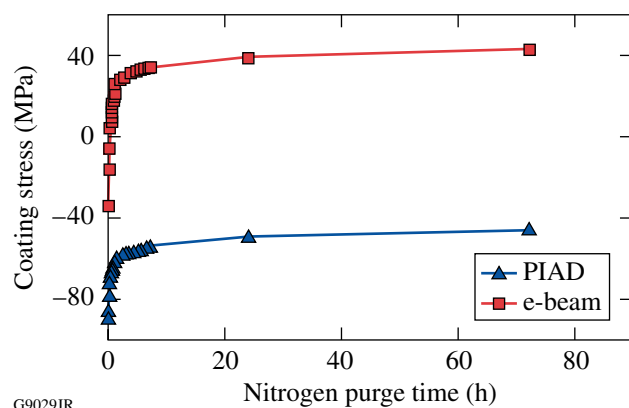


Figure 124.26 (a) Influence of plasma-assist voltage on the stresses in hafnia monolayers. An assist of approximately 145 V at 35 A is sufficient to transition from tensile to compressive stress. (b) Influence of plasma-assist voltage on the stresses in silica monolayers. Note that all silica stresses are compressive, except the evaporated silica (no PIAD) in a dry environment.

Development of the plasma-assist process continued with the deposition of multilayer high-reflector coatings using a broad range of deposition conditions, including variations of plasma voltage, current, gas flows, deposition rates, substrate temperature, and chamber pressure. The influence of the depo-

sition conditions on film stress and laser-damage resistance was evaluated to determine optimal deposition conditions. In general, the addition of energetic ions through PIAD resulted in a more-compressive coating with a reduced sensitivity to relative humidity than a comparable coating produced with only electron-beam evaporation, as shown in Fig. 124.27. The PIAD results shown are from a coating deposited with a 170-V/40-A plasma, leading to greater densification of the film and a reduced sensitivity to humidity. The chamber temperature was adjusted to 140 °C, which is as low as possible while maintaining a controlled, constant temperature during PIAD operation.



G9029JR

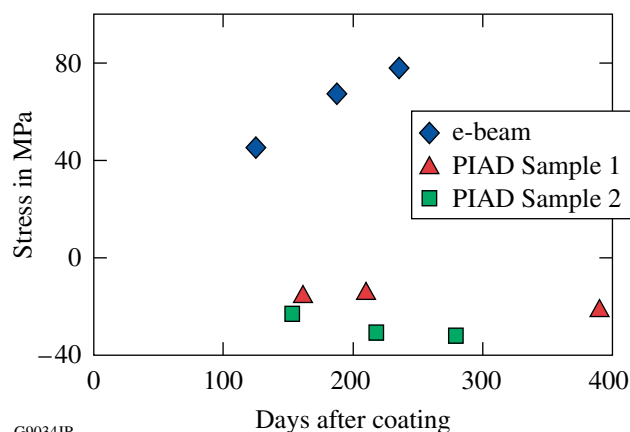
Figure 124.27

Change in film stress for PIAD and electron-beam–deposited coatings as the ambient relative humidity changes from 40% RH to 0% RH. While the % RH of the measurement environment changes almost immediately, the removal of water from the film pores is a much slower process, dependent on the diffusion of water through the film structure. Note that PIAD coatings are more compressive, with a smaller change in film stress as the coating is dried.

The densification of only single materials within multilayer coatings was explored by operation of the plasma source during hafnia or silica layers. Hafnia was considered since it is the primary source of tensile stress, as shown in Fig. 124.26(a). Silica was pursued since it undergoes the most significant change in stress as a function of time.⁴ However, the presence of porous layers between dense diffusion barriers led to irregular water penetration around film defects, leading to subsequent spotting of the coating. Furthermore, the argon backfill required to idle the plasma sources resulted in a poorer vacuum during nondensified layers. The densification of alternating layers was determined to be problematic and not pursued further.

Selected deposition processes were used to deposit high-reflector coatings centered at $\lambda_0 = 1053$ nm on 310-mm-diam \times 14-mm-thick fused-silica substrates for evaluation on an 18-in. Zygo interferometer and large-aperture laser conditioning sta-

tion according to NIF protocol.²⁸ As shown in Fig. 124.28, the stress in the electron-beam–deposited coating continued to become more tensile as the coating aged, with changes in film stress apparent more than six months after deposition. PIAD samples 1 and 2 show a film stress that remained constant, within ± 10 MPa, over an extended duration. A controlled compressive stress with a magnitude of 20 to 30 MPa is ideal to avoid difficulties arising from tensile-stress failures (crazing), while imparting minimal reflected wavefront deformation caused by stress.



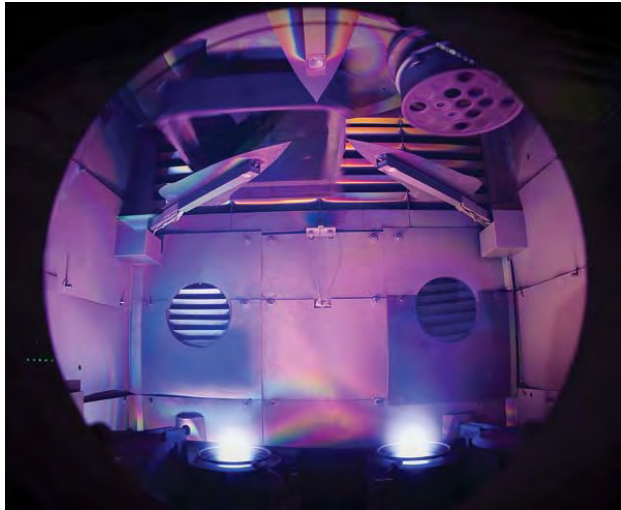
G9034JR

Figure 124.28

Change in film stress for PIAD and electron-beam–deposited coatings at 0% RH as a function of aging. While e-beam–deposited coatings continue to change significantly over periods of months, partially dense PIAD coatings with near-neutral stress maintain a consistent film stress.

The dual-source system was operated at 145 V with a beam current of 20 A from each source, introducing 50 sccm of O₂ during hafnia deposition and 15 sccm of O₂ during silica deposition. Meter-scale high-reflector coatings were produced with a compressive stress of the order of 50 to 80 MPa in a use environment of 0% relative humidity and a laser-damage threshold of 6.7 J/cm² at 1053 nm with a pulse length of 10 ps. Laser-damage testing was performed in an ambient humidity environment at 29° incidence. This process was used to fabricate an 0.8-m mirror, designated as SPHR10, on a BK7 substrate for use in vacuum on the OMEGA EP Laser System, as shown in Fig. 124.29. Measurement of the coated surface indicated 0.38 waves peak-to-valley of surface power on a 1064-nm–wavelength interferometer. Measurement of the film stress for BK7 substrates in a dry environment indicated a stable film stress of approximately 50 MPa. The stress aging of the PIAD coating, as shown in Fig. 124.30, indicated that the aging effects typical of evaporated hafnia silica coatings have been effectively eliminated, even for a PIAD coating with significant porosity and humidity susceptibility.^{4,28} The

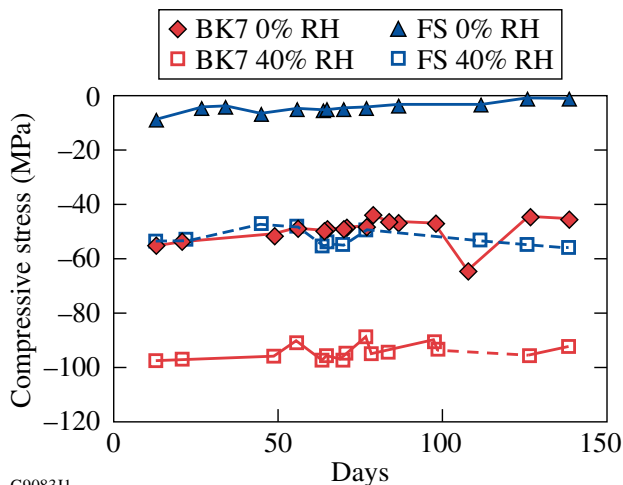
spectral shift in the optical thickness of the coating from a 0%- to 40%-relative-humidity environment was measured as $1.54 \pm 0.14\%$ over a 0.9-m aperture, indicating significant but quite uniform film porosity, although the film was more dense than the reference electron-beam–deposited film with a typical 2.7% spectral shift. The consistency of the film porosity, as determined by the spectral shift in different humidity environ-



G9092JR

Figure 124.29

The dual-source PIAD system in the 72-in. coating chamber was used to deposit the SPHR10 coating. The plasma effectively fills the entire deposition region, providing a uniform densification of the film over the full aperture of the substrate.



G9083J1

Figure 124.30

Stress-aging measurements of PIAD coatings indicate negligible changes in stress as a function of time after deposition. In comparison, the stress of the e-beam–deposited coating in Fig. 124.28 continues to change significantly six months after deposition.

ments, demonstrated that film densification was quite uniform over the substrate aperture, particularly since the film was only partially densified. Laser-damage thresholds for 1053-nm, 1-ns pulses were measured at 22.09 J/cm^2 in a 1:1 defect-targeting mode. The laser-damage threshold for defect-free sites was determined to be 26.67 J/cm^2 , indicating a decrease in laser-damage threshold relative to standard evaporated coatings, which tend to be $>85 \text{ J/cm}^2$ for defect-free sites.^{1,28}

Conclusions

Plasma-assisted deposition provides a means of tuning the film stress of optical coatings while maintaining high-peak-power laser-damage thresholds. Installation of a plasma-assist process is unique for a given deposition system since each chamber configuration will have a different set of optimal operating parameters for neutral film stress based on the substrate size, rotation geometry, radial position of the source, and other considerations. This development effort provides guidance for tuning the process in different systems. Increased plasma voltage leads to greater densification of the film and a more-compressive film stress. The use of more-energetic oxygen, by ionizing it with a plasma source, leads to a denser coating and improved laser-damage thresholds, particularly for lasers in the ultraviolet region of the spectrum, which are more susceptible to film absorption. Likewise, reduced chamber pressures lead to decreased evaporant scattering and a less-porous film structure.

Controlled compressive film stresses of $<50 \text{ MPa}$ can be established and maintained in a dry-use environment on fused-silica substrates through plasma-assisted deposition, providing a means of avoiding tensile-stress failures in vacuum while maintaining high-quality surface flatness of the laser components. A plasma-assist process for multilayer coatings has been demonstrated with a low-magnitude compressive stress utilizing a nominal voltage of 145 V during hafnia and silica deposition, with plasma current being adjusted to achieve the desired film stress and densification. This process was integrated in a 72-in. coating chamber to deposit high-precision coatings over 0.9-m aperture optics. The measured laser-damage threshold for a 29° high-reflector coating is 6.7 J/cm^2 (1053 nm, 10-ps pulse) with a compressive film stress of 50 MPa.

ACKNOWLEDGMENT

The authors wish to express their appreciation to Alex Maltsev for his efforts on the fabrication of extremely high quality, high-aspect-ratio substrates for this study. This work was supported by the U.S. Department of Energy Office of Inertial Confinement Fusion under Cooperative Agreement No. DE-FC52-08NA28302, the University of Rochester, and the New York State Energy Research and Development Authority. The support of DOE does not constitute an endorsement by DOE of the views expressed in this article.

REFERENCES

1. J. B. Oliver, A. L. Rigatti, J. D. Howe, J. Keck, J. Szczepanski, A. W. Schmid, S. Papernov, A. Kozlov, and T. Z. Kosc, in *Laser-Induced Damage in Optical Materials: 2005*, edited by G. J. Exarhos *et al.* (SPIE, Bellingham, WA, 2005), Vol. 5991, pp. 394–401.
2. E. Lavastre *et al.*, in *Optical Interference Coatings*, OSA Technical Digest (Optical Society of America, Washington, DC, 2004), p. TuF3.
3. Y.-H. Chuang, L. Zheng, and D. D. Meyerhofer, *IEEE J. Quantum Electron.* **29**, 270 (1993).
4. H. Leplan *et al.*, *J. Appl. Phys.* **78**, 962 (1995).
5. D. J. Smith *et al.*, in *Laser-Induced Damage in Optical Materials: 2008*, edited by G. J. Exarhos *et al.* (SPIE, Bellingham, WA, 2008), Vol. 7132, p. 71320E.
6. M. Alvisi *et al.*, *Thin Solid Films* **358**, 250 (2000).
7. R. Thielsch *et al.*, *Thin Solid Films* **410**, 86 (2002).
8. F. Placido *et al.*, in *Advances in Thin-Film Coatings for Optical Applications III*, edited by M. J. Ellison (SPIE, Bellingham, WA, 2006), Vol. 6286, p. 628602.
9. H. R. Kaufman and J. M. Harper, in *Advances in Thin Film Coatings for Optical Applications*, edited by J. D. T. Kruschwitz and J. B. Oliver (SPIE, Bellingham, WA, 2004), Vol. 5527, pp. 50–68.
10. M. Kennedy, D. Ristau, and H. S. Niederwald, *Thin Solid Films* **333**, 191 (1998).
11. E. H. Hirsch and I. K. Varga, *Thin Solid Films* **69**, 99 (1980).
12. B. G. Bovard, in *Thin Films for Optical Systems*, edited by F. R. Flory (Marcel Dekker, New York, 1995), pp. 117–132.
13. J. R. Kahn, H. R. Kaufman, and V. V. Zhurin, in *46th Annual Technical Conference Proceedings* (Society of Vacuum Coaters, Albuquerque, NM, 2003), pp. 621–625 (Paper 110).
14. D. E. Morton and V. Fridman, in *Proceedings of the 41st Annual Technical Conference of the Society of Vacuum Coaters* (Society of Vacuum Coaters, Albuquerque, NM, 2003), pp. 297–302 (Paper 53).
15. K.-H. Müller, *J. Vac. Sci. Technol. A* **4**, 184 (1986).
16. J. D. Targove and H. A. Macleod, *Appl. Opt.* **27**, 3779 (1988).
17. G. Atanassov *et al.*, *Thin Solid Films* **342**, 83 (1999).
18. H. Kersten *et al.*, *Vacuum* **46**, 305 (1995).
19. J. V. Sanders, in *Chemisorption and Reactions on Metallic Films*, edited by J. R. Anderson, *Physical Chemistry, A Series of Monographs* (Academic Press, London, 1971), pp. 1–38.
20. J. A. Thornton, in *Modeling of Optical Thin Films*, edited by M. R. Jacobson (SPIE, Bellingham, WA, 1988), Vol. 821, pp. 95–103.
21. B. A. Movchan and A. V. Demchishin, *Fiz. Met. Metalloved* **28**, 653 (1969).
22. G. G. Stoney, *Proc. R. Soc. Lond. A* **82**, 172 (1909).
23. J. B. Oliver and D. Talbot, *Appl. Opt.* **45**, 3097 (2006).
24. H. R. Kaufman, R. S. Robinson, and R. I. Seddon, *J. Vac. Sci. Technol. A* **5**, 2081 (1987).
25. D. Gibson, European Patent No. EP 1 154 459 A2 (14 November 2001).
26. S. Papernov, D. Zaksas, J. F. Anzellotti, D. J. Smith, A. W. Schmid, D. R. Collier, and F. A. Carbone, in *Laser-Induced Damage in Optical Materials: 1997*, edited by G. J. Exarhos *et al.* (SPIE, Bellingham, WA, 1998), Vol. 3244, pp. 434–445.
27. S. Papernov and A. W. Schmid, *J. Appl. Phys.* **82**, 5422 (1997).
28. J. B. Oliver, J. Howe, A. Rigatti, D. J. Smith, and C. Stolz, in *Optical Interference Coatings*, OSA Technical Digest (Optical Society of America, Washington, DC, 2001), p. ThD2.
29. B. Andre, J. Dijon, and B. Rafin, U.S. Patent No. 7,037,595 (2 May 2006).
30. J. B. Oliver, S. Papernov, A. W. Schmid, and J. C. Lambropoulos, in *Laser-Induced Damage in Optical Materials: 2008*, edited by G. J. Exarhos *et al.* (SPIE, Bellingham, WA, 2008), Vol. 7132, p. 71320J.
31. B. D. Cullity, *Elements of X-Ray Diffraction*, 2nd ed. (Addison-Wesley, Reading, MA, 1978).

Improved On-Shot Focal-Spot Measurement on OMEGA EP Using Phase-Retrieval-Enhanced Wavefront Measurements

Introduction

Intensity at the target plane is a critical parameter in many inertial confinement fusion (ICF) experiments conducted on the short-pulse OMEGA EP laser.¹ Measuring the focal-spot intensity at the target plane on a high-energy shot, however, is a challenging task. Remote camera measurements can be made with a sampled diagnostic beam, but it is not easy to account for the effect of the final optics that focus the beam to target and the optics for the diagnostic. For OMEGA EP, a remote wavefront-measurement system has been developed to make on-shot target-plane focal-spot predictions for the short-pulse beams.² Limitations in the wavefront sensor and errors in the calibration and on-shot measurement, however, can lead to erroneous wavefront measurements that in turn yield poor focal-spot predictions.

In many applications where wavefront information is desired, phase-retrieval techniques have been effective in estimating wavefront based on a series of intensity measurements.^{3–7} Often, these measurements are made simultaneously in two different planes, e.g., a pupil plane and a far-field plane, or two or more far-field planes at different defocus distances. A variety of algorithms have been used to estimate the phases of the optical fields in these planes based on the rules of propagation between them. These can generally be classified into two categories: iterative-transform methods and gradient-search methods.⁵ In the former category, an initial guess is made about the phase profile in one plane, and the field is propagated back and forth between the planes with the magnitude of the field being replaced with the measured value and the phase being based on the calculated phase at each iteration.³ In the latter category, a merit function is produced and minimized by utilizing its gradient over a discrete set of variables.^{5,6} Gradient-search algorithms can be point-by-point (independently varying the wavefront at discrete points over the planes of interest) or modal (modifying the coefficients of a modal expansion of the wavefront).

In this article, we demonstrate the use of phase retrieval to improve the focal-spot measurement on OMEGA EP. As

a result of this work, the on-shot focal-spot measurement has been improved to the point that it reliably matches direct measurements of the focal-spot intensity at low energy. This article is organized as follows: OMEGA EP and the on-shot target-plane focal-spot measurement technique are reviewed and initial performance of the focal-spot measurement is assessed; four problems with the focal-spot measurements are described and phase-retrieval techniques for mitigating them are described; the results of applying these improvements to the focal-spot measurement are described with the accuracy and reliability assessed over a population of shot data; and finally, conclusions are presented.

Overview of Focal-Spot Measurement

The focal-spot diagnostic (FSD) was deployed on OMEGA EP to characterize on-shot, target-plane fluence distributions for the short-pulse beamlines. The OMEGA EP short-pulse system uses optical parametric chirped-pulse amplification (OPCPA) to generate a high-energy, high-peak-power laser pulse.¹ A seed pulse is stretched and amplified using both parametric amplification and conventional amplification in the front-end laser system and large-aperture beamline. At its fully amplified level, the beam is stretched to approximately 1-ns duration and amplified to multiple kilojoules. It then propagates into a grating compression chamber (GCC), a large vacuum chamber containing a four-grating pulse compression system, where it is compressed to between 700 fs (best compression) and 100 ps.

Figure 124.31 shows a diagram of one of the compressors in the OMEGA EP short-pulse system, indicating the location of key diagnostics relative to the beam for the on-shot focal-spot measurement. After undergoing amplification, pulse recompression, and wavefront correction, the beam propagates to a leaky diagnostic mirror within the GCC. A small percentage of the beam (~0.5%) transmits through the diagnostic mirror and is provided to a suite of laser diagnostics—the short-pulse diagnostics package (SPDP). The main beam, i.e., the portion reflected from the diagnostic mirror, is transported to the target chamber via a series of mirrors and focused by an $f/2$ off-axis parabola (OAP).

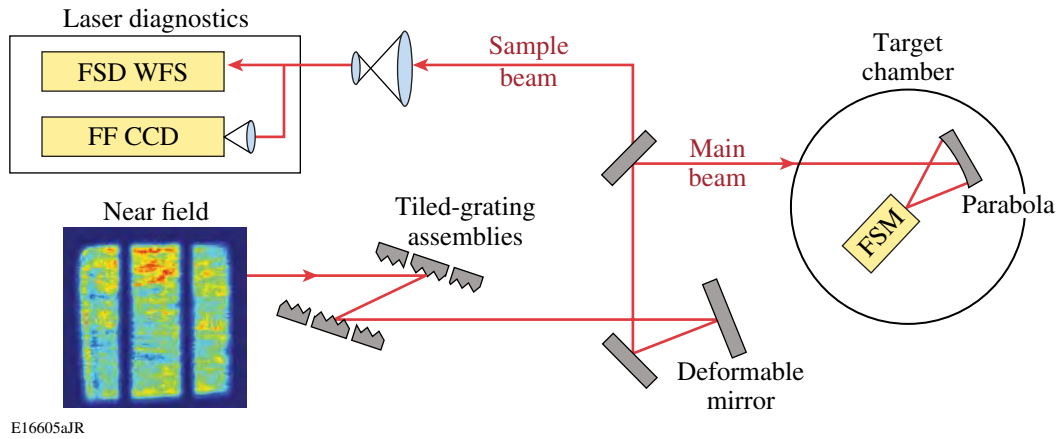


Figure 124.31

A diagram of the OMEGA EP short-pulse system indicates the location of key diagnostics relative to the beam for on-shot focal-spot measurement. After undergoing amplification, pulse recompression, and wavefront correction, the main OMEGA EP beam propagates to a leaky diagnostic mirror within the vacuum grating compression chamber. A small percentage of the beam (~0.5%) leaks through the diagnostic mirror and is provided to a suite of laser diagnostics, including the focal-spot diagnostic wavefront sensor (FSD WFS) and a far-field camera (FF CCD). The main beam is transported to the target chamber and focused at target chamber center by an $f/2$ off-axis parabola. For low-energy qualification shots, a focal-spot microscope (FSM) was inserted to directly image the focal spot at the target plane.

The FSD is a high-resolution wavefront sensor installed in the SPDP,⁸ denoted FSD WFS in Fig. 124.31. The FSD wavefront sensor provides a full measurement of the (temporally and spectrally averaged) near-field amplitude and phase of the sample beam that can be numerically propagated to calculate the focal-spot fluence distribution.⁹

In close proximity to the FSD is a 16-bit, cooled, far-field charge-coupled-device (CCD) camera (FF CCD in Fig. 124.31) that records the focal-spot fluence distribution of the sample beam. Both the FSD and this FF CCD acquire data on every OMEGA EP shot. In addition, for some low-energy shots, a focal-spot microscope (FSM) has been inserted into the target chamber to directly image the focal spot at the target plane

onto another 16-bit cooled CCD camera.² These two cameras provide the direct focal-spot intensity measurements that are used as inputs to the phase-retrieval algorithms discussed in this article. The image data from both of these CCD's also provide a check of the quality of the phase-retrieval results.

One of the challenges of this approach to measuring the target-plane focal spot is the indirect nature of the wavefront measurement. The measurement requires a careful calibration of the FSD wavefront sensor to “transfer” (or reference) the wavefront of the sample beam measured in the SPDP to the wavefront of the main beam inside the target chamber. The FSD is calibrated using the two-step process described in detail in Ref. 2 and illustrated in Fig. 124.32. A brief description is

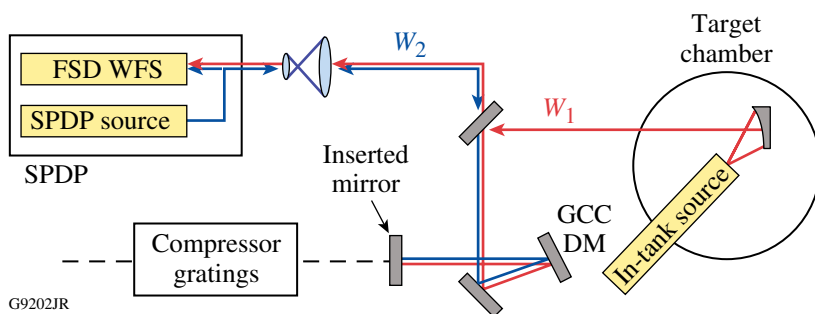


Figure 124.32

The FSD is calibrated using the two-step process illustrated. In the first step, a laser source is inserted into the target chamber with a focus at target chamber center (TCC) and propagated backward to the FSD wavefront sensor via an inserted alignment mirror. The wavefront W_1 is measured in this configuration. Next, a laser source on the SPDP diagnostic table is propagated to the alignment diagnostic mirror (DM) and back to the wavefront sensor, where the wavefront contribution W_2 is measured. The transfer wavefront, essentially $W_1 - W_2$ with pre-measured source wavefront contributions also compensated, is added to on-shot wavefront measurements to obtain the wavefront error of the main beam inside the target chamber.

given here. In the first step, an in-tank laser source is focused to target chamber center (TCC) and propagated backward to the FSD wavefront sensor via an inserted alignment mirror. The wavefront W_1 is measured in this configuration. Next, a laser source in the SPDP is propagated to the alignment mirror and back to the FSD wavefront sensor, where the wavefront contribution W_2 is measured.

A “transfer wavefront” is defined essentially as $W_1 - W_2$. When added to the directly measured sample-beam wavefront, the transfer wavefront removes the wavefront contributions from the diagnostic beam path (between the diagnostic mirror and the FSD sensor) and adds the wavefront contributions from the beam transport to the target (between the diagnostic mirror and the target). Additionally, another correction factor is applied, based on the pre-characterized wavefront contributions of the two sources used for the calibration. The measurement of the wavefront contributions from these two sources is thought to be one of the primary sources of error in the calibration process.

To evaluate the focal-spot measurement, the far-field distribution calculated from the FSD near-field measurement is compared to the directly measured far field from the appropriate CCD camera (either the far-field CCD or the FSM). The agreement is quantified by the cross-correlation

$$C = \frac{\max \left[\iint F_{\text{FSD}}(x - \Delta_x, y - \Delta_y) F_{\text{CCD}}(x, y) dx dy \right]}{\left[\left(\iint F_{\text{FSD}}^2 dx dy \right) \left(\iint F_{\text{CCD}}^2 dx dy \right) \right]^{1/2}}, \quad (1)$$

where F_{FSD} and F_{CCD} are the far-field fluence distributions from the FSD and the camera, respectively. The cross-correlation is normalized in such a way that a perfect agreement results in a value of unity. In practice, a value $C > 0.9$ has been found to normally indicate an acceptable measurement.

Initially, when focal-spot intensity distributions were measured using the FSD wavefront sensor, the results were often quite poor. An example of this is shown in Fig. 124.33, where the focal spot of the sample beam as predicted by the FSD wavefront sensor [Fig. 124.33(a)] and measured by the SPDP far-field CCD camera [Fig. 124.33(b)] are displayed side by side. Both focal spots are plotted as normalized fluence (fluence divided by total energy, in cm^{-2}) over a square $100\text{-}\mu\text{rad}$ field of view. The poor agreement ($C = 0.71$) between these two diagnostics, which measured the same beam in close proximity, illustrates the challenge of the on-shot focal-spot measurement.

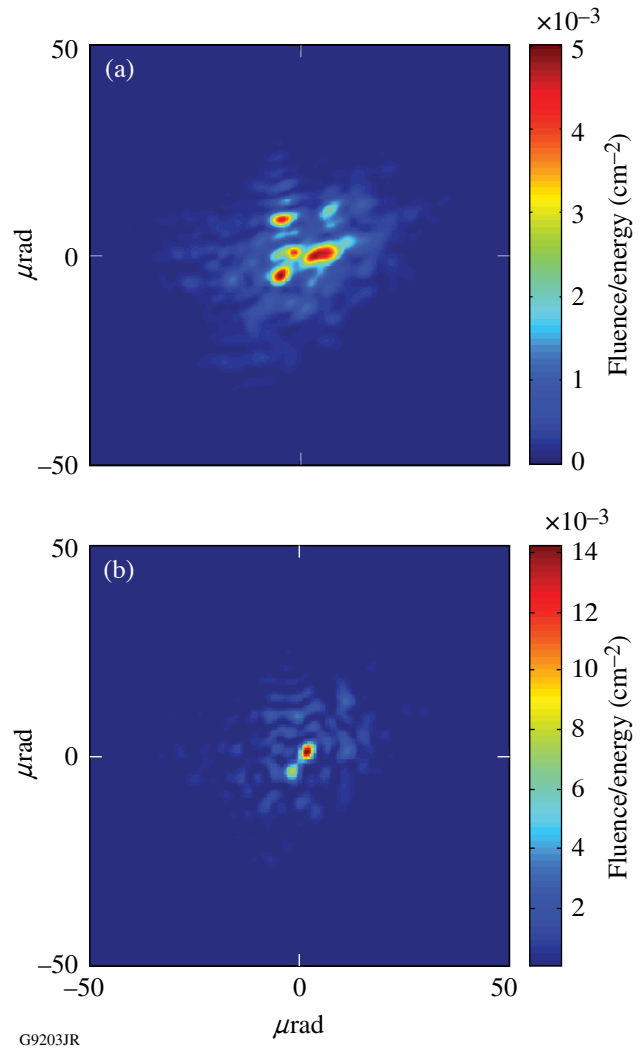


Figure 124.33

An example of an early focal-spot measurement of the sample beam. The color map (a) is a direct measurement using the FF CCD camera, while (b) shows the initial result using the FSD near-field measurement. Both focal spots are expressed in normalized fluence (fluence divided by total energy, in cm^{-2}) and are plotted over a square $100\text{-}\mu\text{rad}$ field of view. The poor agreement by two diagnostics measuring the same beam in close proximity illustrates the challenge of the on-shot focal-spot measurement.

Four problems, discussed in further detail in the next section, have led to poor FSD focal-spot measurements of the type shown in Fig. 124.33. The first problem is a fixed wavefront error between the FSD wavefront measurement and the wavefront incident on the FF CCD. The second is the inability of a Shack–Hartmann wavefront sensor to measure the mean relative wavefront (piston phase) between discrete beam segments that are generated by the tiled-grating compressor. The third problem is chromatic wavefront errors that are undetectable by the Shack–Hartmann wavefront sensor and have a significant

effect on the fidelity of the focal spot. Finally, fixed errors in the FSD calibration process further degrade the quality of the remote focal-spot measurement at the target plane. Each of these problems has been mitigated by retrieving phase information embedded within the focal-spot measurements from the FF CCD and the focal-spot microscope.

Phase-Retrieval Applications and Results

1. Phase Retrieval of SPDP Transfer Wavefront from Multiple Measurements

Whereas the FSD wavefront sensor is in very close proximity to the FF CCD camera, differences between the measured wavefront and the actual wavefront of the focusing beam at the FF CCD must be considered. First, the Shack–Hartmann wavefront measurement is a relative measurement against a reference beam. Wavefront errors in the reference beam translate directly into errors in the measured wavefront. For the FSD, a reference wavefront was acquired using an alignment laser located in the diagnostic package (the SPDP source in Fig. 124.32), reflected from a reference mirror back into the FSD. In principle, this removes the wavefront contributions from the four-element relay lens used to image the pupil onto the FSD wavefront sensor. Wavefront error in the reference laser itself, however, will introduce errors in the reference measurement. These errors were characterized separately and compensated for; however the accumulation of errors can be significant.

In addition, the optics between the FSD and the FF CCD must be considered. Aside from two planar reflective optics, a four-element focusing lens produces a far-field image on the sensor plane of the FF CCD. There is also a window on the camera (wedged and tilted to remove artifacts) as well as various neutral density filters, but these are all in close proximity to the far-field plane and therefore have little effect on the focal spot.

To account for these errors, an SPDP transfer wavefront analogous to the transfer wavefront used to produce target-plane wavefront measurements was defined. The SPDP transfer wavefront is a static quantity (assuming no system configuration changes) that is added to every FSD wavefront sensor measurement to obtain the wavefront at the exit pupil of the FF CCD lens. It was inferred from simultaneous FSD and FF CCD measurements over multiple laser shots using phase retrieval.

The classical iterative transform methods of phase retrieval were attempted on this problem but were generally unsuccessful. These included the so-called Gerchberg–Saxton algorithm³ and various refinements such as the input–output algorithm of Fienup.⁵ These algorithms produced nonphysical results

in which zeros would appear in the near field around which the phase would process continuously over a 2π range. When the phase was unwrapped, branch cuts would be required, leading to unphysical discontinuities in the wavefront. The problem appears to have been caused by a combination of polychromatic effects and a small incoherent background in the far-field measurements.

To improve focal-spot predictions, a modal phase-retrieval method that has proven to be successful and robust was employed. It is based closely on a gradient-search algorithm reported by Fienup.⁶ A block diagram of the algorithm is shown in Fig. 124.34. The inputs to the algorithm are the measured near-field intensity and wavefront from the FSD wavefront sensor and the measured focal-spot intensity from the FF CCD camera. The algorithm produces a single low-order SPDP transfer wavefront expressed as a two-dimensional Legendre polynomial, as well as the piston phases in the left and right beam segments (as discussed in the following subsection). Multiple shots are evaluated simultaneously to improve accuracy.

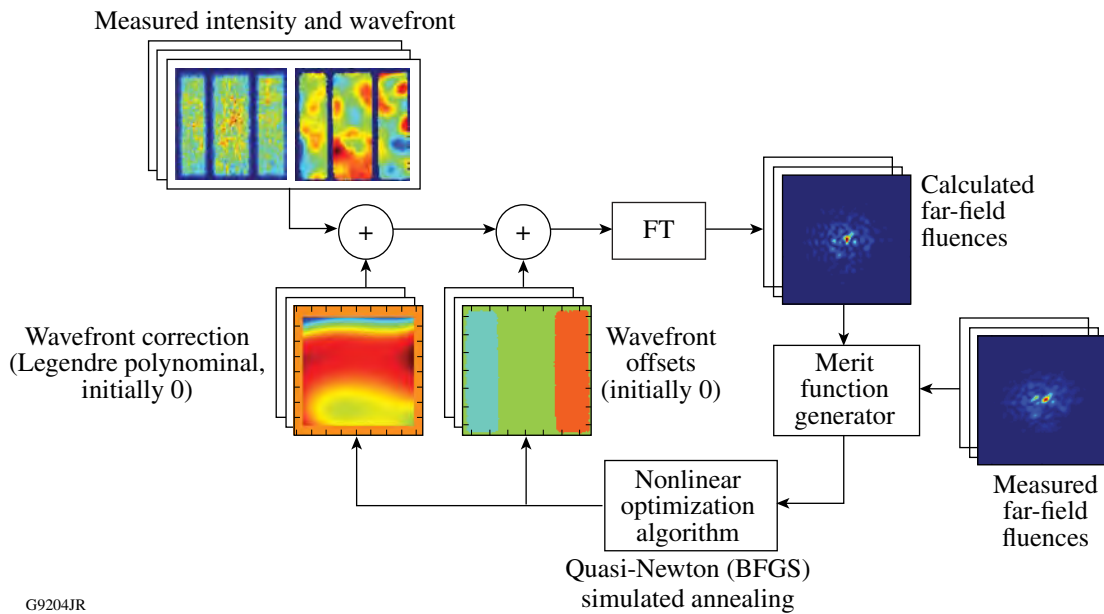
The algorithm proceeds from the near-field intensities and wavefronts measured by the FSD wavefront sensor. The current SPDP transfer wavefront is added to all the wavefronts, and the wavefront offsets are added to the outer tiles of the appropriate wavefronts. The far-field fluence distributions are then calculated from the near-field intensity and the corrected wavefront. These are compared to the measured values to generate a merit function, which is based on the root-sum-square (rss) error,

$$\text{rss error} = \left\{ \iint [F_{\text{FSD}}(x,y) - F_{\text{CCD}}(x,y)]^2 dx dy \right\}^{1/2}. \quad (2)$$

The rss errors from all shots are summed to produce an overall merit function that takes into account errors over the entire data set.

A nonlinear optimization algorithm is employed to modify the optimization parameters for the subsequent iterations. In most cases, a quasi-Newton, Broyden–Fletcher–Goldfarb–Shanno (BFGS) algorithm¹⁰ is used, which is a true gradient-search algorithm. Alternatively, to attempt to find a global solution, a simulated annealing algorithm has initially been employed¹¹ to identify the approximate solution, followed by a gradient search algorithm to obtain a more-accurate estimate. The algorithm continues until the merit function is minimized.

This modal phase-retrieval algorithm was used to measure the SPDP transfer wavefront for the FSD sensors in both the upper and lower compressors on OMEGA EP. A fourth-order



G9204JR

Figure 124.34

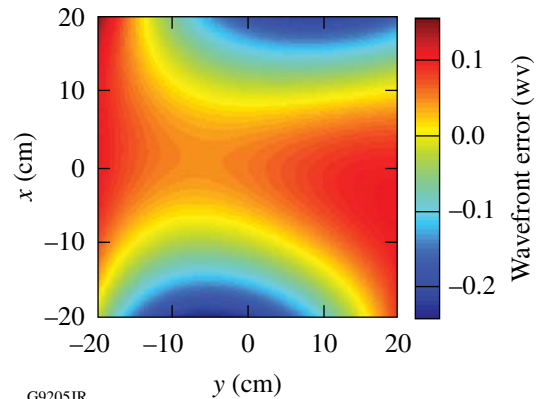
A block diagram illustrating the modal phase-retrieval algorithm used to measure the SPDP transfer wavefront. The inputs to the algorithm are the measured near-field intensity and wavefront from the FSD wavefront sensor and the measured focal-spot intensity from the FF CCD camera. Multiple shots are evaluated simultaneously to improve accuracy. The far-field fluence distributions are calculated from the measured near fields using Fourier transforms (FT) and compared to the measured values to generate a merit function. This merit function is minimized by using a nonlinear optimization algorithm to vary the SPDP transfer wavefront (estimated as a Legendre polynomial) and the average phase in the outer beam segments for each shot. The SPDP transfer wavefront and average phases are added to the original measurements in the subsequent iteration. The algorithm continues until the merit function is minimized.

Legendre polynomial was used to estimate the SPDP transfer wavefront in the phase-retrieval algorithm. The result for the upper compressor, retrieved from approximately 20 low-energy shots, is displayed in Fig. 124.35. The SPDP transfer wavefront is added to all FSD wavefront measurements.

To evaluate the improvement gained by use of the SPDP transfer wavefront measurement, focal-spot measurements at the SPDP were performed with a narrowband laser¹² propagated through the beamline and through the compressor to the diagnostic table. The outer segments of the beam were obscured in order to illuminate only the central grating tile in the grating compressor (see the next section). Therefore, the pupil had a single rectangular area and the spectral width was essentially monochromatic compared to the 8-nm OPCPA spectrum.

Figure 124.36 shows how the application of the SPDP transfer wavefront improves the focal-spot prediction in this single-segment, quasi-monochromatic scenario. The cross-correlation between the FSD-generated far-field distribution and the measured intensity from the FF CCD is shown for six different shots. For each shot, the correlation before (blue diamonds) and after (red squares) applying the SPDP transfer

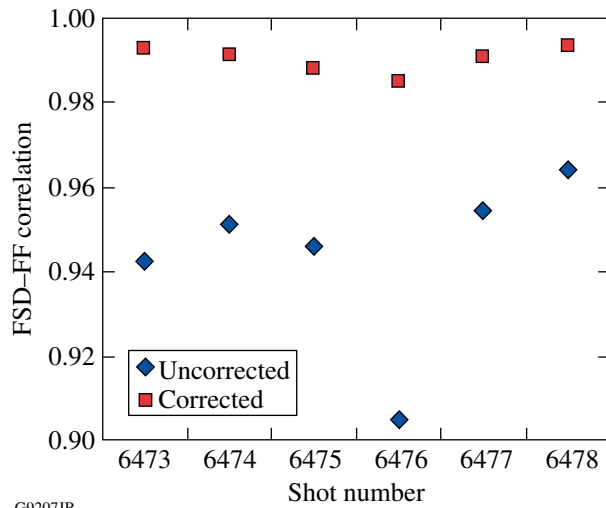
wavefront correction is shown. The correction was seen to improve the focal-spot cross-correlation from an average of 0.944 to 0.990, and the standard deviation was reduced from 0.021 to 0.003.



G9205JR

Figure 124.35

The SPDP transfer wavefront for the upper compressor. This wavefront was retrieved from a large number of shot measurements using the modal phase-retrieval algorithm with FSD wavefront sensor and FF CCD image data. The SPDP transfer wavefront was added to all FSD wavefront measurements to improve agreement with the FF CCD images.



G9207JR

Figure 124.36

The effect of the SPDP transfer wavefront on the quality of the FSD measurement is shown for the single-tile monochromatic beam. The cross-correlation between the FSD-generated far-field distribution and the measured intensity from the FF CCD is shown for six different shots. For each shot, the correlation before (blue diamonds) and after (red squares) applying the SPDP transfer wavefront correction is shown. The correction was seen to improve the correlation from an average of 0.944 to 0.990, and the standard deviation was reduced from 0.021 to 0.003.

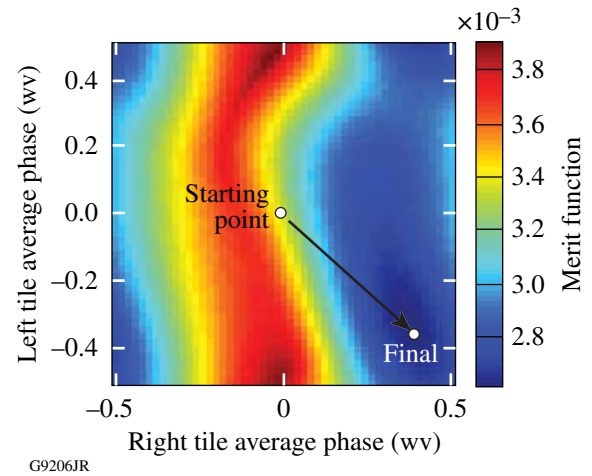
2. Single-Shot Retrieval of Average Relative Wavefront in Outer-Beam Segments

The pulse-compression system in OMEGA EP uses four tiled-grating assemblies, each comprised of three closely spaced, interferometrically aligned grating segments, to produce an effective meter-scale grating.¹³ To prevent damage associated with high-energy illumination of the edges of the grating tiles, the short-pulse beams in OMEGA EP are apodized in the region of the gaps between tiles. This produces the three-segment beam profile shown in the inset of Fig. 124.31 and further complicates the focal-spot measurement.

The FSD wavefront sensor, being a Shack–Hartmann type, fundamentally measures the local wavefront slopes across the pupil. Spatial-integration algorithms are used to reconstruct the wavefront,¹⁴ but there is an inherent uncertainty in the average wavefront in each discrete segment of the beam. This is normally not an important issue when measuring a beam with a single continuous pupil area because the overall piston phase is unimportant. In the case of OMEGA EP's three-segment beams, however, this limitation results in an inherent uncertainty in the relative average wavefront between the adjacent segments. Consequently, there is a differential piston artifact in the measurement that can significantly impact the focal-spot

prediction. Fortunately, this uncertainty can again be resolved by retrieving the relative average phase in the outer-beam segments from the FF CCD image.

Figure 124.37 shows a typical plot of the rss error merit function in Eq. (2) versus the relative piston phase (in waves) in the two outer beam segments. To retrieve the average relative wavefront in the outer segments, one searches for the minimum of the merit function in this plot. Note that the merit function has periodic boundary conditions, with one full period shown. A grid search followed by a quasi-Newton gradient-minimization search has proven to be a reliable means of finding the optimum solution for all shots encountered.



G9206JR

Figure 124.37

A typical plot of the merit function versus the piston wavefront in the outer beam segments. To retrieve the average relative wavefront in the outer segments, one searches for the minimum of the merit function in this plot. Note that the merit function has periodic boundary conditions, with one full period shown.

To test the retrieval of the relative phase in the outer beam segments, the experiment with the narrowband laser described in the previous subsection was repeated, illuminating multiple beam segments. The obscuration in the beam was removed to propagate first two, then all three beam segments through the compressor. The results of this experiment are summarized in Fig. 124.38. The plot shows the average and range of cross-correlations over six shots, illuminating one, two, and three beam segments. For each configuration, the red squares and error bars were generated with the outer-segment piston phase retrieved, while the blue diamonds were generated without performing that step (by optimizing wavefront continuity across beam segments). The error bars represent the minimum and maximum values over the six measurements. The SPDP transfer wavefront

was applied for all shots. Note that the corrected measurements remained at a high value (>0.97 for all measurements) for all the shots in this monochromatic case. Conversely, when the average relative phase in the outer segments was not retrieved, the cross-correlation and variability became progressively worse as more beam segments were introduced.

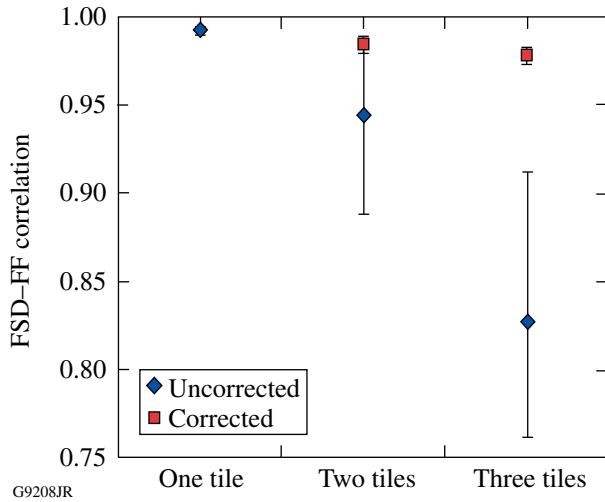


Figure 124.38

Monochromatically illuminating multiple tiles, the effect of the average relative wavefront between the beam segments is illustrated. The plot shows the average and range of correlations over six shots illuminating one, two, and three tiles. For each configuration, the correlations with (red squares) and without (blue diamonds) solving for the relative wavefront in the outer segments are shown, and the error bars represent the minimum and maximum values over six measurements. The SPDP transfer wavefront was applied for all shots. The corrected measurements remained at a high value (>0.97 for all measurements) for all three beam segments for this monochromatic case.

3. Estimating Effects of Polychromatism on Focal-Spot Structure

Despite the relatively narrow spectral widths involved (~ 8 nm unamplified and ~ 3.3 nm amplified), the short-pulse system on OMEGA EP can exhibit strong chromatic aberrations. The dominant chromatic aberration observed thus far has been attributed to residual angular dispersion, which can arise either in the stretcher or in the pulse compressor, and produces a wavelength-dependent tilt term. The polychromatism has been observed to significantly affect the far field, as demonstrated in Fig. 124.39. The focal-spot distribution in Fig. 124.39(a) shows the predicted focal-spot fluence based on monochromatic propagation of the measured near field of the FSD. The actual focal spot from the full 8-nm OPCPA bandwidth as measured by the FF CCD is shown in Fig. 124.39(b). The polychromatism is evident in the reduced sharpness of the focal spot and the peak fluence, which is lower by a factor of ~ 2 . The blurring

of the focal spot is typically along a preferential axis, which is indicative of a wavelength-dependent tilt term as expected from residual angular dispersion. Note that the blurring of the sort shown was not observed in the narrowband experiment described in the previous subsections and, consequently, cannot be explained by the modulation transfer function of the FF CCD lens.

The polychromatic blurring cannot be explained simply by the spectral content of the beam without a chromatically vary-

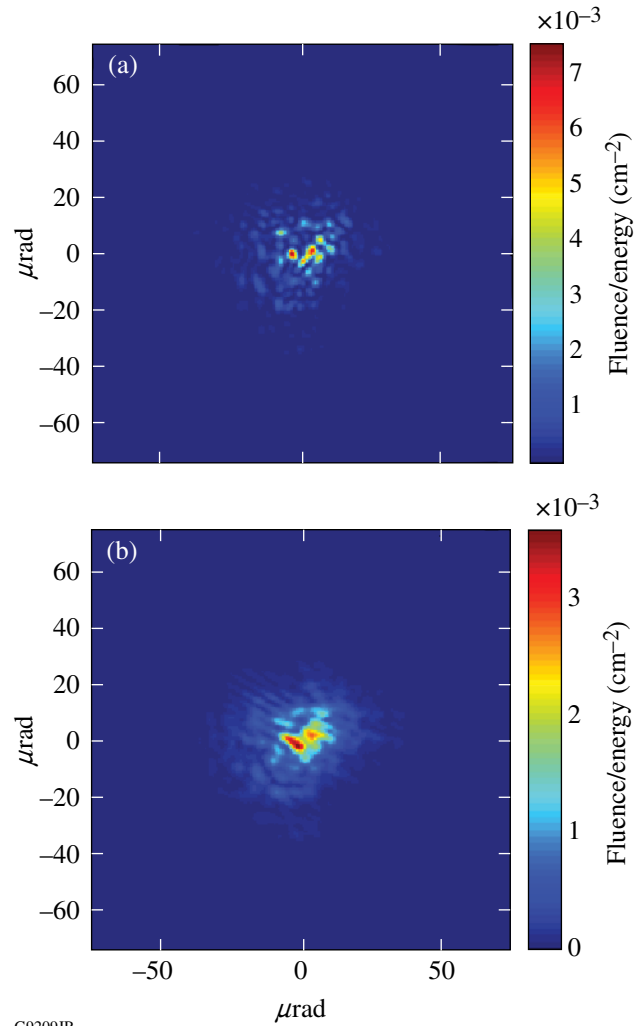


Figure 124.39

Polychromatism has been observed to blur the fine features of the far-field intensity pattern when the OPCPA beam is measured. The focal-spot distribution in (a) shows the predicted focal-spot fluence based on monochromatic propagation of the measured near field of the FSD. The actual focal spot from the full 8-nm OPCPA bandwidth as measured by the FF CCD is shown in (b). The polychromatism degrades the sharpness of the focal spot and reduces the peak fluence by approximately a factor of 2 in this case.

ing component of the wavefront. In other words, if the far field is polychromatically generated from the measured wavefront, by incoherently summing the far fields propagated from the near field using a range of wavelengths, the effect on the predicted focal spot is insignificant. The type of blurring we have observed would be seen over this narrow spectral width only if there was a significant variation in the wavefront (particularly tilt) over the spectral range.

Because the FSD wavefront sensor is not spectrally sensitive, it cannot provide information on the chromatic aberrations and, instead, produces a spectrally averaged wavefront measurement. To estimate the effects on polychromatism,

however, a Fourier analysis has been developed (Fig. 124.40). In the first step of the process, the focal-spot intensities measured by the FF CCD and monochromatically calculated from the FSD wavefront sensor are both Fourier transformed. A polychromatic transfer function is then estimated by taking the ratio of the Fourier transforms, smoothing, and fitting an elliptical Gaussian function. In the third step, the polychromatic transfer function is inverse Fourier transformed to generate a polychromatic impulse response. Finally, the original monochromatically calculated FSD focal-spot measurement is convolved with the polychromatic impulse response to obtain a focal-spot fluence distribution that includes an estimate for polychromatic effects.

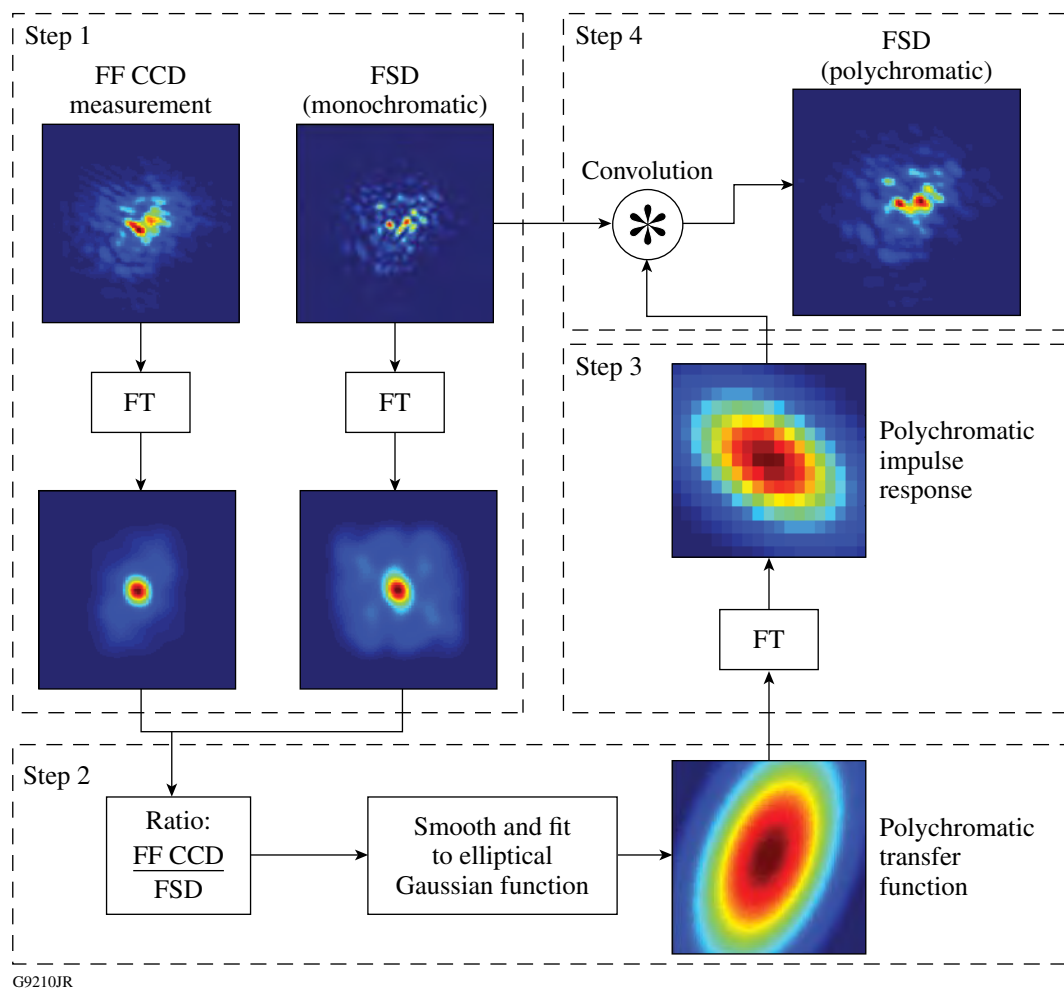


Figure 124.40

The four-step algorithm for estimating the effects of polychromatic blurring. In Step 1 of the process, the focal-spot intensities measured by the FF CCD and monochromatically calculated from the FSD wavefront sensor are Fourier transformed. In Step 2, the polychromatic transfer function is estimated by taking the ratio of the Fourier transforms from Step 1, smoothing, and fitting to an elliptical Gaussian function. The polychromatic transfer function is then inverse Fourier transformed to generate the polychromatic impulse response in Step 3. Finally, in Step 4 the original monochromatically calculated FSD focal-spot measurement is convolved with the polychromatic impulse response to obtain a focal-spot fluence distribution that includes an estimate for polychromatic effects.

We emphasize that this system provides only an *estimate* for polychromatism and is, in fact, only appropriate if residual angular dispersion is the dominant mechanism. Other sources of polychromatic error will affect the focal spot in a more-complex way than can be modeled with an intensity impulse response. For example, there is longitudinal chromatic aberration in the spatial-filter lenses in the beamline. This, in principle, is corrected using a diffractive optical element in the injection lens,¹⁵ although its performance in the system has not yet been experimentally verified. There is also a chromatic contribution associated with the spatial chirp on the beam at the second and third gratings in the compressor. The surface errors in those tiled-grating assemblies produce a wavefront error that has a wavelength-dependent horizontal displacement on the beam. These effects, which are not addressed with this method, will be a subject for further development.

4. Phase Retrieval to Improve FSD Calibration

The final issue that was addressed was the appearance of fixed errors in the calibration of the FSD wavefront sensor. It is believed that the primary source of error in the FSD calibration process is contributed by the two reference sources used in the calibration measurements. These were characterized offline and compensated as part of the calibration process, but changes in the wavefront performance of the laser sources and measurement errors both contribute to calibration errors. There also exist optical elements that are inserted into the beam path for the calibration process but removed under normal operating conditions, which could contribute fixed wavefront errors. Finally, because the FSD wavefront is effectively “transferred” to the FF CCD to use the earlier phase-retrieval techniques, any wavefront error in the far-field lens is effectively added to the

wavefront measurement. This wavefront error in the far-field lens must be removed via the transfer wavefront, introducing another error in the FSD calibration.

These fixed calibration errors were inferred using the modal phase-retrieval process described above, but this time using image data from the FSM from a number of low-energy shot campaigns. In each campaign, a series of shots was acquired with the OPCPA beam propagating through both the passive beamline and the compressor. The deformable mirror (see Fig. 124.31) was used to introduce phase diversity in the shot sequence to improve the phase-retrieval results. The FSM was inserted into the target chamber and aligned to image the focal spot at the center of the target chamber. For each shot, the techniques described earlier were used to correct the FSD wavefront measurement and to retrieve the polychromatic impulse response to obtain agreement between the FSD and the SPDP far-field CCD. The transfer wavefront measured during FSD calibration prior to each shot campaign was then applied to obtain an initial estimate for the wavefront converging to the target plane. A transfer-wavefront correction was then retrieved by using a variant of the modal phase-retrieval process described above using FSD and FSM data as inputs from a large number of shots. One key difference from the earlier modal phase-retrieval application is that the average phase in the outer beam segments was not varied when retrieving the transfer wavefront correction. These parameters were determined via phase retrieval using the FF CCD image and are therefore fixed at this stage. Furthermore, the transfer-wavefront correction is expected to be continuous over the beam aperture.

The resulting transfer-wavefront corrections (Fig. 124.41) have been evaluated for three different target configurations:

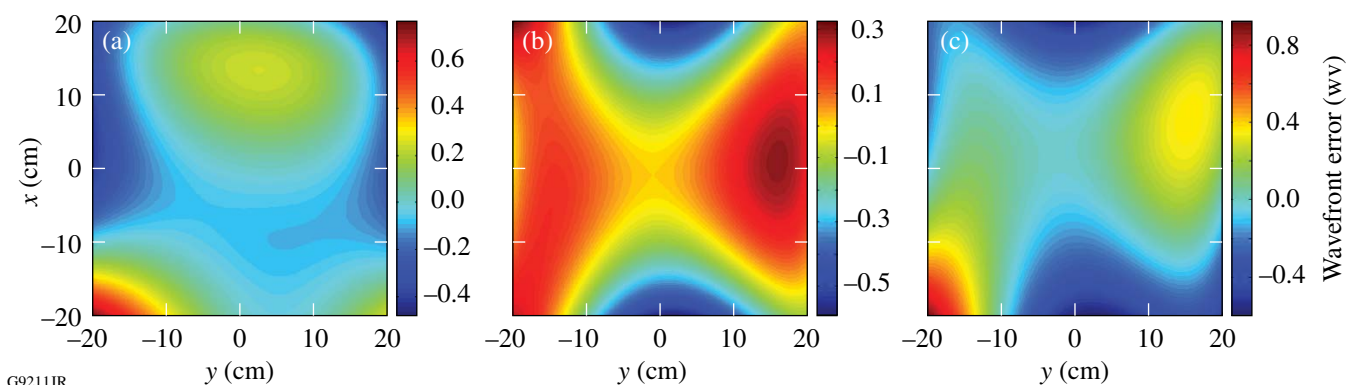


Figure 124.41

Transfer-wavefront corrections are shown for (a) upper compressor to the OMEGA EP backlighter, (b) lower compressor to the OMEGA EP sidelighter, and (c) upper compressor to the OMEGA backlighter. These were retrieved from low-energy shot campaigns using FSM measurements in conjunction with FSD wavefront measurements using a phase-retrieval process similar to that shown in Fig. 124.34. These correction wavefronts were applied to all FSD calibration measurements obtained using the technique in Fig. 124.32.

(a) the upper compressor propagating to the backlighter OAP in the OMEGA EP target chamber, (b) the lower compressor to the OMEGA EP sidelighter OAP, and (c) the upper compressor to the OMEGA target chamber OAP. As before, the correction wavefront is estimated by a fourth-order Legendre polynomial. It is important to also note that the transfer-wavefront correction has been confirmed to be reasonably stable over multiple shot campaigns conducted over approximately one year. The transfer-wavefront correction measurements will be performed periodically in the future to confirm its stability or adapt to changes in the system performance. Variability observed in the transfer-wavefront correction is used to estimate the uncertainty of the target-plane measurement.

Note that special consideration must be made for defocus when measuring the transfer-wavefront correction. In shot campaigns in general, defocus within the target chamber is an unknown parameter, affected by both the positioning of the OAP and the target itself. Furthermore, during the FSD calibration, longitudinal errors in the placement of the in-tank source will lead to a defocus error. Finally, during the FSM shot campaigns, errors in alignment of the FSM to the OAP focal plane led to defocus in the measured focal spot that introduced a defocus term into the transfer-wavefront correction via the phase-retrieval process. To deal with the defocus uncertainty, a through-focus scan was conducted as part of each FSM shot campaign to measure the FSM defocus relative to the OAP. As a result, defocus was effectively removed from the transfer-wavefront correction.

Results

To evaluate the performance of the phase-retrieval techniques described in the previous section, they have been applied to a number of on-shot focal-spot measurements and compared to available direct focal-spot measurements. First, the accuracy of the sample-beam focal-spot measurement is considered by comparing the FSD result with the FF CCD.

As an example of the impact of these phase-retrieval improvements, the sample-beam focal-spot measurement shown in Fig. 124.33 is again considered in Fig. 124.42. The direct focal-spot measurement from the FF CCD camera is repeated in Fig. 124.42(a). The far-field fluence calculated using near-field measurements by the FSD wavefront sensor, including correction for the SPDP transfer wavefront, the average phase in the outer beam segments, and estimation of polychromatic effects, is shown in Fig. 124.42(b). The corrected FSD prediction shows a much-better qualitative correspondence with the direct FF CCD measurement than the uncorrected

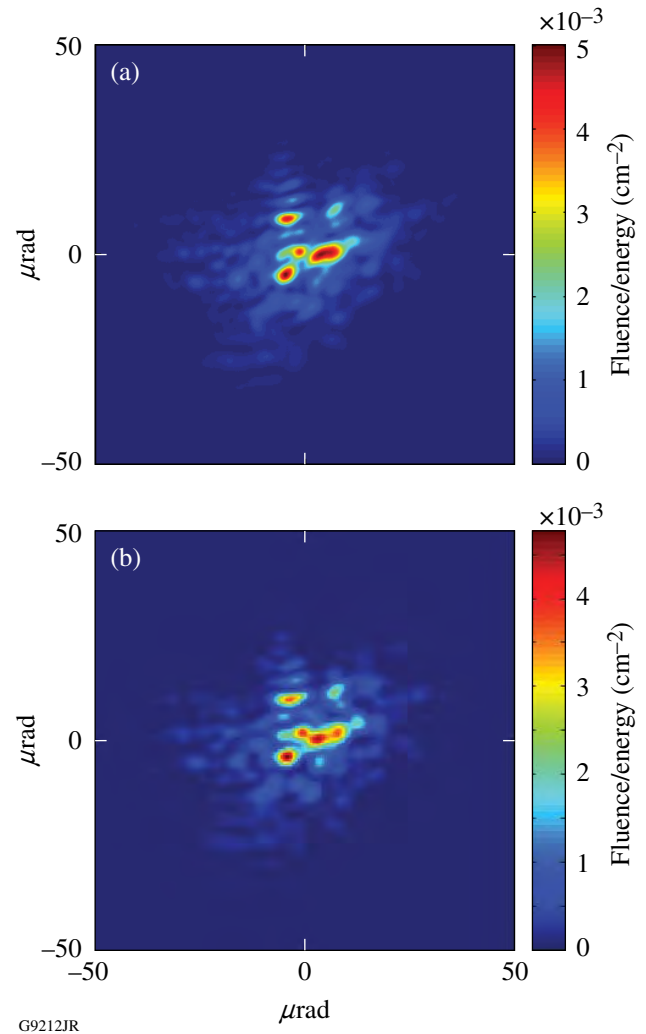


Figure 124.42

The sample-beam focal-spot measurement shown in Fig. 124.33 is repeated here using the phase-retrieval techniques described. (a) The direct focal-spot measurement from the FF CCD camera. (b) The far-field fluence calculated using near-field measurements by the FSD wavefront sensor, including correction for the SPDP transfer wavefront, the average phase in the outer beam segments, and estimation of polychromatic effects. The two focal-spot agreements match much better qualitatively than the uncorrected case shown in Fig. 124.33. The quantitative agreement is also much better, with the cross-correlation improving from 0.71 to 0.95.

case shown in Fig. 124.33. The quantitative agreement is also much better, with the cross-correlation improving from 0.71 to 0.95. The prediction of the peak intensity has also improved to within 10% accuracy, compared to the initial estimate that overpredicted the peak intensity by $>2\times$.

The improved focal-spot measurement of the sample beam has also proven to be very reliable and stable over a large number of shots. To illustrate this, the cross-correlation has been

evaluated over a population of 175 low-energy shots, which spanned approximately 18 months. Figure 124.43 is a histogram showing the frequency of cross-correlations within intervals of 0.01. The filled bars correspond to the corrected measurements, i.e., when the SPDP transfer wavefront (assumed static over the entire time period), the average phase in the outer segments, and the effects of polychromatism have all been applied. The white bars give the cross-correlation values without these corrections. There is a clear improvement in performance after applying the phase-retrieved corrections, with the mean cross-correlation increasing from 0.826 to 0.965. The consistency of the measurement was also much improved, with the standard deviation of the cross-correlation reduced from 0.044 to 0.010.

Amplifying the beam did not adversely affect the quality of focal-spot measurement, as demonstrated in the histogram in Fig. 124.44. The cross-correlation between the FSD and the FF CCD was calculated after applying all the phase-retrieved corrections. The white bars represent the rate of occurrence for each cross-correlation value for all high-energy shots over a recent 6-month period, representing a population of 220 samples. The filled bars represent the same data for all the low-energy FSM campaign shots evaluated in Fig. 124.43. The statistics are quite similar: the low-energy and high-energy mean cross-correlations are 0.965 and 0.967, respectively, which are effectively identical considering the standard deviations (0.010 and 0.009, respectively).

To achieve consistent performance over the wide range of shot conditions included in this study, it was necessary to account for changes in the system configuration in the diagnostic package. Specifically, wavefront contributions from neutral-density filters inserted in front of the FSD wavefront sensor can be significant. The wavefront introduced by each of these filters is characterized *in situ* in an offline measurement and removed from each on-shot wavefront measurement as appropriate.

The true test of the FSD measurement accuracy is its ability to accurately measure the focal spot remotely in the target chamber. The cross-correlation between the FSD focal-spot prediction and the direct measurement using the FSM was evaluated for all the low-energy shot campaigns described earlier. A histogram of the cross-correlation data is presented in Fig. 124.45. The histogram in Fig. 124.45(a) shows the effect of the phase-retrieval corrections on the focal-spot measurement. The white bars give the distribution of cross-correlation values between the FSD and direct FSM measurements when no phase-retrieval corrections have been applied. The filled bars, which show the corresponding cross-correlations with the addition of the phase-retrieval corrections, demonstrate the improvement in overall quality and reliability. The histogram in Fig. 124.45(b) compares the quality of the measurement of the sample beam at the SPDP table (filled bars) and the main beam in the target chamber (white bars). All phase-retrieval corrections were applied for this data. The measurement accuracy

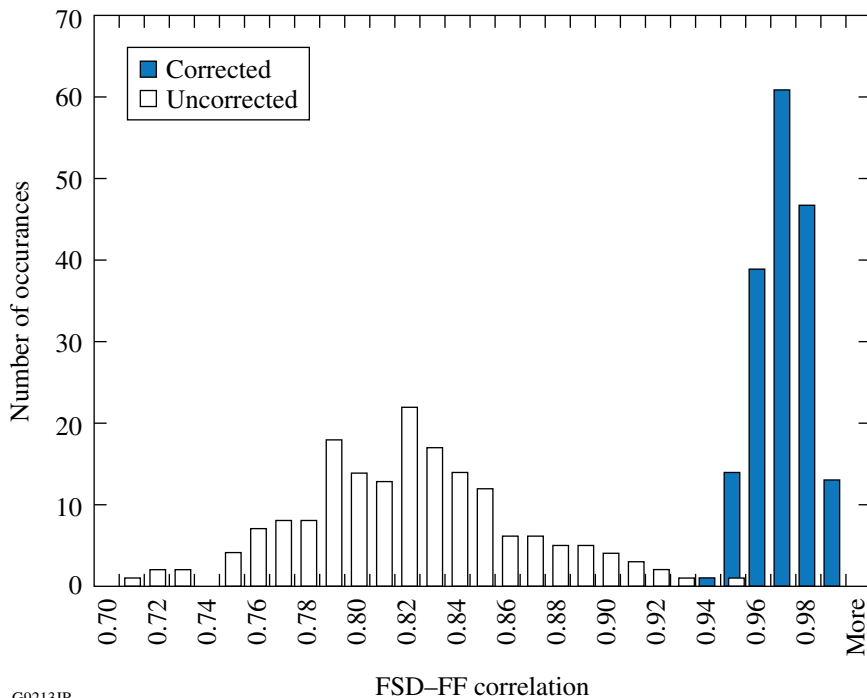


Figure 124.43

A histogram of the cross-correlations between the FSD and FF CCD measurements. The filled bars give the values when the SPDP transfer wavefront, the average phase in the outer segments, and the effects of polychromatism have all been retrieved. The white bars give the values without these corrections. The histograms consist of low-energy shots with the full OPCPA bandwidth, acquired during the shot campaigns to the FSM, which spanned approximately 18 months.

G9213JR

is slightly worse in the target chamber, likely because of the variability in the transfer-wavefront correction from campaign to campaign; however, the measured cross-correlation reliably exceeds 0.9 with >95% probability.

Unfortunately, confirming an accurate measurement of the focal-spot measurement at high energy is currently not possible since a high-energy shot cannot be sufficiently attenuated to the level required for the focal-spot microscope. Other target

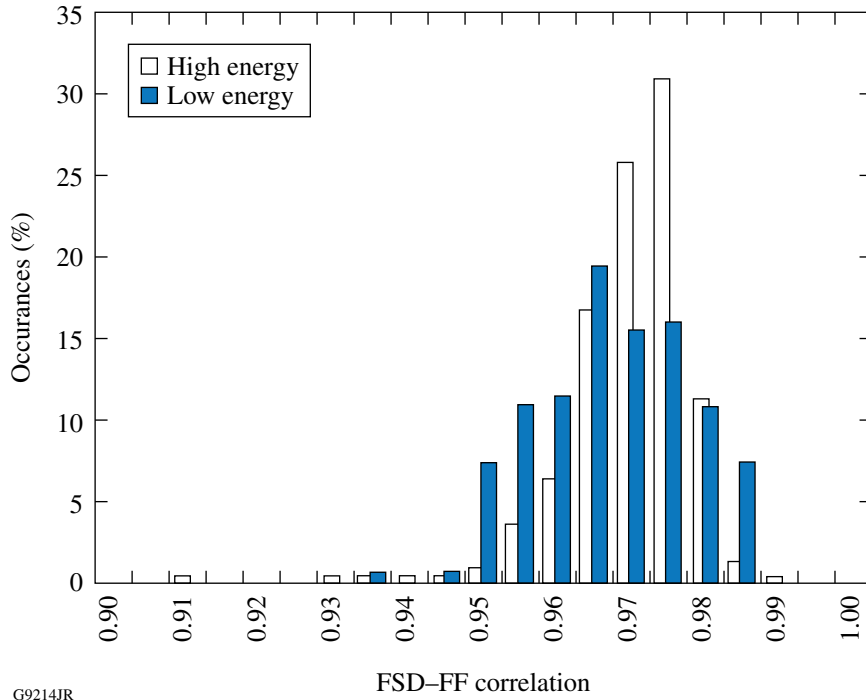
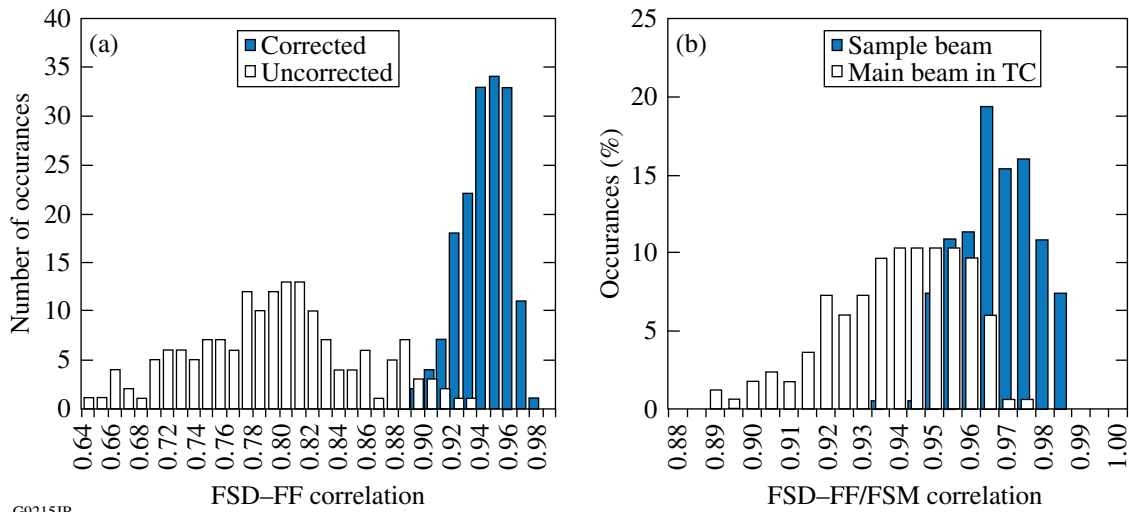


Figure 124.44

A histogram demonstrating that the consistently high sample-beam focal-spot measurement accuracy is maintained for high-energy OMEGA EP shots. The white bars represent the rate of occurrence for each cross-correlation between the FSD and the far-field CCD for all high-energy shots over a recent 6-month period. The filled bars represent the same data for all the low-energy FSM campaign shots, as also plotted in Fig. 124.43. The values are calculated with all phase-retrieved corrections.

G9214JR



G9215JR

Figure 124.45

The accuracy of the focal-spot measurement of the main beam in the target chamber is evaluated in the histograms. (a) The effect of the phase-retrieval corrections on the focal-spot measurement. The white bars give the distribution of cross-correlation values between the FSD and direct FSM measurements when no phase-retrieval corrections have been applied. The filled bars, which show the corresponding cross-correlations with the addition of the phase-retrieval corrections, demonstrate the improvement in overall quality and reliability. (b) A comparison of the quality of the measurement of the sample beam at the SPDP table (filled bars) and the main beam in the target chamber (TC) (white bars). All phase-retrieval corrections were applied for this data. The measurement accuracy is slightly worse in the target chamber, likely because of the variability in the transfer-wavefront correction from campaign to campaign.

diagnostics, such as x-ray pinhole cameras, have poor resolution and do not provide a true measure of focal-spot fluence because of the complexities of the target interaction. For this reason we must rely on the low-energy results to assess the performance of the focal-spot measurement at the target plane. To maximize the confidence in the measurement at high energy, we have accounted for all changes to the system configuration for these shots, e.g., attenuators inserted before the SPDP. The wavefront errors contributed by all configuration changes were measured individually offline. On high-energy shots, the wavefront contributed by each inserted aberrator was removed from the measurement to correct for potential measurement error.

Conclusions

Phase retrieval has been a useful technique for obtaining consistently high quality remote predictions of the on-shot target-plane fluence distribution. A modal phase-retrieval technique based on a gradient-search algorithm was used to retrieve correction wavefronts for the FSD that produce focal spots in consistent agreement with direct measurements of the sample beam and main beam at the target plane for low energy. Phase retrieval was also used to provide phase information beyond the capabilities of the Shack–Hartmann wavefront sensor. The relative piston phase between the discrete segments of the OMEGA EP beam was retrieved on each shot using an image of the sample-beam focal spot. Further, an estimate of the effects of chromatic aberration on the focal-spot fluence distribution was obtained from the sample-beam focal-spot image using a Fourier technique.

Analysis of a large population of on-shot measurements has proven the focal-spot measurement to be reliable. Cross-correlation with direct focal-spot fluence measurements using the far-field CCD and the FSM consistently exceeded 90%, although no direct measurement at the target plane at high energy is currently possible.

As a result of the improved accuracy of the on-shot focal-spot measurement, scientists conducting experiments on the OMEGA EP short-pulse beamlines now have critical information about on-target intensity distributions. This information is proving to be very useful and is enhancing the value of OMEGA EP experiments for furthering our understanding of ICF physics.

ACKNOWLEDGMENT

The authors thank Prof. James Fienup for insightful discussions on phase-retrieval algorithms. This work was supported by the U.S. Department of Energy Office of Inertial Confinement Fusion under Cooperative Agreement No. DE-FC52-08NA28302, the University of Rochester, and the New York State Energy Research and Development Authority. The support of DOE does not constitute an endorsement by DOE of the views expressed in this article.

REFERENCES

1. J. H. Kelly, L. J. Waxer, V. Bagnoud, I. A. Begishev, J. Bromage, B. E. Kruschwitz, T. J. Kessler, S. J. Loucks, D. N. Maywar, R. L. McCrory, D. D. Meyerhofer, S. F. B. Morse, J. B. Oliver, A. L. Rigatti, A. W. Schmid, C. Stoeckl, S. Dalton, L. Folnsbee, M. J. Guardalben, R. Jungquist, J. Puth, M. J. Shoup III, D. Weiner, and J. D. Zuegel, *J. Phys. IV France* **133**, 75 (2006).
2. J. Bromage, S.-W. Bahk, D. Irwin, J. Kwiatkowski, A. Pruyne, M. Millecchia, M. Moore, and J. D. Zuegel, *Opt. Express* **16**, 16,561 (2008).
3. R. W. Gerchberg and W. O. Saxton, *Optik* **35**, 237 (1972).
4. R. A. Gonsalves, *J. Opt. Soc. Am.* **66**, 961 (1976).
5. J. R. Fienup, *Appl. Opt.* **21**, 2758 (1982).
6. J. R. Fienup, *Appl. Opt.* **32**, 1737 (1993).
7. S.-W. Bahk, J. Bromage, I. A. Begishev, C. Mileham, C. Stoeckl, M. Storm, and J. D. Zuegel, *Appl. Opt.* **47**, 4589 (2008).
8. Imagine Optic, 91400 Orsay, France (<http://www.imagine-optic.com/>).
9. J. W. Goodman, *Introduction to Fourier Optics* (McGraw-Hill, New York, 1968).
10. C. G. Broyden, *IMA J. Appl. Math.* **6**, 76 (1970); R. Fletcher, *Comput. J.* **13**, 317 (1970); D. Goldfarb, *Math. Comput.* **24**, 23 (1970); D. F. Shanno, *Math. Comput.* **24**, 647 (1970).
11. S. Kirkpatrick, C. D. Gelatt, Jr., and M. P. Vecchi, *Science* **220**, 671 (1983).
12. A Q-switched diode-pumped Nd:YLF laser from Photonics Industries was used, model DS10-1053; Photonics Industries International, Inc., Bohemia, NY 11716 (<http://www.photonix.com>).
13. J. Qiao, A. Kalb, T. Nguyen, J. Bunkenburg, D. Canning, and J. H. Kelly, *Opt. Lett.* **33**, 1684 (2008).
14. cf. D. L. Fried, *J. Opt. Soc. Am.* **67**, 370 (1977); this work used the method described in S.-W. Bahk, *Opt. Lett.* **33**, 1321 (2008).
15. T. J. Kessler, H. Huang, and D. Weiner, in *International Conference on Ultrahigh Intensity Laser Development, Science and Emerging Applications 2006* (ICUIL, Cassis, France, 2006), pp. 126–128.

The Second Omega Laser Facility Users Group Workshop 28 April–1 May 2010

Overview

More than 115 researchers from 44 universities and laboratories and 9 countries gathered at the Laboratory for Laser Energetics (LLE) for the second Omega Laser Facility Users Group (OLUG) Workshop (see Fig. 124.46). The purpose of the three-day workshop was to facilitate communications and exchanges among individual OMEGA users and between users and LLE; to present ongoing and proposed research; to encourage research opportunities and collaborations that could be undertaken at the Omega Laser Facility and in a complementary fashion at other

facilities [such as the National Ignition Facility (NIF) or the Laboratoire pour l'Utilisation des Lasers Intenses (LULI)]; to provide an opportunity for students and postdoctoral fellows to present their research at LLE in an interactive and informal atmosphere; and to provide feedback to LLE about ways to improve the facility and future experimental campaigns. The interactions were stimulating and lively, as can be seen in photographs shown in this document. There are 180 members in the OMEGA Users Group; their names and affiliations can be found at www.lle.rochester.edu/about/omega_laser_users_group.php.



U1092JR

Figure 124.46

More than 115 researchers from around the world and from 44 universities and laboratories participated in this year's OMEGA Laser Users Workshop. Plans for the next workshop, on 27–29 April 2011, are well underway, with significant NNSA support already allocated for student/postdoctoral travel expenses.

During the first two mornings of the workshop, 17 science and facility talks were presented. The facility talks proved especially useful for those not familiar with the art and complexities of performing experiments on OMEGA. The overview science talks, given by leading world authorities, described the breadth and excitement of high-energy-density (HED) science undertaken at the Omega Laser Facility. The next section of this document contains a summary of the presentations.

A total of 45 students and postdoctoral fellows, 37 of whom were supported by travel grants from the National Nuclear Security Administration (NNSA), attended the workshop and presented 31 of the 59 contributed poster and oral presentations. The presentations ranged from target fabrication to simulating important aspects of supernovae, all of which generated spirited discussions, probing questions, and many suggestions. In total there were 76 presentations, including both invited and contributed.

An important function of the workshop was to develop a set of recommendations and findings to help set future priorities for the Omega Laser Facility. These findings were grouped into three areas—60-beam OMEGA, OMEGA EP, and broader facility-improvement issues—and comprise a report given to the management of the Omega Facility. The report, along with management's response, can be found at the end of this document. LLE management is using these recommendations as a guide for making decisions about the Omega Laser Facility operations, priorities, and future changes.

One highlight of the workshop was a panel of students and postdoctoral fellows who discussed their experiences at the facility and their thoughts and recommendations on facility improvements. Wide-ranging and engaging discussions were sparked by this forum, which resulted in the student/postdoctoral report reproduced at the end of this document.

Another important event was a job fair designed to bring students together with potential future employers. This fair will be expanded at the next workshop.

Finally, one of the important decisions made at the workshop was to schedule the next one, which will be held at LLE on 27–29 April 2011. During their meetings, the Users Group and interested members of the HED community are formulating plans for this third workshop and reviewing progress on the **Findings and Recommendations** (p. 208) of the second workshop. In the future, a semiannual meeting will always take place at a satellite meeting during the fall American Physical Society's Division of Plasma Physics Conference.

The Presentations

A wide-ranging series of 76 talks and posters were presented over a two-day period. In the morning sessions, invited talks covered the facility and science. The invited science talks focused on several important topics, including high-energy-density plasmas, laboratory astrophysics, ignition in inertial confinement fusion (ICF), the physics of fast ignition, and future experiments on OMEGA and the NIF.

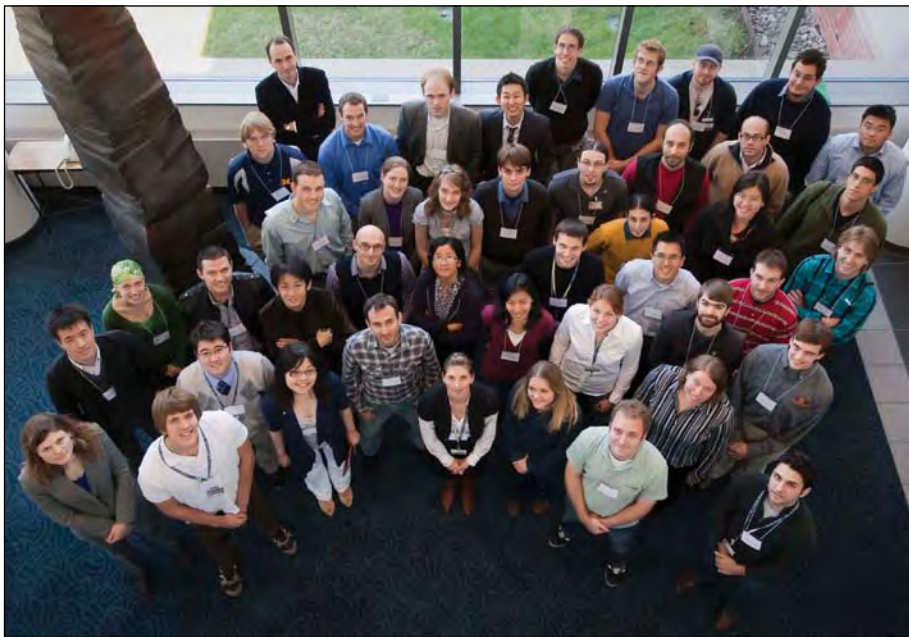


Figure 124.47
A total of 45 students and postdoctoral fellows attended and made 31 engaging presentations.

U1093JR



U1094JR

Figure 124.48

In the plenary sessions, 17 authorities spoke about the science and opportunities of high-energy-density physics and described the evolving capabilities of the Omega Laser Facility needed to reach new science frontiers.

The facility talks presented important details and developments on the status and performance of OMEGA/OMEGA EP from pulse shaping and duration to beam smoothing; the qualification process for interfacing new experiments; the present, and soon-to-be operating, set of diagnostics; and the critical role of targets, from design to procurement, full characterization, fielding, and, finally, shooting.

In addition to the 17 invited presentations, 59 contributed posters and talks covered a wide spectrum of work on OMEGA from target fabrication to fast-ignition experiments to basic and novel nuclear physics experiments. Additional presentations covered opportunities for taking physics platforms developed at OMEGA to larger (the NIF) and smaller (e.g., Jupiter, Trident, and LULI) facilities. The invited, contributed, and poster presentations formed much of the basis for wide-ranging lively discussions resulting in the **Findings and Recommendations** (p. 208) for the Omega Facilities and future capabilities, found at the end of this document.

The photographs on the following pages provide a representative sampling of the workshop's talks, interactions, and ambience.



U1095JR

Figure 124.49

Professor Robert Rosner of the University of Chicago kicked off the workshop with an astrophysicist's perspective on high-energy-density physics.

Findings and Recommendations of the Executive Committee

Executive Committee:

Richard Petrasso, Committee Chair,
Massachusetts Institute of Technology
Hector Baldis, University of California–Davis
James Cobble, Los Alamos National Laboratory
Paul Drake, University of Michigan
James Knauer, LLE, University of Rochester (designated)
Roberto Mancini, University of Nevada–Reno
Peter Norreys, Rutherford Appleton Laboratory

1. Introduction

The OMEGA Laser Users Group warmly thanks LLE’s management for taking actions on the recommendations from our last report and for expeditiously addressing the issues identified therein. It is a strong testament to the professionalism of the facility staff that the tasks were executed with good speed and due diligence. The activities undertaken are a great credit to the Laboratory and to the University of Rochester. They are certainly highly appreciated by the academic and research user community.



U1096JR

Figure 124.50

The challenges and science of fast ignition were the focus of Professor Peter Norreys of Rutherford Appleton Laboratory (RAL). Professor Norreys is a member of the Users Executive Committee.



U1097JR

Figure 124.51

Dr. Guy Dimonte of Los Alamos National Laboratory (LANL) discussed the role of particle interactions in the equilibration of high-energy-density plasmas.

The OMEGA and OMEGA EP lasers are world-class facilities that provide academic access to cutting-edge energies and intensities on target. As with any high-performance device, however, critical enhancements are needed to continue to see progress in forefront science. This document describes the academic and research user community’s observations, distilled from its April 2010 workshop, of those elements and components that can maintain LLE’s leading position at the forefront of high-energy-density physics (HEDP). The OLUG looks forward to hearing progress on these recommendations at the semiannual satellite meeting in November (at the APS Conference) and at its next annual workshop (27–29 April 2011).



U1098JR

Figure 124.52

Dr. Brent Blue from General Atomics discussed the science and technology of developing and fielding complex targets for OMEGA experiments.

2. OMEGA (60 beams)

a. Three independent legs will add substantial improvement and flexibility to future experiments. Greatly expanded experimental design options would develop if it were possible to use all three of the existing drivers, with each driving one of the OMEGA legs. Ideally, each driver would be able to drive any leg to accommodate the constraints imposed by diagnostic configurations. Improved experiments and new classes of experiments would then become possible. The OLUG considers this a high priority.

Request: Present a plan to the Executive Committee on the implementation of three independent legs. In addition, include this and additional options for discussion at next year's workshop.

LLE Response: Preliminary concepts for this project have been developed and will be advanced further in FY11. Pending the availability of LLE resources, the implementation will commence in FY11. At a minimum, LLE will complete a plan for the implementation.

b. Request: Compile a list of qualified diagnostics that can be fielded for joint operations.



U1099JR

Figure 124.53
Moving physics platforms and experiments from OMEGA to the NIF was the focus of remarks by General Atomics' Joe Kilkenny. Dr. Kilkenny gave many concrete examples of this migration including x-ray, neutron, and charged-particle diagnostics.



U1100JR

Figure 124.54
(a) Professor Roberto Mancini from the University of Nevada and (b) Dr. Carolyn Kuranz from the University of Michigan posed questions in a plenary session. Prof. Mancini is a member of the Users Executive Committee.

LLE Response: The requested information will be made more readily accessible, and the OLUG Executive Committee will be notified as soon as the data are published on the Website.

c. It is common to drive experiments with ten OMEGA beams and very common to conduct two separate experiments in one day. The workhorse distributed phase plates (DPP's) are the SG8's. Many users have found that the limited number of these specific DPP's has compromised the quality or productivity of their experiments, especially when they had shots on the second half-day of a shared day. In the area of chamber optics, OLUG would prioritize this item second behind the provision of four 750- μm phase plates for OMEGA EP.

Request: Acquire enough SG8's to make 20 available to the user community (if this will not jeopardize the higher-priority 750- μm phase plate purchase needed for OMEGA EP).

LLE Response: The acquisition of additional SG8 DPP's is included in LLE's FY11 budget. The implementation date is contingent on vendor availability. There are currently 12 SG8

DPP's available, and these can continue to be shifted to accommodate campaign transitions as required in the interim period.

d. Request: Acquire a high-resolution neutron spectrometer to measure neutrons with energies in the 2- to 3-MeV range.

LLE Response: LLE is working with users to develop the requirements for this diagnostic and will then determine if it is feasible. If so, LLE will initiate a project to implement it.

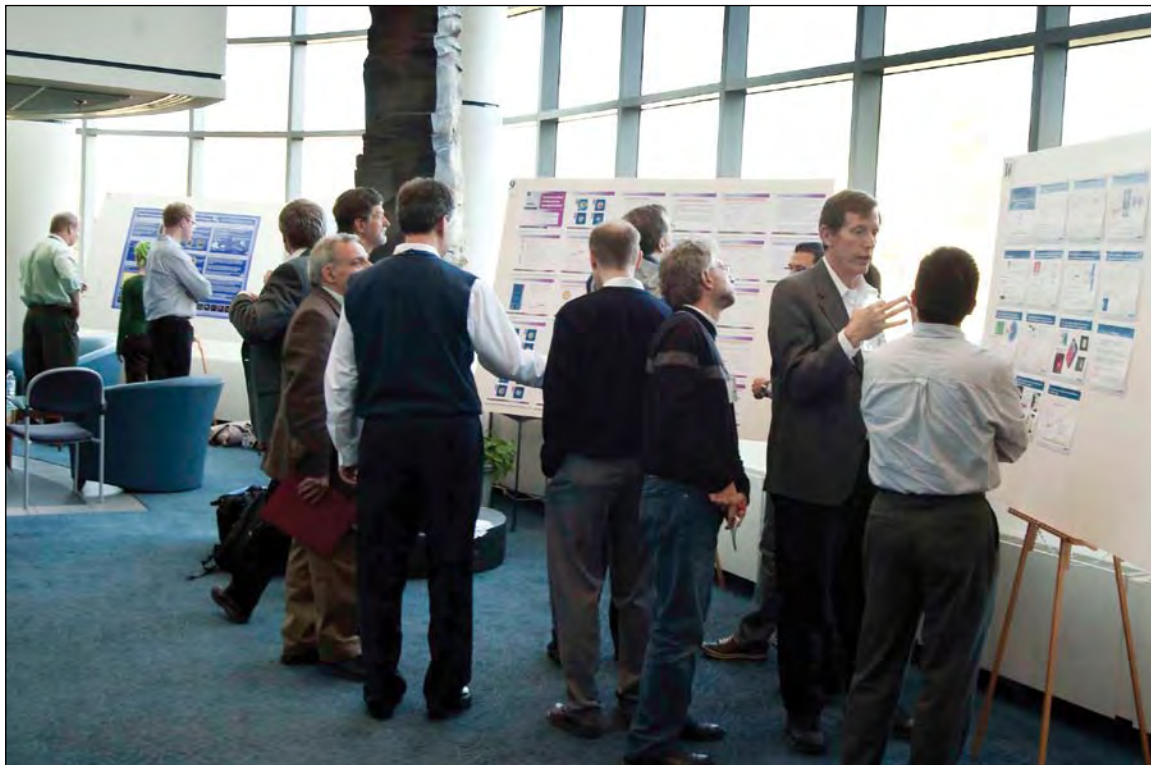
e. Upgrade the backlighter driver to operate at the nominal specified performance. The existing backlighter driver is unable to support the full energy that OMEGA's 60 beams are capable of producing. Because most backlighting and x-ray-probing experiments are photon limited, this is a significant shortfall for some experiments.

Recommendation: Improve the backlighter driver in order to support full-energy operation of the beams that it drives.

LLE Response: The backlighter source will be reworked in FY11 to increase the available operating envelope to match the other laser drivers.

f. OMEGA EP petawatt (PW) beam delivering two foci onto target. There is a need for simultaneous pump/probe experiments on OMEGA using the OMEGA EP PW beam. The availability of this feature would greatly increase the capability of the facility and would lead to the undertaking of many new experiments. Examples include hard x-ray radiography of integrated fast-ignition experiments. The OLUG recognizes, however, that space limitations impose a restriction on the provision of a single off-axis focusing parabolic mirror. The OLUG considered the possibility of splitting the PW beam into two beamlets at the final turning mirror to generate two focal spots.

Request: The OLUG requests that LLE investigate the possibility of splitting the petawatt beam and report back to the Executive Committee.



U1101JR

Figure 124.55

Two poster sessions, during which 43 posters were presented, offered ample opportunities for informal discussion about OMEGA experiments and their connections to important work at other HED facilities.

LLE Response: In FY11 the beam-combiner optic in the grating compressor chamber will be reinstalled. With this optic, the two short-pulse beams can be independently directed to two foci with a small separation. This capability will be developed and demonstrated on the OMEGA EP target chamber initially in FY11 and may be available on OMEGA in late FY11. The requirements for focal-spot separation, quality, and timing need to be refined to determine if this flexibility will meet user requirements. LLE will provide status updates on this effort to the OLUG Executive Committee. Should a “split mirror” be required, the design, fabrication, and integration effort will likely take of the order of 18 to 24 months. LLE recommends that users who need this feature refine their requirements so that this assessment can be made as soon as practical.

g. Integrated experiments require smaller focal spots for the petawatt beam. This is the same problem as Issue (g) (p. 216) in the section devoted to **OMEGA EP**.

Endorsement: OLUG strongly endorses the development and implementation of the new phase-front corrector as a matter of high priority.

LLE Response: The FY11 phase-front-correction effort will initially concentrate on a proof-of-principle experiment. If this demonstration is successful, a second-generation device will be fabricated at large aperture to refine the technique. Concurrent with this work is LLE’s effort to operate the existing adaptive-optic, closed-loop system as close as practical to shot



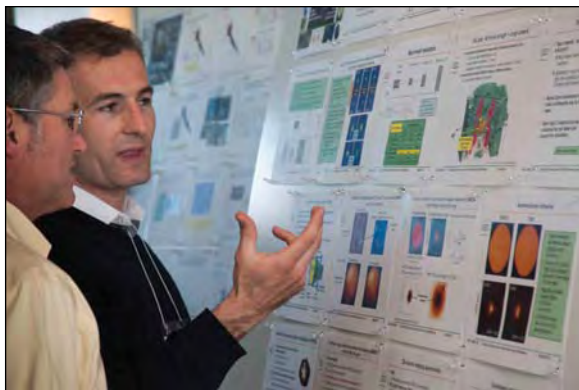
U1102JR

Figure 124.56
University of Michigan student Elisio Gamboa discussed his work on x-ray Thomson-scattering imaging with National Nuclear Security Agency’s (NNSA) Allan Hauer. Dr. Hauer presented a talk on the importance to NNSA of high-energy-density laboratory physics.



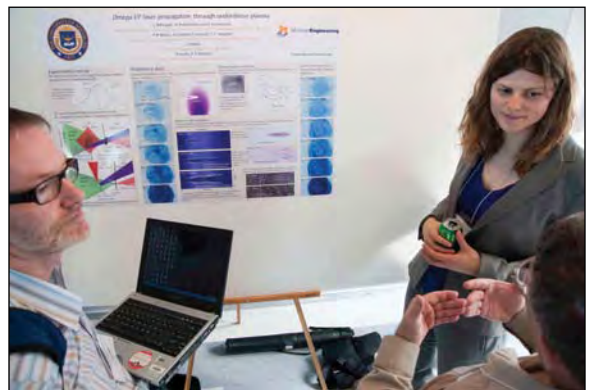
U1104JR

Figure 124.58
Frank Phillipe (left), from France (Commissariat à l’énergie atomique), chatted with Chikang Li of MIT. Drs. Phillipe and Li recently collaborated on OMEGA experiments involving rugby-shaped hohlraums.



U1103JR

Figure 124.57
Dr. Tony Caillaud, from France (Commissariat à l’énergie atomique), showed Professor Linn Van Woerkom (Ohio State University) neutron images of OMEGA DD and DT implosions.



U1105JR

Figure 124.59
Postdoctoral fellow Louise Willingale, from Prof. Karl Krushelnick’s group at the University of Michigan, and Peter Norreys of RAL listen to comments about her OMEGA EP research on proton backlighting of laser channeling.

time to improve repeatability. Finally, high-spatial-resolution phase-front control will be investigated using the active device presented to the OLUG community on 29 April 2010. Note that the implementation of dynamic control may not be complete until FY12.

h. OMEGA 60-beam timing measurement accuracy. At present, for delays or advances (offsets) of beams beyond about 10 ns from time zero, the accuracy with which one knows the beam timing drops to ± 0.5 ns. This often becomes the largest uncertainty in experiments with offsets in the 10-ns to 30-ns range.



U1106JR

Figure 124.60
Dr. Kazuo Tanaka (Osaka University) and Dr. Wolf Seka (LLE) conversed during the poster session. Dr. Tanaka presented work on the self-focusing of relativistic electrons.



U1107JR

Figure 124.61
Dr. Jim Cobble (left, from LANL), a Users Executive Committee member, spoke with Professor David Meyerhofer (LLE) about the Recommendation and Findings report for the LLE management. This report is used to help prioritize LLE facility upgrades and directions.

Request: Develop the means to determine the beam’s temporal offsets actually achieved on each shot, with an accuracy on the order of ± 0.1 ns. Such a capability would significantly improve the quality of experimental results from certain experiments.

LLE Response: The P510 streak camera system has an option currently available for a 40-ns sweep speed that is calibrated to give timing to < 0.1 ns over the requested 10- to 30-ns window. LLE recommends consulting with the Laser Facility Manager during the proposal phase (~2 months prior to shot day) to optimize configuration of the laser streak system to yield satisfactory pulse-shape measurement and precision timing simultaneously.

i. Photographic documentation of some diagnostic and related systems. To understand complex mechanical systems, it is often helpful to have photographic (and/or CAD) images to complement sets of mechanical drawings. This is definitely true of the ten-inch manipulators (TIM’s). We suggest that such images be made available online for the TIM’s. Users and the facility should both consider whether there are other systems that would also merit photographic and/or CAD documentation.

LLE Response: LLE concurs with the request to make a photograph-enhanced diagnostic glossary and will develop a standardized “cut sheet” for each diagnostic. The OLUG Executive Committee will be notified as soon as the data are published on the Website.



U1108JR

Figure 124.62
Dr. Frederick Séguin (MIT) gave a contributed talk about observations of the electromagnetic fields associated with coronal filamentation in direct-drive ICF implosions.

3. OMEGA EP

a. Bring OMEGA EP performance up to its full specification. We fully appreciate that the OMEGA EP IR and UV beam energy must be limited to ensure minimum damage to expensive and difficult-to-obtain optical components during operations with the existing gratings and UV optics. On the other hand, it is OLUG's duty to note that the user community needs access to the full performance of the laser facility to ultimately allow one to explore the exciting new regimes in high-energy-density physics. The constraints, while essential, limit the experiments that have been conducted as well as the results that have been obtained so far. Although it should be pointed out that outstanding results have been obtained with the present operating parameters of OMEGA EP, it is still the desire of the user community to have the facility operating at its specified performance at the earliest practical opportunity.

Endorsement: OLUG endorses LLE's plan to develop and acquire high-laser-damage-threshold IR and UV optics that

will make it possible for OMEGA EP to routinely operate at its design performance. OLUG requests that facility management keep the OLUG Executive Committee apprised of the research and development plans that will make it possible for OMEGA EP to reach design performance.

LLE Response: LLE is aggressively working to expand the operational envelope limits of OMEGA EP. The IR and UV energies on target are currently limited by laser-induced damage. The constraints are due to the laser-damage-threshold limits of gratings (short-pulse IR) and transmission optics (long-pulse UV). LLE will continue to share progress and plans on this item with the OLUG Executive Committee.

b. Bring design options forward to next OLUG workshop for 2 ω and 3 ω conversion of the PW beam. There are some preliminary and tentative indications, from experiments performed in France, that the fast electron energy transfer and heating of background plasma is enhanced with frequency-converted



U1109JR

Figure 124.63
Productive discussions among researchers from around the world occurred in several informal settings.



U1110JR

Figure 124.64
Benchmarks for achieving ignition were the subject of Professor Riccardo Betti's presentation.

light. This past summer at the TITAN facility, more evidence was gathered that added to the knowledge base. Certainly, much greater control over the energy content of the amplified spontaneous emission pedestal associated with petawatt laser pulses is ensured with conversion to 2ω and 3ω . This has been established as an important factor in cone-guided experiments. It is prudent to have available engineering plans for frequency conversion of the PW beam if required for future experiments by the user community.

Recommendation: The OLUG requests that facility management provide options for discussion at the next OLUG Workshop for frequency conversion of the PW beam.

LLE Response: LLE will commence a scope study to identify viable concepts for implementation of short-pulse frequency conversion. There is a high likelihood that conversion crystals, mounts, diagnostics, beam transport, and focusing systems will constitute a significant investment of LLE resources and require an NNSA-approved construction project. A case study representing the need for this item would be beneficial in garnering NNSA support for a capital project.

c. Two Cu K_{α} imaging crystal spectrometers are needed for both OMEGA 60 and OMEGA EP. Understanding the physics of fast electron energy transport from petawatt-power laser-plasma interactions with solid targets requires the deployment of sophisticated x-ray diagnostics. Cu K_{α} imaging spectrom-

eters have been developed in the United States over the past decade and have proven to be powerful tools in diagnosing the heating of dense matter using intense laser pulses. These instruments are required on both chambers so that independent experiments can be carried out simultaneously. In each target chamber, they need to be deployed in orthogonal directions so that spatial nonuniformities can be identified and characterized.

Recommendation: The OLUG requests that LLE management validate and deploy these imaging spectrometers as a matter of high priority in the coming year. The OLUG recognizes that the deployment of orthogonal instruments may pose difficulties, but the requirement for these instruments for each chamber is vital to the user program. We request that OMEGA provide a deployment plan to the Executive Committee for their consideration and report to the workshop next year on arising issues.

LLE Response: A prototype crystal imager is being developed for the Multi-Terawatt laser with plans to install a complete system on OMEGA EP in FY11. In the interim a “fast-track” crystal imager was installed on OMEGA EP in FY10. In FY11, LLE will initiate projects to add a second crystal imager on OMEGA EP and two on OMEGA. Depending on resources available and other priorities, these projects may be carried out in FY11.

d. Two electron spectrometers are needed for both target chambers. Electron spectrometers are important tools for char-



U1111JR

Figure 124.65
Dr. Al Trivelpiece (left) and Jim Decker brought some unique experience and valuable insights to the workshop.

acterizing the behavior of intense laser–plasma interactions. They have applications in many areas, including wakefield acceleration, betatron x-ray source characterization, channel formation, and positron generation, among many others. The development of a university-based program requires the deployment of spectrometers with electromagnets that provide a wide window up to GeV of particle energies. OLUG understands that Lawrence Livermore National Laboratory (LLNL) colleagues have validated and deployed low-energy electron spectrometers in their experiments; these instruments should be made available to the wider community.

Recommendation: The OLUG requests that LLE management initiate a design and validation program for an electromagnet-based electron spectrometer for wakefield acceleration studies up to GeV particle energies. They request that electron spectrometers based on the LLNL design be made available to the wider academic community.

LLE Response: In FY11, LLE will initiate projects to ensure that there are two electron spectrometers on OMEGA EP and two on OMEGA. Depending on resources available and other priorities, these projects may be carried out in FY11.

e. LLE’s contrast-ratio improvement program. The OLUG was impressed with the presentation of Christophe Dorrer relating to the intensity contrast issues of the petawatt beam. The audience appreciated the identification of all the different components in the laser chain that contribute to the pedestal over its full range—some nanoseconds ahead of the pulse, some on its leading edge. The enhancement program was warmly received by the audience.

Endorsement: The OLUG strongly endorses LLE’s contrast-ratio improvement program. They fully endorse the time frame outlined and want to be updated on progress at the next OLUG Workshop.



U1112JR

Figure 124.66

Professor Paul Drake (University of Michigan), a Users Executive Committee member, presented a talk about the opportunities for doing laboratory astrophysics on OMEGA and OMEGA EP.

LLE Response: The OLUG Executive Committee will be kept abreast of all developments in the short-pulse laser's contrast enhancement.

f. Status of the 4 ω probe. The OLUG was impressed with the presentation of Wolfgang Theobald on the fourth-harmonic probe status. The probe commissioning is proceeding with good speed and the audience was delighted with progress so far. Nevertheless, concern was raised that the seeds are not from the same source and much closer attention to minimizing and measuring timing jitter is needed. In addition, the pulse energy is marginal and needs to be increased by an order of magnitude.

Recommendation: The OLUG requests that the timing-jitter issue be addressed and an additional amplifier stage be added so that the probe energy can be increased when required. These changes should be reported to the Executive Committee.

LLE Response: The concerns of the OLUG have been communicated to the development team and will be closely monitored through the initial implementation of the 4 ω probe

laser at its baseline performance level. Any requirements analysis for specific experiments that users can provide to the team would be helpful in motivating changes to the baseline requirements for this system. LLE will work to include design features for operation of the probe with maximum precision timing and as much energy as practical.

g. OMEGA EP focal-spot size of the PW beam. The community welcomed Brian Kruschwitz's characterization of the OMEGA EP focal-spot quality. They were satisfied that the encircled energy measurements he reported were consistent with other plasma diagnostics. Concern was raised, however, that the focus of the OMEGA EP was insufficient for many future experiments and that effort is needed to reduce the 80% encircled energy radius by a least a factor of 2 (from 40 μm to 20 μm). They were delighted to hear about the new phase-front-corrector technology that will make this development possible.

Endorsement: OLUG strongly endorses the development and implementation of the new phase-front corrector as a matter of high priority.



U1113JR

Figure 124.67
From far left, Alberto Marochinno (University of Rome), Tazio Levato (INFN Frascati), Patrizio Antici (INFN Frascati), Rich Petrasso (MIT), Riccardo Betti (LLE), Lois Buitano (NNSA), Orlando Ciricosta (University of Pisa), and Angelo Schiavi (University of Rome) are captured together during the poster session.

LLE Response: See response to **OMEGA** Item (g) (p. 211).

h. Polarization smoothing on all four UV beams. The community was very impressed by the quality of the presentation from Samuel Morse. They received with great pleasure the news of the concerted effort to address issues raised at the last workshop. They were particularly struck by the quality of his argument that the polarization-smoothing technology had reached sufficient maturity to implement on OMEGA EP and that the advantages over smoothing by spectral dispersion were apparent.

Endorsement: OLUG unanimously accepted LLE's recommendation for polarization smoothing on all beams. They look forward to rapid implementation of the proposal and to receiving an updated progress report at next year's meeting.

LLE Response: User need for this feature remains unclear. If there is any specific analysis of an experiment that would benefit from this capability, please communicate to LLE since it will aid in justification of the cost. LLE is pursuing this item with no guarantee that the acquisition will be selected for funding in FY11. The time frame for implementation of polarization smoothing is 18 to 24 months after optics are ordered. Every effort will be made to expedite this acquisition as well as the

mounts that will support the optics, once the funding commitment is secured.

i. The planar cryogenic target handler should be implemented on OMEGA EP for users. A number of academics in the community raised the issue of fielding planar cryogenic-deuterium targets for the OMEGA EP chamber. They expressed concern that this technology was not available for cutting-edge transport and hydrodynamic experiments.

Recommendation: OLUG strongly endorsed the implementation of planar cryogenic target-handling technology as a high priority. The community wants to see this target-handling technology made available at the earliest opportunity.

LLE Response: LLE will consider the OLUG endorsement of this project in prioritizing laboratory resources in FY11. It is likely to take 12 to 18 months from project inception to initial capability deployment. LLE will keep the OLUG Executive Committee informed of the project status.

j. A full set (4) of 750- μ m phase plates is needed. The community expressed great pleasure that a number of phase plates had been acquired in response to their requests at last year's workshop. After considerable debate over different phase-plate



U1114JR

Figure 124.68

The student/postdoctoral panel presented important insights from young researchers working at the Omega Facility. Left to right: Dr. Maria Barrios (University of Rochester, LLE), Dr. Tammy Ma (University of California, San Diego), Dr. Hiroshi Sawada (University of California, San Diego), Dr. Ryan Rygg (LLNL), Dan Casey (MIT), Dr. Andrea Kritcher (LLNL), and Dr. Louise Willingale (University of Michigan).

sizes, it was felt that a full set (4) of 750- μm phase plates is needed. These would be useful in the context of the long-duration hydrodynamics and laboratory astrophysics experiments that OMEGA EP uniquely makes possible by stacking beams in time. By running the specified maximum of 6 kJ in a 10-ns pulse, a 750- μm phase plate produces an average intensity of $1.4 \times 10^{14} \text{ W/cm}^2$. Using an 1100- μm phase plate reduces the intensity to below $7 \times 10^{13} \text{ W/cm}^2$. This is an important difference. One definitely wants to be above 10^{14} W/cm^2 for most experiments. In solid plastics, shocks will be driven not much more than 1 mm in 40 ns; therefore, 2-D expansion is a smaller concern than having adequate intensity.

Endorsement: A full set (4) of 750- μm phase plates should be purchased and made available to the community.

LLE Response: LLE appreciates the aggregation of OLU requirements and distillation to a well-defined recommendation. The acquisition of additional 750- μm distributed phase plates to obtain a full set of four operational optics is in the FY11 acquisition plan.

k. Requirement for a limited-reservoir gas-jet target. Some academics expressed the view that gas-jet targets should be implemented on OMEGA EP. They accepted the facility

management’s argument that an unlimited reservoir gas line might put the OMEGA EP compressor grating actuators at risk. They recognized, however, that many experiments would benefit from a gas-jet arrangement. It was felt that the burden of commissioning this technology should not fall on a single institution but should be shared as a common resource. They agreed that a limited reservoir would add capability to a wide range of experiments.

Recommendation: The facility should design, validate, and implement a limited-reservoir gas-jet target and make it available to the user community.

LLE Response: Development of equipment to provide a gas jet in the Omega Facility will require significant resources. Users interested in this capability should contact John Soures, who will facilitate formation of a subcommittee to investigate the development of this capability. LLE resource allocation to this project is subject to balancing laboratory priorities. Project selection depends on developing a set of requirements that can be met within the system’s safety constraints.

l. Requirement for added flexibility for long-pulse operation. The community was delighted by the performance of the long-pulse beams in their current configuration. The arrangement



U1115JR

Figure 124.69
A “town hall” meeting on the importance and role of high-energy-density physics, from the DOE perspective, was led by Mark Koepke (left; Office of Fusion Energy Science), Kim Budil (Office of the Under Secretary for Science), and Lois Buitano (National Nuclear Security Agency).



U1116JR

Figure 124.70
Kim Budil (Office of the Under Secretary for Science) discussed her office’s perspective on high-energy-density physics.



U1117JR

Figure 124.71

Facility presentations, like this one by Samuel Morse (LLE), related new and ongoing developments on OMEGA and briefed younger researchers on the effective use of the facility. Mr. Morse's extensive knowledge of the facility is invaluable to those planning OMEGA experiments.

had produced some outstanding results that were received by the audience with acclaim. After much debate, the community felt that if different ports, originally earmarked for long-pulse operation, were made available, it would add substantial flexibility to experiment design and effectiveness. They endorsed the option of irradiation from opposite sides as one example.

Recommendation: The OLUG recommends that all ports originally earmarked for long-pulse operation be brought into facility capability. The OLUG welcomes a report at next year's meeting on progress with options.

LLE Response: The 48°-cone-angle ports were proposed as an option in the OMEGA EP project, but it was not supported by the users or NNSA at that time. It would be very expensive to fit out with UV-beam-transport paths, which would take significant facility time and would require capital project support from NNSA. A potential smaller-scale, higher-payoff alternative, suggested at the OLUG meeting in April 2010, was to bring one or more beams to the back side of the target chamber. A feasibility study will be conducted to assess potential UV-beam routing to the opposite side of the target chamber from the existing 23° UV-beam ports.

m. Equivalent-plane monitors for all UV beams. The community felt that while the focal-spot monitor was adequate for

some experiments, all experiments were complicated by a lack of knowledge of the quality of all beams away from their foci.

Recommendation: Equivalent-plane monitors should be implemented for all beams. The OLUG welcomes a report on this issue at next year's meeting and trusts that this can be implemented with little disruption to operations.

LLE Response: The request for UV far-field measurements on all beams will be carefully considered. It would be helpful if the experimentalists requesting this feature would provide a range of spot sizes of interest for measurement. The UV diagnostic package has provision for locating a far-field monitor, and the LLE plan is to implement a phase-plate holder in the diagnostic path for at least one beam. LLE will keep OLUG apprised of the progress in meeting this recommendation.

n. A new gamma-ray spectrometer diagnostic is required. The community felt that a new gamma-ray spectrometer needs to be designed, validated, and commissioned for the facility. Users requested that the spectrometer have a spectral range up to 20 MeV.

Recommendation: The OLUG requests that management consult the Executive Committee on the design, validation, and implementation of this new instrument for the community.



U1118JR

Figure 124.72

Brian Kruschwitz (LLE) discussed the latest techniques for characterizing the OMEGA EP laser's focal spot. Such information is essential for planning experiments.

LLE Response: OLUG scientists interested in this spectrometer should contact John Soures, who will facilitate formation of a subcommittee on high-energy photon spectroscopy. Once a consensus of requirements for sensitivity, spectral range, resolution, and other features is generated, the subcommittee and OLUG Executive Committee can provide LLE with more definition of what is desired. LLE resource allocation to this project is subject to balancing laboratory priorities.

o. See also Items (f) and (g) (pp. 210,211) of OMEGA (60 beams).

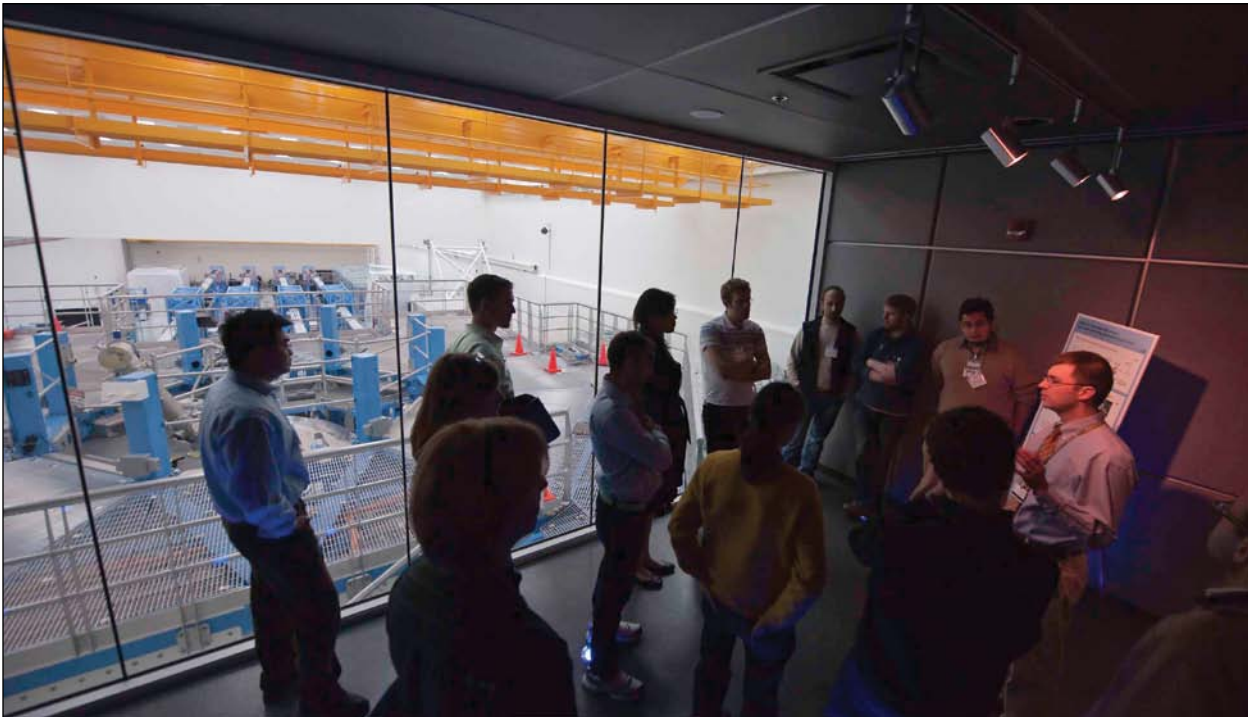
4. Other Facility Improvements

a. Dedicated user support for experiment design and theoretical modeling. To maximize the productivity of both OMEGA (60 beams) and OMEGA EP, it is important to have access to theoretical and computational support for both experiment design and data interpretation for university-based academics. Individual academics, who are motivated by curiosity-driven research in high-energy-density science, often find that they do not have access to the necessary sophisticated computational models at all stages in the training cycle. The

very nature of university life, where there is a high turnover of doctoral and postdoctoral research fellows, means that modeling skills nurtured by the teams and applied to specific problems can suddenly evaporate, leaving them without vital tools at critical stages in the research effort.

Ideally, the theoretical support team must be located within the larger-scale facilities. It must be of critical size to provide the facility users with a wide range of modeling capability (e.g., one- and two-dimensional magnetohydrodynamic simulations, implicit and explicit particle-in-cell and hybrid models for high-intensity laser-matter interactions, quantum molecular dynamics for warm dense matter studies, etc.) and have dedicated access to large-scale, high-performance computing resources. Here are some desirable characteristics of the support team:

- Team members should be involved at all stages in the experiment cycle, obviously requiring a collaborative approach by all parties.
- The team must be university focused and highly responsive to user demands. The team should assist with interpretation



U1119JR

Figure 124.73

David Canning (LLE) led a tour of the OMEGA EP laser and discussed its capabilities. For many new researchers, this was an ideal opportunity to learn about the facility.

of smaller-scale experiments undertaken on university-scale facilities. This is particularly important to the reduction in cost and size of intense laser systems and the proliferation within academic institutions.

- The team must be of sufficient size so that members have enough time to develop their own research interests, in addition to their support duties. This should allow team members time to devote to the development of new codes, algorithms, and possibly visualization routines.
- The team must be involved in training students and post-doctoral fellows in high-energy-density science, e.g., by co-supervision of Ph.D. students, etc.

Clearly, a balance must be struck between supporting experiments themselves and maintaining a critical size in the modeling support team.

Recommendation: The OLUG requests that LLE management establish a university-focused support team, ideally comprising four staff members, with academics from other programs at LLE and/or other institutions. The team will make a huge difference in the quality and depth of publications arising from the facility.

LLE Response: After the 2010 OLUG report is completed, LLE will request additional funding from NNSA and the Office

of Science to support this request. LLE may request a letter from the Executive Committee endorsing this request.

b. Increased support from DOE to the National Laser Users' Facility (NLUF) Program. The OLUG recognizes and applauds the increased funding to the NLUF Program in FY11/12 from the DOE (\$1.3M to \$1.6M). This has allowed facility management to increase access under the NLUF Program for the university community. The OLUG is also highly appreciative of the efforts of DOE officials to achieve this increase. The OLUG firmly believes that the establishment of new academic positions for young researchers in high-energy-density physics, working in partnership with the established academics and consortia (e.g., the Fusion Science Center), is a high priority for the growth of the field.

Recommendation: The OLUG strongly urges DOE to maintain the percentage increase in funding to the NLUF.

Recommendation: The OLUG urges DOE to develop and fund a program to accelerate the career progression for the brightest young dynamic researchers working in experimental high-energy-density physics by sharing the cost of their appointment with universities while they are at the assistant-professor level.

LLE Response: LLE recognizes the value of these requests, but clearly it is an issue for OLUG to communicate directly with DOE.



U1120JR

Figure 124.74

Members of the OMEGA Users Executive Committee. Back row (left to right): Paul Drake (University of Michigan), Jim Knauer (LLE), Jim Cobble (LANL), and Peter Norreys (RAL). Front row (left to right): Ryan Rygg (LLNL), Rich Petrasso (MIT), Roberto Mancini (University of Nevada).

Findings and Recommendations of the Student/Postdoctoral Panel

Student/Postdoctoral Panel

Ryan Rygg (LLNL), Chair

Maria Barrios (LLE)

Dan Casey (MIT)

Andrea Kritcher (LLNL)

Tammy Ma (University of San Diego)

Hiroshi Sawada (University of San Diego)

Louise Willingale (University of Michigan)

1. Interest continued in having extensive diagnostic information available online, such as reference papers and sample/calibration data linked from the Shot Request Form. The OMEGA staff has created a diagnostics forum, with threads for individual diagnostics. It is up to the users, however, to take the discussion there and populate it with useful information, such as optimal setup or analysis techniques.

2. Published papers typically include descriptions of the basic experimental setup, results, and conclusions, but rarely include the full nitty-gritty details necessary to run experiments at OMEGA, or to analyze the raw data produced. Completed theses of prior students were identified as often including many of the useful details left out of published articles. University of Rochester theses containing work done at the Omega Facility are available on the LLE Website. It would be useful if theses from other institutions performed using OMEGA diagnostics were also collected and made available. It was also pointed out that the LLE Review has many articles that include such useful details not contained in published articles. Although back issues of the LLE Review are available on the LLE Website, the content is not easily searchable.

3. Since HEDP is still a growing field, most academic institutions do not have enough interested students to hold dedicated classes on topics relevant to HEDP. It was suggested



U1121JR

Figure 124.75

The OMEGA Users banquet offered another opportunity for attendees to interact informally, reinforce old friendships, and create new working relationships.

that experts in the field may be able to offer lecture series or entire courses online. Roberto Mancini's recent spectroscopy class was held up as an excellent example, and additional topics would also be of interest. The MIT open courseware site was recommended as a model to enable instructors and students to share lecture notes and assignments.

4. The forum concluded with a discussion of the availability and acquisition of jobs in the field, including those in academia, government laboratories, publishing, and government administration.

Conclusions and Future Workshops

This OLUG workshop, with over 115 attendees, was part of a process that will keep members of the inertial confinement fusion and high-energy-density physics communities involved in conversations and collaborations with each other and with the Omega Facility. In addition, OLUG Executive Committee members and the LLE management have been meeting on a bi-monthly basis to assess progress, compatibility with facility resources, and impact toward the implementation of the Findings and Recommendations. Progress will be presented at a

satellite meeting at the Chicago APS Meeting (9 November 2010) and in depth at the next Users Workshop.

The next OMEGA Laser Users Workshop will be held at LLE on 27–29 April 2011; plans for it are already well underway. To this end, significant financial support from NNSA has already been procured to help defray the cost of student and postdoctoral travel. We anticipate that this next workshop will be as exciting and memorable as the first two. Come join us!

ACKNOWLEDGMENT

For capturing the ambience and spirit of the workshop through his camera lens, we thank Eugene Kowaluk. To NNSA, we gratefully acknowledge the financial assistance for student/postdoctoral travel expenses. We thank the University of Rochester Fusion Science Center, and the Office of Fusion Energy Science, for co-sponsoring the OMEGA Users Group Workshops. We thank LLE for supporting this workshop in numerous ways and for their responsiveness in addressing the Findings and Recommendations of the Users.

This synopsis was compiled and edited by R. D. Petrasso (petrasso@psfc.mit.edu) of the MIT Plasma Science and Fusion Center, with critical input and contributions from workshop attendees, the Executive and Student/Postdoctoral Workshop Committees, and the LLE management. Please send corrections to R. Petrasso. The final synopsis will be posted at www.lle.rochester.edu/about/omega_laser_users_group.php.

LLE's Summer High School Research Program

During the summer of 2010, 16 students from Rochester-area high schools participated in the Laboratory for Laser Energetics' Summer High School Research Program. The goal of this program is to excite a group of high school students about careers in the areas of science and technology by exposing them to research in a state-of-the-art environment. Too often, students are exposed to "research" only through classroom laboratories, which have prescribed procedures and predictable results. In LLE's summer program, the students experience many of the trials, tribulations, and rewards of scientific research. By participating in research in a real environment, the students often become more excited about careers in science and technology. In addition, LLE gains from the contributions of the many highly talented students who are attracted to the program.

The students spent most of their time working on their individual research projects with members of LLE's technical staff. The projects were related to current research activities at LLE and covered a broad range of areas of interest including experimental diagnostic development, computational modeling of implosion physics, opacity data for hydrodynamic simulations, laser physics, experimental and theoretical chemistry, materials science, cryogenic target characterization, target positioning and viewing systems, and database development (see Table 124.II).

The students attended weekly seminars on technical topics associated with LLE's research. Topics this year included laser physics, fusion, holography, nonlinear optics, atomic force microscopy, electrostatics, and electronic paper. The students also received safety training, learned how to give scientific presentations, and were introduced to LLE's resources, especially the computational facilities.

The program culminated on 25 August with the "High School Student Summer Research Symposium," at which the

students presented the results of their research to an audience including parents, teachers, and LLE staff. The students' written reports will be made available on the LLE Website and bound into a permanent record of their work that can be cited in scientific publications.

Two hundred and sixty-five high school students have now participated in the program since it began in 1989. This year's students were selected from over 60 applicants.

At the symposium LLE presented its 14th annual William D. Ryan Inspirational Teacher Award to Mr. Brad Allen, a physics teacher at Brighton High School. This award is presented to a teacher who motivated one of the participants in LLE's Summer High School Research Program to study science, mathematics, or technology and includes a \$1000 cash prize. Teachers are nominated by alumni of the summer program. Mr. Allen was nominated by Leela Chockalingam, Aaron Van Dyne, and Harvest Zhang, participants in the 2009 program. Leela described Mr. Allen as "one of the most fantastic science teachers I have had the opportunity to learn under. . .He took the fear and mystery out of physics and made it fun. Mr. Allen guided me toward my love of science." Aaron wrote, "Mr. Allen is a large part of why so many people learn a subject as difficult as physics so painlessly. . .He is just plain good at his job, which is preparing the next generation of scientists. . .He has an ability to make physics seem logical to everyone, and yet to challenge even the most talented students." Harvest was also very appreciative, writing, "Mr. Allen shares his brilliance with his students and stays after school almost every day to help students at all levels of physics. . . We will go on to college and learn more advanced physics. . .but it was Mr. Allen who laid the rock-solid foundation on which all future lessons in physics will rest." Brighton High School Principal Mrs. Nancy Hackett added that Mr. Allen has done "a fabulous job" and that his "good energy" has dramatically improved the level of science education at Brighton High School.

Table 124.II: High School Students and Projects—Summer 2010.

Name	High School	Supervisor	Project Title
James Baase	Victor	D. J. Lonobile, G. Brent	Optimizing the Movement of a Precision Piezoelectric Target Positioner
Andrew Chun	Brighton	F. J. Marshall	X-Ray Imaging with Compact Kirkpatrick–Baez Microscopes
Robert Cooper	Allendale-Columbia	R. W. Kidder	Designing an Ontology for Experimental Diagnostics at LLE
Luke Coy	Greece Arcadia	R. Rombaut, R. S. Craxton	A Graphical User Interface for User-Generated Opacity Data
Kyra Horne	Fairport	M. J. Guardalben	Reducing UV Near-Field Beam Modulation on OMEGA EP by Angularly Detuning the Frequency Conversion Crystals
Karin Hsieh	Webster Schroeder	W. T. Shmayda	Modeling Water Desorption from Stainless Steel
Connie Jiang	Brighton	D. W. Jacobs-Perkins, R. Huff	Testing and Installation of the Reticle Projector on OMEGA's Target Viewing System
George Liu	Pittsford Sutherland	R. Epstein	Imploded Shell Parameter Estimation Based on Radiograph Analysis
Thomas Mo	Webster Schroeder	R. S. Craxton	X-Ray Backlighting of a Shock-Ignition Experiment on the NIF
Eric Pan	Webster Thomas	T. B. Jones	Using <i>Surface Evolver</i> Software to Model the Behavior of Liquid Deuterium
Ryan Shea	Fairport	W. T. Shmayda	Water Desorption from Stainless Steel at Variable Temperatures
Laura Tucker	Brighton	R. S. Craxton	A Design for a Shock-Ignition Experiment on the NIF Including 3-D Effects
Katherine Wegman	Pittsford Mendon	K. L. Marshall	Liquid Crystal Beam-Shaping Devices Incorporating Coumarin-Based Photoalignment Layers
Francis White	McQuaid	D. H. Edgell, M. D. Wittman	Determination and Correction of Optical Distortion in Cryogenic Target Characterization
Barry Xu	Brighton	S. X. Hu	Electron-Ion Relaxation Rates in Inertial Confinement Fusion
Andrew Yu	Pittsford Sutherland	K. L. Marshall	Modeling Absorption Spectra of Optically Switchable Azobenzenes

FY10 Laser Facility Report

During FY10 the Omega Facility conducted 1343 target shots on OMEGA and 480 target shots on OMEGA EP for a record total of 1823 combined target shots (see Tables 124.III and 124.IV).

Many changes were made to the laser system to improve low-adiabat, direct-drive cryogenic implosion performance. OMEGA conducted 38 DT spherical implosions and 40 planar cryogenic target experiments in support of shock timing. Triple-picket operational improvements highlighted the ongoing

development of direct-drive cryogenic implosion capability. The OMEGA Availability and Experimental Effectiveness averages for FY10 were 93% and 94%, respectively.

OMEGA EP was operated extensively in FY10 for a variety of internal and external users. A total of 308 short-pulse IR target shots were conducted. Of these, 232 target shots were taken into the OMEGA EP target chamber and 76 joint target shots were taken into the OMEGA target chamber. A total of 117 OMEGA EP target shots included UV beams. OMEGA EP averaged 4.9 target shots per operating day with Availability and Experimental Effectiveness averages for FY10 of 86% and 94%, respectively.

Table 124.III: Omega Facility target shot summary for FY10.

OMEGA Target Shot Summary					
Laboratory	Planned Number of Target Shots	Actual Number of Target Shots	NIC	Shots in Support of NIC	Non-NIC
LLE	352	361	0	339	22
LLNL	320	376	212	0	164
NLUF	135	150	0	0	150
LANL	130	135	55	0	80
LBS	155	190	0	0	190
CEA	45	55	0	0	55
AWE	30	37	0	0	37
U. Mich.	15	19	0	0	19
FSC	20	20	0	0	20
Total	1202	1343	267	339	737

Table 124.IV: Omega EP Facility target shot summary for FY10.

OMEGA EP Target Shot Summary					
Laboratory	Planned Number of Target Shots	Actual Number of Target Shots	NIC	Shots in Support of NIC	Non-NIC
LLE	200	206	0	193	13
LLNL	95	107	31	5	71
LBS	75	89	0	0	89
NLUF	40	47	0	0	47
LANL	20	24	0	0	24
CEA	5	7	0	0	7
Total	435	480	31	198	251

Highlights of achievements in FY10 include the following:

OMEGA Three-Color-Cycle (3CC) Beam Smoothing

Three-color-cycle (3CC) smoothing by spectral dispersion (SSD) is shown to improve picket-pointing performance in simulations. In April, the OMEGA laser was returned to a 3CC-SSD configuration. For the last decade, OMEGA had operated in the 0.8-color-cycle (or terahertz) SSD configuration. The principal motivation for this action is that the three-color-cycle, 1/3-THz SSD system provides a readily available reduction in the dynamic SSD mispointing error (SSD mpe). SSD mpe became an important parameter when the drive pulse shapes for high-performance cryogenic implosions were converted from continuous foot pulses to discrete picket pulses for adiabat control. Since the ~100-ps pickets sample only a fraction of the full bandwidth, they are susceptible to a pointing deviation from the time-integrated far field. The 3CC-SSD system reduced the SSD mpe from ~40 nm to ~5 nm in the direction of the 10.4-GHz modulator. The system provides smoothing equivalent to the 1-THz, 2-D SSD system for ℓ modes < 200. The 3CC-SSD system uses less bandwidth and has the benefit of frequency converting more efficiently, providing improved power balance and greater available on-target energy.

OMEGA Pulse Shaping

OMEGA pulse-shaping capability continues to evolve to meet the demands of producing triple-picket-shaped pulses

for cryogenic experiments. Additional improvements to the Driver Electronics Room's temperature and humidity stability were implemented, significantly improving temporal pulse-shape stability. As a result, triple-picket pulse shapes now routinely achieve precision picket-pulse-shape requirements. Pulse-shape measurement diagnostics and analysis software continue to become more sophisticated to accurately predict picket energies and UV pulse shapes.

Efforts to facilitate on-target picket power balance resulted in significantly improved target-irradiation uniformity for cryogenic implosions. The P510 streak cameras were upgraded with new electronics to further improve pulse-shape measurement capability. Stage-F amplifier gain adjustments were routinely implemented for experiments to balance picket energies as measured by the enhanced P510 streak cameras. Prior to this effort, beam-to-beam picket-pulse energy performance was greater than 10%. Beam-to-beam picket-pulse energy performance of 5% or less is now routinely achieved.

To improve picket energy and pointing performance, the phase of the SSD modulators was synchronized to the system's radio frequency. Simulations indicate that this work will improve cryogenic pulse-shape performance and repeatability on target.

OMEGA Pulse-Shape Measurement Diagnostic

A new short-pulse timing diagnostic was deployed and calibrated on OMEGA EP. The pulse-shape measurement (PSM) diagnostic uses high-bandwidth oscilloscopes and photodiodes to measure short-pulse timing at the output of the grating compressor chamber (GCC). The PSM diagnostic is calibrated using target implosions on both OMEGA and OMEGA EP and is the primary diagnostic for routinely achieving short-pulse beam timings to within 50 ps on the first shot of the day. This diagnostic is also being employed to measure the drift sources of the OMEGA EP Laser System to understand and account for sources of error.

OMEGA Multilayer Dielectric Gratings

A full complement of 12 multilayer dielectric gratings was acquired from a commercial vendor to improve short-pulse energy performance on one of the OMEGA EP beamlines. These gratings followed a development effort and qualification testing of appropriate sub-aperture samples. Notable improvements were made to the production grating cleaning and vacuum-damage test protocols. The 12 compressor gratings were inserted into the GCC upper compressor in two batches: six in June in the first and second tiled-grating assemblies, and

the remaining six in the chamber vent at the end of the fiscal year. It is expected that the operational energy envelope of this compressor will be increased by ~50% to >1.5 kJ at 10 ps in the coming year.

Knowledge of the damage limits of currently available large-area diffraction gratings is being improved. A dedicated vacuum short-pulse damage facility has been developed and is being used to study multilayer dielectric gratings under use conditions to guide safe operational limits as well as improve grating-fabrication processes. Furthermore, an *in situ* grating-damage observation system (see **Grating Inspection System for Large-Scale Multilayer Dielectric Gratings for High-Energy Laser Systems**, p. 165) makes it possible to detect damage on the final gratings during operations.

OMEGA EP Focal-Spot Diagnostic

The accuracy of target-plane, on-shot focal-spot predictions using the OMEGA EP focal-spot diagnostic (FSD) has been improved. The FSD uses a wavefront measurement in the short-pulse diagnostics package to predict the target-plane fluence distribution. Phase-retrieval techniques have been implemented that produce a more reliably accurate wavefront measurement that in turn yields significantly more accurate focal-spot predictions (see **Improved On-Shot Focal-Spot Measurement on OMEGA EP Using Phase-Retrieval-Enhanced Wavefront Measurements**, p. 192). As a result, on-shot target-plane focal-spot fluence data are now provided post-shot for short-pulse shots on OMEGA EP (see Fig. 124.76). The improved FSD will

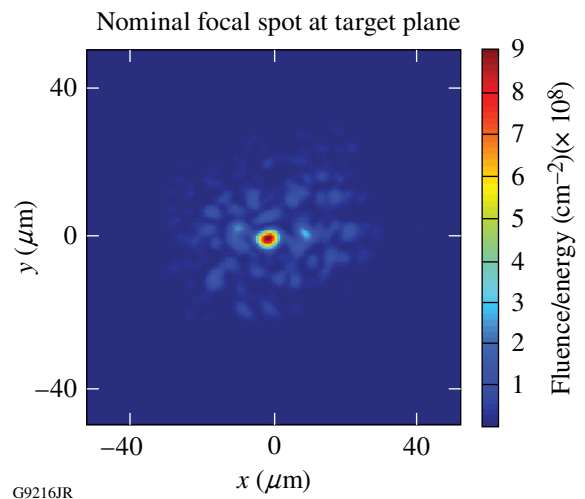


Figure 124.76

An example of an on-shot target-plane fluence measurement provided by the OMEGA EP focal-spot diagnostic on a short-pulse target shot.

play a central role in efforts to improve focal-spot repeatability and focusability.

OMEGA EP Contrast Diagnostic

Temporal contrast is now being measured in the short-pulse OMEGA EP beamlines using the high-contrast diagnostic suite (see Fig. 124.77). The on-shot contrast of short-pulse beams has been characterized using a set of calibrated fast photodiodes. This diagnostic is now operating on all high-energy shots, and nanosecond-contrast data are provided to the users. The nanosecond contrast is dominated by the parametric fluorescence from the front end that extends over a few nanoseconds, and the power of the associated pedestal is typically $10^6\times$ lower than the peak power. The contrast of the optical parametric chirped-pulse amplifier (OPCPA) front end propagating through the entire laser system has been measured using a high-resolution scanning nonlinear cross-correlator in a temporal window starting 700 ps before the main pulse. No significant discrete prepulse has been observed. These diagnostics have been used to study the contrast of OMEGA EP and support contrast-improvement campaigns. Contrast improvements have been realized by optimizing the wavelength of the seed source for the OPCPA pump, the timing between the pump and signal

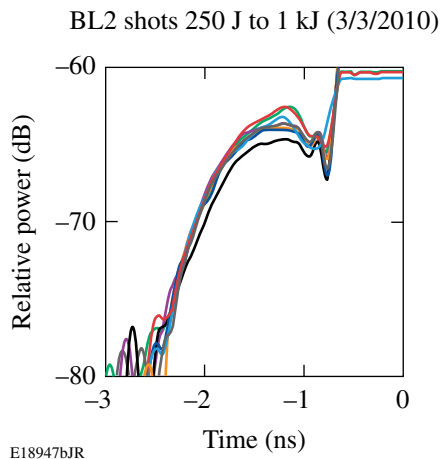


Figure 124.77
Nanosecond contrast data of shots taken on 3 March 2010. On-target contrast improvements have been measured with the high-contrast diagnostic suite.

in the OPCPA, and the nonlinear crystal configuration in the OPCPA front end. The contrast data are combined with data from the FSD to predict the on-shot intensity contrast of the pulse and the intensity of the nanosecond pedestal.

OMEGA EP Distributed Phase Plates

The first two distributed phase plates were deployed on OMEGA EP in November 2009. These UV phase plates produce 750- μm -diam focal spots and have been used extensively for experiments.

OMEGA EP Parabola Vacuum Antechambers

Vacuum antechambers for the backlighter and sidelighter off-axis parabolas (OAP's) were deployed on the OMEGA EP target chamber. These antechambers facilitate storage of the parabolas behind a protective gate valve when not in use. Access to the parabola for work such as optics replacements, installation/removal of the disposable debris shield in front of an OAP, and other maintenance no longer requires the OMEGA EP target chamber to be vented.

Experimental Diagnostics

Two new ten-inch manipulators were installed on the OMEGA EP target chamber, increasing our non-fixed diagnostic fielding capacity by 40%. A number of facility tools to better support the scientific user were implemented; for example, online availability of diagnostic documentation packages and diagnostic calibration data is now accessible by the user community.

Experimental capability evolved with the addition of 22 new diagnostics for use on OMEGA and 17 for OMEGA EP. Much of this activity involved other laboratories (e.g., LLNL, LANL, NRL, CEA, AWE), and included diagnostics such as the spherical crystal x-ray imager, electron-positron-proton spectrometers, neutron-detector test platforms for NIF diagnostics, and numerous x-ray spectrometers. Upgrades to existing diagnostic subsystems, such as the proton film pack, OMEGA high-resolution velocimeter, 4ω Thomson-scattering spectrometer, gamma reaction history diagnostic, and the DANTE x-ray diode array were also completed.

National Laser Users' Facility and External Users' Programs

Under the facility governance plan implemented in FY08 to formalize the scheduling of the Omega Laser Facility as an NNSA User Facility, Omega Facility shots are allocated by campaign. The majority (65%) of the FY10 target shots were allocated to the National Ignition Campaign (NIC) conducted by integrated teams from the national laboratories and LLE and to the high-energy-density campaigns conducted by teams led by scientists from the national laboratories.

In FY10, 30% of the facility shots were allocated to basic science experiments. Half of these were dedicated to university basic science under the National Laser Users' Facility (NLUF) Program, and the remaining shots were allotted to the Laboratory Basic Science (LBS) Program, comprising peer-reviewed basic science experiments conducted by the national laboratories and LLE/FSC.

The Omega Facility is also being used for several campaigns by teams from the Commissariat à l'énergie atomique (CEA) of France and the Atomic Weapons Establishment (AWE) of the United Kingdom. These programs are conducted on the facility on the basis of special agreements put in place by the DOE/NNSA and the participating institutions.

The facility users during this year included 11 collaborative teams participating in the NLUF Program; 12 teams led by LLNL and LLE scientists participating in the LBS Program; many collaborative teams from the national laboratories conducting experiments for the NIC; investigators from LLNL and LANL conducting experiments for high-energy-density physics programs; and scientists and engineers from CEA and AWE.

In this section, we briefly review all the external user activity on OMEGA during FY10.

FY10 NLUF Program

In FY10, DOE issued a solicitation for NLUF grants for the period of FY11–FY12. A total of 15 proposals were submitted to DOE for the NLUF FY11–12 program. An independent DOE Technical Evaluation Panel comprised of

Dr. Damien Hicks (LLNL), Prof. John K. McIver (University of Idaho), Dr. Gregory Rochau (SNL), Prof. Sharon Stephenson (Gettysburg College), Dr. Alan Wooton (University of Texas), Dr. Jonathan Workman (LANL), and Dr. John Soures (Committee Chair, non-voting) reviewed the proposals on 18 August 2010 and recommended that 11 proposals receive DOE funding and 31 days of shot time on OMEGA in each of FY11 and FY12. Table 124.V lists the successful NLUF proposals.

FY10 was the second of a two-year period of performance for the NLUF projects approved for the FY09–FY10 funding and OMEGA shots. Eleven NLUF projects were allotted Omega Facility shot time and conducted a total of 197 target shots on the facility. This work is summarized in this section.

Systematic Study of Fast-Electron Generation and Transport

Principal Investigator: F. N. Beg (University of California, San Diego)

Co-investigators: T. Yabuuchi, H. Sawada, and M. S. Wei (University of California, San Diego); R. B. Stephens (General Atomics); S. P. Regan, K. Anderson, C. Stoeckl, W. Theobald, and R. Betti (LLE); and P. K. Patel, A. J. Mackinnon, H. S. McLean, S. C. Wilks, and M. H. Key (LLNL)

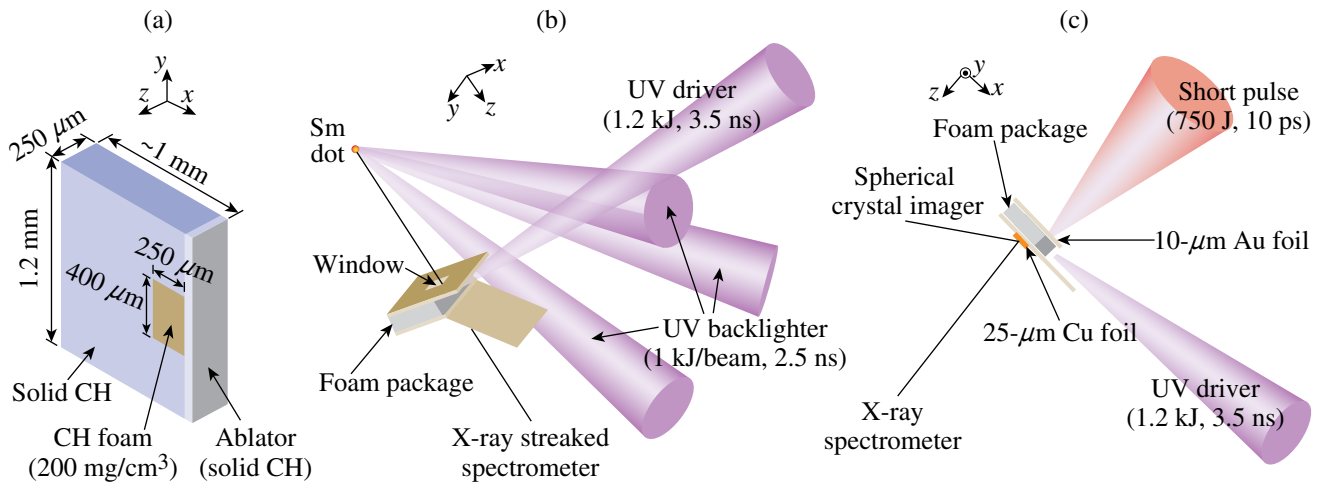
Understanding fast-electron generation and transport in the cone tip and warm dense plasma is very important for the success of the cone-guided fast ignition. We have performed two experiments in FY10 on OMEGA EP regarding this important topic. The goal of the first experiment was to characterize a plasma to be used as the transport medium in the second experiment, using the x-ray line absorption spectroscopy. The goal of the second experiment was to study the fast-electron transport in the characterized plasma. In both experiments, the warm dense plasma was created by using a shock to heat a foam target. The foam target package consisted of 200-mg/cm³ CH foam doped with aluminum inside a solid plastic container. The shock was created by irradiating a plastic foil in front of the foam with a long-pulse laser (1.2 kJ/3.5 ns in UV) as shown

in Fig. 124.78. A two-dimensional *DRACO* simulation shows that the foam plasma had a peak temperature (density) of 30 to 50 eV (110 to 180 mg/cc) at about 7 to 8 ns.

A laser-irradiated samarium dot target was used as the x-ray point source for the absorption spectroscopy. The x rays (1.4 to 1.6 keV) with a smooth, broad spectrum penetrated the foam

Table 124.V: Approved FY11 and FY12 NLUF proposals.

Principal Investigator	Affiliation	Project Title
F. Beg	University of California, San Diego	Systematic Study of Fast-Electron Transport in Imploded Plasmas
R. P. Drake	University of Michigan	Experimental Astrophysics on the OMEGA Laser
T. Duffy	Princeton University	Ramp Compression for Studying Equations of State, Phase Transitions, and Kinetics on OMEGA
R. Falcone	University of California, Berkeley	Detailed <i>In-Situ</i> Diagnostics of High-Z Shocks
P. Hartigan	Rice University	Clumpy Environments and Interacting Shock Waves: Realistic Laboratory Analogs of Astrophysical Flows
R. Jeanloz	University of California, Berkeley	Recreating Planetary Core Conditions on OMEGA
K. Krushelnick	University of Michigan	Intense Laser Interactions with Low-Density Plasma Using OMEGA EP
R. Mancini	University of Nevada, Reno	Investigation of Hydrodynamic Stability and Shock Dynamics in OMEGA Direct-Drive Implosions Using Spectrally Resolved Imaging
R. D. Petrasso	Massachusetts Institute of Technology	Charged-Particle Probing of Inertial Confinement Fusion Implosions and High-Energy-Density Plasmas
A. Spitkovsky	Princeton University	Collisionless Shocks Laboratory High-Energy-Density Plasmas
R. Stephens	General Atomics	Investigation of Laser-to-Electron Energy Coupling Dependence on Laser-Pulse Duration and Material Composition



U1124JR

Figure 124.78

(a) Schematic of the foam package target. Au foils coated with plastic on both sides were used for both experiments as seen in the experimental setup for (b) plasma characterization and (c) fast-electron transport. The foils on the target-side faces had a hole to transmit backlighter x rays for the characterization experiments. The holes were covered with Au and Cu foils in the transport experiment.

plasma through small windows on the target walls and were absorbed by aluminum atoms doped in the foam target. The line-absorption features in the spectra depend on the density and the temperature of the plasma. Figure 124.79 shows a temporal evolution of the absorbed spectra recorded with an x-ray streaked spectrometer. Preliminary analysis of the temperature of the foam using an atomic physics code *FLYCHK* indicates that the plasma temperature was about 30 eV at 7 ns after the start of the long-pulse–laser irradiation. The presence of the lower-charge-state (i.e., O-like and F-like) features later in time indicates a clear trend of the plasma cooling in time.

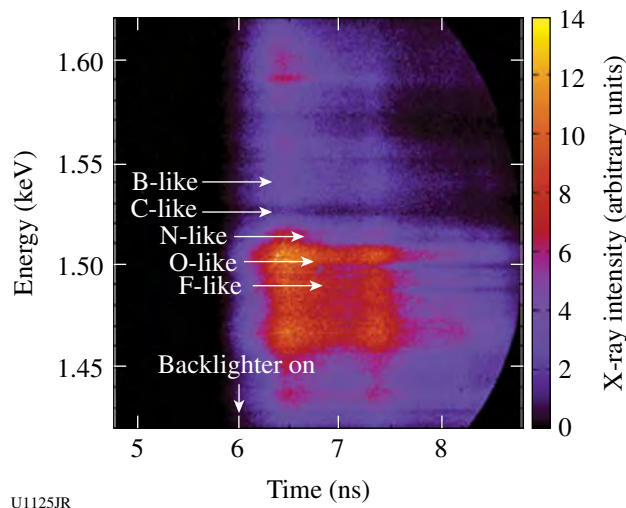


Figure 124.79

Streaked x-ray spectrum observed with Al-doped CH foam target driven by a 1.2-kJ, 3.5-ns UV long-pulse laser. Several Al absorption lines can be seen as indicated by arrows.

An OMEGA EP short-pulse laser irradiated the driven foam target at 7 ns in the transport study. The windows on the sides of the package targets were covered with Au (10- μ m) and Cu (25- μ m) foils. The Au foil served as the laser–plasma interaction layer, and the Cu foil served as a fluorescence layer of K_{α} x rays emitted by the binary collisions of fast electrons and the Cu atoms. The K_{α} x rays were monitored with an x-ray spectrometer and a newly developed spherical crystal imager. The transport medium was varied from the laser-driven foam plasma to undriven foam and a solid plastic, which had the same areal density as the undriven foam. As shown in Fig 124.80, a small spot of K_{α} x rays was observed with cold targets; however, no clear structure was found in the case where the foam plasma was the transport medium, which indicates a large divergence of the electron beam. In addition, a reduction of the K_{α} x-ray yield by a factor of 20 was measured when the target was driven. The physical mechanisms contributing to a large divergence angle

and low transport efficiency with the driven-foam target will be studied with hybrid particle-in-cell (PIC) codes.

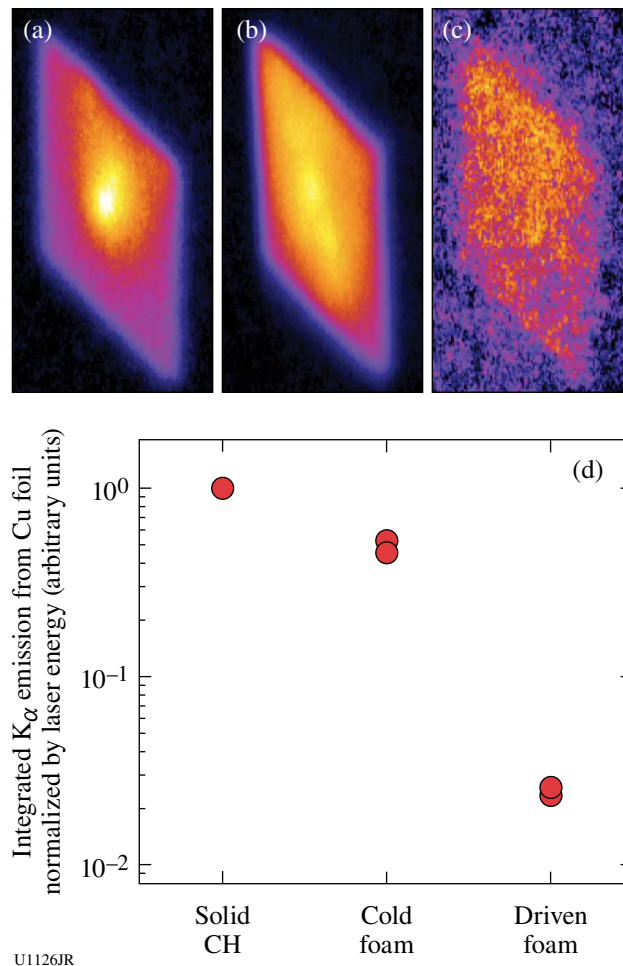


Figure 124.80

Cu K_{α} images observed with a spherical crystal imager when the transport medium was (a) 50 μ m of solid CH, (b) 250 μ m of cold foam, and (c) 360 μ m of driven foam. (d) Integrated K_{α} x-ray yield measured with the x-ray spectrometer for three cases.

Experimental Astrophysics on the OMEGA Laser

Principal Investigator: R. P. Drake (University of Michigan)
 Co-investigators: D. Arnett (University of Arizona); T. Plewa (Florida State University); J. Glimm, D. Swesty, X. Li, and A. Calder (State University of New York–Stony Brook); I. Sokolov, J. Holloway, K. Powell, and C. Kuranz (University of Michigan); J. P. Knauer and T. R. Boehly (LLE); and B. Remington, H. Robey, F. Hansen, A. Miles, S. Glenzer, and H.-S. Park (LLNL)

The OMEGA laser can create systems with very high energy densities that are relevant to astrophysical phenomena.

This is possible because OMEGA can deposit large amounts of energy into areas measuring square millimeters, generating pressures of greater than 10 Mbars (~10-million atmospheres). In some astrophysical systems, radiation can play a dominant role in the hydrodynamic behavior of the system. This occurs, for example, in radiative shocks in which the shocked matter is so hot that it radiates away most of its energy. This project has explored two types of radiative shocks—a driven radiative shock and a radiative reverse shock. These types of shocks can be found in supernova remnants, where a fast-moving shock encounters a low-density gas, and cataclysmic variables, where a supersonic plasma flow is impeded by a dense accretion disk.

In March 2010, a campaign was continued using the OMEGA laser to create a driven radiative shock in a xenon-filled shock tube. Ten OMEGA laser beams irradiated a Be disk for 1 ns. The beams deposited a total energy of ~3.8 kJ, giving an average irradiance of $\sim 7 \times 10^{14}$ W/cm² and generating an ablation pressure of ~46 Mbars in the disk. The Be acts as a piston to drive a shock in 1.1 atm of Xe with speeds in excess of 100 km/s. This velocity exceeds the threshold where radiative effects play an important role in the dynamics of the experiment. The cooling by escaping radiation creates a collapsed dense layer of xenon, which is preceded in the tube by a radiation-heated precursor region and followed by a downstream layer of expanding Be.

The most-recent efforts to diagnose a driven radiative shock employed the streaked x-ray radiography and x-ray Thomson scattering (XRTS) diagnostic techniques simultaneously to differentiate measurements from the different regions of the shock system. For each region, x-ray Thomson scattering may provide information on electron temperature and ionization state, while streaked radiography yields shock velocity and acceleration. Example streak camera and XRTS data are shown in Figs. 124.81 and 124.82. Figure 124.81 shows a streaked x-ray radiograph indicating the distance of the shocked layer from the drive disk versus time. The fiducial wire is seen in the lower part of the image, and the sloped line moving from the left to the upper right indicates the motion of the shocked Xe layer. Figure 124.82 is a plot of intensity versus energy obtained using the XRTS technique. For this experiment, a Zn source with He_α emission near 9 keV was used to probe the dense, shocked Xe layer. The incident signal is represented by the black curve, and scattered light from free and loosely bound electrons is represented by the blue curve.

A second type of radiative shock that this project has explored is a radiative reverse shock. The first experimental

attempt at creating this type of shock took place in August 2010. In this experiment, ten OMEGA laser beams irradiated a plastic-coated tin disk for 1 ns. The beams deposited a total

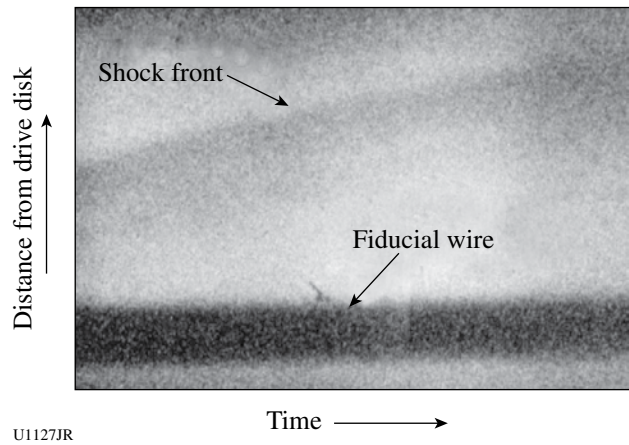


Figure 124.81
A streaked x-ray radiograph of a dense Xe layer, which provides a measure of shock velocity and acceleration. The shock is moving to the upper right in this image. An opaque wire was used to calibrate the spatial scale and determine the position of the shock at the time of imaging, while streak camera timing fiducials (not shown) calibrate the temporal scale.

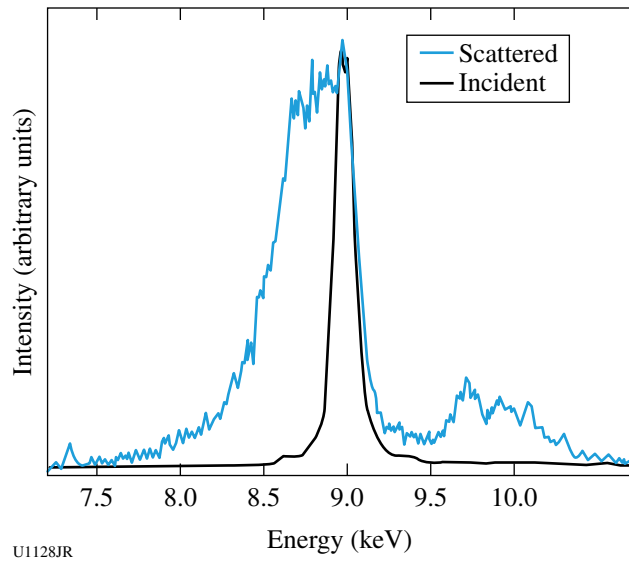
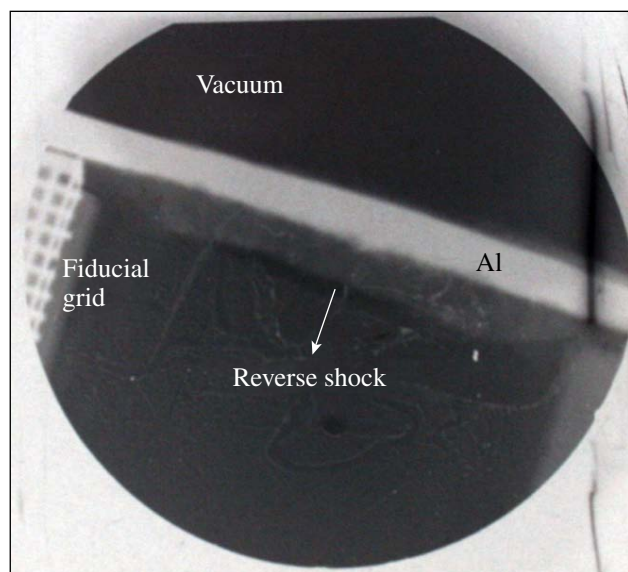


Figure 124.82
Incident and scattered spectra from March 2010 OMEGA experiments. A zinc source with He_α emission near 9 keV is used to interrogate the dense, shock-compressed Xe layer (black curve). Inelastic collisions with free and loosely bound electrons red-shift the input signal, generating the Compton feature seen below 9 keV (blue curve, normalized to match input curve's peak intensity).

energy of ~ 4.5 kJ, giving an average irradiance of $\sim 10^{15}$ W/cm². This creates a fast (greater than ~ 100 km/s) tin plasma flow through a millimeter-scale shock tube that is at vacuum. This supersonic plasma flow was impeded by a $100\text{-}\mu\text{m}$ Al “wall,” which would create a reverse shock. This shock was imaged using x-ray radiography, and self-emission from the radiative shock was recorded using a streaked optical pyrometer (SOP).

Figure 124.83 is an x-ray radiograph of a radiative reverse shock. The Al wall is labeled in the image, and the Sn plasma flow originates about 4 mm from the wall from the lower-left direction. Figure 124.84 shows data from the SOP, which captured about 100 ns of data. The directions of space and time are labeled on the image and the approximate location of the Al wall is also labeled. When the supersonic plasma flow collides with the Al, a reverse shock forms, but a strong transmitted shock is created in the Al; both are indicated in Fig. 124.84.

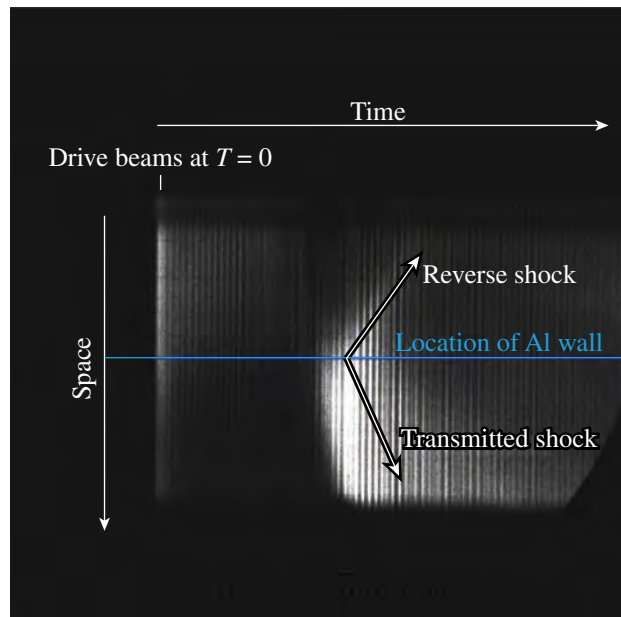


U1129JR

Figure 124.83
An x-ray radiograph of a radiative reverse shock. The Al wall is labeled in the image, and the Sn plasma flow originates about 4 mm from the wall from the lower left direction. The radiative reverse shock is moving away from the wall to the lower left.

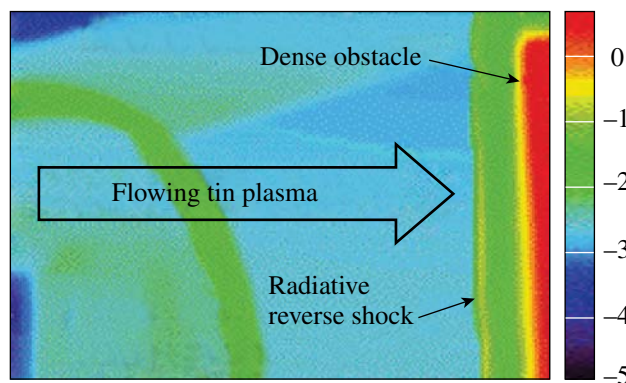
This experiment was modeled using the *CRASH* code. The *CRASH* code is a multidimensional physics code that has been developed at the University of Michigan’s Center for Radiative Shock Hydrodynamics. The density plots shown in Fig. 124.85 are simulation results from the *CRASH* code, and the laser-energy deposition was modeled using the

2-D *HYADES* code and then used to initialize the *CRASH* simulation. Figure 124.85 shows the direction of the incoming plasma flow (to the right); the Al wall is the dense obstacle in this case. The radiative reverse shock is a thin, dense layer that is moving to the left of the Al.



U1130JR

Figure 124.84
Thermal emission data over 100 ns from a streaked optical pyrometer of a radiative reverse shock. The approximate temporal location of the initial laser pulse is labeled as well as the approximate spatial location of the Al wall. Emission from reverse shock shows the shock moving away from the Al wall.



U1131JR

Figure 124.85
Results from a *CRASH* simulation of a radiative reverse shock system. The Sn plasma flow is moving to the right and collides with the dense Al. This creates a thin, dense radiative reverse shock moving to the left.

Detailed In-Situ Diagnostics of Multiple Shocks

Principal Investigator: R. W. Falcone (University of California, Berkeley)

Co-investigators: T. Ma, T. Doepfner, O. L. Landen, and S. H. Glenzer (LLNL); and H. J. Lee (SLAC Stanford Linear Accelerator Laboratory)

X-ray Thomson scattering was used to directly provide the temperature and density of shock-compressed matter.¹ Accurate characterization of dense states of matter is vital for understanding high-energy-density experiments, as well as the validation of equation of state (EOS) and plasma model assumptions. In this experiment, 250- μm Al and Be foils were shock compressed in a counter-propagating geometry using 12 drive beams with a total energy of 6 kJ at 351 nm in a 3-ns pulse. SG4 distributed phase plates were used to achieve a

smooth 800- μm focal spot, yielding a total drive intensity of $\sim 2 \times 10^{14}$ W/cm² on each side of the foil sample.

The shocked samples were probed at 140° scattering angles and varying delay times by Zn K_{α} x rays, at 8.6 keV (in the case of the Be foil), or Mo He_{α} x rays at 18.9 keV (in the case of the shocked Al foil). For both samples, the noncollective scattering regime was accessed, where $\alpha = 0.3$, $k = 8.2 \text{ \AA}^{-1}$, and $\alpha = 0.1$, $k = 17.1 \text{ \AA}^{-1}$ for the Be and the Al, respectively. The prominent Compton feature with elastic peak responding to Mo He_{α} in Fig. 124.86(b) demonstrates the feasibility as a backlighter for probing Al, the highest-Z material probed to date. The increase in the strength of the Compton feature with time as seen in Fig. 124.86(c) shows that the electron density changes with shock propagation.² The Compton feature at each time of 2.37 ns, 2.85 ns, and 3.83 ns presents the response of compressed state before, during, and

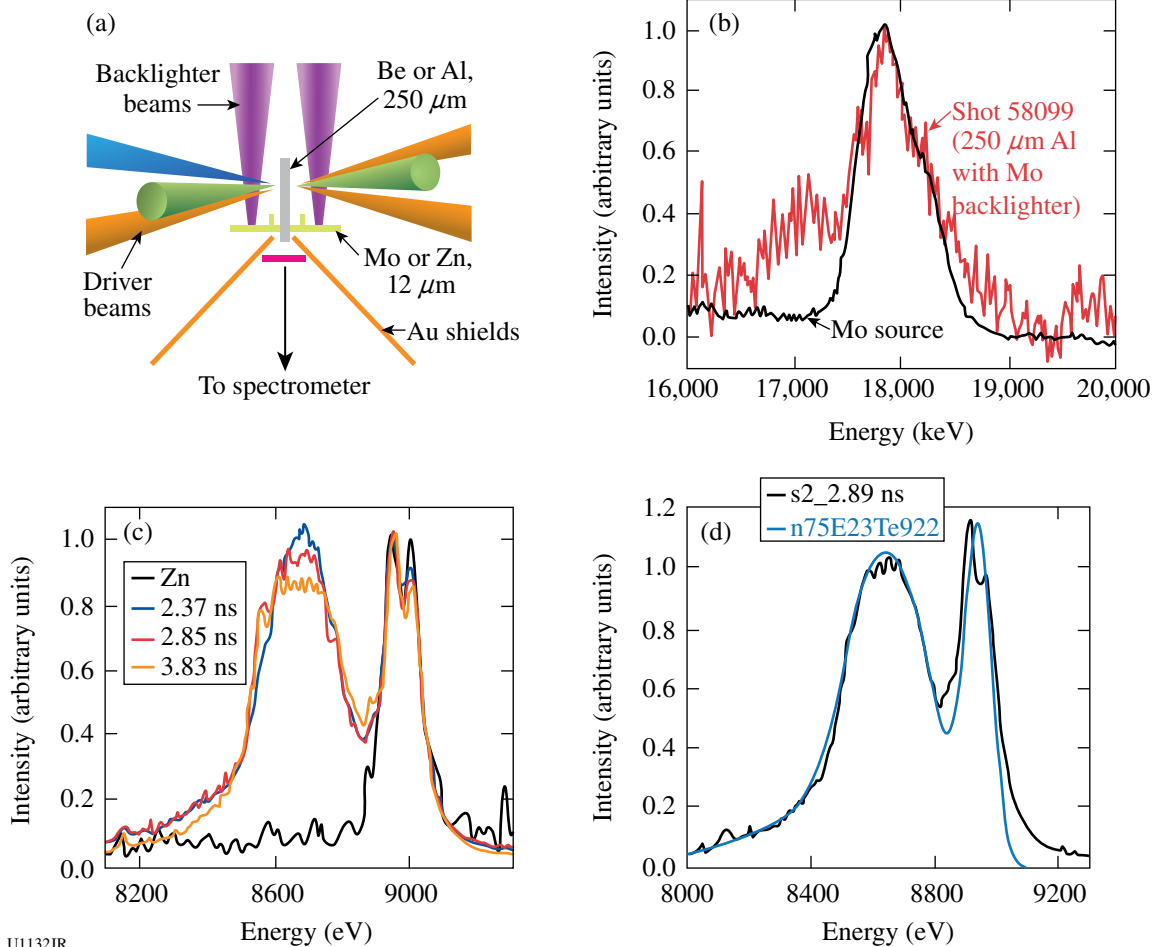


Figure 124.86

(a) Experimental configuration; (b) Mo He_{α} backlighter and scattering spectrum in compressed Al; (c) Zn K_{α} backlighter and scattering spectrum on shock-compressed Be at 2.37, 2.85, and 3.83 ns; and (d) scattering data for compressed Be and fit at 2.89 ns.

after the collision of counter-propagating shocks. A theoretical fit to the spectra at 2.89 ns in Fig. 124.86(d) allows one to infer the temperature, electron density, and ionization state. Analysis is ongoing to develop a more complete picture of the density and temperature of shock-compressed matter by counter-propagating shocks, which will address the radiation–hydrodynamic models.

OMEGA EP–Generated X-Ray Source for High-Resolution 100- to 200-keV Point-Projection Radiography

Principle Investigator: U. Feldman (Artep Inc.)

The first-year goal of this project was to design and construct a ten-inch manipulator (TIM)–compatible OMEGA EP transmission crystal spectrometer (TCS) capable of measuring the size of the target region from which energetic (20- to 100-keV) photons produced by fast electrons are being emitted. The recording media, which could be located at distances of 20, 40, and 60 in. from target center, were designed to be image plates. During the first part of 2009, the TCS was designed and constructed (Fig. 124.87), and on 26–27 August it recorded spectra from a number of OMEGA EP shots. The recorded spectral lines indicated that, although the OMEGA EP beams were tightly focused (30 to 40 μm), the diameter of the area from which the hard x rays were emitted (a measure of the spread of the hot electrons) was 350 to 400 μm .

Our goal for the second year was to replace the image plate at the 60-in. location, which has pixel sizes of 100 μm or larger, with an electronic detector with pixel sizes of the order of ~ 25 μm . In early July 2010, the TCS was delivered to LLE, where it was mechanically and electronically checked by the LLE technical staff and Artep team members. On 15 September, the TCS was installed in the OMEGA EP chamber and recorded spectra from several specially designed targets.

The September experiments provided high-quality x-ray spectra on the TCS image-plate (IP) channels. Sample spectra from IP positions A [on the Rowland circle (RC)—focusing] and B (500 mm off the RC—source size broadened) are shown on Fig. 124.88. With careful analysis, the x-ray source size can be determined from the source-size–broadened spectrum (IP B).



U1133JR

Validating Inelastic X-Ray Scattering from H and H/He Warm Dense Matter with Shock-Velocity Measurements: Toward the Equation of State of Jupiter's Core

Principal Investigator: S. P. Regan (LLE)

Co-investigators: T. R. Boehly and P. B. Radha (LLE); and G. Gregori (Oxford)

The objective of this experiment is to measure the equation of state (P , ρ , n_e , T_e , Z) of direct-drive, shock-heated and compressed, planar cryogenic H and H/He mixtures using spectrally resolved x-ray scattering (i.e., inelastic x-ray scattering) and shock-velocity measurements on the OMEGA Laser System. The dynamics at the shock front and the plasma conditions in the bulk of the shocked material will be probed simultaneously with complementary diagnostics: the electron density (n_e) will be inferred from collective inelastic x-ray scattering (i.e., scattering from electron-plasma waves or plasmons);³ the electron temperature (T_e) and average ionization (Z) will be inferred from the noncollective x-ray scattering (i.e., scattering from individual electrons);^{1,4} and the pressure (P) and mass density (ρ) will be inferred from the velocity interferometer system for any reflector (VISAR) diagnostic.⁵ Equation-of-state (EOS) measurements typically diagnose the shock velocity (U_s) using the VISAR diagnostic and infer the particle velocity (U_p) by an impedance-matching analysis.⁶ The quantities U_s and U_p are related to P and ρ through the Rankine–Hugoniot relations.^{7–9} The ablation pressure inferred from the VISAR observation is critical for the EOS measurement. On the first LBS project shot day in FY10, the U_s in liquid D_2 irradiated for 6 ns with an intensity around 10^{13} W/cm^2 was measured with VISAR. The result is shown in Fig. 124.89 with the laser irradiation starting at $t = 0$ ns. Ionization of the CH ablator blocks the VISAR laser signal from the reflective, advancing shock front for the first 1.5 ns. The shock velocity in the time interval between 4 and 6 ns, when x-ray scattering measurements are typically performed, is 18 $\mu\text{m}/\text{ns}$. Using the U_s – U_p relation for shocked D_2 reported by Hicks *et al.*,⁶ a pressure of 0.4 Mbar and four-fold compression were inferred. Figure 124.90 presents measurements of the noncollective inelastic x-ray scattering from a liquid-deuterium target irradiated with a similar laser drive on the second

Figure 124.87

The transmission crystal spectrometer (TCS) with an electronic detector.

shot day of the experiment. Analysis is in progress to infer the shocked conditions from the VISAR and inelastic x-ray scattering measurements. The warm dense matter created in these experiments with laser-ablation-driven shock waves had plasma conditions comparable to those predicted in planetary interiors (i.e., dense, Fermi-degenerate matter). While Jupiter is mostly made of hydrogen, with only a fraction of He (<25%) and a few metals,^{10–16} the concentrations of other giant planets in the solar system are significantly enriched with C, O, and N. These form the so-called “ices” that are typical of the giant planets, such as Uranus and Neptune, and possibly extrasolar planets, such as GJ436b.^{17–19}

Development of a Platform for Laser-Ramp Compression of Planetary Materials on OMEGA

Principal Investigators: Y. M. Gupta (Washington State University) and T. S. Duffy (Princeton University)

Co-investigators: J. Montoya, J. Wang, and G. Finkelstein (Princeton University); R. F. Smith, J. H. Eggert, P. M. Celliers, D. Braun, and M. Bastea (LLNL); and T. R. Boehly (LLE)

This experiment was allocated 1.5 shot days on OMEGA in FY10 to develop a high-pressure, low-temperature ramp-compression drive, which permits one to explore new regions of thermodynamic space of particular relevance to material

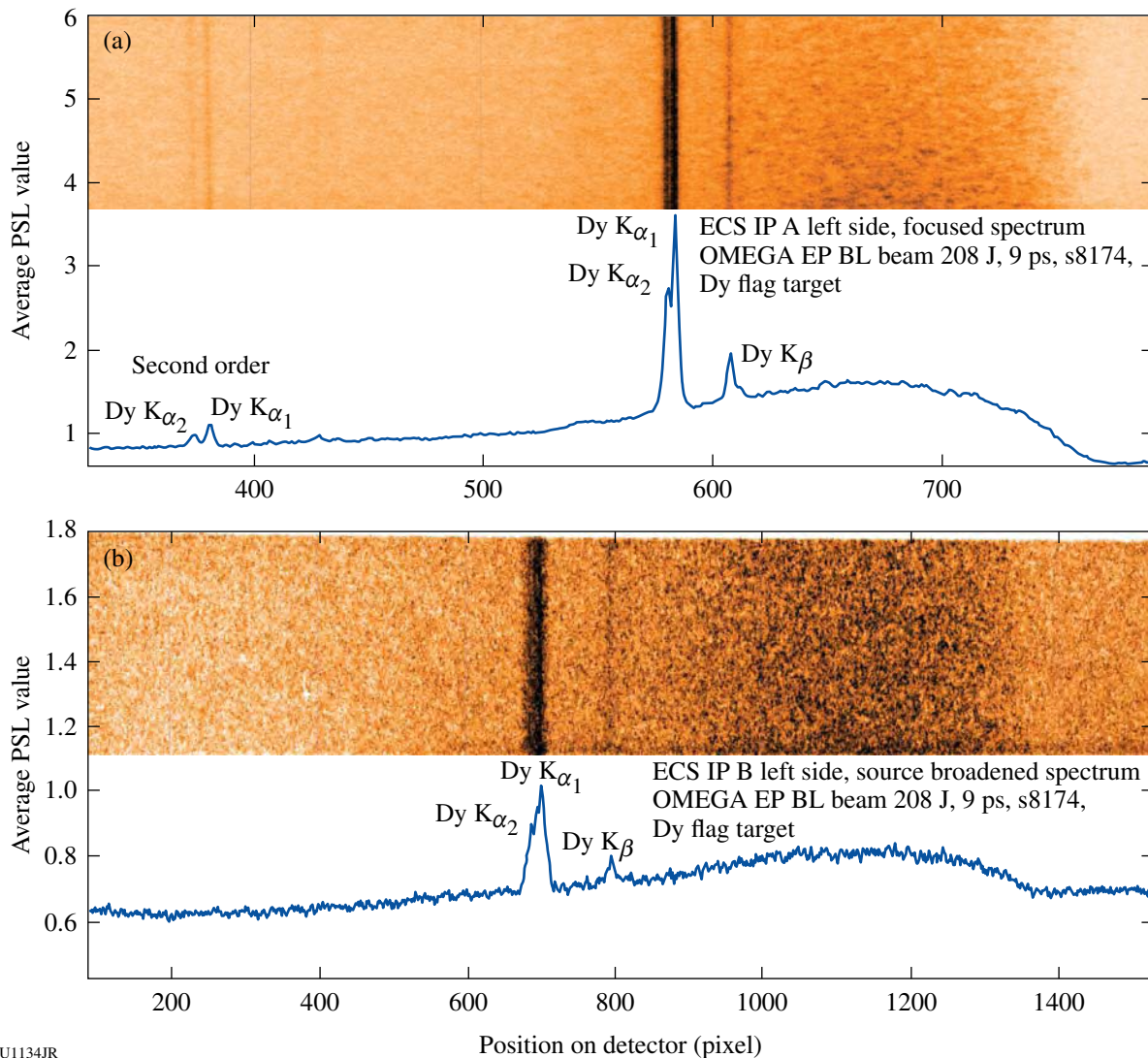
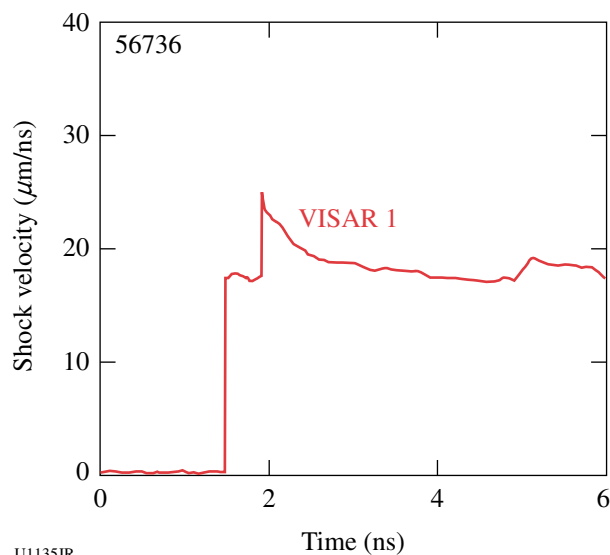


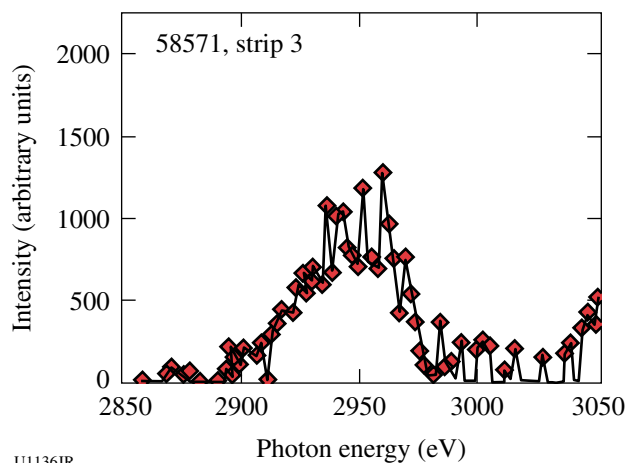
Figure 124.88 Sample spectra of the TCS taken on OMEGA EP from campaign PPRad-EP-10. Spectral images and column averages showing characteristic Dy K lines (K_{α_1} : 45.99 keV). (a) Lines in first and second order on IP A on the focusing Rowland circle and (b) IP B providing source size broadening of the spectral lines at a 500-mm distance from the focusing Rowland circle position.



U1135JR

Figure 124.89

Shock-velocity measurement taken on OMEGA shot 56736 with VISAR of a liquid-D₂ target irradiated for 6 ns with an intensity around 10^{13} W/cm² starting at $t = 0$ ns. Ionization of the CH ablator interrupts the VISAR laser signal for the first 1.5 ns. The average shock velocity in the time interval when x-ray scattering measurements are performed ($4 \text{ ns} < t < 6 \text{ ns}$) is $18 \mu\text{m/ns}$.



U1136JR

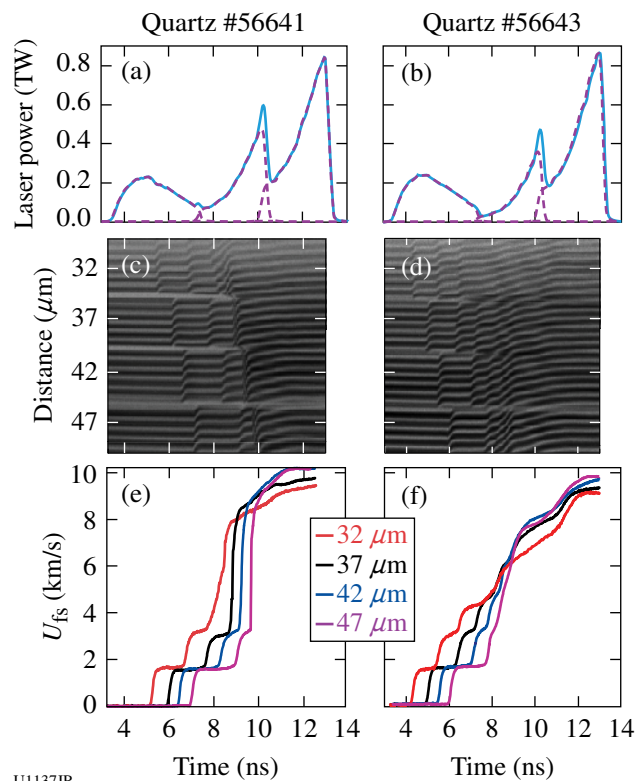
Figure 124.90

Inelastic x-ray scattering measurement taken on OMEGA shot 58571 of a liquid-D₂ target irradiated for 6 ns with an intensity around 10^{13} W/cm² starting at $t = 0$ ns. Observation was recorded at $t = 6$ ns. Analysis to infer shocked conditions in liquid D₂ is in progress.

conditions found in planetary interiors. Ramp compression achieves high compression at relatively modest temperatures and can be used to extract quasi-isentropic equation-of-state data, study solid–solid phase transitions, and compress materials in the solid state to higher pressures than can be achieved with diamond-anvil-cell (DAC) or shock-wave methods. An experimental platform for ramp loading of quartz (SiO₂) and

iron (Fe) has been established and tested in experiments at the Omega Laser Facility. Target packages consist of stepped samples and a diamond ablator attached to a Au halfraum. Composite laser pulses are used to drive a ramp-compression wave into the sample. The target and laser-ramp designs have been tested and optimized by combining experiments with computer simulations using a hydrodynamics code. A spatially planar ($\Delta t/t = 0.9\%$) ramp wave drive has been achieved in both SiO₂ and Fe stepped samples to peak stress around 250 GPa and 400 GPa, respectively, over nanosecond time scales.

Figure 124.91 shows the input laser profile, VISAR streak camera records, and corresponding free-surface velocity histories for two typical quartz experiments. The extracted free-surface velocity histories in Figs. 124.91(e,f) show a very structured breakout with a series of ramped “plateaus” consistent with drops in the bulk sound speed caused by the onset of



U1137JR

Figure 124.91

(a) and (b) Laser pulse for two representative quartz shots (56641 and 56643). The dashed lines show the individual pulses and the solid line is the composition pulse shape. (c) and (d) Line VISAR streak camera images (1.971 km/s per fringe) from ramp-compressed multi-stepped quartz targets (56641 and 56643) corresponding to (a) and (b), respectively. In (c) and (d), different step thicknesses are indicated. (e) and (f) Extracted free-surface velocity profiles from (c) and (d), respectively.

elastic-plastic deformation or a polymorphic phase transformation. The input laser profile was designed to generate an initial steady shock in quartz followed by subsequent ramp compression. An unusual feature of these profiles is the convergence of wave-arrival times for multiple steps in the 7- to 9-ns range (Fig. 124.91). It is believed that this feature is an artifact of the complicated wave interactions between free-surface reflections that combined with the onset of a phase transformation. In future experiments, the use of a lithium fluoride (LiF) window may suppress the effects of interactions. Figure 124.92 shows a sequence of measured pulses and the corresponding wave profiles for the first target step in Fe samples for several differ-

ent shots. By changing the time delay between the two pulses, it was possible to decrease the amplitude of the second shock and achieve a more ramp-like compression. However, it was not possible to completely eliminate the second shock (shots 58591 to 58593). Keeping the same delay, but increasing the power in the second pulse strongly increased the amplitude of the second shock (shot 58594). Figure 124.93 shows preliminary pressure-density curves for Fe and SiO₂ calculated with standard Lagrangian sound speed analysis. The complexity of the wave interactions caused some discrepancies among different shots. Further work will focus on the development of new analytical tools to analyze ramp-compression data for

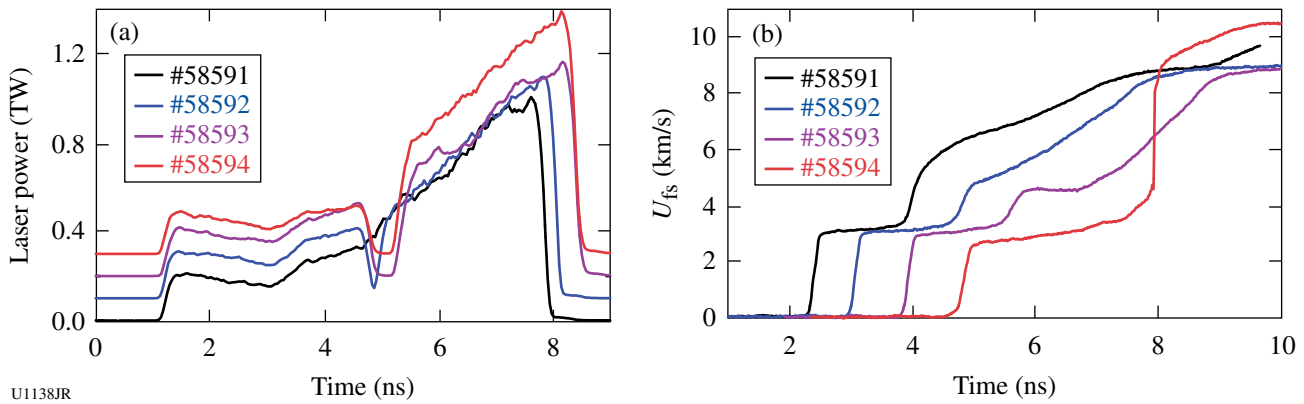


Figure 124.92

(a) Composite laser pulse shapes from a series of shots on Fe targets along with free-surface velocity profiles for the first step corresponding to each laser drive. (b) Shots 58591 to 58593 correspond to delays between the pulses of 3.5 ns, 3.65 ns, and 3.88 ns. For shot 58594, the delay was maintained the same (3.88 ns), but the power was increased. In (a), the traces are offset in amplitude (by 0.1 TW) for clarity, and the traces are offset temporally in (b).

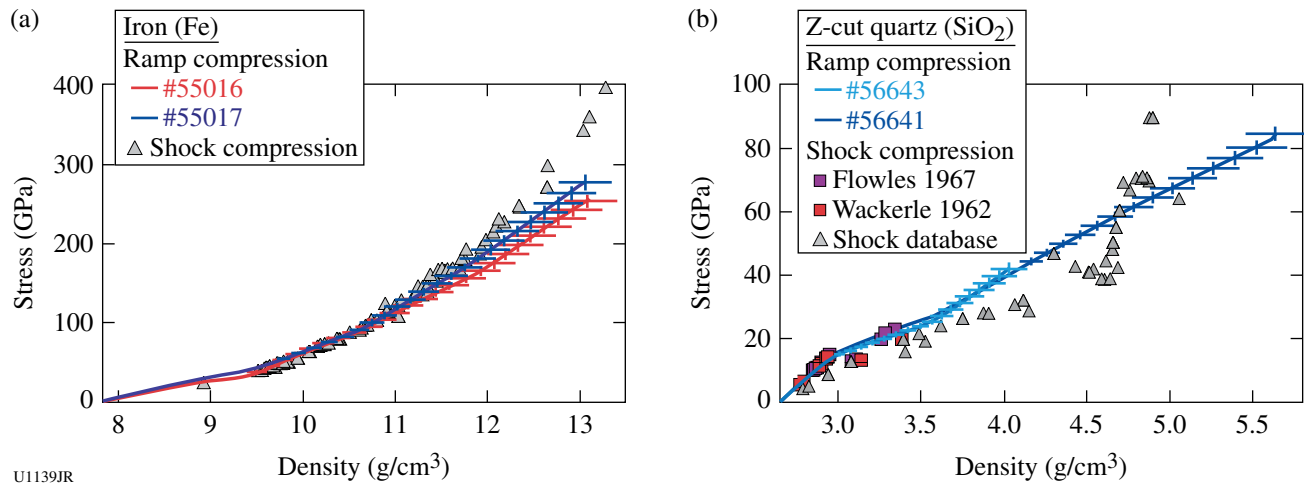


Figure 124.93

Preliminary pressure-density curves for Fe and SiO₂ calculated with standard iterative-characteristic Lagrangian sound speed analysis developed by Rothman. (a) Data are shown for two separate shots taken during an NLUF shot day on 23 July 2009. Also shown are previous data taken from shock experiments. (b) Data are shown for two different shots taken during an NLUF shot day on 20 January 2010, and shock data are shown from previous studies.

materials undergoing time-dependent compression, including treating the initial shock and phase transformation.

Laboratory Experiments of Supersonic Astrophysical Flows Interacting with Clumpy Environments

Principal Investigator: P. Hartigan (Rice University)

Co-investigators: J. Palmer (Rice University); J. Foster and P. Rosen (AWE); B. Wilde and M. Douglas (LANL); A. Frank (University of Rochester); and B. E. Blue and F. Hansen (General Atomics)

A primary goal of the NLUF program is to study how strong shock waves propagate through clumpy media such as those encountered by astrophysical jets as they interact with their nascent molecular clouds. In the current program, an experimental design was developed that allows one to observe a strong shock as it sweeps past a collection of obstacles in its path. The laboratory work complements new astrophysical images from the Hubble Space Telescope (HST) that were taken as part of a previous NLUF program.

Samples of some of the shots and numerical simulations of the experiments from the last year appear in Fig. 124.94. The target consists of cylindrical foam into which are embedded anywhere from a few to several dozen sapphire spheres. A database is being accumulated that will answer the question of how the packing fraction and clump size within the obstacle affect the propagation speed and coherence of the strong shock wave that is driven through the foam. Numerical support is provided by the *RAGE* code (see Fig. 124.94). The experiments provide important tests of the code in a complex regime that is inherently 3-D and includes multiple shocks and mixing of post-shock material. The experiments reveal dynamical changes that occur when one sphere lies in the wake of another, and they expand on previous work with two spheres, where it was learned how a planar shock creates vorticity as it interacts with the spheres.

This ongoing NLUF work is producing a series of publications in the primary refereed journals of the field, and numerous contributed and invited talks have been given at recent conferences. In 2009, this OMEGA collaboration published a large paper in the *Astrophysical Journal*,²⁰ and another paper was just accepted into *Physics of Plasmas* related to Mach stem work.²¹ This latter paper is now motivating a new line of research that the group plans to pursue in the next two years. Another large *Astrophysical Journal* paper nearing completion concerns motions within shocked jets; a paper on the vorticity between two shocked spheres is in preparation; and our current set of shot data will produce a thorough study of shocked

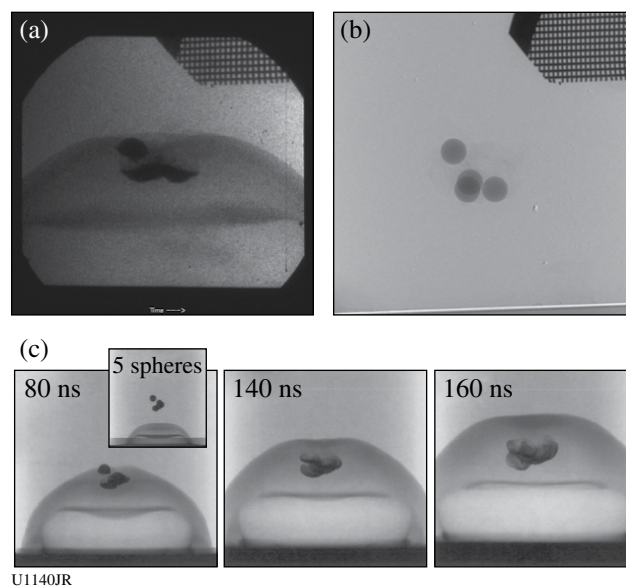


Figure 124.94

(a) Shot data (taken at 100 ns) and (b) pre-shot radiograph of a target containing four spheres. The shock wave moves upward and has just overtaken the spheres, flattening and distorting them. (c) Time-sequence numerical simulation (from *RAGE*) of a target with five spheres. A filamentary structure develops as bow shocks around each sphere interact and shadow one another. This filamentary structure resembles features we observe in the working surfaces of astrophysical jets.

clump phenomena. Student participation includes two recent Ph.D.'s (one of whom will be taking up a position at a national lab) and an M.S. thesis in its final stage.

Measurements of the Equation of State of H_2/He Mixtures Under Deep Planetary Conditions

Principal Investigator: R. Jeanloz (University of California, Berkeley)

Co-investigators: P. Loubeyre (CEA); J. H. Eggert, D. G. Hicks, P. Celliers, and G. W. Collins (LLNL); and T. R. Boehly (LLE)

Using the Omega Laser Facility, this project is demonstrating that laboratory experiments can provide crucial data to model the interior structure of the planets. Specifically, measuring the equation of state of planetary constituents is complementary to space missions for understanding the interiors and evolution of giant fluid planets. The immediate goal of these experiments is to measure the equation of state of hydrogen and helium warm dense fluids, and to quantify the miscibility gap in hydrogen/helium mixtures. The experiment is based on the generation of a laser shock in a precompressed sample. The precompressed target offers two new opportunities over the usual cryogenic targets: mixtures of H_2/He can be studied, whereas they phase-separate in a cryogenic target; the initial density of the mixture

can be significantly increased. Measurements on He, H₂, and H₂/He samples have been performed up to precompressions of 1.5 GPa. The Hugoniot data on helium have been published.^{7,22} The Hugoniot data on H₂ and D₂ have been recently measured, and their analysis is being finalized for publication (Fig. 124.95).

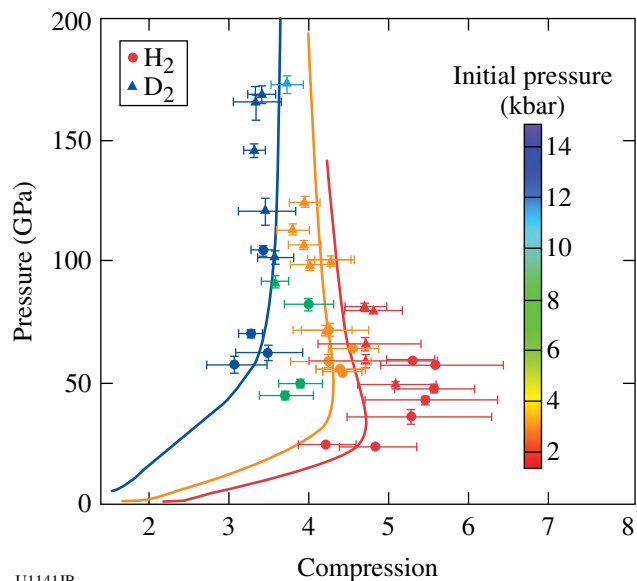


Figure 124.95

Summary of Hugoniot measurements collected at Omega on H₂ (dots) and D₂ (triangles), with the color scale indicating the initial pressure of the sample. The agreement between D₂ and H₂ measurements validates the impedance-matching construction that we used based on quartz with a Grüneisen equation of state of molten SiO₂. The full lines represent *ab-initio* calculations for comparable Hugoniots.

Last year, a special effort was made to extend the precompression on H₂/He mixtures to cover the thermodynamic domain where phase separation of the mixture is predicted to occur in the interiors of Jupiter and Saturn. To reach this domain, a precompression of more than 4 GPa is needed, and this has been achieved by a new design of diamond window with lateral support (Fig. 124.96). A typical diameter of the H₂/He sample is 300 μm, and, as a result of this new design, 6 kJ have been effectively coupled to the target.

The shock state is monitored through the back diamond using in-line imaging VISAR, along with streaked optical pyrometry (SOP) for temperature. Quartz is the reference material used as a standard for impedance-matching determination of pressure and density and relative measurements of reflectivity and temperature.

Data for H₂/He mixtures have been obtained along three Hugoniots corresponding, respectively, to a precompression of 0.4 GPa, 2 GPa, and 4 GPa (Fig. 124.97). The data have been

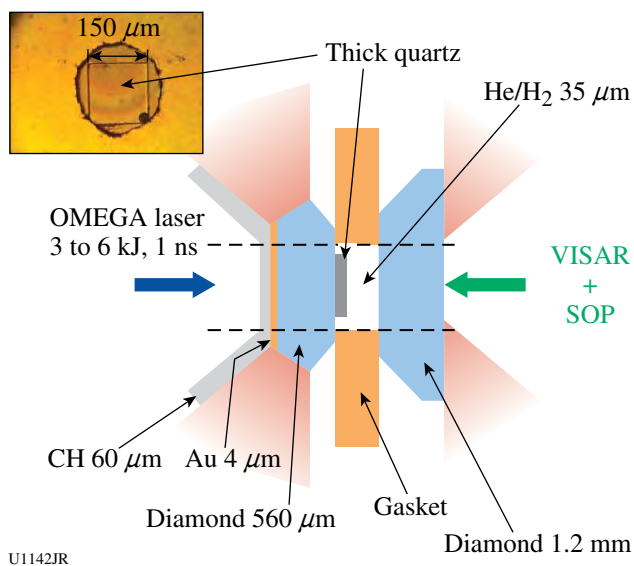


Figure 124.96

Experimental layout: schematic cross section of a precompressed target at 4 GPa. The inset (upper left) shows a picture of the sample before the shot.

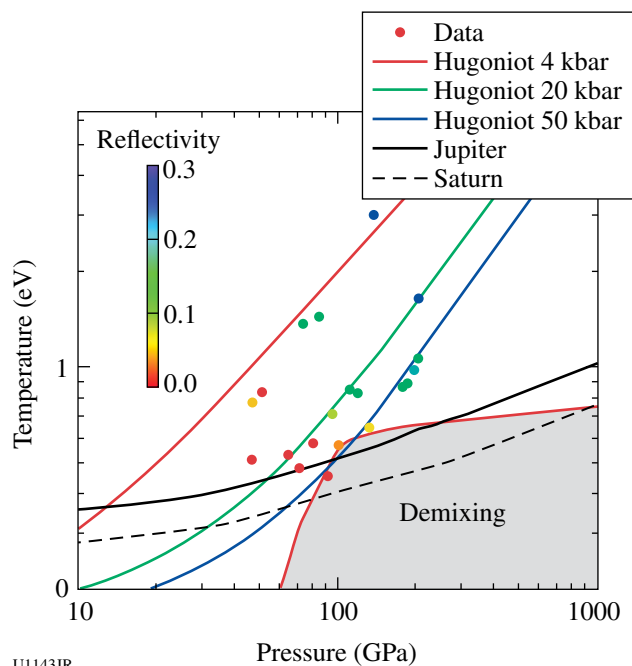


Figure 124.97

Hugoniot measurements on precompressed H₂/He mixtures collected along three paths, corresponding to precompressions of 0.4, 2, and 4 GPa at ambient temperature. The color scale gives the observed reflectivity. The phase-separation domain, calculated by *ab-initio* calculations, is given by the light red-colored domain. Isentropes for the interiors of Jupiter and Saturn are indicated by solid and dashed black lines, respectively.

collected under conditions for which H_2 is electrically conducting (metallic fluid) but He is not. The order-of-magnitude range of precompressions significantly shifts the Hugoniot points to a higher density and cooler temperature. Therefore, the measured Hugoniot of fluid H_2/He precompressed to 4 GPa crosses the Jupiter adiabat. The signature of phase separation—a jump in reflectivity along the Hugoniot—is not observed here. These data are just at the limit of the domain at which phase separation has been predicted by theoretical calculations.²³ It appears that the calculations may be overestimating phase separation; therefore, there is no phase separation within Jupiter.

Three-Dimensional Studies of Low-Adiabatic Direct-Drive Implosions on OMEGA

Principal Investigators: R. C. Mancini (University of Nevada, Reno) and R. Tommasini (LLNL)

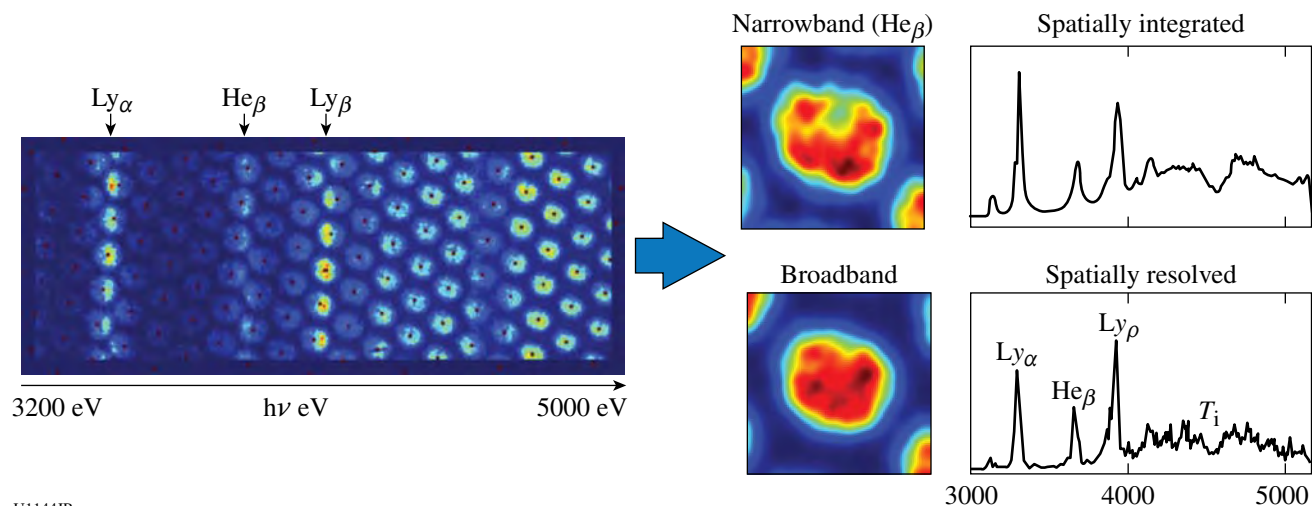
Co-investigators: J. A. Delettrez and S. P. Regan (LLE); V. A. Smalyuk (LLNL); and L. A. Welsch-Sherrill (LANL)

Determining the spatial structure of implosion core temperature conditions is important for inertial confinement fusion experiments. The emphasis of this NLUF research is to establish the direct-drive multi-monochromatic imager's (DDMMI) instrument capabilities and to develop a quantitative method for spectrally resolved image data analysis with the goal of studying the 3-D spatial structure of implosion cores in low-adiabat OMEGA direct-drive implosions. In this connec-

tion, the team has demonstrated that processing the spectrally resolved image data recorded with DDMMI produces several types of images or spectra, namely (1) broadband images, (2) narrowband images, (3) spatially integrated spectra, and (4) spatially resolved spectra. Figure 124.98 shows gated, spectrally resolved images from an argon-doped implosion core recorded by DDMMI in OMEGA shot 49956. The red dots indicate the location of the image centers.

Being able to obtain spatially resolved spectra from the spectrally resolved image data recorded with DDMMI is important because the problem of extracting the 3-D spatial structure of the implosion core can be cast in terms of analyzing a series of spatially resolved spectra recorded simultaneously along three quasi-orthogonal lines of sight (LOS's). Electron-temperature and density spatial information is encoded in the intensity and broadening changes observed in the spectra. This type of 3-D analysis for the reconstruction of spatial structure is called a *polychromatic tomography* since, unlike the tomography techniques commonly used in medicine, we work with a limited number of LOS's but we benefit from having multiple chords and multiple wavelengths associated with each LOS.

To implement the idea of polychromatic tomography, we perform searches in parameter space driven by a Pareto genetic algorithm (PGA), for the temperature and density spatial distributions that yield the best simultaneous and



U1144JR

Figure 124.98

Gated, spectrally resolved images of the implosion core recorded by the DDMMI instrument in OMEGA shot 49956, and broad- and narrowband core images and spatially integrated and a sample of spatially resolved spectra extracted from these data. The line emission spectral features are due to the Ar tracer added to the D_2 -gas fill of the core. At high photon energies, line absorption caused by a Ti tracer located in the shell is also observed. Color coding is adjusted for the visualization of each image.

self-consistent fits to all spatially resolved spectra recorded along the three quasi-orthogonal LOS's. The PGA combines a genetic algorithm with the Pareto domination technique of multi-objective optimization. This implementation of polychromatic tomography is an example of multi-objective data analysis, where the key question is what can be extracted by analyzing simultaneously and self-consistently multiple pieces of data that cannot be extracted by analyzing each piece of data on an individual basis? In previous and current NLUF research, several applications of multi-objective data analysis to x-ray spectroscopy of implosion cores have been developed. It should be noted that this method is unbiased since each PGA run with the same data starts from a randomly initialized first generation of populations (i.e., solution candidates), and the same data set can be analyzed multiple times starting from different first generations in an effort to check the uniqueness of the solution. Moreover, the result obtained with the PGA is subsequently fed to a Levenberg–Maquardt nonlinear least-squares minimization method that quickly improves the search by performing a “fine-tuning” step to find the optimal solution. Before applying this analysis method to actual data, the technique was extensively tested with a series of synthetic data test cases. Polychromatic tomography of data from several OMEGA implosion experiments has been performed, and work is in progress to compare this data with 2-D and 3-D hydrodynamic simulations.

Response of BCC Metals to Ultrahigh Strain

Rate Compression

Principal Investigator: M. Meyers (University of California, San Diego)

Co-investigators: B. Maddox, H. S. Park, B. Remington, S. Pollaine, and S. Hau-Riege (LLNL); and J. Wark (Oxford)

The goal of this campaign was to recover isentropically compressed Ta samples of various microstructures, from single crystal to nanocrystal, and to measure the loading profile using Al/LiF targets and the TIM5 ASBO (active shock breakout) on the OMEGA laser. The experimental setup is shown in Figure 124.99 and consisted of two targets simultaneously driven using a set of six beams each, one target aligned along the H3–H18 axis and the other along the H7–H14 axis. The configuration shown in Fig. 124.99 shows a VISAR witness target on H7–H14 and the Ta recovery sample on H3–H18. The VISAR witness targets were 1-mm-thick LiF coated with 10 μm of aluminum and mounted on a 10-mm-diam washer. The LiF was surrounded by a 3-mm-long Au cylinder that shielded the LiF from unconverted light. The recovery targets

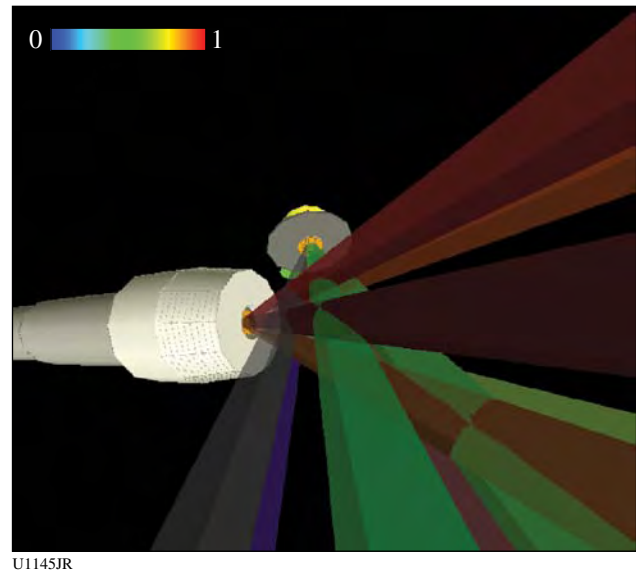


Figure 124.99

Experimental setup for BCCMet-10A showing the Ta recovery target along the H3–H18 axis and the VISAR witness target along the H7–H14 axis. The VISAR target was replaced with another recovery target after the first four shots.

consisted of a 5.5-cm-long stainless-steel recovery tube filled with 50 mg/cc of aerogel for soft recovery of laser-driven samples. The Ta target package was mounted at the end of the recovery tube and consisted of a 20- μm -thick polycarbonate ablator backed by a 180- μm BrCH (2%) reservoir. This ablator/reservoir was separated from the sample to be studied by a 300- μm -thick washer. The isentropic drive was created by the unloading of the BrCH reservoir across this gap. The VISAR target was replaced by a second Ta recovery target after the first four shots. A total of 12 successful shots were completed, resulting in 20 recovered samples, and four successful drive measurements were obtained. The recovered targets are currently being analyzed using contact profilometry, scanning electron microscopy, transmission electron microscopy, and x-ray diffraction.

Proton Radiography of Direct- and Indirect-Drive ICF Experiments and HEDP Plasmas

Principal Investigators: R. D. Petrasso and C. K. Li (Massachusetts Institute of Technology)

Co-investigators: F. H. Séguin and J. A. Frenje (MIT); J. P. Knauer (LLE); and J. R. Rygg (LLNL).

During the present and previous NLUF programs, the MIT-developed method of monoenergetic, charged-particle radiography²⁴ has been used in new types of studies of electromagnetic fields and plasmas in high-energy-density physics (HEDP) and

in inertial confinement fusion (ICF) physics. These projects, undertaken at the Omega Laser Facility,²⁵ were performed because of their importance to the future of ICF, HEDP, and the physics of fields generated by laser–plasma interactions. Topics studied include the imaging, identification, and measurement of electric and magnetic fields in laser-generated plasmas; reconnection of megagauss magnetic fields in high- β plasmas; self-generated electromagnetic fields in ICF implosions; the dynamics of ICF capsule implosions; and electromagnetic fields in laser-driven hohlraums. This work has resulted in nine publications in *Science*^{26,27} and *Physical Review Letters*,^{28–34} plus seven other papers, eleven invited talks, and many contributed talks at conferences. The experiments have successfully addressed basic physics issues and those issues directly relevant to the future success of ignition experiments at the National Ignition Facility (NIF). These NLUF experiments also provided unique research opportunities for the seven MIT graduate students in HEDP and will result in major parts of their theses.

As described in the 2010 *Science* article,²⁷ the first observations and measurements of indirect-drive ICF implosions and self-generated fields using monoenergetic proton radiography were conducted during this project.²⁴ The experimental setup and data are shown in Fig. 124.100. The hohlraums were of OMEGA scale-1.5 size with a 30- μm -thick Au wall, 100% laser entrance hole (LEH), 2.4-mm diameter, and 3.8-mm length. Each hohlraum was driven by 30 laser beams forming four irradiation rings with a total laser energy ~ 11 kJ in a 1-ns square pulse. The individual laser beams had full spatial and temporal smoothing. The radiographs, made with 15-MeV D^3He protons, covered a typical indirect-drive ICF implosion sequence. The images are displayed to show proton fluence versus position, providing time-dependent information about field distributions, capsule compression, and hohlraum plasma conditions. A striking feature in these images is a five-pronged, asterisk-like pattern surrounding the imploding capsule—a consequence of the laser-beam positions on the hohlraum wall. It was shown that the asterisk spokes were formed between two expanding plasma bubbles that were generated by “nearest neighbor” laser-beam pairs, while the periodic patterns (narrow fingers) between these spokes were associated with the remaining laser-beam distributions. Plasma flow, supersonic jets, and self-generated B fields were observed; the areal density (ρR) and implosion symmetry were determined; and different implosion phases were sampled. The views of the spatial structure and temporal evolution of both the drive and implosion properties provide essential insight into, and modeling validation of, x-ray–driven implosions.

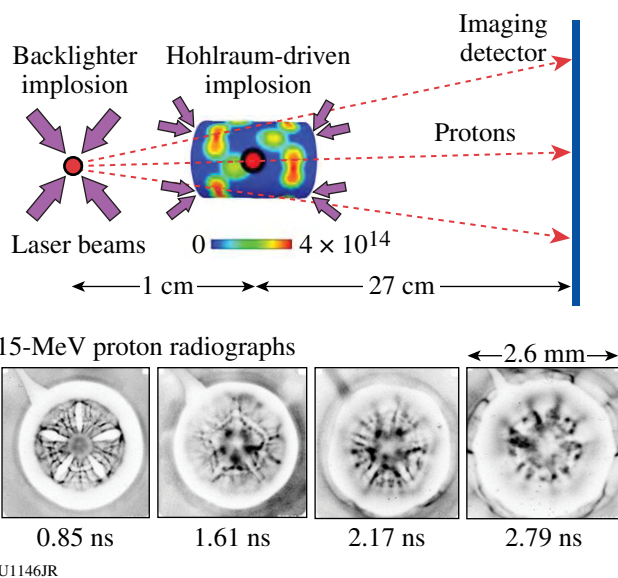


Figure 124.100

A recent experiment at the Omega Laser Facility used fusion to study fusion. A laser-driven ICF capsule produced monoenergetic 3- and 15-MeV protons through fusion reactions, and the protons were used to make radiographs of another ICF capsule imploded by x rays generated by the interaction of 30 laser beams with the inner wall of a Au hohlraum. The colors inside the hohlraum wall indicate laser intensity in units of watts per cm^2 . In the 15-MeV radiographs shown here (recorded at different times during the laser drive), the capsule is in the center, the Au hohlraum is the light-colored outer ring, and the patterns between capsule and hohlraum are due to electromagnetic fields and plasma jets. Within each image, darker means higher proton fluence. This work is discussed in Ref. 27.

Intense Laser Interactions with Low-Density Plasmas Using OMEGA EP

Principal Investigators: L. Willingale, A. Maksimchuk, and K. Krushelnick (University of Michigan)

Co-investigators: P. M. Nilson, R. S. Craxton, C. Stoeckl, and T. C. Sangster (LLE); J. Cobble (LANL); and P. Norreys and R. Scott (RAL)

Propagation of high-power, short-duration laser pulses through underdense plasma is of interest to research areas such as understanding laser beam self-focusing, channel and blast wave formation, filamentation, soliton production, electron and ion acceleration, and x-ray generation. The formation of a channel through an underdense plasma by a 740-J, 8-ps (90-TW) laser pulse focused to a peak vacuum intensity of around 2.8×10^{19} W/ cm^2 was investigated using proton probing. These parameters are relevant to conditions required for the hole-boring fast-ignition scheme.³⁵ The CH plasma–plume underdense target was created by a UV beam (2.5 ns, 1160 J in an 800- μm -diam focal spot). Two-dimensional *SAGE* modeling indicated that this produced a 650- μm -wide Gaussian density profile with

a peak density of $5.3 \times 10^{19} \text{ cm}^{-3}$ along the laser propagation axis. The proton beam was generated using the second short-pulse beam interacting with a 50- μm -thick copper target.

Figure 124.101 shows the interaction at an early time when the laser was still propagating through the plasma; the proton probe images illustrate the expansion of the channel, filamentation, and channel-wall modulations. The time at which the leading edge of the pulse arrived at focus and reached half-maximum intensity is defined as t_0 . Self-correction of the filaments into a single channel is seen from the single-shot sequence on the right side of Fig. 124.101. Bubble-like structures, which develop at later times, are illustrated in Fig. 124.102 by the proton probe images from shots with different relative beam timings. Two-dimensional particle-in-cell simulations are being performed to identify the origin of the channel-wall modulations and bubble structures.

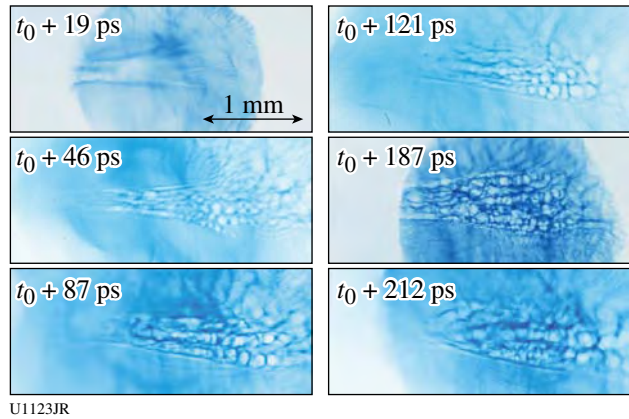


Figure 124.102
Proton probe image sequence from shots with different relative beam timings, which show the temporal evolution of the channel and the formation of bubble-like structures.

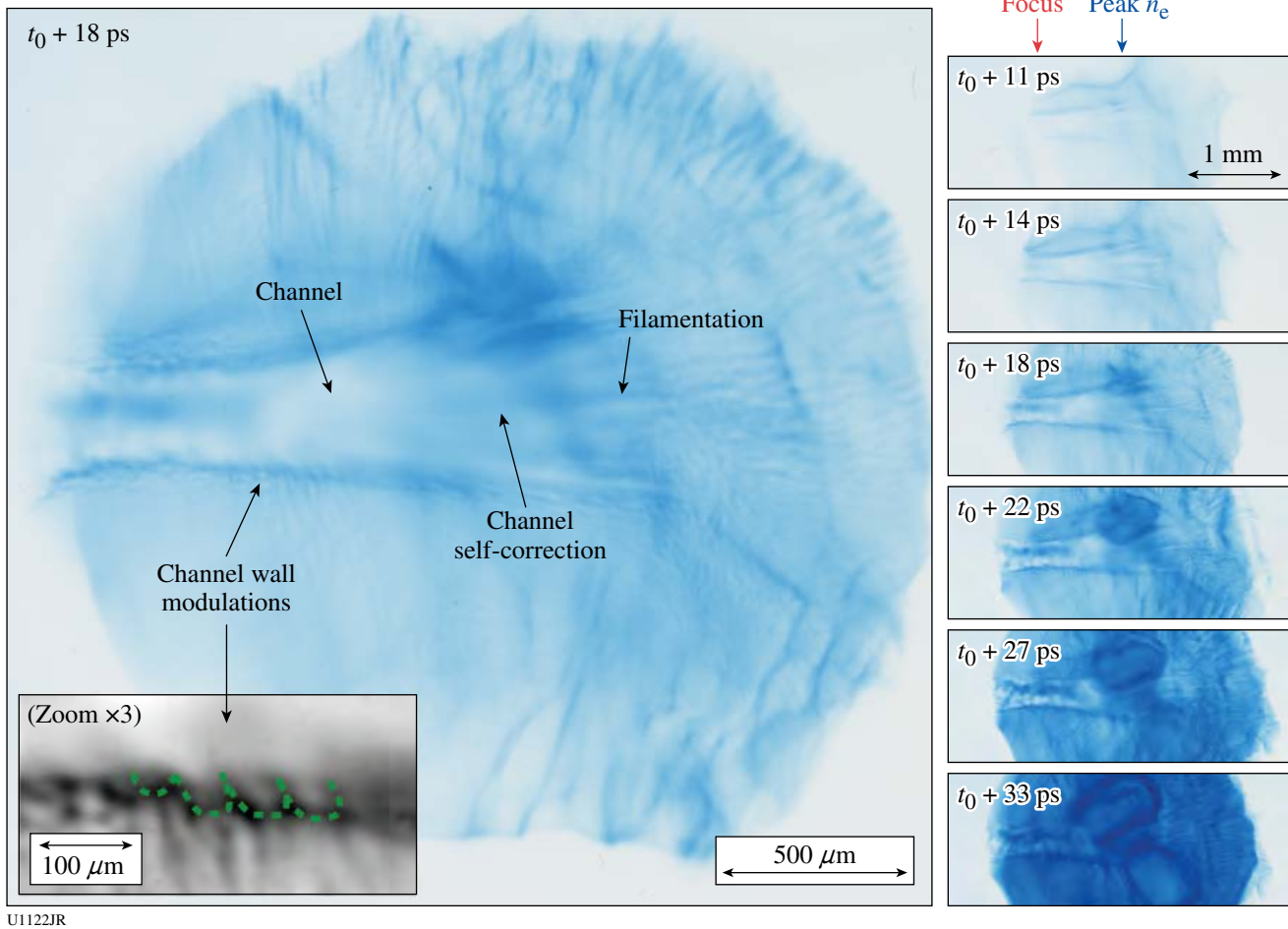


Figure 124.101
Proton probe images of the laser pulse propagating through the plasma from left to right. The time sequence is shown on the right-hand side and shows channel-wall modulations, filamentation, and channel self-correction.

FY10 Laboratory Basic Science Programs

In FY10, LLE issued a solicitation for LBS proposals to be conducted in FY11. A total of 23 proposals were submitted. An independent review committee comprised of Prof. Farhat Beg (University of California, San Diego), Dr. Robert Heeter (LLNL), Prof. Karl Krushelnick (University of Michigan), Dr. Carolyn Kuranz (University of Michigan), Dr. Nicholas Lanier (LANL), Prof. Roberto Mancini (University of Nevada, Reno), Dr. Rick Olson (SNL), Prof. Stephen Padalino (State University of New York–Geneseo), Dr. Wolf Seka (LLE), and Dr. John Soures (Committee Chair, non-voting) reviewed the proposals and recommended that 16 proposals receive 29 shot days on the Omega Laser Facility in FY11. Table 124.VI lists the successful LBS proposals.

Eleven LBS projects were allotted Omega Facility shot time and conducted a total of 303 target shots on the facility in FY10. This work is summarized in this section.

Producing Pair Plasma and Gamma-Ray Burst Using OMEGA EP

Principal Investigator: H. Chen (LLNL)

In August 2010, an LLNL/LLE/NRL team performed an LBS experiment on the OMEGA EP Laser System to study

positron production in high-intensity–laser interactions with high-Z targets. This experiment was a follow-up to that in April 2009 where a record number of positrons were produced using the 1-kJ, 10-ps OMEGA EP backlighter interacting with a 1-mm-thick Au target.³⁶ The 2010 experiment had two main objectives; to examine the positron acceleration and to measure the high-energy gamma radiation. The results are shown in Figs. 124.103 and 124.104 for the positron energy spectra and gamma spectra, respectively. Quasi-monoenergetic positrons with energies peaked at ~25 MeV, the highest positron energy from lasers, were observed. This is nearly 7 MeV higher than that observed in previous OMEGA EP experiments. It is attributed to more-efficient acceleration using laser normal incidence on the same target. The experiments were the first time that high-energy (up to 1 MeV) gamma radiation was observed in laser–solid interaction using a single-hit charge-coupled–device (CCD) detector. This information is important to understanding the physics of laser–plasma interaction that produced electron–positron pairs. The misalignment of the diagnostic and the misfocusing of the laser beam caused by the debris shield made it impossible to observe the electron–positron annihilation feature.

Positron research extends over diverse fields from particle physics and astrophysics to medical applications. These appli-

Table 124.VI: Approved FY11 LBS proposals.

Principal Investigator	Institution	Project Title
H. Chen	LLNL	Exploring Pair Plasma and its Applications Using OMEGA EP
S. X. Hu	LLE	Charged-Particle Stopping Power in Warm Dense Plasmas
R. Betti	LLE/FSC	Shock-Ignition Experiments on OMEGA
I. V. Igumenshchev	LLE	Investigation of Self-Generated Electromagnetic Fields in Directly Driven ICF Implosions Using Proton Radiography
D. Hicks	LLNL	Multi-Megabar Ramp Compression: Studies Using X-Ray Absorption Fine Structure
R. A. Kritcher	LLNL	Capsule Adiabatic Measurements with X-Ray Thomson Scattering
P. Patel	LLNL	Electron Source Characterization for Cone-Guided Fast Ignition
S. P. Regan	LLE	Diagnosing P , ρ , n_e , T_e , Z of H/He, CH ₄ , and NH ₃ Warm Dense Matter
G. Fiksel	LLE	Laser-Driven Magnetic-Flux Compression Experiments on OMEGA
V. A. Smalyuk	LLNL	Measurement of Ablative Rayleigh–Taylor Instability in Deeply Nonlinear Regime
R. Smith	LLNL	Measurement of Nucleation and Growth of the Fe α -to- ϵ Phase Transformation
B. Maddox	LLNL	Ultrahigh Pressure Lattice Dynamics in High-Z Materials
H. Park	LLNL	Astrophysical Collisionless Shock Generation in Laser-Driven Experiments
O. Hurricane	LLNL	Measurements of Linear, Nonlinear, and Turbulent-Mixing Regimes in Kelvin–Helmholtz Instability in the Subsonic Regime
C. Stoeckl	LLE	Fast-Electron Transport in Solid-Density Matter
J. M. McNaney	LLNL	Short-Pulse-Laser–Based Neutron Resonance Spectrometry

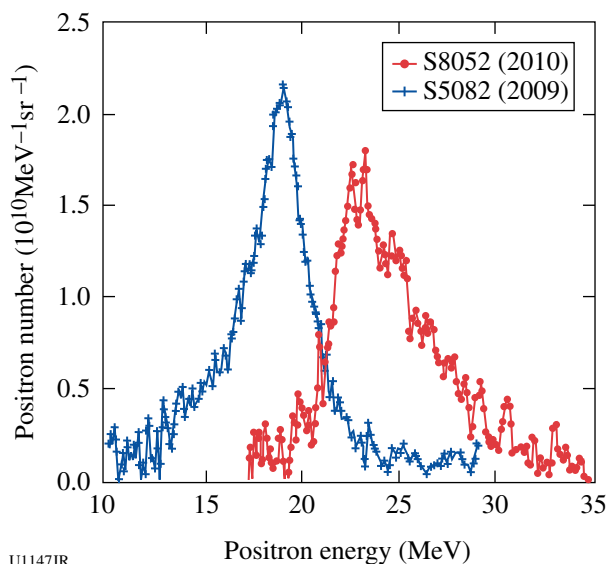


Figure 124.103
Positron spectrum measured on the OMEGA EP laser.

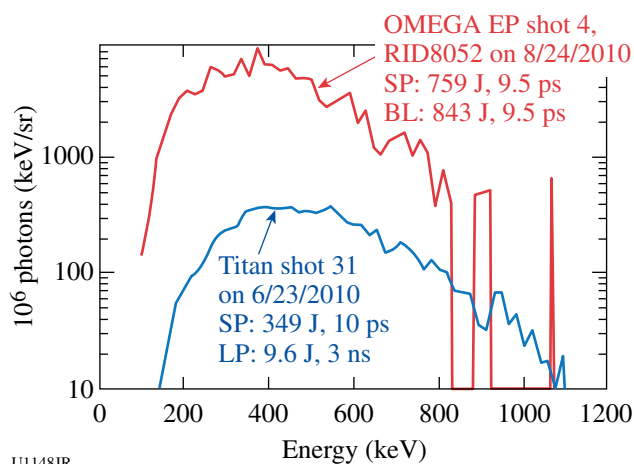


Figure 124.104
High-energy gamma spectrum measured by the NRL single-hit CCD detector.

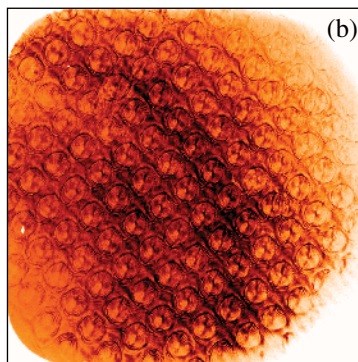
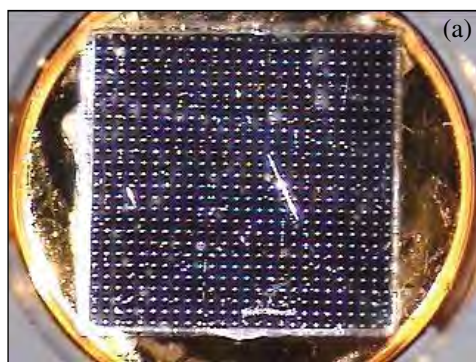


Figure 124.105
(a) Example of a fused-SiO₂ viscosity target sample with the etched array of pits clearly visible in the metrology photograph; the hohlraum is behind the sample. (b) Raw intensity record from one of the channels of the OHRV for the same target probed at 2.6 ns following the passage of a shock through the perturbed interface, showing the probe light reflected directly from the shock front and revealing the pattern of expanding ripples created by the array of etched pits.

cations often require the production of large numbers of positrons on a short time scale, which have been difficult to supply. The new OMEGA EP results could significantly affect the quest for a laser-produced positron source for research in these fields.

Measurements of the Viscosity of Shock-Compressed Fluids: Studies of Water and Silica (Viscosity-10A)

Principal Investigator: P. M. Celliers (LLNL)

The Viscosity-10A campaign was carried out as part of the LBS program. The goal was to demonstrate a method for determining the viscosity of a high-pressure fluid created by the propagation of a strong shock front through an initially transparent sample. In this campaign the sample under study was liquid silica (SiO₂), produced by propagating a shock through samples of either alpha-quartz or fused SiO₂. The viscosity of high-pressure liquid SiO₂ has obvious geophysical relevance, and measurements in the Mbar domain are not possible with conventional methods. The measurement technique is based on observing the evolution of a spectrum of perturbations imposed on a multi-Mbar shock front passing through the sample material. The viscosity of the liquid state just behind the shock front is expected to influence the decay rate of the perturbations as the shock front propagates, and detailed measurements of the perturbation state can be compared with calculations to assess the viscosity. The measurement technique employed the OMEGA high-resolution velocimeter (OHRV) to observe the velocity perturbations directly on the surface of the reflecting shock front. The shocks were driven using a hohlraum coupled to a 50- μ m polystyrene ablator followed by the sample. The perturbation spectrum was generated by an etched array of shallow pits, a few microns deep and 10 μ m in diameter, that were created on the sample surface at the interface with the ablator. As the shock passed through this interface, the perturbations created a pattern of expanding ripples riding on top of the shock front, which were detected and measured quantitatively by the OHRV (Fig. 124.105). During the campaign,

U1149JR

we carried out three drive-characterization experiments using ASBO/SOP to characterize the shock velocity. These were followed by eight perturbation experiments probing 3-Mbar and 6-Mbar shocks in the SiO₂ samples. High-quality data were recorded on all shots.

Optical Properties of LiF

Principal Investigator: D. E. Frantanduono (LLE)

Co-investigators: M. A. Barrios, T. R. Boehly, and D. D. Meyerhofer (LLE); and D. G. Hicks, J. H. Eggert, R. Smith, and P. M. Celliers (LLNL)

Direct laser ablation was used to ramp-compress lithium fluoride (LiF) to 800 GPa. LiF was observed to remain transparent over this pressure range; this is the highest-pressure insulator ever observed. The refractive index of ramp-compressed LiF was measured up to 800 GPa and observed to increase linearly with compressed density over this range. These highest-pressure measurements of refractive index to date were used to infer the pressure-induced band-gap closure of compressed LiF. An effective single-oscillator model of this behavior shows that the optical gap closes monotonically with increasing density.

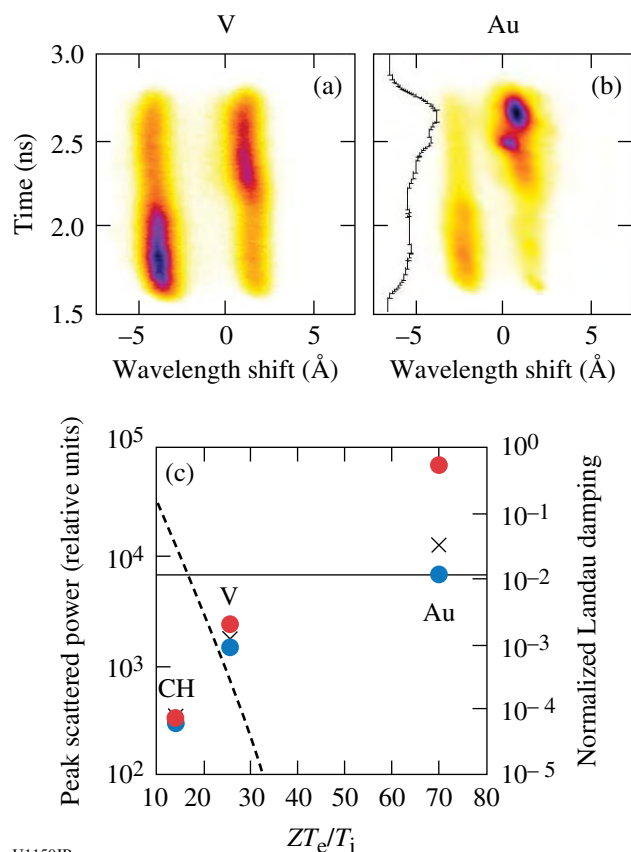
Extrapolation of these results suggests that metallization of LiF should occur at pressures of 4200 GPa. If true, LiF will prove to be a valuable window for extremely high pressure, ramp-compression experiments.

Ion-Acoustic Wave Instability from Laser-Driven Return Currents

Principal Investigators: D. H. Froula, S. X. Hu, and J. F. Myatt (LLE)

Co-investigators: J. S. Ross, L. Divol, and S. H. Glenzer (LLNL)

Thomson-scattering measurements of the amplitude and frequency of ion-acoustic waves show an instability when ion-wave damping is reduced. Experimental results from the OMEGA laser used simultaneous measurements of the electron-plasma wave and ion-acoustic wave features to characterize the plasma (T_e , T_i , Z , n_e) and to directly probe the amplitude of the ion-acoustic waves (Fig. 124.106). The ion Landau damping was varied by changing the target material: CH, V, Ag, and Au. For plasma conditions where the ion Landau damping was large ($ZT_e/T_i = 10$), the amplitude of the ion-acoustic waves was stable. Reducing the ion Landau damping ($ZT_e/T_i = 30$) increased the amplitude of the ion wave, but the electron Landau damping was sufficient to maintain stability. The ion-acoustic waves became unstable when the ion Landau damping was weak ($ZT_e/T_i = 70$). As the waves grew to wave-



U1150JR

Figure 124.106

(a) The Thomson-scattering spectrum provides a measurement of the electron temperature, density, charge state, and, from the asymmetry in the scattered power between the ion-acoustic features, the relative drift between the electrons and ions driven by the heat-flux-driven return current. (b) As the ion damping was reduced, the system became dominated by the electron Landau damping, which became Landau growth in the weakly damped systems.

breaking amplitudes, their frequency shifted and turbulence was expected. These results confirm the speculation that heat-flux-driven ion-acoustic fluctuations exist in laser-produced plasmas, which was previously invoked to increase the collision rate and account for anomalous absorption.³⁷

X-Ray Absorption Fine Structure Measurements on Multishock Compressed Iron

Principal Investigators: Y. Ping and D. G. Hicks (LLNL)

X-ray absorption fine structure (XAFS) measurements were performed on iron that was multishock compressed to a few megabar. By dynamically compressing a few-micron-thick iron sample sandwiched between thin diamond anvils, near-constant pressure conditions were produced inside the iron, the bulk of the pressure evolution taking place in the adjacent, x-ray-transparent diamond anvils. A spherical, imploding

backlighter source was used to produce a smooth, broadband source of x rays for the absorption measurement. The VISAR was used to track the rear surface of the diamond from which the pressure inside the iron sample could be inferred. An example of an XAFS spectrum obtained at 3.5 Mbar is shown in Fig. 124.107. This was analyzed using the FEFF code³⁸ and found to give a compression in Fe of 1.6 and a temperature of 6000 K. Improved fits were found for a c/a ratio of 1.73, indicating that pressure, density, temperature, and c/a ratio could be obtained from a single shot.

Capsule Adiabatic Measurements with X-Ray

Thomson Scattering

Principal Investigators: A. Kritcher, T. Doeppner, O. L. Landen, and S. H. Glenzer (LLNL)

Experiments to characterize spherically imploded inertial fusion-type targets using x-ray Thomson scattering were recorded at the Omega Laser Facility in January and May of 2010 to study the properties of compressed ICF ablaters. Measurement of the temperature and density allows one to infer the capsule adiabat—a measure of the plasma pressure normalized by the Fermi pressure—and can be used to test low-adiabat pulse-shaping methods. In these experiments the noncollective, or microscopic, particle behavior of imploding CH and Be shells was probed using a 9-keV Zn He $_{\alpha}$ x-ray source at scattering angles of 113° and 135°. Figure 124.108(a) shows a schematic of the experimental setup including time-resolved pinhole images of the imploding capsules. The capsules attached to Au

half-cones were hemispherically driven using 36 drive beams. The Zn He $_{\alpha}$ probe was created by laser irradiation of a Zn foil positioned on the inside of the Au cone. Figures 124.108(b) and 124.108(c) show radiation–hydro–dynamic calculations of the mass density as a function of time and radius for the two pulse shapes used in these experiments.

Figure 124.109 shows scattering spectra from Be (+2) capsules driven with pulse shape LA2201 shown in Fig. 124.108(b), at 4.2 ns after the start of the drive beams and a scattering angle of 135°. The measured electron density and temperature determined from theoretical fitting to the experimental data was 14 ± 3 eV and $1.1 \pm 0.15 \times 10^{24}/\text{cc}$, respectively. For these partially degenerate plasmas, the width of the inelastic Compton feature provided the electron-velocity distribution, which is a direct measure of the electron density. The electron temperature was determined from the semi-Gaussian shape of the Compton feature, independent of the choice of structure factor model. Sensitivity of theoretical fitting to the red wing of the Compton feature for varying electron temperatures is shown in Fig. 124.109. In this geometry, the larger scattering angle of 135° resulted in the Compton red wing shape depending less on the finite size of the source and scattering volume, enabling us to better determine the temperature and density. Also, with this new geometry we were able to use additional probe beams, which resulted in an increase in signal to noise. These experiments demonstrate the viability and investigate the error in using this diagnostic to study the properties of implosion targets at the National Ignition Facility.

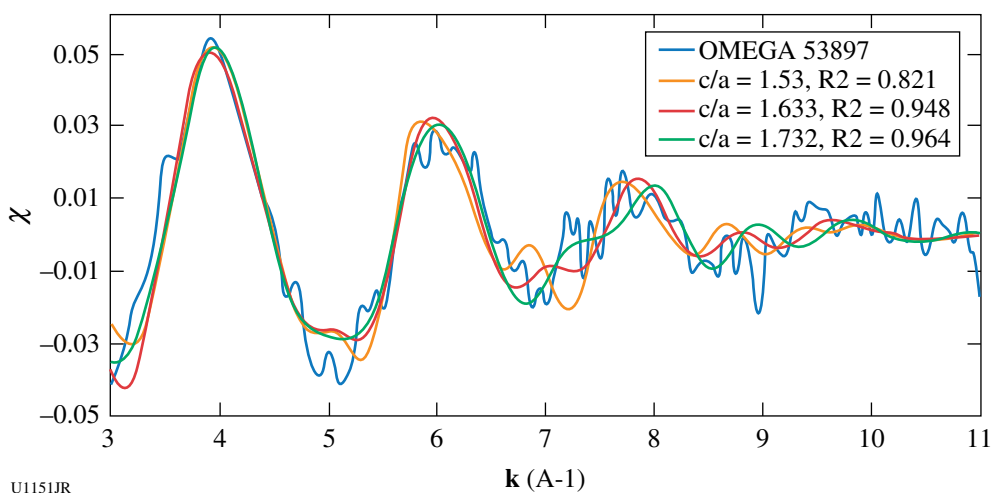
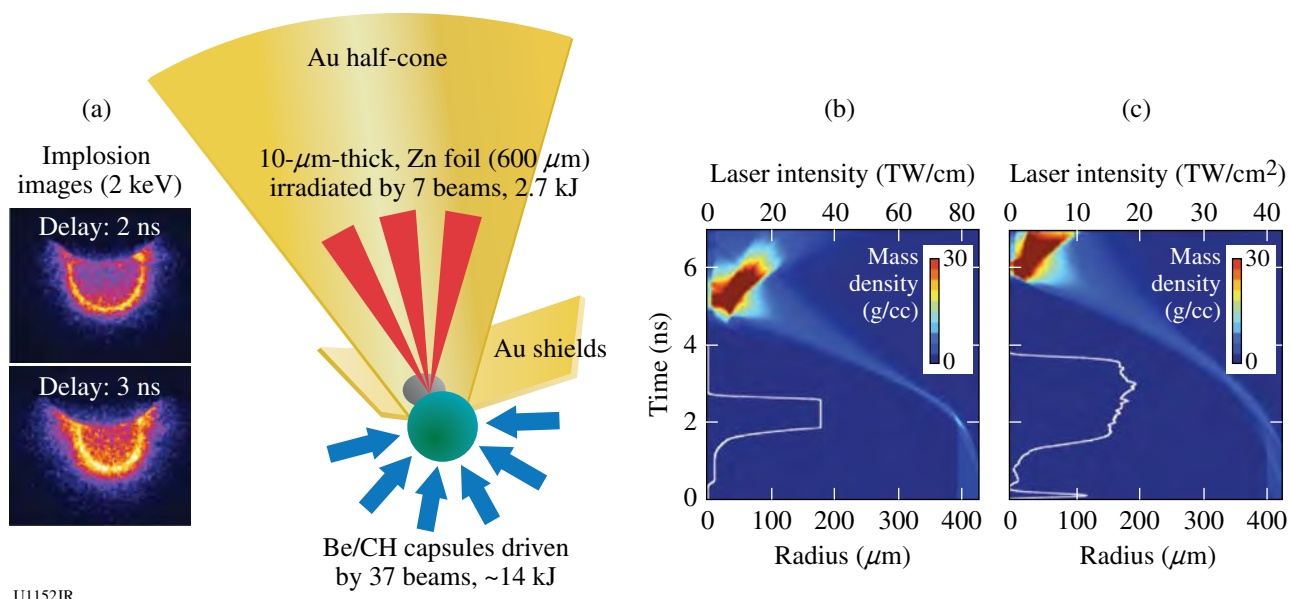


Figure 124.107

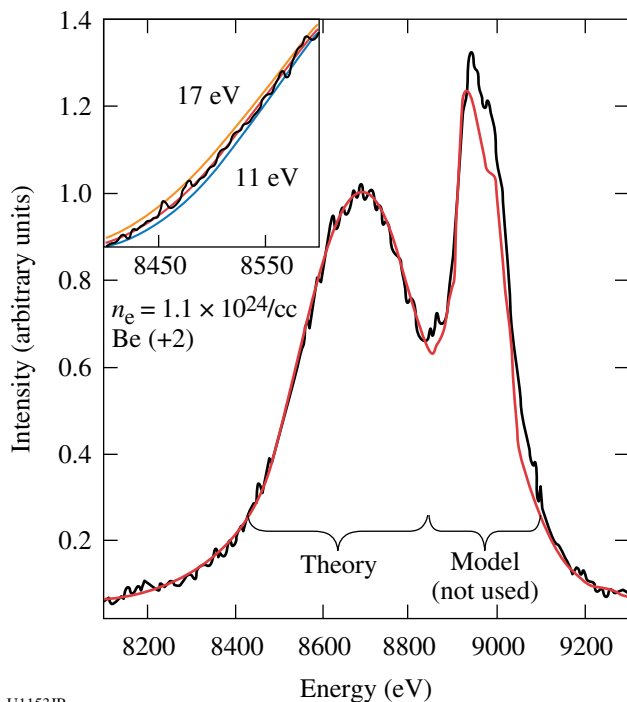
XAFS spectrum of iron compressed at 3.5 Mbar. The residual, normalized x-ray absorption coefficient χ (dimensionless) plotted versus wave vector k (inverse angstroms) is fit to an hcp crystal configuration to determine the density, temperature, and c/a ratio.



U1152JR

Figure 124.108

(a) Schematic of the experimental setup. Here, Zn He_α x rays, produced via laser irradiation of a 10- μm -thick Zn foil, were scattered from imploding Be and CH capsules that were compressed using 36 additional shaped laser beams. The Zn foil was attached to gold half-cones with Au flaps that shielded the detector from the source x rays. Also shown (left) are time-resolved x-ray images of the implosion. (b) and (c) Radiation-hydrodynamic calculations of the mass density, plotted as a function of time and target thickness, where $t = 0$ denotes the start of the drive beams. Profiles of the drive-beam waveforms (white) are overlaid on the mass-density contour, listed as a function of time and laser intensity.



U1153JR

Figure 124.109

In-flight x-ray Thomson scattering data (4.2 ns) from laser-compressed Be cone-in-shell targets [see Fig. 124.108(b) for the drive-pulse shape]. Data include an elastically scattered Raleigh peak at ~ 9 keV and an inelastically scattered Compton feature at ~ 8.7 keV. Theoretical fits to the experimental data yielded an electron temperature and density of about 14 eV and $1.1 \times 10^{24}/\text{cc}$, respectively.

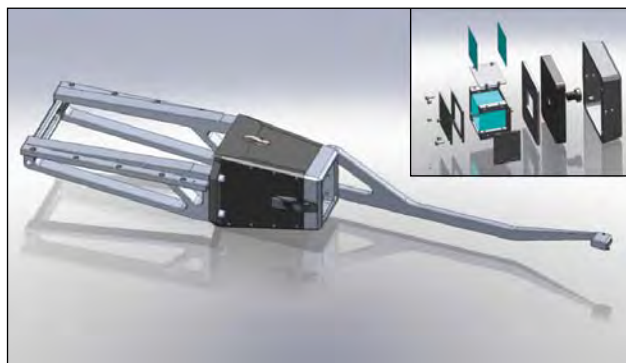
Study of High-Z Material Properties Under Compression Using High-Energy Backlighter Diffraction

Principal Investigators: B. Maddox and H. S. Park (LLNL)

This project was carried out as a series of four distinct series of shots on the OMEGA EP Laser System under the series name of DynDiff.

DynDiff-10A. This experimental campaign was designed to test two different diffraction schemes, Bragg (reflection) and Laue (transmissions), for diffraction off high-Z metals using x rays produced by laser-driven foil targets. Two new diagnostics were designed to accomplish this: For Bragg diffraction, the Bragg diffraction imager (BDI) consists of a large Hevimet housing and an Al arm that holds a Hevimet beam block close to the crystal target. The beam block prevents the x rays from the backlighter from reaching the detector while making it possible for diffracted x rays to pass. For Laue diffraction, the Laue diffraction imager (LDI) consists of the same Hevimet housing as the BDI, but with a collimator snout instead of an Al arm. This collimator snout creates a collimated x-ray beam that then diffracts off a crystal housed inside. Figure 124.110 shows a drawing of the BDI diagnostic. The inset shows the front snout that attaches to the main body to turn the BDI into the LDI. Targets for Bragg diffraction consisted of 600- μm -thick Mo (111) crystals mounted onto glass stalks. Targets for Laue dif-

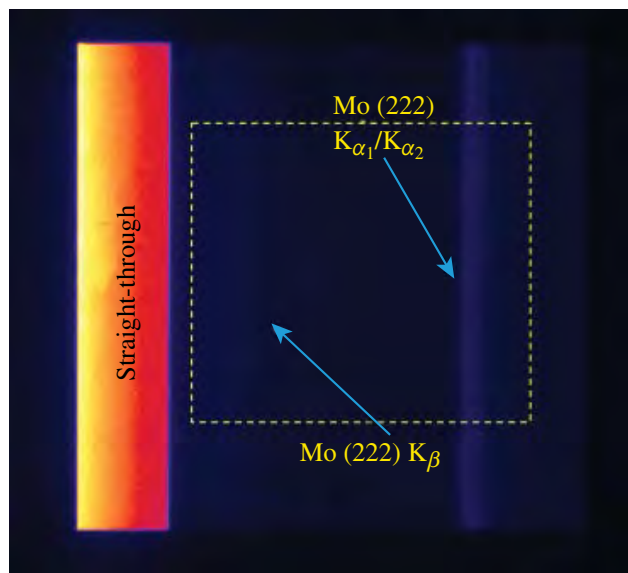
fraction consisted of 5- μm -thick Ta mounted on a rotation stage inside the LDI. X rays were produced by irradiating a metal foil using either the short-pulse backlighter beam (for Bragg diffraction) or the long-pulse UV beams (for Laue diffraction). Figure 124.111 shows an image obtained using the BDI on a Mo (111) crystal using a 17.478-keV Mo K_{α} backlighter. Similar quality results were obtained using the LDI to measure Laue diffraction from Ta single crystals. These results were used in DynDiff-10B to attempt to measure Bragg diffraction from a shock-compressed Mo crystal.



U1154JR

Figure 124.110

The Bragg diffraction imager (BDI). Inset shows the front nose assembly that turns the BDI into the Laue diffraction imager (LDI).



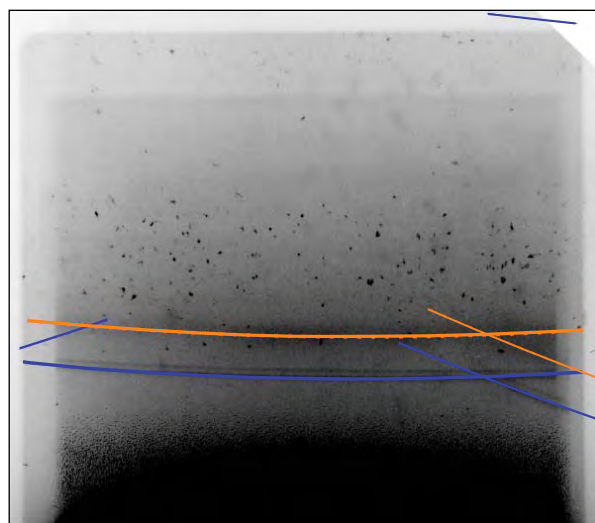
U1155JR

Figure 124.111

Diffraction image obtained using the BDI on a Mo (111) crystal using a 17.478-keV Mo backlighter.

DynDiff-10B. The goal of this campaign was to build on the success of DynDiff-10A to measure Bragg diffraction from a shock-compressed Mo (111) single crystal and to measure the drive characteristics of the OMEGA EP UV long-pulse beams using VISAR. The Mo crystal target consisted of a 600- μm -thick Mo (111) single crystal with a 20- μm parylene-n ablator and was mounted on a glass fiber stalk. The VISAR witness target was 1-mm-thick LiF coated with 10- μm -thick Al and mounted on a 7.5-mm-diam Al washer. The crystals and LiF targets were driven using a single long-pulse UV beam (Beam 4) using a 4-ns square pulse at an energy of 300 J and defocused to a 6-mm-diam spot. The x-ray backlighter target was a 250- μm -diam, 12- μm -thick Mo foil and was driven by the OMEGA EP short-pulse backlighter beam at 900 J in 100 ps with a 200- μm spot diameter. Good VISAR data were obtained; however, because of an alignment error of the BDI beam block, no driven diffraction was detected. It was concluded that the alignment tolerance was too tight and a new beam block needed to be designed that would allow for a greater alignment variance.

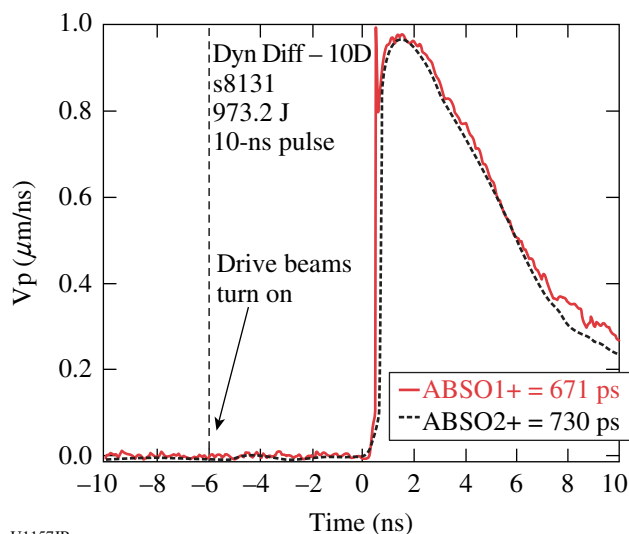
DynDiff-10C. The goal of this campaign was to measure Bragg diffraction of 17.478-keV Mo x rays off shock-compressed single-crystal Mo on OMEGA EP using a new, specially designed beam block and arm for the BDI that had a greater alignment tolerance than the original beam block. A secondary goal was to measure the shock-loading profile using Al/LiF targets and the TIM12 ASBO. A total of six target shots were conducted. The VISAR targets consisted of LiF (1 mm thick) coated with Al (10 μm thick) and a parylene-n ablator (20 μm thick), all mounted on a 7.5-mm-diam Al washer. Crystal targets consisted of a 6-mm-diam, 250- μm -thick Mo single crystal with a 20- μm -thick parylene-n ablator. Because of a target build error, no ASBO data were obtained during this campaign; however, the first driven Bragg diffraction using a petawatt-laser x-ray backlighter was observed. Figure 124.112 shows a diffraction image obtained using the BDI on a driven Mo (111) crystal along with a preliminary fit to the compressed diffraction pattern. The drive laser (UV beam 1) was set to 616 J in a 10-ns square pulse using a 5-mm-diam spot size and fired 7 ns before the backlighter beam. Although no ASBO data were obtained during this campaign, scaling from data obtained during the DynDiff-10B campaign suggests ~ 25 -GPa peak pressure. The fit to the diffraction pattern shown in Fig. 124.112 gives a strain along the compression direction of $\sim 5.8\%$. This technique was used during the DynDiff-10D campaign to measure the 3-D lattice relaxation time scale in bcc Mo by taking Bragg-diffraction snapshots, like the one shown in Fig. 124.110, at various times after the start of the laser drive.



U1156JR

Figure 124.112
Diffraction pattern obtained using the BDI of a shock-loaded Mo (111) crystal and a 17.478-keV Mo backlighter. The solid blue and orange lines show fits to the undriven and driven portions of the lattice.

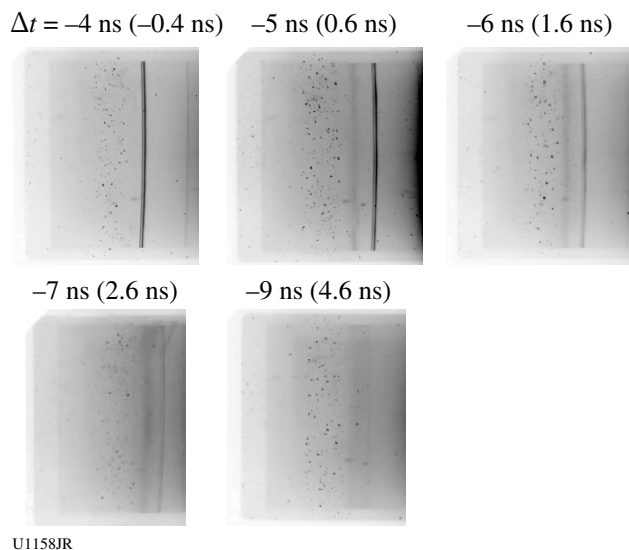
DynDiff-10D. This campaign was an extension of DynDiff-10C, and the goal was to use time-resolved Bragg diffraction to study the lattice dynamics of single-crystal bcc Mo. A total of five target shots were conducted: one VISAR shot to measure the laser drive and four successful diffraction shots at different times after initial compression. Targets were of the same design as those used in DynDiff-10C. The laser setup was also similar to that used during DynDiff-10C except for the introduction of a second UV drive beam (Beam 4) to enhance the drive uniformity across the crystal target. Figure 124.113 shows the



U1157JR

Figure 124.113
VISAR data obtained during the DynDiff-10D campaign.

VISAR data obtained. Using the shock-arrival time coupled with the Al thickness, the breakout time of the shock into the Mo crystals was calculated. Figure 124.114 shows a series of diffraction images taken at different times after the shock wave entered the crystal, starting with an undriven crystal. A compressed Mo (222) line is seen at a higher angle (left side of the images) that gradually shifts to lower compression. These data are currently being analyzed.



U1158JR

Figure 124.114
Diffraction plots as a function of time after compression for bcc Mo (111) showing a static (222) diffraction line and a compressed (222) line.

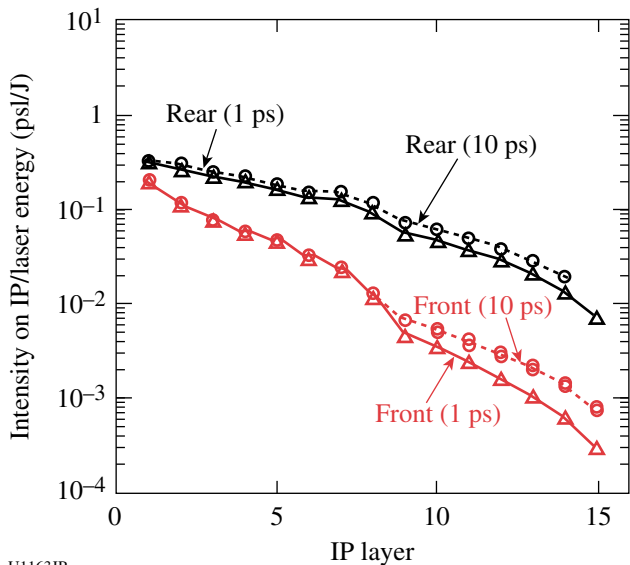
Relativistic Laser-Plasma Interaction

Principal Investigators: P. Patel (LLNL) and H. Sawada (University of California, San Diego)

Co-investigators: C. D. Chen, H. S. McLean, and M. H. Key (LLNL); T. Yabuchi and F. N. Beg (University of California, San Diego); R. B. Stephens and K. U. Akli (General Atomics); and W. Theobald, P. M. Nilson, and C. Stoeckl (LLE)

The objective of this campaign was to characterize fast electrons created by the high-energy OMEGA EP short-pulse laser interacting with planar and cone targets. The FY10 focus was on investigating two critical parameters: electron energy spectrum (T_{hot}) and conversion efficiency from laser to fast electrons (η). Experiments were performed using the OMEGA EP backlighter beam at 150 to 250 J in 1 ps and 1000 J in 10-ps-pulse duration. These laser parameters have been used in integrated fast-ignition (FI) experiments on OMEGA.³⁹ This study provided direct information about the electron source in integrated experiments.

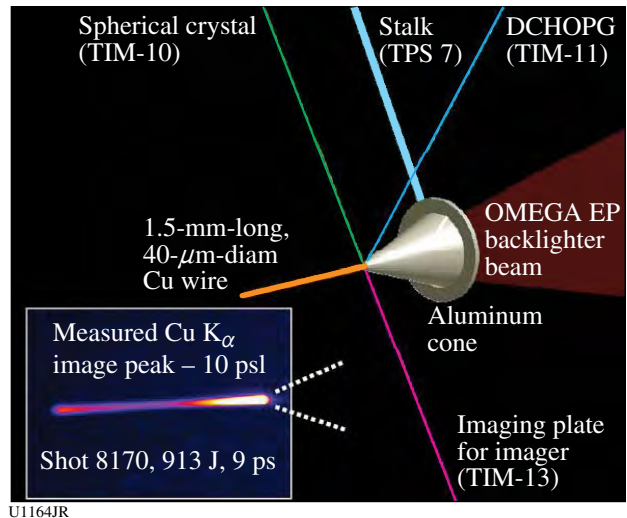
Multilayer planar targets were used to measure up-to-750-keV bremsstrahlung emission to infer T_{hot} and η . A planar target is less sensitive to the beam-pointing stability, target positioning, and pre-pulse level compared to a cone. The target consisted of an ~1-mm-thick planar Al with a 25- μm -thick Cu layer buried at 100 μm from the front surface. To prevent electron refluxing caused by the sheath fields, 1-mm-thick CH was attached to the rear side. The x rays were measured with two bremsstrahlung x-ray spectrometers (BMXS's) at the rear side on the laser axis and 49° from the incoming laser axis. Figure 124.115 compares the measured signals on the stack of 15 imaging plates in the BMXS at 150 J in the 1-ps shot and 1000 J in the 10-ps shot. These raw data normalized by the laser energy indicate similar fast-electron spectra and conversion efficiencies at a laser intensity of $\sim 5 \times 10^{18} \text{ W/cm}^2$ at both 1 and 10 ps. The preliminary analysis using a Monte Carlo code ITS⁴⁰ shows that the total conversion efficiency is estimated to be 14% to 35% for the 1-ps shot and 13% to 37% for the 10-ps shot with an assumption of the classical ejection angle. For further analyses, a PIC simulation using simulated pre-plasma profile from a radiation-hydrodynamics code *HYDRA* will be performed to calculate the divergence of the electron beam. This electron source will be fed into a hybrid transport code calculating the bremsstrahlung emission to match the measurements. The inferred T_{hot} and η will be compared to the simulated results.



U1163JR

Figure 124.115
Measured signals of front and rear bremsstrahlung spectrometers for 1-ps (shot 7694) and 10-ps (shot 7698) pulses.

The study was extended to cone-wire targets, which are more relevant to integrated experiments. Cone-wire targets were used to study the electron production in the cone and transport through the cone tip to the wire, where transport is simplified to quasi 1-D geometry in the wire direction. Figure 124.116 shows the overview of the cone-wire experiment. The backlighter beam was focused onto the Au or Al cone tip to generate electrons. The electrons transported through the cone tip were coupled to the 1.5-mm-long (40- μm -diam) Cu wire attached to the cone tip. From the wire 8.05-keV K_{α} was measured with the absolutely calibrated DCHOPG spectrometer and a spherical crystal imager (SCI) for the imaging of the wire. A version of SCI was deployed for these experiments at the end of Q4. The inset of Fig. 124.116 shows the monochromatic image of the wire at 1000 J in a 10-ps shot (shot 8170). K_{α} yields were obtained as well as wire images at both 1- and 10-ps pulse durations. The falloff of the wire emission and the Cu K_{α} yield will be modeled with a hybrid transport code to infer the T_{hot} and coupling efficiency to the wire. The SCI will enable one to study another critical parameter in future experiments: the divergence of forward-going electrons.



U1164JR

Figure 124.116
Experimental configuration of the cone-wire experiment. Inset: The measured monochromatic image of the Cu wire is shown for shot 8170.

Kinetic Behavior of Crystalline Iron Undergoing Multi-Mbar Compression and Release

Principal Investigators: R. Smith, Y. Ping, and D. G. Hicks (LLNL)

The kinetic behavior of iron during rapid compression and release was studied using x-ray absorption fine structure

(XAFS). A 4- μm iron sample, sandwiched between diamond layers, was multishock compressed up to 3.5 Mbar and then released (Fig. 124.117). The pressure history in the iron was tracked using a VISAR reflection from the rear diamond. By probing the XAFS spectrum of the iron on multiple shots before and after the peak of the compression wave, the rapid evolution of short-range atomic order in the crystal was examined. We observed that with increasing pressures, the spacing between XAFS peaks increased along with increased damping of the peaks at higher k . This indicates an increase in the density of the hcp phase from 1.65- to 1.8-fold compression and an increase in the temperature from 4000 to 10,000 K. These changes are undone on release of the wave. Detailed examinations are being made to determine whether the changes are fully reversible.

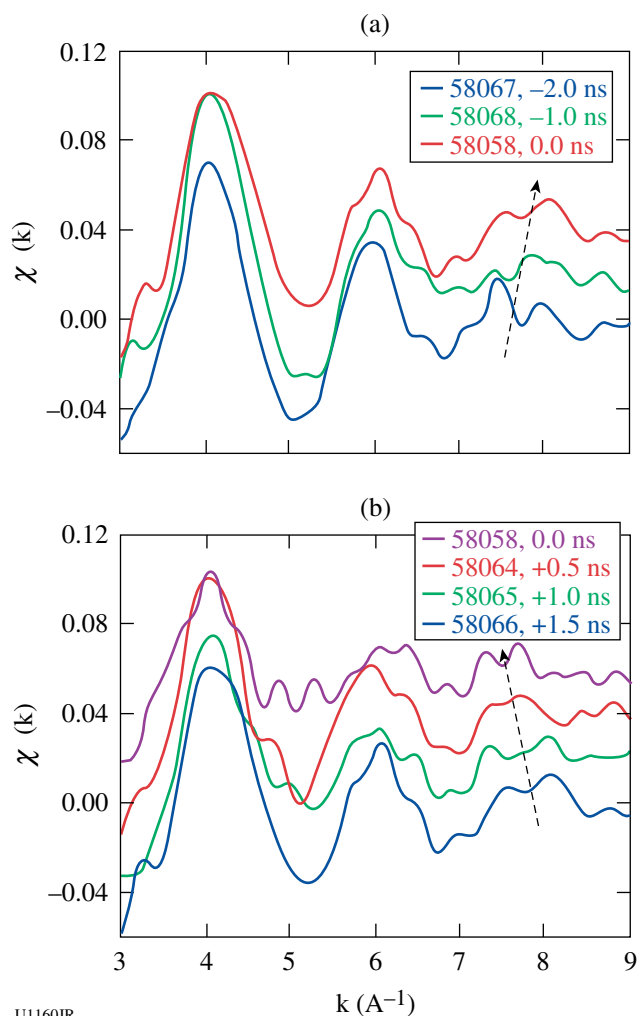


Figure 124.117
Changes in the Fe XAFS spectra observed on (a) compression and (b) release of a 3.5-Mbar pulse.

Integrated Shock-Ignition Experiments on OMEGA

Principal Investigator: R. Betti (LLE/FSC)

Co-investigators: W. Theobald, O. V. Gotchev, K. A. Anderson, and P.-Y. Chang (LLE)

Shock ignition is a two-step ICF scheme where ignition is achieved by launching a strong spherically convergent shock into the imploding capsule at the end of the compression. The laser intensities at the end of the pulse are $\sim 5 \times 10^{15} \text{ W/cm}^2$ and significantly higher than what is currently available with standard 60-beam implosions on OMEGA. A new experimental platform has been developed on OMEGA that uses 40 beams to compress D_2 -filled plastic shells on a low adiabat and the remaining 20 beams to generate a strong shock. The 20 beams are delayed and tightly focused onto the imploding shell to reach intensities of up to $\sim 8 \times 10^{15} \text{ W/cm}^2$.

Initial 40-beam implosions had a strong $l = 2$ nonuniformity as shown in the two top pinhole-camera images in Fig. 124.118(a). The implosion was improved by repointing the 40 drive beams so that a more-uniform illumination was achieved. This is clearly seen in the two bottom x-ray pinhole-camera images shown in Fig. 124.118(b). The core brightness

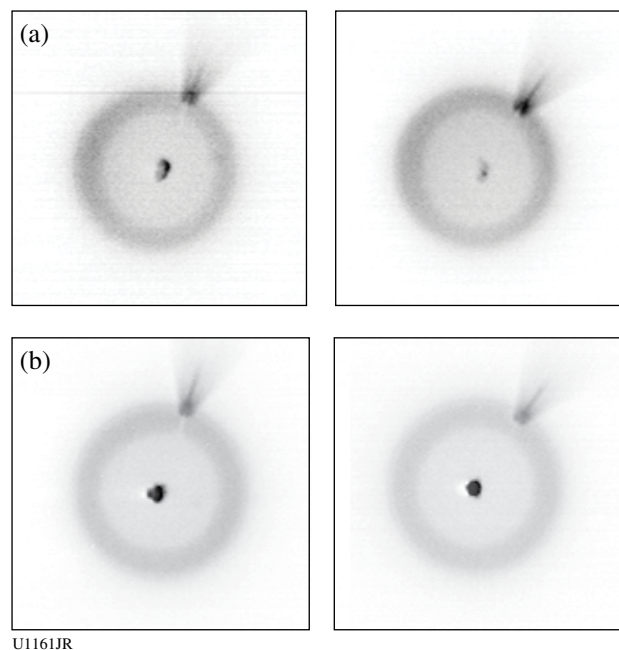


Figure 124.118
X-ray pinhole camera images from two different implosions. (a) Shot 52480, an implosion with 40 drive beams that were all pointed to the center of the capsule; (b) Shot 55737, an implosion where the 40 beams were repointed to achieve a more-uniform illumination. Two pinhole-camera images are shown for each shot.

increased and the shape of the core is more circular. By repointing the beams, the neutron yield increased by a factor of ~ 5 from $(2.6 \pm 1.1) \times 10^8$ to $(1.5 \pm 0.2) \times 10^9$. This shows that repointing significantly improved the symmetry of the implosion, reducing the calculated power imbalance from $\sim 8\%$ to $\sim 3\%$ root mean square.

Another objective of the campaign was to study the interaction of the 20 high-intensity beams. The neutron yield increased by a factor of 2 to $(3.3 \pm 0.2) \times 10^9$ when the 20 beams were added to the optimized target. The plasma reflectivity was measured for various laser intensities from ~ 2 to $8 \times 10^{15} \text{ W/cm}^2$. This was achieved through an intensity scan by shifting the focus of the 20 shock beams relative to the center of the shell. Figure 124.119 shows the measured fraction of (a) SBS and (b) SRS laser backscatter energy of one shock beam versus laser intensity. SBS increased moderately from 7% to 12% with intensity, while SRS increased by a factor of ~ 6 from 4% to 24% and dominated the backscattering at the highest intensity. The sum of SRS and SBS (c) increased from 10% to 36%.

The backscatter is highly directional. The simultaneously measured back-reflection through a neighboring drive-beam port was $\sim 4\%$; it remained constant at all levels of intensities and was comparable to the measured backscatter for implosions without the 20 beams. About 10% of the high-intensity beam energy was converted into hot electrons with a temperature of $42 \pm 5 \text{ keV}$, independent of laser intensity. The measurements indicate that SRS is the primary mechanism for generating the hot electrons with a relatively low temperature. No significant contribution from the two-plasmon-decay instability was observed. This would be beneficial for shock ignition since these electrons are stopped in a thin outer layer of the imploding target and might augment the strong hydrodynamic shock.

The reduction in driver energy caused by backscatter losses might be compensated by increasing the incident laser energy without the danger of preheating the target.

Integrated Core Heating for Fast Ignition

Principal Investigators: W. Theobald and C. Stoeckl (LLE)

This campaign had two primary objectives: First, the neutron-yield enhancement was measured from compressed deuterated plastic shells that were heated by fast electrons for various injection times of the short-pulse OMEGA EP laser. Second, the shock-breakout times in cone-in-shell targets were measured for the same compression condition as in the integrated fast-ignition shots for various cone-tip thicknesses.

Integrated fast-ignition experiments with hollow cone targets mounted into deuterated plastic shells were performed with 1 kJ of short-pulse energy and $\sim 20 \text{ kJ}$ of drive energy. The measured neutron yield as a function of the arrival time of the OMEGA EP pulse is shown in Fig. 124.120. The neutron yield peaks at a delay time of $3.65 \pm 0.02 \text{ ns}$. The gray bar shows the yield without the OMEGA EP pulse. The measurement demonstrates an enhancement in neutron yield by more than a factor of 4 for a properly timed OMEGA EP beam. An additional yield of $(1.4 \pm 0.6) \times 10^7$ was produced by the ultra-intense, short-pulse laser in a narrow time window of less than 100 ps. Data points in the peak were taken on several shot days, months apart, demonstrating high reproducibility of this experimental platform.

Integrated *DRACO + LSP* simulations were performed to estimate the coupling efficiency of fast electrons to the compressed core. The fraction of OMEGA EP laser energy that is coupled into the core is $3.5 \pm 1.0\%$. The coupling is lower

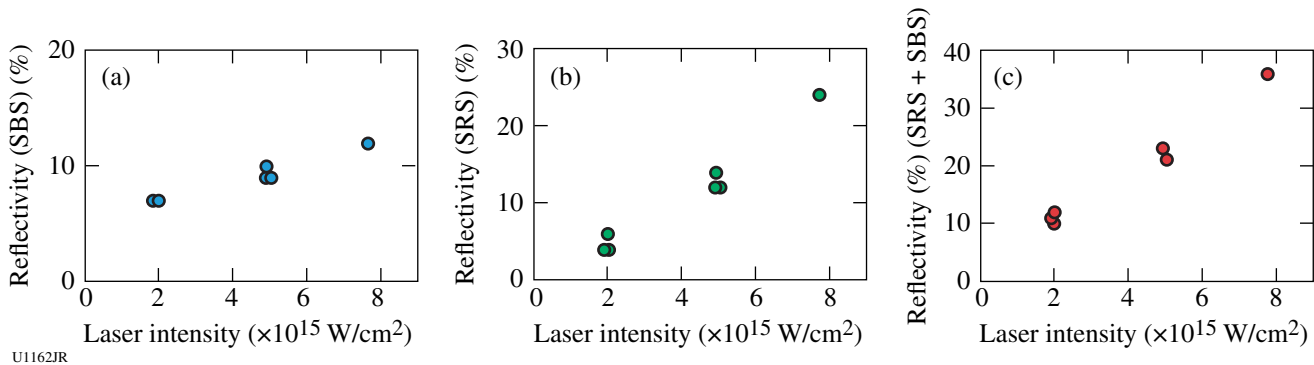
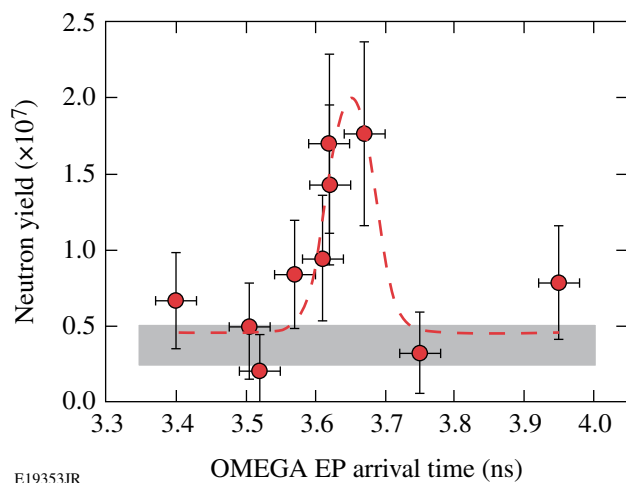


Figure 124.119
Measured backscattered light versus laser intensity for (a) SBS, (b) SRS, and (c) the sum of SBS and SRS.



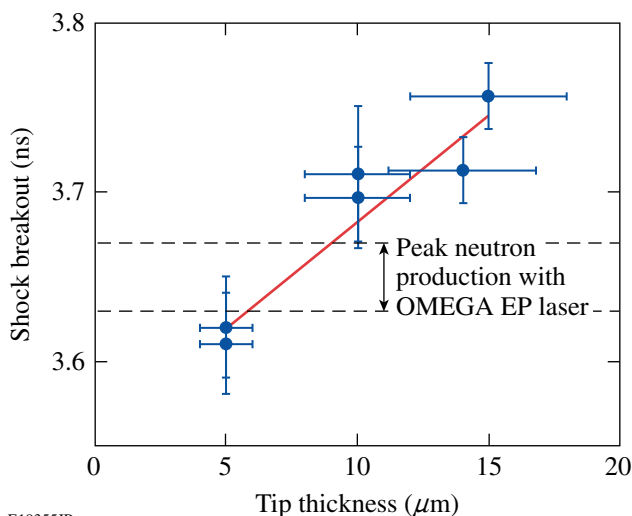
E19353JR

Figure 124.120

Measured neutron yield as a function of the arrival time of the short-pulse laser. The gray bar marks the yield without a heating beam. The dashed curve is a fit of a Gaussian profile to the integrated shot data.

compared to other experiments. A possible explanation is the formation of a pre-plasma in the cone. A pre-plasma in hollow cones has been shown in other experiments to strongly affect the ultra-intense laser-plasma interaction.

Shock-breakout measurements were performed by imploding cone-shell targets with various tip thicknesses without a short-pulse beam. VISAR and SOP diagnostics measured the time when optical emission appeared inside the cone. Figure 124.121 shows the time of shock breakout as a function



E19355JR

Figure 124.121

Measured breakout time of the shock inside the hollow Au cones. The shock breakout is later for thicker cone tips.

of tip thickness. With increasing tip thickness, the breakout is delayed. For thicknesses of 10 and 15 μm , the shock breakout time was at 3.70 ± 0.03 ns and 3.74 ± 0.03 ns, respectively. Shock breakout appeared 50 to 100 ps after the peak of neutron production, confirming that the cone tip was intact at the time when the OMEGA EP beam interacted with the target.

FY10 LLNL OMEGA Experimental Programs

In FY10, LLNL conducted several campaigns on the OMEGA and OMEGA EP Laser Systems, as well as campaigns that used the OMEGA and OMEGA EP beams jointly. Overall, LLNL led 376 target shots involving OMEGA and 107 target shots involving OMEGA EP. Approximately 50% of the total number of shots (212 OMEGA shots, 31 OMEGA EP shots) supported the National Ignition Campaign (NIC). The remainder were dedicated to experiments for high-energy-density (HED) physics (164 OMEGA shots, 64 OMEGA EP shots).

Objectives of the LLNL-led NIC campaigns at OMEGA included

- *Reactivation of the 4ω Thomson-scattering diagnostic*
- *Study of bremsstrahlung backlighters for Compton radiography of inertial confinement fusion (ICF) implosions*
- *High-resolution measurements of velocity nonuniformities created by microscopic perturbations in NIF ablator materials*
- *Equation-of-state measurements of Ge-doped CH*
- *Validation of the Compton-radiography diagnostic platform for ICF experiments*
- *Experiments to study the physical properties (thermal conductivity) of shocked-fusion fuels*
- *Characterization of hard x-ray sensitivity of MCP-based gated imagers*
- *Characterization of the plasma conditions at the laser entrance hole (LEH) of a gas-filled hohlraum using Thomson scattering*
- *Validation of the modeling of multibeam scattering occurring in NIC targets*
- *Measurement of the plasma conductivity by means of collective x-ray Thomson scattering*

The LLNL-led HED campaigns covered five main areas of research:

1. *Material dynamics and equation of state*
 - a. *Quasi-isentropic compression experiments (ICE) for material properties such as strength, equation of state, phase, and phase-transition kinetics under high pressure*
 - b. *Platform development using radiographic mea-*

- measurements of instability growth in tantalum to infer material strength using the joint OMEGA-OMEGA EP configuration
 - c. Properties of shocked CH and Si aerogel foams used in high-energy-density experiments
 - d. The equation-of-state of a CO₂ mixture along the Hugoniot
 - e. Initial experiments to develop an experimental platform to measure the melt and resolidification of tin
2. Opacity
 - a. Opacity studies of high-temperature plasmas under LTE conditions
 - b. Initial experiments to compare short- and long-pulse techniques to heat materials to high temperature for opacity data
 3. Hydrodynamics
 - a. Measurements of the Kelvin-Helmholtz instability in laser-driven shock tubes
 - b. The hydrodynamic evolution of high-mach-number copper-foam jets
 4. X-ray source applications
 - a. Development of multi-keV x-ray sources for radiography and for the study of material response in samples
 5. Diagnostic technique development
 - a. Development of a target-mounted turning mirror for use with the VISAR diagnostic
 - b. Demonstration of ultrafast temperature and density measurements with x-ray Thomson scattering from short-pulse-laser-heated matter
 - c. Comparison of short- and long-pulse-generated x-ray backlighters
 - d. Development of diffraction (white-light Laue and powder) to measure the structure of solids (Ta, Fe, Sn)

1. National Ignition Campaign Experiments

4 ω Thomson-Scattering Reactivation: The 4 ω Thomson-scattering diagnostic was reactivated using a half-day of laser time on OMEGA. The diagnostic has been redesigned to measure the high- and low-frequency Thomson-scattered features. Figure 124.122 shows the first measurement of Thomson scattering from the electron-plasma wave resonance using a 4 ω probe beam. The Thomson-scattering probe beam was aligned 400 μ m off the surface of a vanadium foil target. The target was heated with a single 3 ω beam, and the 4 ω probe beam was delayed from the heater beam by 1 ns.

The wavelength of the Thomson-scattered electron feature shown in Fig. 124.122 can be used to measure both the electron temperature and density. The density is decreasing in time

because of the expansion of the blowoff plasma, which can be seen in the increasing wavelength of the blue-shifted electron feature.

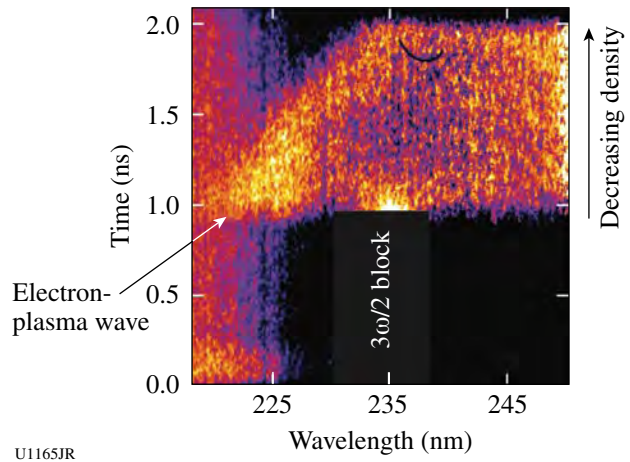


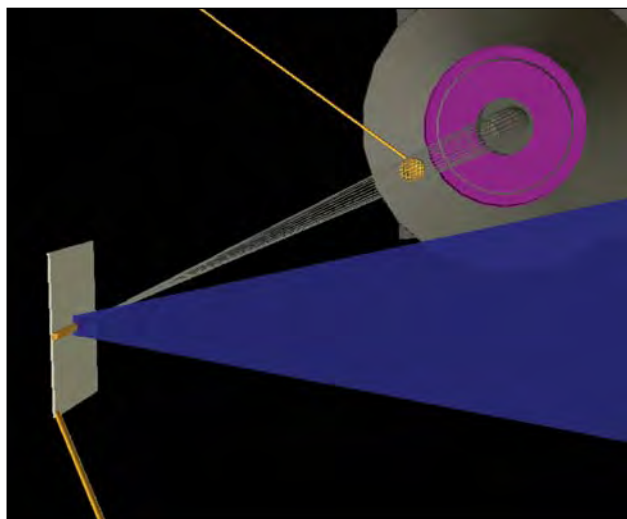
Figure 124.122
Thomson scattering from the electron-plasma wave resonance.

High-Resolution Bremsstrahlung Backlighters: The motivation of the bremsstrahlung backlighters campaign is to develop and characterize broadband x-ray sources emitting around and above 75 keV to be used in the Compton radiography of ICF targets. In FY09, Au microwire backlighters irradiated by 10-ps-long OMEGA EP pulses were characterized.

In FY10, Au microwire backlighters irradiated by 100-ps-long OMEGA EP pulses (1ω) and OMEGA pulses (3ω) were characterized with the primary goal of measuring the effect of longer laser pulse widths on backlighter source size.

As backlighters, 10- μ m-diam, 300- μ m-long Au wires were used on a CH substrate in a point-projection, end-on geometry. The bremsstrahlung radiation was generated by irradiating the Au wires with either the OMEGA EP short-pulse beam, delivering up to 1000 J in 100 ps (1ω), or six OMEGA short-pulse beams, delivering a total of 250 J in 100 ps (3ω).

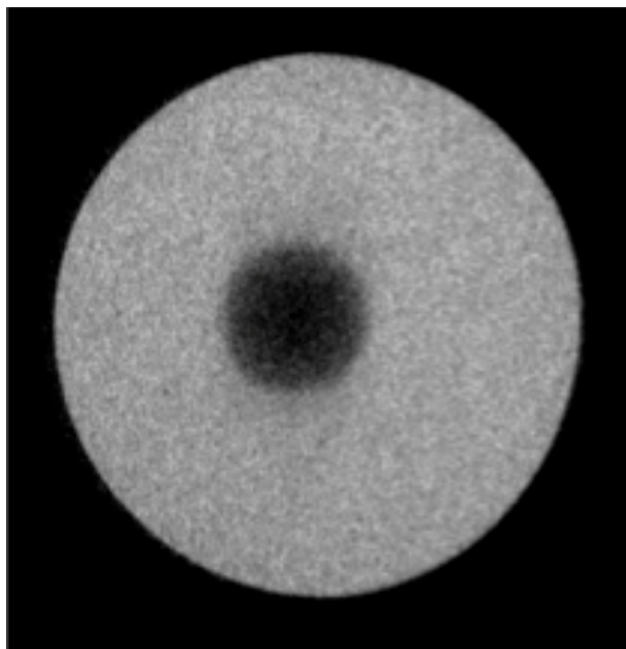
Solid W spheres with diameters of 200 μ m and 250 μ m located 10 mm from the backlighters were used as radiography samples (Figs. 124.123 and 124.124). The Compton radiography snout was used to record the radiographs and measure the backlighter spectra. A combination of high- and low-Z filters was used inside the snout to restrict the backlit photon energies to above 75 keV. A Fuji BAS imaging plate, placed at 400 mm from the backlighter, was used as a detector. An analysis of the radiographs of the W sphere allows one to reconstruct



U1166JR

Figure 124.123

Geometry used in the OMEGA EP target chamber to obtain 2-D radiographs of W spheres at photon energies above 75 keV. The short-pulse beam drives an Au microwire on a low-Z substrate.



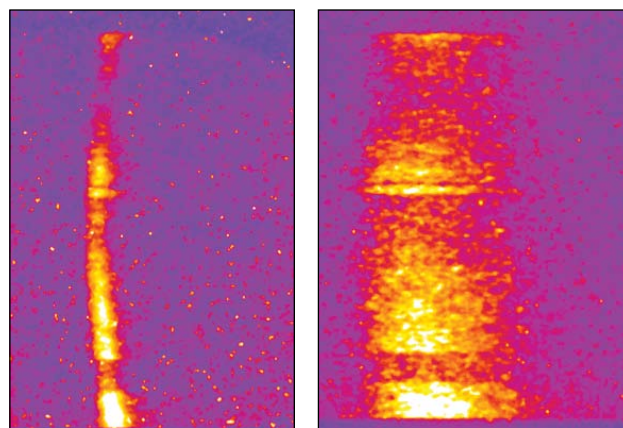
U1167JR

Figure 124.124

Point-projection radiograph of 200- μm -diam W sphere using 10- μm -diam Au microwire and six OMEGA beams (1ω , 40 J/beam/100 ps). The spatial resolution was $\sim 10\ \mu\text{m}$.

the source size of the backlights. No significant difference was found between 10-ps and 100-ps OMEGA EP-produced x-ray backlighter (1ω) and 100-ps OMEGA-produced x-ray

backlighter (3ω). In all cases, source sizes between 10 μm and 12 μm were measured. For the experiments performed in the OMEGA EP target chamber, the ultrafast x-ray streak camera was deployed, which provided durations of the soft x-ray emission from the Au microwires of ~ 12 ps and 80 ps for backlighters produced by 10-ps and 100-ps OMEGA EP pulses, respectively. First results show that the hard x-ray conversion efficiency of the lower-intensity 3ω probe is 10 to 20 \times less than the 1ω probe, as expected (Fig. 124.125). These results pave the way for the implementation of Compton radiography on the NIF, using relatively long pulses and 3ω laser irradiation for the backlighters.



U1168JR

Figure 124.125

An analysis of the streaked images shows pulse durations of the soft x-ray emission from the Au microwires of 12 ps (FWHM), when irradiated by 1 kJ/10-ps (left), and 80 ps, when irradiated by 1 kJ/100-ps (right) OMEGA EP pulses.

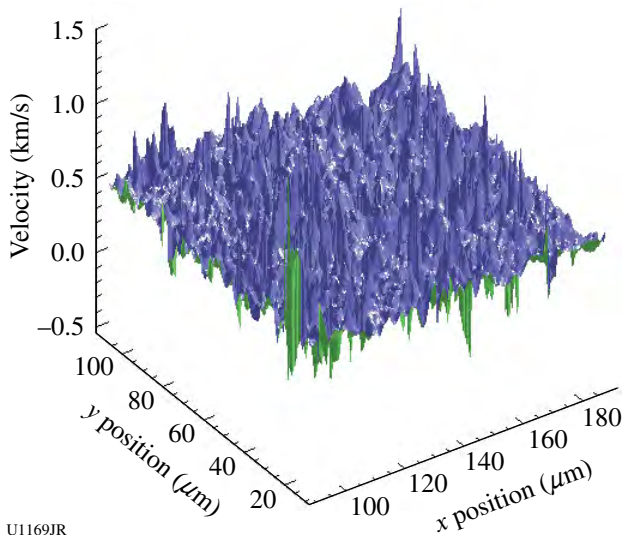
High-Resolution Measurements of Velocity Nonuniformities Created by Microscopic Perturbations in NIF Ablator Materials: Two FY10 CapSeed campaigns took place in January and March. The primary goals of these campaigns were to produce a survey of clean CH samples, to complete the studies of Be ablator samples, and to continue the survey of diamond samples near the melt curve, including the first 2-D velocity measurements of shock fronts propagated through single-crystal diamond samples. An upgrade to the OHRV diagnostic incorporated vacuum boxes around the interferometers to improve the noise performance of the instrument. The experimental campaigns produced preliminary data on CH, although the data collection was impeded by a pair of previously unencountered problems. During the first campaign, inadequate antireflection coatings on many of the targets degraded the data quality to an extent that required that the measurements be repeated. On the second campaign, unconverted light affected the package

more than during previous campaigns, owing to a minor design change. Better quality control on the antireflection coatings solved the first problem, and a new shield design to mitigate the unconverted light issue has already been tested successfully (on a later non-CapSeed campaign). The study of the Be ablators was completed during these campaigns, with the new data confirming results that had been achieved previously. A highlight of the CapSeed-10B campaign was the observation that the shock front of an ~ 500 -GPa shock front in a single-crystal diamond sample (below melt) was highly roughened (Fig. 124.126), equivalent to previous observations on poly-

crystalline diamond, suggesting, as a result, that the processes leading to the roughening are an intrinsic property of diamond.

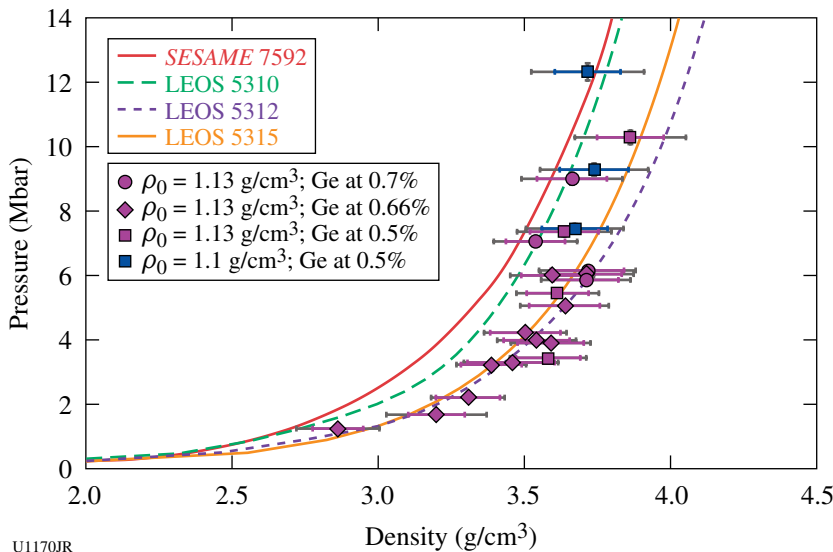
Equation-of-State Measurements of Ge-doped CH: Knowledge of the EOS of NIF ablator materials is important for correctly predicting shock timing in an implosion. Plastic ablators in current NIF capsules are composed of layers of pure and Ge-doped $\text{CH}_{1.3}$. Recent shock Hugoniot measurements on both CH and CH_2 showed good agreement with models between 1 to 10 Mbar, providing confidence in the EOS for undoped plastic. In FY10, new shock Hugoniot measurements were performed on Ge-doped $\text{CH}_{1.3}$. Using impedance matching to a SiO_2 standard, the pressure and density of several samples doped with between 0.5 and 0.7 atm% Ge were measured. These data, supplemented by additional data from LLE shots, are shown in Fig. 124.127. From 1 to 6 Mbar, the data are in good agreement with LEOS 5315 (0.5% Ge) and LEOS 5315 (0.2% Ge)—models currently being used in simulations of NIF implosions—but are less compressible than these models at higher pressures (for comparison, two models for pure CH, *SESAME 7592* and LEOS 5310 are shown). Although it is unclear why there is a tendency toward stiffer behavior above 6 Mbar, the agreement in the 2- to 3-Mbar range corresponding to NIF first shocks justifies the use of these EOS tables in current simulations.

Compton Radiography: The goal of the Compton radiography campaign is to build a novel diagnostic platform for ICF to characterize the shape and density of the fuel in ICF implosions. After the successful demonstration of Compton radiography of implosions in FY09, it was applied to three kinds of implosions in FY10.



U1169JR

Figure 124.126
Two-dimensional velocity fluctuations over a $100 \times 100 \mu\text{m}^2$ region of a ~ 500 -GPa shock front traveling through a single-crystal diamond sample with $\langle 100 \rangle$ orientation.

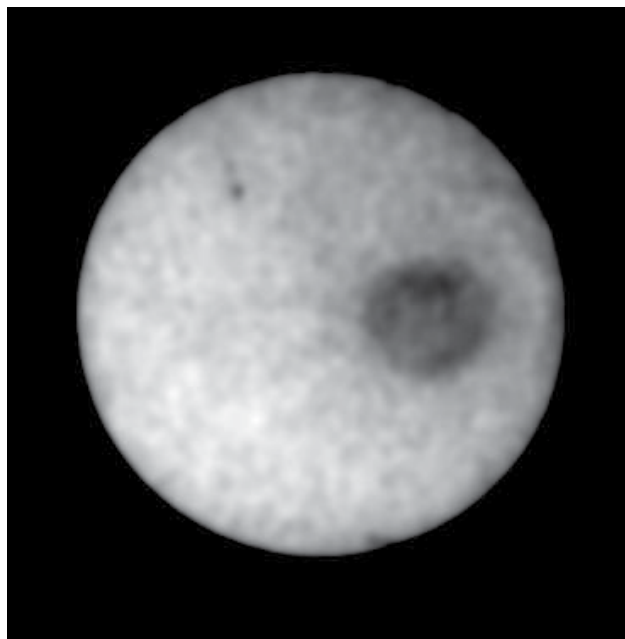


U1170JR

Figure 124.127
Summary of shock-Hugoniot measurements on Ge-doped $\text{CH}_{1.3}$.

In the first experiment, 60 beams of OMEGA were used to directly drive implosions of 40- μm -thick, 870- μm -diam CH capsules filled with 8 atm of D_2 gas, located at OMEGA's target chamber center. A 10- μm -diam, 300- μm -long Au wire was used as a backlighter in a point-projection, end-on geometry 10 mm from the CH shell. The backlighter was driven by the OMEGA EP short-pulse beam, delivering ~ 1 kJ at 10 ps in a 100- μm square spot size.

The time delay between the OMEGA EP short pulse and the OMEGA laser pulses was varied to bracket the peak compression time predicted by *LILAC* 1-D simulations. As an example, Fig. 124.128 shows a radiograph of the imploding CH shell, near peak compression, obtained at a photon energy of ~ 100 keV, where Compton effects dominate the fuel opacity. The radiograph, having about 10-ps and 10- μm temporal and spatial resolution, respectively, shows a limb-darkened shell of about 90- μm diameter.



U1171JR

Figure 124.128

Compton radiograph of an 870- μm -diam CH capsule filled with 8 atm of D_2 , near peak compression. The radiograph has been recorded at an effective photon energy $\langle h\nu \rangle \sim 100$ keV, where Compton effects dominate the fuel opacity. The radiograph shows an object about 90 μm in diameter inside the shadow of the Compton radiography snout collimator.

In a second experiment, at photon energies $\langle h\nu \rangle \sim 70$ keV, radiographs were successfully recorded of 54 OMEGA beam direct-drive implosions of cone-in empty CD shells and 60 OMEGA beam direct-drive implosions of empty CD shells,

without cones. Again, the Au microwire backlighters, with 10-ps and 10- μm temporal and spatial resolution, respectively, were driven by the OMEGA EP short-pulse beam, delivering ~ 750 J at 10 ps in a 100- μm square spot size. The radiographs of cone-in-shell implosions show the shell near peak compression, at a distance of 50 μm and with a diameter of about 50 μm . A third experiment was dedicated to recording Compton radiographs of cryogenic direct-drive implosions. This effort is a work in progress since the experimental setup imposes very tight tolerances on the alignment of the target and backlighter and relies on an improvement of the cryogenic-target alignment system. The CompRad campaigns fully validated a novel diagnostic technique, Compton radiography, which will be extremely useful when implemented on NIF implosions.

Conductivity of D_2 and CH: The thermal-transport properties of D_2 and CH at high densities have important implications for the stability of ICF implosions. The OMEGA laser was used to prepare off-Hugoniot states of these materials using multishock compression. Pressure, density, temperature, and optical properties of the compressed materials were determined by simultaneous VISAR and SOP measurements (Fig. 124.129). D_2 states up to 10 Mbar and 3 g/cc have been achieved at temperatures below 1 eV. CH states up to 8 Mbar and 4.5 g/cc have been achieved at temperatures near 3 eV. A Drude-like model was used to infer band-gap closure and electrical and thermal conductivities from the optical behavior at different states. Preliminary results indicate that D_2 thermal conductivity at such high-density, low-temperature states may be well below theoretical predictions.

Characterization of Hard X-Ray Sensitivity of MCP-Based Gated Imagers: An MCP-based gated x-ray imager is one of the most important diagnostics of the NIC. In FY09, the neutron-induced background of the MCP-based x-ray imagers with a CCD (Kodak KA-16801E) and a photographic-film readout (TMAX 3200) was characterized on OMEGA high-neutron-yield shots.⁴¹ In FY10, a new MCP-based x-ray framing camera, radiation hardened gated x-ray imager (hGXI) was assembled, and its x-ray sensitivity was tested at the Omega Laser Facility.

To optimize experimental setup of NIF implosion experiments, it is crucial to know the absolute sensitivity of the gated x-ray imager for 10- to 20-keV x rays. To test x-ray sensitivity in this energy region, calibration experiments were performed on OMEGA.

A Au-coated spherical target (1.015-mm diameter) was irradiated by 60 laser beams (UV, 500 J/beam, 1-ns square pulse).

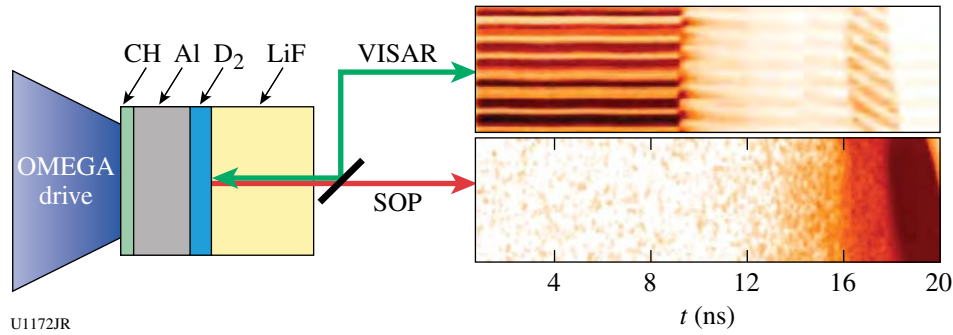


Figure 124.129

A sequence of three OMEGA laser-driven shocks was sent into a thin layer of liquid D_2 trapped between an Al pusher and a LiF window. For the states reached in this experiment, the LiF remained transparent, and the VISAR and SOP records tracked the velocity, reflectance, and optical emission of the D_2 -LiF interface. A dramatic increase in the D_2 reflectance was observed upon the arrival of the third shock at this interface (at ~ 16 ns), corresponding to a large increase in the conductivity. The three shocks coalesce in the LiF at about 18 ns, increasing the LiF temperature and ending its transparency.

The laser intensity on the sphere was $1.2 \times 10^{15} \text{ W/cm}^2$. Absolute x-ray emission spectrum was recorded by x-ray spectrometers (HENWAY and DCS). To compare relative sensitivities, three different gated x-ray imagers (hGXI, XRFC1, XRFC3) were located 1600 mm from the target chamber center. In front of the MCP, a 2.5-mm-thick-polyimide, 0.6-mm-thick-Al filter was used to cut off a low-energy component ($<7 \text{ keV}$) and attenuate the x-ray fluence. Figure 124.130 shows estimated x-ray production on the target and spectrum through the filters. The estimated x-ray flux on the MCP is 2.5 to 5 kW/cm^2 . Figure 124.131 shows images obtained with this experiment. The signal intensity obtained by those cameras (hGXI: OD = 1.97, 193 merg/cm^2 ; XRFC1: 1250 ADU/pix; XRFC3: 1750 ADU/pix) was consistent with our numerical model. Those numbers will be used to benchmark the MCP model.

Plasma Characterization of the LEH Region of Gas-Filled Hohlräume: The objective of this campaign was to characterize the plasma conditions at the laser entrance hole (LEH) of a gas-filled hohlraum using Thomson scattering. This region is of special interest for crossed-beam energy transfer, which is a process that can transfer a large percentage of laser energy between beam cones. The energy transfer is governed by the

electron temperature, plasma-flow velocity, and laser-beam wavelength. Thomson-scattering measurements from the ion feature were made for a series of hohlraums with LEH diameters of 800, 1000, and 1200 μm (Fig. 124.132).

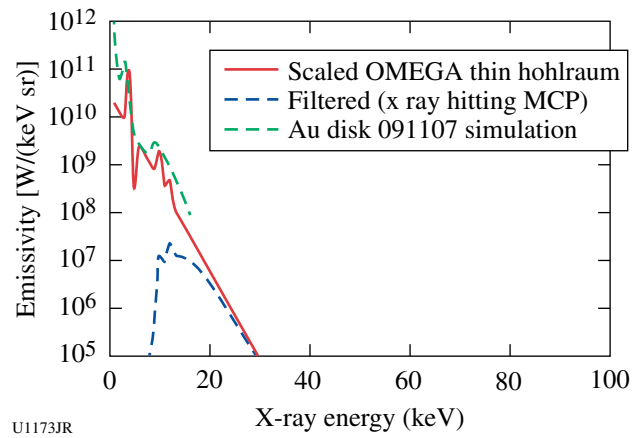


Figure 124.130

X-ray production and spectrum from the Au sphere. X-ray conversion efficiency was estimated by a radiation-hydrodynamic simulation and extrapolating x-ray spectra of previous experiments.

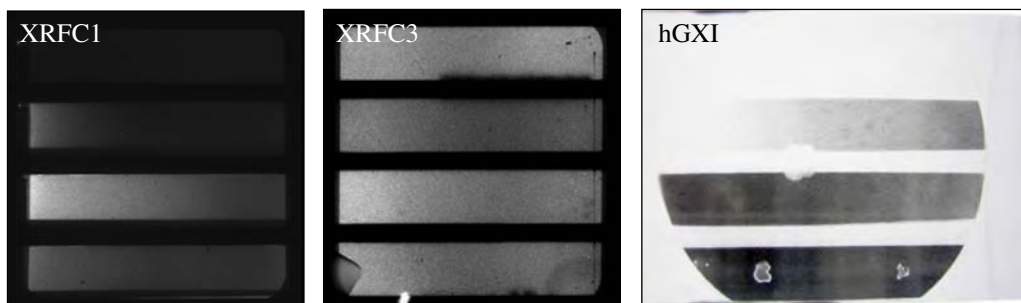


Figure 124.131

Images obtained on a flat-fielding experiment from three different x-ray imaging systems: XRFC1, XRFC3, and hGXI.

U1174JR

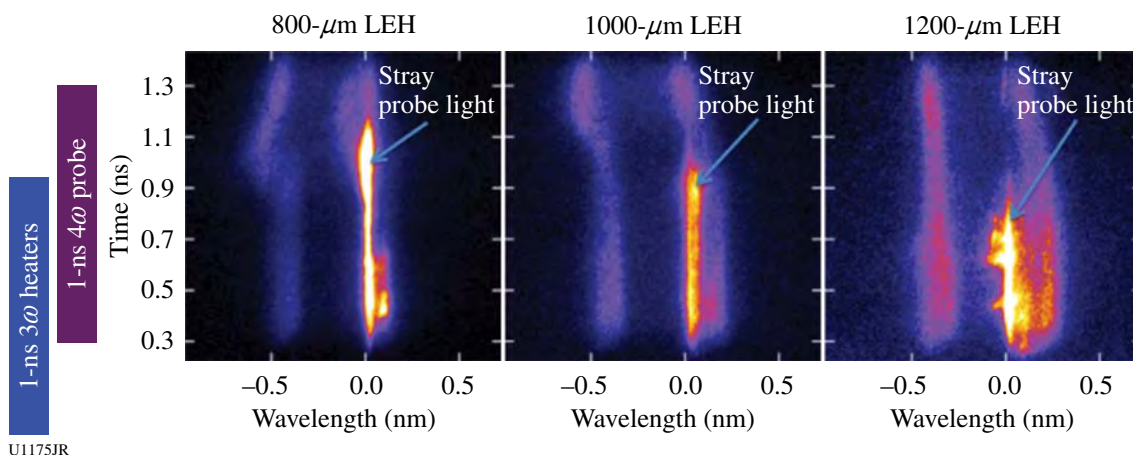


Figure 124.132
Thomson-scattering measurements of the LEH region of a gas-filled hohlraum.

The Thomson-scattering measurements are compared to hydrodynamic simulations using the code *HYDRA* in Fig. 124.133. The plasma-flow velocity is shown for three different locations along the simulation hohlraum axis. Large gradients in this region are predicted by the modeling. The measured electron temperature and flow velocity will be used to benchmark different heat-transport models.

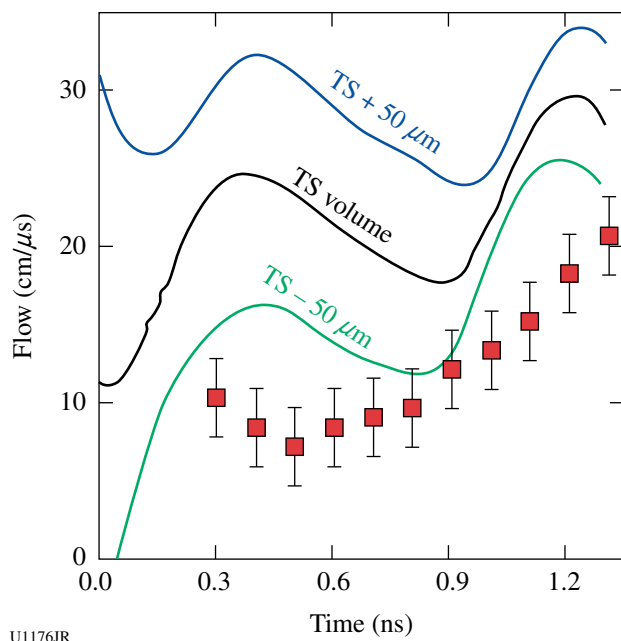


Figure 124.133
The experimental measurements (red squares) are compared to hydrodynamic simulations at different locations outside the LEH.

Validation of the Modeling of Multibeam Scattering Occurring in NIC Targets: A series of experiments was carried out to verify a critical component of the model of backscatter from the multiple NIC beams that indicates that backscatter from the interior of the hohlraum can be amplified by each of the crossing beams it encounters as it exits the laser entrance hole. The model predicts that even with a small gain exponent from each of several crossing beams, the overall gain exponent and amplification produced by all the beams can be quite significant with the additive gain exponents of linear waves. The OMEGA experiments used a 3- μm -thick CH foil target illuminated with 28 heater beams to produce plasma conditions similar to what are found in NIC ignition targets and the Mach-1 flow velocity that is necessary to produce resonant amplification of a seed with the same wavelength as the pumps, as shown in Fig. 124.134.

Experiments were performed in which the transmission of a seed beam (B46) was measured in the case of no pump beam and one and two crossing pump beams (B30, B50); the transmitted power in each case is shown in Fig. 124.135.

Note that a single pump beam produces enhanced transmission relative to the no-pump case near 1.4 ns, as expected from the simulations of the resonance conditions, and a second pump beam produces an even greater increase in the power at a somewhat later time. These results were obtained at three different seed intensities, and similar amplifications were found in each case, consistent with a linear ion-acoustic wave response. Further experiments were carried out to demonstrate the control of energy and power transfer by the relative align-

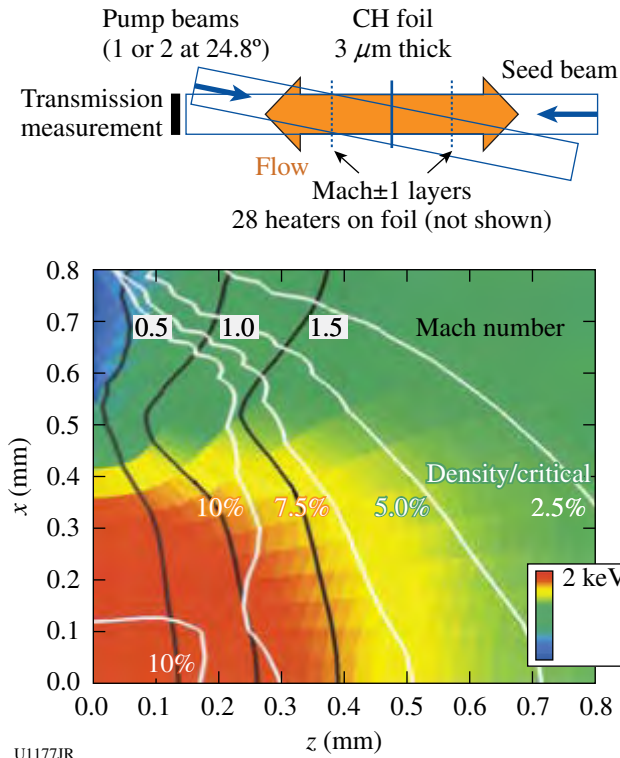


Figure 124.134 The experimental geometry of a foil target used to produce the plasma conditions and Mach-1 flow, shown at 1.4 ns, that is necessary for resonant amplification of a seed of 351-nm light representing the SBS backscatter produced in the interior of the NIC hohlraum.

ment of the polarization vectors of the pump and seed beam, as shown in Fig. 124.136.

To change the polarization, the half-wave plate, or polarization rotator, was installed in B50 and its polarization was rotated through 90° with respect to the seed-beam polarization. The experiments demonstrated greatest amplification when the polarizations were aligned, as determined from the energy-amplification factor measured in three experiments and shown in Fig. 124.136. The greatly reduced amplification when the polarization angle was near 90° demonstrates the importance of relative polarization in controlling this effect. This work has increased confidence in the modeling of multibeam scattering occurring in NIC targets.

Measurements of the Plasma Conductivity by Means of Collective X-Ray Thomson Scattering: The goal of this experiment was to measure the electron-ion collision frequency n_{ei} in isochorically heated Be from the broadening of plasmon signals measured with x-ray Thomson scattering.⁴² The n_{ei} is directly related to the conductivity, which is an important

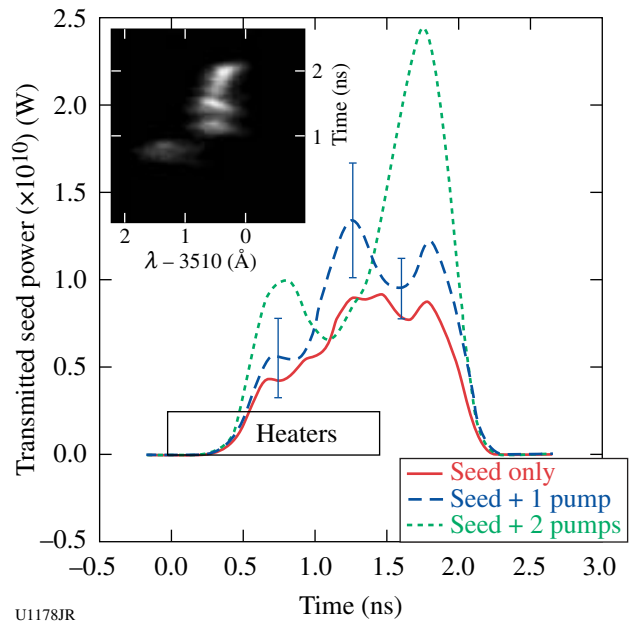


Figure 124.135 Streaked spectrum and transmitted power waveforms of the seed beam transiting the foil target plasma, for the cases of no amplifying pump and one and two amplifying pumps, showing enhancements in the seed power produced by energy transfer from the pumps to the seed beam.

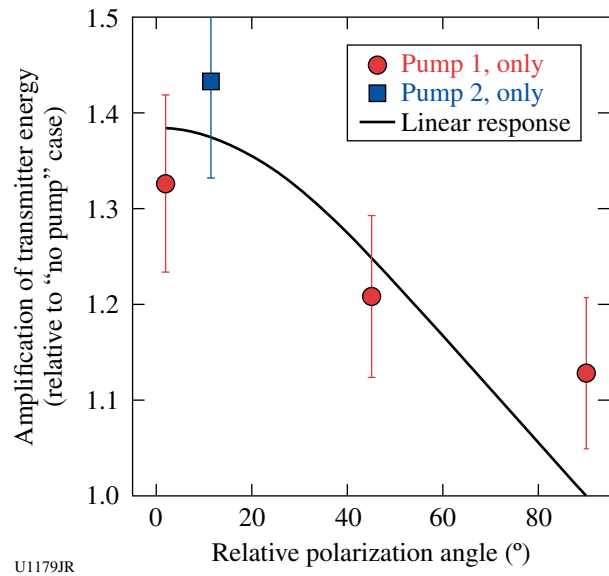


Figure 124.136 Energy-amplification factor produced by a single pump beam as a function of its polarization angle relative to the seed beam.

parameter to correctly model capsule implosions on the NIF; at the same time, it is known only with great uncertainty from theoretical predictions.

On this joint OMEGA–OMEGA EP shot day, the OMEGA EP beam (250 J in 10 ps) was used to isochorically heat a 200- μm Be cube to 35 eV, assuming 20% conversion efficiency into hot electrons ($T_{\text{hot}} \sim 200$ keV), as shown in Fig. 124.137(a). Since it is properly shielded, the Be's front surface, which gets much hotter, is not seen by the scattering experiment. The size of the gold shields was chosen such that plasma moving around the shield and still emitting line radiation would be imaged to the detector well separated from the scattering signal. This is important because gated detectors cannot be used in this short-pulse environment. Fourteen OMEGA beams at 3ω drive irradiated a 12- μm -thick Saran foil to create the Cl Ly_α probe line at 2.96 keV. A pulse width of 200 ps was chosen to achieve an adequate time resolution of the scattering experiment. Radiation–hydrodynamic simulations show that at temperatures of a few 10 eV, the Be cube does not disintegrate within the first 750 ps. The scattering angle was at 30° to ensure a large collectivity parameter $\alpha \sim 1.7$, necessary to observe plasmon broadening caused by collisions.

To measure the scattering spectrum, a new high-efficiency von-Hamos geometry Bragg crystal spectrometer was developed using a cylindrical curved HOPG crystal [see Fig. 124.137(b)]. The signal was recorded on image plates. The CLVH spectrometer was successfully fielded for the first time on this shot day. For cross-calibration, and as source monitors, the Cl K-shell emission was monitored with the GTS and XRS1 spectrometers, operated with image plates, and with SSCA on the OMEGA-only shots.

A total of nine shots were taken, including three joint shots at full energy, two OMEGA EP–only shots, and four OMEGA-only shots. On the low-energy qualification shot of the OMEGA EP beam, the emission from an Au-coated CH sphere was used to measure the timing between the OMEGA and OMEGA EP lasers and to establish a 400-ps delay of the OMEGA probe beams with respect to the OMEGA EP beam. During the day, conditions used to create the x-ray probe were varied. On most of the targets, the Saran foil had a 30- μm

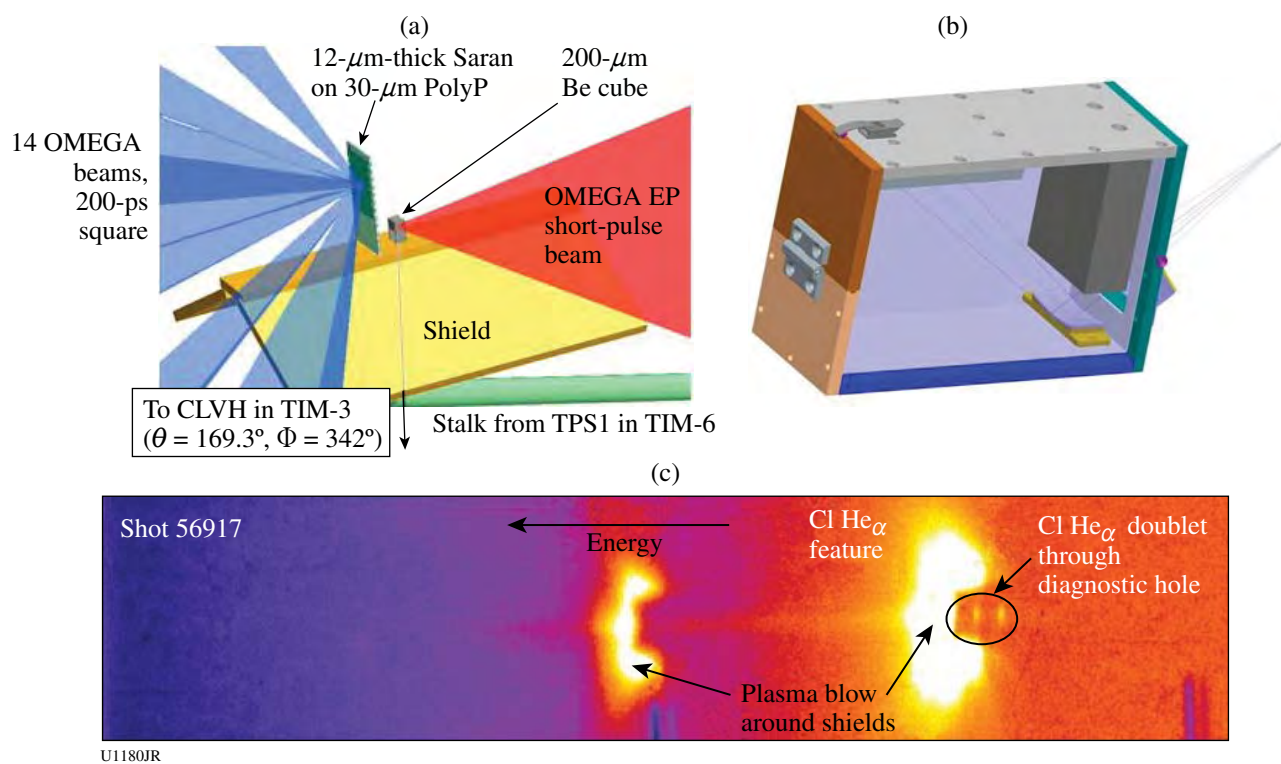


Figure 124.137

(a) Experimental setup to isochorically heat a 200- μm Be cube and characterize the plasma conditions with x-ray Thomson scattering using the Cl Ly_α line at 2.96 keV. (b) The CLVH spectrometer, utilizing a cylindrically curved HOPG crystal in von-Hamos geometry to achieve high detection efficiency, was developed for this campaign and successfully fielded for the first time. (c) Data from CLVH.

polypropylene backing to prevent Cl-containing plasma from moving into the line of sight of the CLVH spectrometer above the Be cube and obscuring the scattering signal. In combination with the low backlighter drive energy (~1 kJ in 0.2 ns compared to ~7.5 kJ in 1 ns for other XRTS platforms), it was not possible to observe a scattering signal. The strongest signal was obtained for a target that had no polypropylene backing, and the OMEGA pulse length was increased to 600 ps, as shown in Fig. 124.137(c).

The most prominent features are due to Cl He α and Cl Ly α emission from plasma that was moving around the shields. In the nondispersive axis the spectrometer was imaging with M = 1, and the extension of the shields of ~±3 mm from the center axis can clearly be seen. X-ray emission from the direction of the Be cube at TCC was imaged to the central axis. Clearly, a weak bremsstrahlung signal and the He α doublet can be identified originating from that direction.

2. High-Energy-Density Experiments

Material Dynamics and Equation of State

Iron equation of state: Ramp compression of Fe to 300 GPa.

The preliminary design for a ramp-compression experiment on Fe up to 300 GPa is shown in the upper right image in Fig. 124.138, along with the ramp laser pulse shape as calculated by a radiation-hydrodynamics code (lower right). The ramped laser pulse shape for the 36 beams focused onto the inner walls of the hohlraum results in a time dependence in the radiation temperature, and subsequently a ramp-compression wave is launched into the stepped Fe sample. The raw VISAR data and the extracted free-surface velocity U_{fs} versus time profiles for 25.5/21.9/38- μ m-thick Fe samples are shown on the left in Fig. 124.138.

The $U_{fs}(t)$ profiles reveal a strong rate dependence associated with the $\alpha \rightarrow \epsilon$ structural phase transformation. The equilibrium pressure for this transformation as measured in

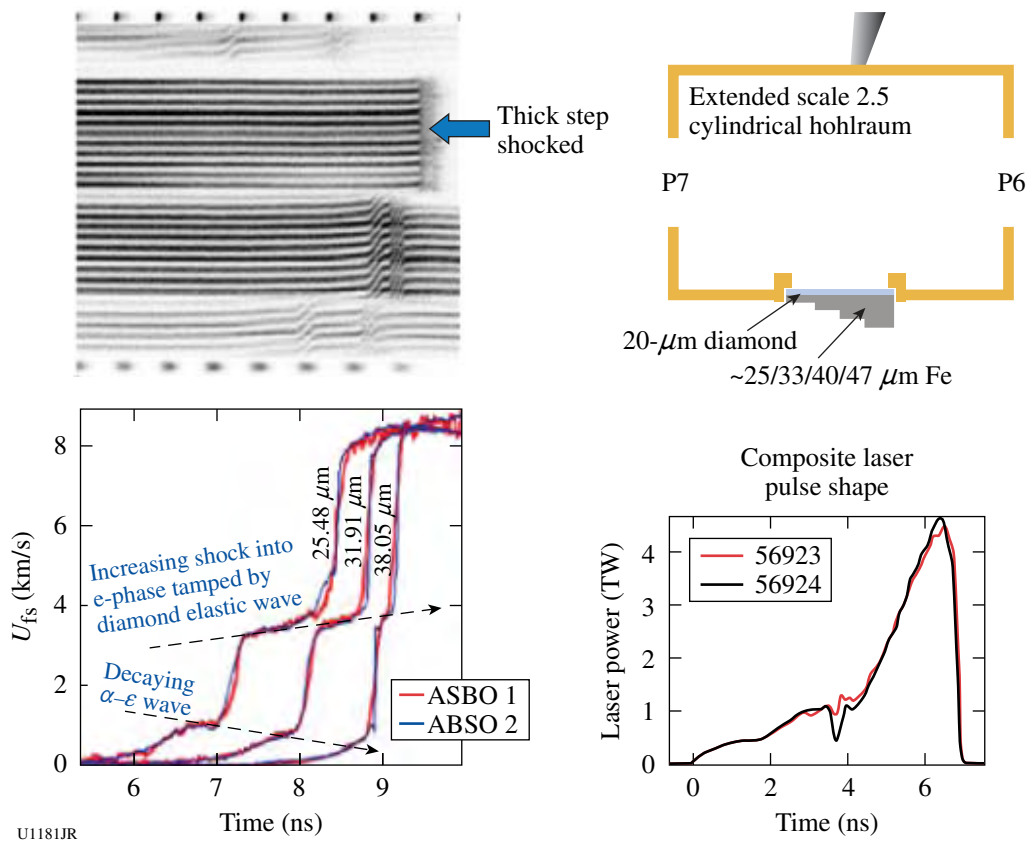


Figure 124.138

Preliminary attempts to ramp compress multisteped Fe samples to a peak stress of ~300 GPa were successful. However, strong time dependence was observed associated with compression across the $\alpha \rightarrow \epsilon$ phase boundary.

shock-compression experiments with millimeter-thick samples is 13 GPa. The measured pressure, however, for the $\alpha \rightarrow \epsilon$ phase transformation in these experiments for thin samples and high strain rates is ~ 20 GPa. This strong time dependence compromises the extraction of stress-density data using the standard ramp-compression analysis techniques. To overcome this difficulty, subsequent experiments have been designed such that a steady initial ~ 70 -GPa shock is launched into the stepped Fe sample followed by subsequent ramp compression to ~ 300 to 400 GPa. This initial shock compresses directly into the ϵ phase by overdriving the $\alpha \rightarrow \epsilon$ phase transformation and therefore avoids the complications associated with the kinetics of this transformation. With the high-pressure ramp-compression platform developed during this period, compression of solid Fe to peak stresses of 300 GPa was demonstrated, and strong time dependence in the structural phase transformations was observed.

Boron ablator for quasi-isentropic compression experiments. The purpose of this campaign was to demonstrate the performance of B as an ablator. By measuring the shock-break times of a stepped reservoir, the ablation pressure created by the ablator material was deduced. The data matched well with the LASNEX simulation with an ablation pressure of 52 Mbar, which will be sufficient to create up to 5-Mbar pressure for the quasi-isentropic drive for the material-strength Rayleigh–Taylor experiments on the NIF.

Tantalum Rayleigh–Taylor experiments. The goal of the ICETaRT experiments is to measure the dynamic properties of solid-state Ta under high pressures (>1 Mbar) and high strain rates (10^6 to 10^8 s $^{-1}$) using the Rayleigh–Taylor (RT) instability. Quasi-isentropic high-pressure conditions were achieved by using a unique plasma piston configuration where

the sample materials stay well below the melting temperature while they are plastically deformed under high pressure, as shown in Fig. 124.139. The growth of the RT instability was measured in V 43 and Ta, and these data were used to compare with predictions using different material strength models. The amount of growth was measured by face-on radiography using laser-driven x-ray backlighters. High-energy backlighter x rays of 20 to 50 keV generated by the OMEGA EP beam were used to probe high-Z materials such as Ta.

The experiment was conducted in the main OMEGA chamber in the joint OMEGA/OMEGA EP shot configuration. A series of successful radiographs were obtained from these experiments. Figure 124.140(a) shows one example of a face-on, 22-keV x-ray radiograph of a rippled sample target of Ta at 60 ns after the initial laser pulse. The driven ripples constitute the circular central part of the image, while the upper portion of the image contains calibration features (stepped filters and knife-edge resolution block) to aid in the extraction of the growth factor. The ripple amplitudes were derived from transmission contrast between the peak and valley of the ripple regions. The initial growth-factor measurements are compared to several strength models in Fig. 124.140(b), including the new Ta multiscale model, which starts with a quantum mechanical interatomic potential and is based on the motion and multiplication of dislocations, 44 and the Preston–Tonks–Wallace (PTW) strength model. 45

Experiments later in the year addressed the effect that grain size (Hall–Petch effect) had on the strength under these high-pressure and high-strain-rate conditions. While there are many measurements of the Hall–Petch effect at ambient conditions, where strength varies as (grain size) $^{-1/2}$ (Ref. 46), no previous theory or experimental measurements under high-

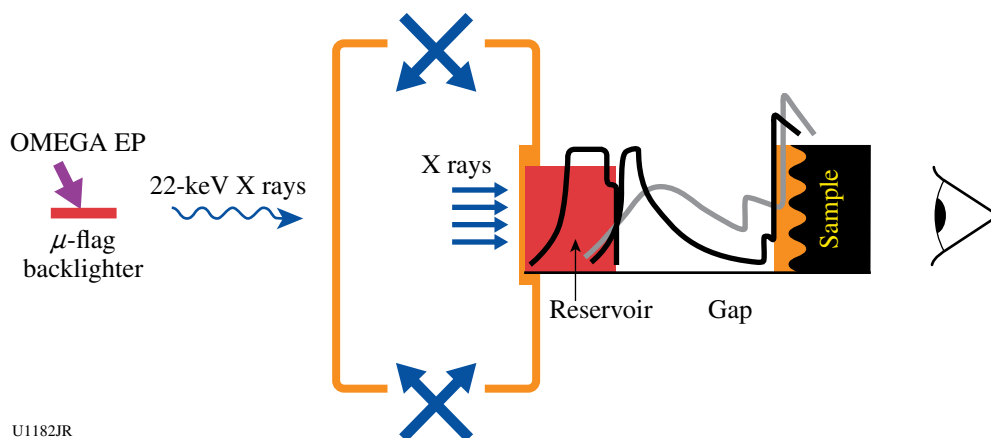


Figure 124.139
ICETaRT experiment configuration for an OMEGA/OMEGA EP joint shot.

U1182JR

pressure, high-strain-rate dynamic conditions existed. Three different types of targets were fabricated, with average grain sizes of 90, 15, and 0.25 μm , as shown in Fig. 124.141(a). The radiography data quality was very high, and useful data were obtained on all shots. The strength is inversely related to the RT growth factor, which is shown as a function of the average grain size in Fig. 124.141(b). Within the error bars of the data, no obvious Hall–Petch effect is observed. The data analysis is still in progress to understand the theoretical and physical implications of these results.

Equation of state of SiO_2 aerogel foam. The study of the EOS of low-density foams allows one to achieve states of matter with high temperatures at lower than solid density. These conditions appeal to a range of interest for high-energy-density science. Foams at different densities can be used in EOS experiments to study points along unloading isentropes, which allows one to study the material EOS of the Hugoniot. Foams also play an important role in laboratory-based astrophysical experiments like supercritical radiative shocks or simulate supernovae remnant formation. All of these uses for foams

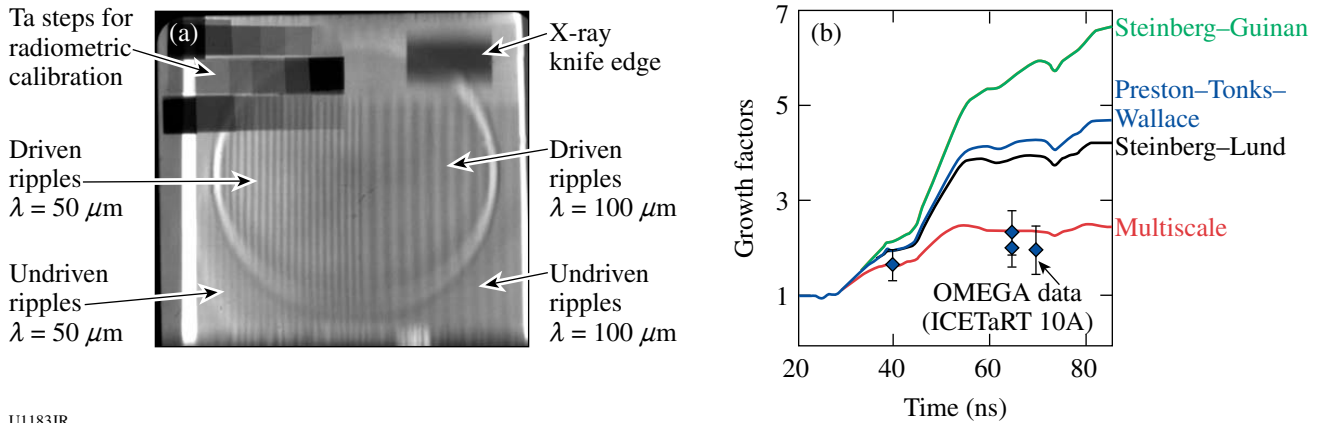


Figure 124.140 (a) Face-on 22-keV x-ray radiograph of a rippled sample target of Ta at 60 ns after the initial laser drive. The driven ripples constitute the center of the image, while the upper portion of the image contains added features (stepped filters and knife-edge resolution block) to aid in the extraction of the growth factor. The ripple amplitudes were derived from transmission contrast between the peak and valley of the ripple regions. (b) Comparison of various model predictions with growth-factor data. The data reach peak pressures between 1.2 and 1.4 Mbar and average strain rates around $2 \times 10^7 \text{ s}^{-1}$.

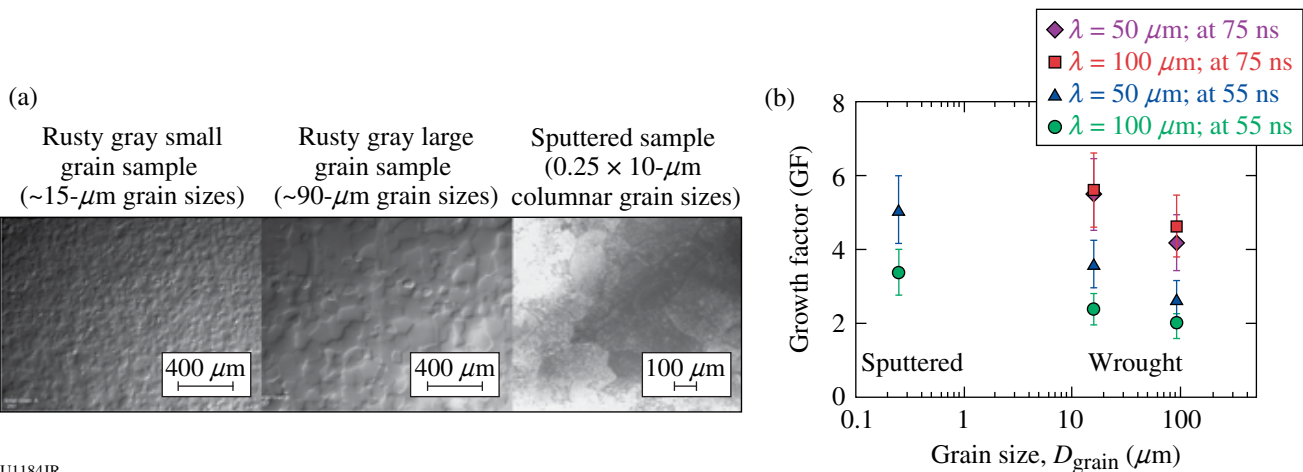


Figure 124.141 (a) SEM and TEM pictures of the different Ta grain-size samples. (b) Growth factor, which is sensitive to material strength, as a function of grain size. No obvious Hall–Petch effect is observed.

require a detailed understanding of the EOS of the foam itself. Unlike other material EOS studies, which vary pressure and temperature, the foam has an adjustable initial density that plays a key role in determining the material's behavior. In these experiments, the foam of interest, in this case 100 mg/cc of SiO₂ aerogel, was placed between two quartz plates, as shown in Fig. 124.142. A decaying shock wave was launched through one of the quartz plates, and the propagation of the reflecting shock front through the quartz and foam was followed by an optical VISAR system. In this system the known Hugoniot of the quartz was used with an impedance-matching model to determine the properties of the foam. Figure 124.143 is a plot of data taken over four shots at a single initial density. The large increase in density at low pressures was caused by the compaction of voids in the material at the higher shock pressures; the compaction of the voids causes heating and the majority of the pressure is due to thermal pressure.

CH-foam shock-breakout experiment. Understanding the behavior of foams in the presence of a strong shock is an ongoing effort at several institutions. A series of experiments were performed to investigate the material properties of a new foam material, dicyclopentadiene (C₁₀H₁₂), at a density of 40 mg/cc. The targets were configured as shown in Fig. 124.144, and were driven by 15 beams with a pulse length of 1 ns. Some targets were driven with a plastic (CH) ablator and an Al piston, while others used a Cu-foam piston (density 0.9 g/cc).

The primary diagnostic was VISAR, including the streaked optical pyrometer (SOP), which was used to measure the shock breakout. Data from these shots are shown in Fig. 124.145. The shock in the foam at full drive (5488 J) showed dramatic

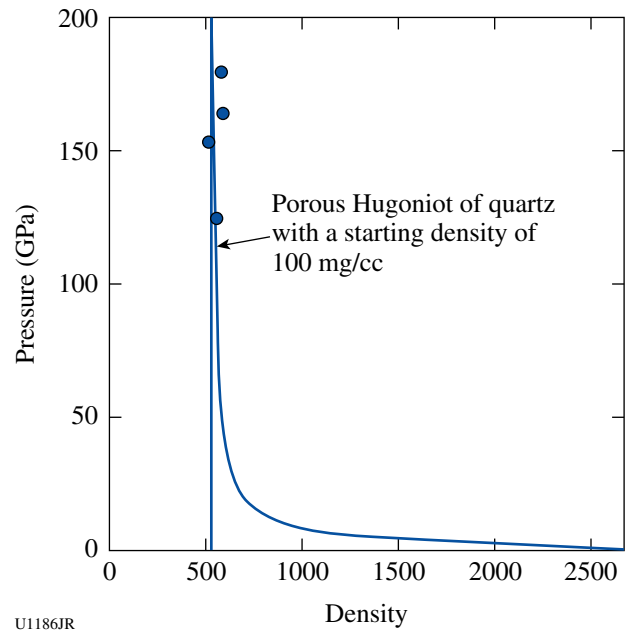


Figure 124.143 Plotting the pressure–density points compared to a model prediction of the shock Hugoniot of 100 mg/cc of SiO₂ aerogel.

evidence of preheat (presumed to be caused by drive x rays preheating the foam), although the shock in the quartz was measurable as may be seen in Fig. 124.145(a). With significantly reduced drive (3057 J), shock breakout from the foam was observed. See Fig. 124.145(b). This experimental series has been put on hold while the mechanical properties of the material for fabricating targets are being evaluated. These were the first targets fabricated from DCPD, and the material appears to have less rigidity than expected.

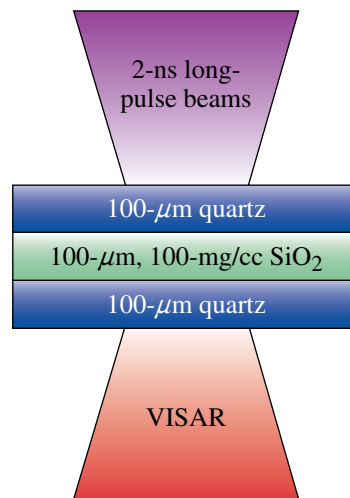
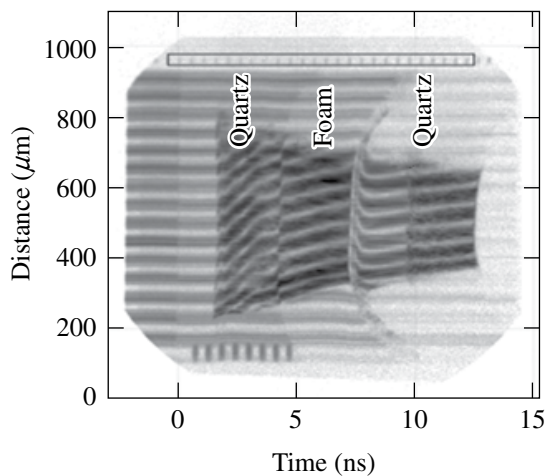
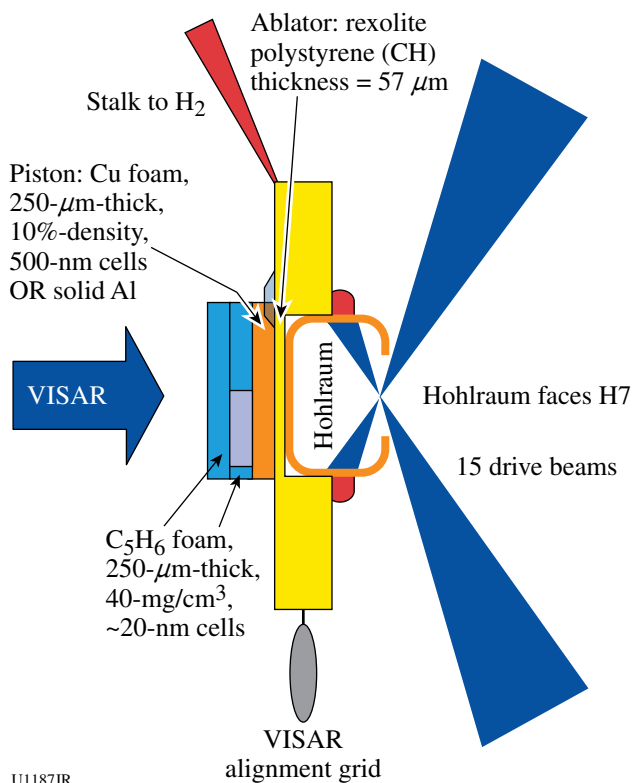


Figure 124.142 Target geometry and example data. The VISAR trace shown follows the shock wave through the quartz and 100 mg/cc of SiO₂ aerogel.

U1185JR

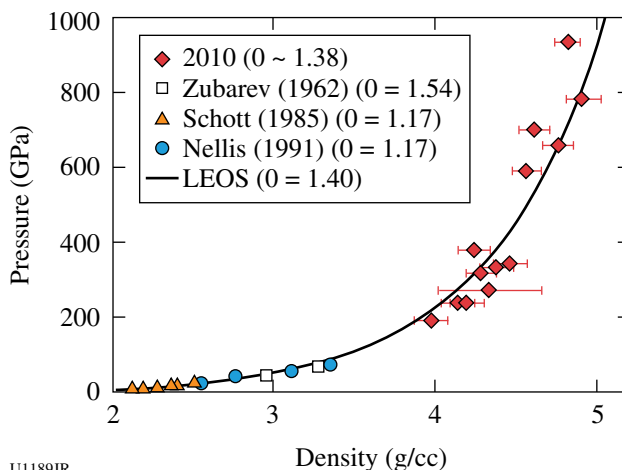


U1187JR
 Figure 124.144
 Target, laser, and diagnostic configuration for the CH-foam shock-breakout campaign.

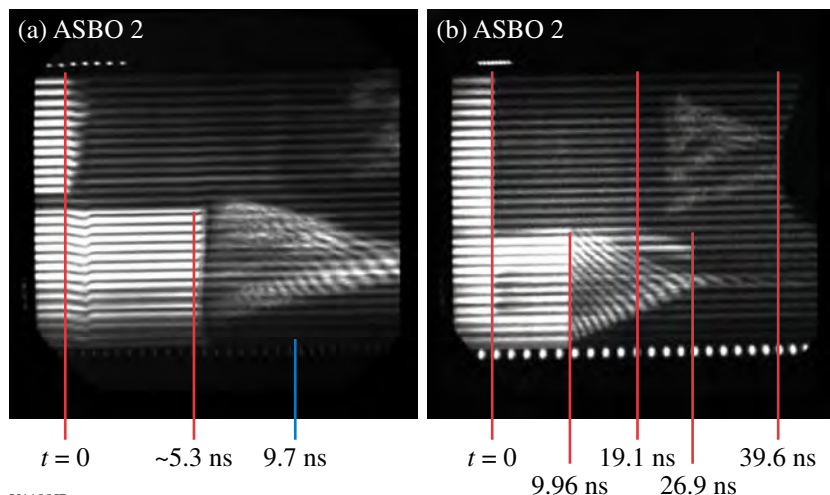
CO₂ Hugoniot measurements to 950 GPa. CO₂ EOS, which is found in the core of giant planets, is of wide scientific interest. It is a mixture that challenges models to accurately predict. Prior experimental data were limited to below 100 GPa. Experimental measurement of the CO₂ Hugoniot was extended up to 950 GPa by launching shocks into CO₂ samples precompressed

in diamond anvil cells to ~0.5 GPa (see Fig. 124.146). VISAR and SOP measurements of the CO₂ shock front in comparison to concomitant measurements in quartz were used to infer pressure, density, reflectance, and temperature of shocked CO₂. CO₂-shock reflectance saturated at about 35% above 350 GPa, and the pressure, density, and temperature results are consistent with the theoretical LEOS table.

Melt and resolidification in Sn. This was the first set of experiments that investigated the use of velocimetry for exploring the melt line of Sn. The strategy was to develop a drive to shock-melt the tin and then ramp-compress it across the liquid-

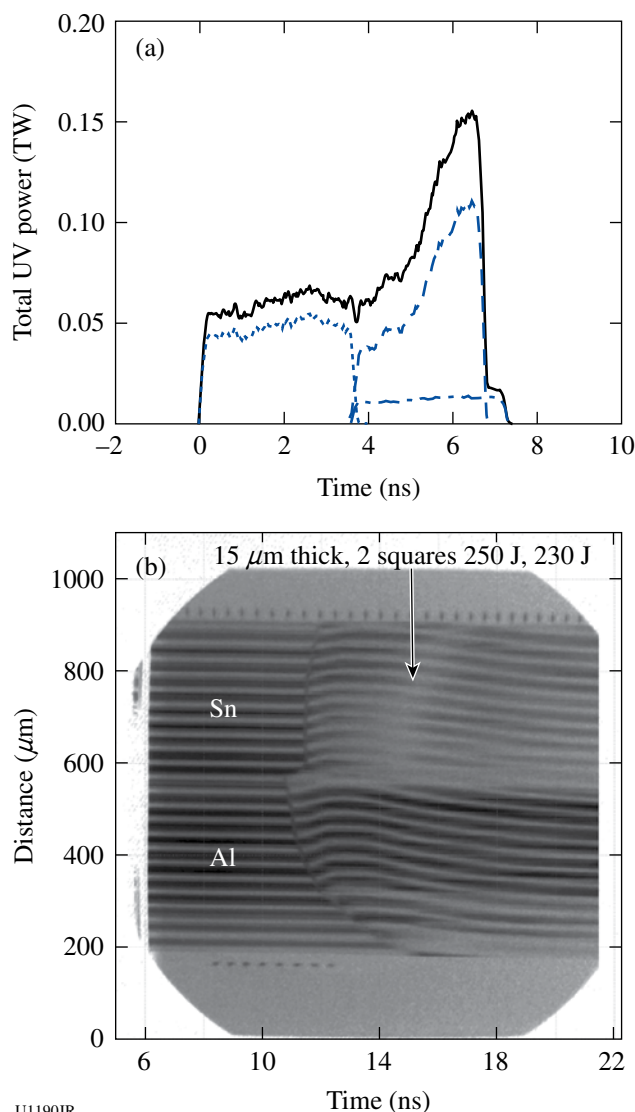


U1189JR
 Figure 124.146
 Previous experimental measurements of the CO₂ Hugoniot (open data points) reached 80 GPa. In FY10, the OMEGA laser was used to extend the range to 200 to 950 GPa (solid diamonds). The CO₂ shock pressure and density were inferred by shock-velocity measurements impedance matched to a SiO₂ standard, using the Hicks (2005) SiO₂ equation of state.⁴⁷



U1188JR
 Figure 124.145
 (a) VISAR signal from the target shown in Fig. 124.144, driven with 5488 J. No shock breakout is visible in the top of the image, and the reflected signal appears to come only from the back surface of the quartz anvil. (b) VISAR signal from a similar target driven with 3057 J. The shock breaks out of the C₁₀H₁₂ at about 19.1 ns and is visible in the quartz anvil before breaking out at 39.6 ns.

solid phase boundary. While analysis of the data is ongoing, a number of important observations were made (Fig. 124.147). It was verified that the sample design was feasible, data were produced across a wide range of shock pressures (20 to 200 GPa), and a reference material (Al) was used on each shot. Initial designs, based on extrapolation of diamond pressure-intensity measurements made at high pressures, proved to overestimate the achieved pressure. It was possible to generate the necessary data by utilizing the calibrant. This data will serve as the basis for future designs. Lastly, an interesting change in the reflectivity of the tin was observed during the apparent release portion of the loading. This remains to be explained.



U1190JR
Figure 124.147

(a) Composite shock-ramp pulse shape used to generate first attempt at compression-driven resolidification in Sn. (b) VISAR recording showing late-time reflectivity changes (arrow) that occur only in the Sn.

High-Temperature Plasma Opacity: Opacity experiments in FY10 had three main goals. The first addressed physics questions from the very successful 2009 Ti opacity shots, where the observed Ti continuum opacity did not match code predictions, although spectral absorption lines from charge states consistent with ~ 120 -eV LTE sample temperatures matched the code quite well. A modification in the configuration was made using thinner Ti samples, and new data were successfully taken on a half-day in January. A follow-up full-day experiment is scheduled for FY11.

The second goal was to better characterize the x-ray framing cameras (XRFC's) used on the experiments. NIF data from November 2009 revealed that the gain along with the gain profile of a microchannel-plate detector strip was sensitive to the relative delays between individual strips, as a result of electromagnetic crosstalk in the pulser input lines and the detector strips themselves. This effect produced $\sim 3\times$ differences in gain between strips, $\sim 2\times$ changes in the relative point-to-point gain in a single strip (compared to a synchronized-strip baseline case), and 30% to 50% changes in gain from one edge of a strip to the other (transverse to the pulse-propagation direction). The latter effect would impair the analysis of space-resolved gated absorption spectra if a similar effect occurred on the cameras used for opacity experiments. Data were taken for three framing cameras on OMEGA on 8 July, measuring these effects as a function of interstrip delay and gated detector pulse width. While the XRFC data showed $\sim 2\times$ differences in gain between strips, and significant (50% to 100%) changes in point-to-point relative gain along a strip, no significant gain variation across the strip was measured. Therefore, the performance of the camera was not a factor in the discrepancy in the Ti data.

The third goal was to compare short-pulse-heated opacity measurements with similar long-pulse conditions (Ti, $T \approx 100$ to 150 eV, density ~ 0.1 to 1.0 g/cm³). In principle, much higher temperatures are possible with short-pulse-heated materials, but questions exist as to whether LTE conditions can be maintained. In these experiments, the OMEGA EP sidelighter beam was operated at 250- to 800-J, 100-ps pulse width and broad focus to heat an opacity sample at intensities between 10^{15} to 10^{17} W/cm². The OMEGA EP backlighter beam was delayed by 100 to 500 ps and then operated at 800 to 1000 J, 10 ps to drive a broadband 3- to 6-keV backlighter. The backlighter x rays probed the hot, expanded opacity sample. A separate line of sight allows one to take space- and energy-resolved sample emission spectra in a different spectral band. The experiment used the two opacity spectrometers that were transferred to OMEGA EP from the 60-beam OMEGA chamber and fielded

with “rotating SPCA” frames and time-integrated image-plate detectors. Shots in February demonstrated an opacity-quality broadband backlighter using a Zn microdot on an Al substrate, with data shown in Fig. 124.148. (Subsequent shots using a CH substrate failed as a result of very high instrument backgrounds but may have reflected a change in the pointing or laser conditions.) Further optimization of the backlighter will take place in FY11. In parallel, space-resolved broadband emission spectra from 10 to 50 Å were obtained from a CH/Ti/CH/Al exploding-foil sample (driven by the OMEGA EP sidelighter at $\sim 10^{16}$ to 10^{17} W/cm²). Al-, C-, and O-line features have been identified from a shot at lower intensity, along with a broad

continuum (see Fig. 124.149). Bright Ti emission was seen at higher intensity. Ti absorption lines were not observed; FY11 shots will assess whether this is caused by cool Ti plasma conditions or perhaps mistiming of the OMEGA EP backlighter and sidelighter. The source of the O lines is being investigated.

Hydrodynamics

Kelvin–Helmholtz instability experiments. A Kelvin–Helmholtz (KH) growth experiment was performed using a platform successfully developed in earlier OMEGA experiments.^{48–50} The main goal of the most recent campaign was to measure turbulent mixing on an interface between CRF foam and I-doped plastic. Figure 124.150 shows a target schematic that consists of a plastic ablator and a shock tube. In the shock tube, the interface between low-density foam and high-density plastic had pre-imposed sinusoidal modulation at a wavelength of 400 μm and an amplitude of 30 μm. The central part of the plastic target contained a layer of I-doped CH to increase a contrast to 5-keV backlighter x rays. The ablator of the target was directly driven with laser light, producing a strong shock that propagated through the target. The shock produced a velocity gradient at the interface between the foam and plastic. This velocity difference between the two materials resulted in the KH growth of the surface modulations. The density of foam was varied from 50 mg/cc to 100 and 200 mg/cm³. Turbulent mixing between a foam and plastic materials was expected to grow from short-scale surface finish modulations (with rms amplitude of 100 nm) on the interface between the two materials.

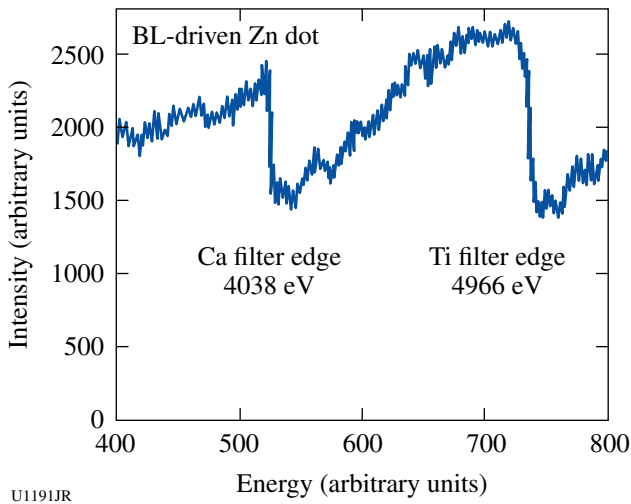


Figure 124.148
Initial Zn microdot broadband backlighter spectra from ~3- to 6-keV photon energy.

Figure 124.151 shows experimental data. The shock travelled from left to right, so the modulations on the left side of

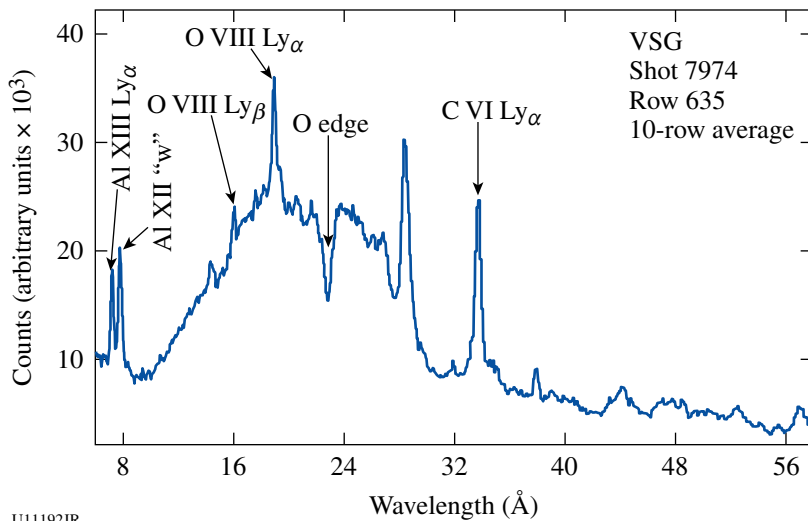
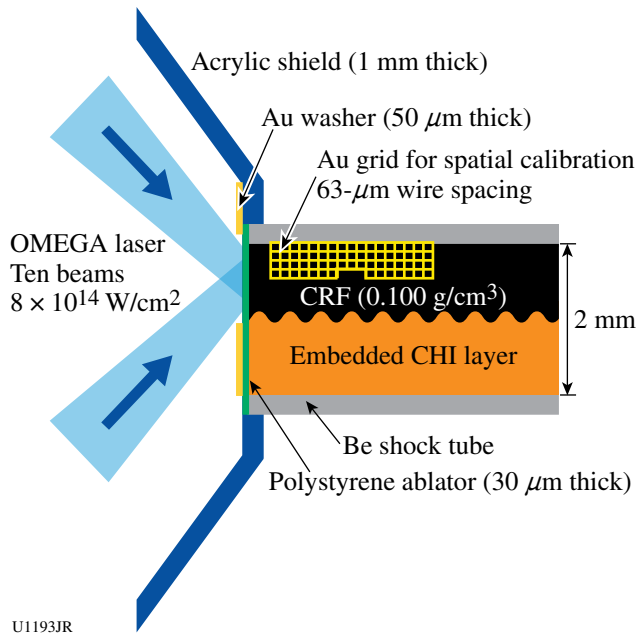
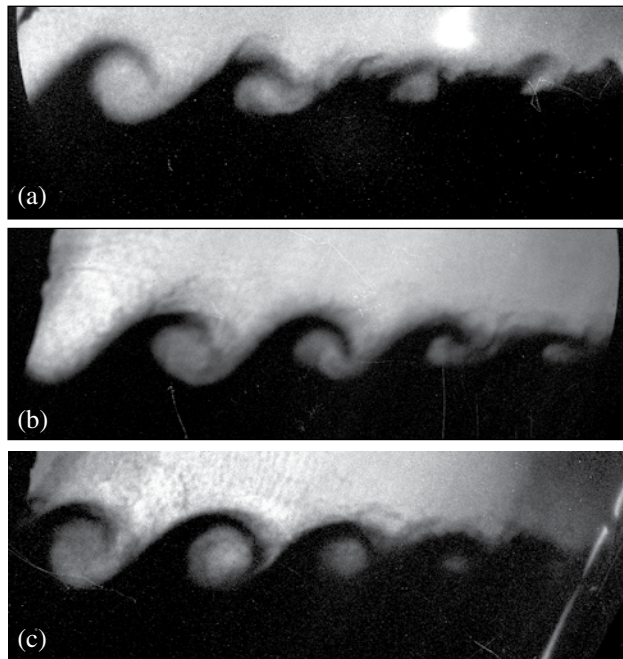


Figure 124.149
X-ray emission spectrum from the interior of the laser-driven CH/Ti/CH/Al foil, with initial line identifications.



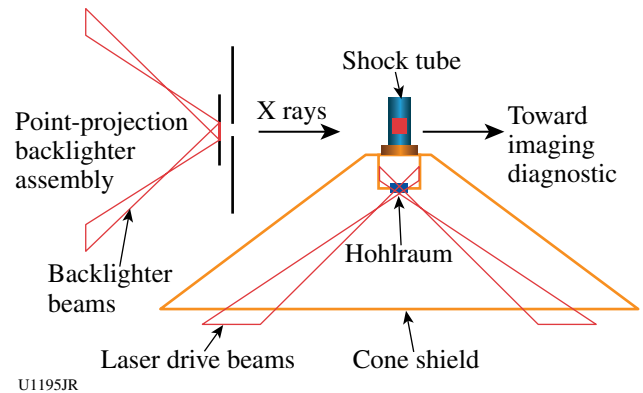
U1193JR
 Figure 124.150
 Experimental configuration. The interface between lower-density CRF foam and higher-density I-doped plastic had a pre-imposed 2-D modulation with 400- μm wavelength. Three densities of CRF foam were used: 50, 100, and 200 mg/cm^3 .



U1194JR
 Figure 124.151
 X-ray radiographs of KH growth were taken with (a) 50 mg/cc of CRF foam at 47 ns, (b) 100 mg/cc of CRF foam at 75 ns, and (c) 200 mg/cc of CRF foam at 117 ns. The vortices on the right-hand side of the images experienced more KH growth than those on the left-hand side. Short-scale mix can be seen as "hair-like" structures on top of the vortices from pre-imposed modulations.

the image had more time to grow than the modulations on the right side. The light color in the image corresponded to foam material, while the dark color corresponded to plastic. The initial sinusoidal 400- μm -wavelength modulation developed into the vortices. In addition, the growth of short-scale modulations caused by surface imperfections developed "hair-like" nonuniformities. These nonuniformities represent turbulent mixing of two materials, as expected since the Reynolds number was high in this experiment, $\text{Re} \sim 1 \times 10^6$. The Reynolds numbers in hydrodynamic simulations, used to model the experiments, typically do not exceed $\sim 1 \times 10^3$ because of the finite spatial resolution of spatial grids. Therefore the simulations themselves are not expected to correctly predict evolution of short-scale mixing. These experimental data are used to develop and validate mix models that are based on post-processing of hydrodynamic simulations, currently in progress.

High-Mach-number Cu-foam jet experiments. Some of the most challenging experiments to model for hydrodynamics codes are jet-evolution experiments. Several aspects of hydrodynamics-code predictions can be validated by these experiments, including physics of shocks, material flows, and equation-of-state physics. The current experiment studied evolution of a Cu-foam jet into a low-density plastic foam. Figure 124.152 shows the experimental setup. A high-Mach-number jet was generated in a shock tube, driven by x rays from a hohlraum irradiated by 12 OMEGA drive beams. A point-projection backlighter x-ray source, driven by three beams, generated $\sim 4.3\text{-keV}$ x rays that illuminated the jet at time intervals ranging from 15 to 35 ns after the beginning of



U1195JR
 Figure 124.152
 Experimental configuration of the high-Mach-number Cu-foam jet campaign. The jet was generated in a shock tube, driven by hohlraum x rays. X rays, generated by a point-projection backlighter, radiographed the jet at various times, from 15 to 35 ns after the beginning of the drive.

the drive. The cone shield prevented x rays generated in the hohlraum from reaching the imaging diagnostic, which would contribute to background on the data.

Figure 124.153 shows an example of a radiograph taken at 30 ns of the jet. In the image, a mushroom-like jet of Cu-foam material (darker color) penetrates the plastic foam (lighter color). The height, width, and position of the jet with respect to the grid (shown on the right side of the image) are some of the measurements used to compare with code predictions. In addition, the shock position and compression of the plastic foam will also be used to test various aspects of hydrodynamics codes. Preliminary simulations of jet evolution and shock propagation are close to experimental data, with much better agreement than in previous campaigns, primarily because of well-fabricated Cu foams.

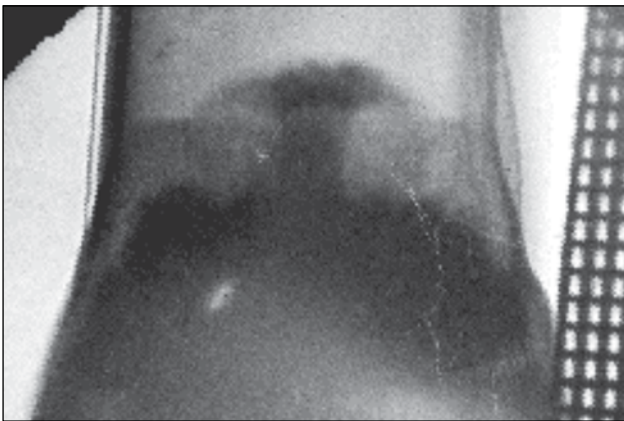


Figure 124.153
X-ray radiograph of a Cu-foam jet driven into a plastic foam with a density of 0.1 g/cc. The image was taken at ~30 ns after the beginning of the drive. The jet structure is clearly visible. The height, width, and position of the jet, as well as the shock position and compression of the plastic foam, will be used to test various aspects of hydrocodes.

X-Ray Source Development and Application: Bright, tunable x-ray sources are necessary for radiography applications, radiation-effects experiments, and use as backlighters for high-energy-density experiments. LLNL's x-ray source development campaign had one full day and two half-days of shots (22 shots total) during which two types of multi-keV x-ray sources were shot. These experiments were performed in collaboration with scientists from CEA (France). Two half-days (XRSD-10A, XRSD-10C) were used to investigate the performance of Ti foil targets confined by cylinders of ultralow-density SiO₂ aerogel material. A photo of one of the targets is shown in Fig. 124.154(a) (with bundled laser beams shown

schematically), and an x-ray image of the Ti K-shell emission (energies > 4.5 keV) from the target in shot 56933 is shown in Fig. 124.154(b). Target yields were studied as a function of the aerogel density, the aerogel volume, the foil thickness, the laser intensity, and the laser pulse length. Data are consistent with CEA predictions of an optimal aerogel density for maximal Ti K-shell radiation production.

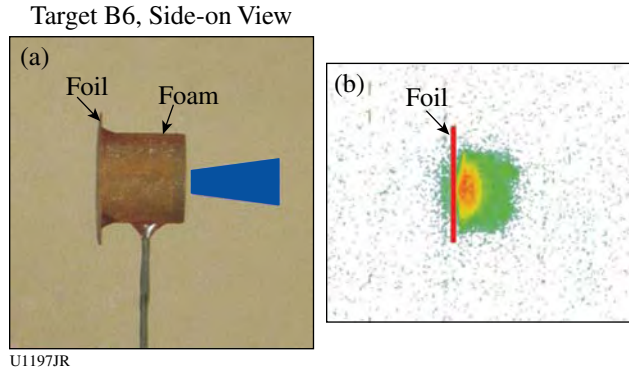


Figure 124.154
(a) A hybrid foam-foil target that was shot in the LLNL-CEA x-ray source development experiments. Five or six OMEGA laser beams entered the target's foam cylinder from the left and created x rays from the Ti foil at the right. (b) An x-ray framing camera image from shot 56933 of a hybrid foam-foil target (2 mg/cm³ of foam, 3-μm-thick foil).

Dedicated investigations of x-ray emission from noble gases were also carried out (XRSD-10B, XRSD-10C). During these experiments, the scaling of x-ray yield from gas-filled Be cans was studied as a function of gas-fill pressure and gas mixture. Pure Ar, Kr, and Xe targets were shot, as were mixed Ar:Xe targets; for all targets, fill pressures ranged from 1.0 to 1.5 atm. Figure 124.155 shows the measured spectra from five Xe-filled targets shot on the two dedicated days. During the XRSD-10B series of shots, the x-ray environments produced by the targets were also applied to investigate changes in the material properties of, and surface interactions on, sets of samples in response to x-ray loading. Samples included radiation-hardened-by-design mirrors and photovoltaic solar cells. An example of one specimen is shown in Fig. 124.155. Changes in reflectivity and surface profiles of the mirrors, and changes in the performance of the solar cells were characterized for exposures of several different fluences and spectral contents, which greatly expands the knowledge of the x-ray survivability of these materials.

Diagnostic Technique Development

Development of VISAR with a target-mounted turning mirror. It is known that measurement of the shock speed inside a quartz (Qz) window is a reliable way to understand the hohl-

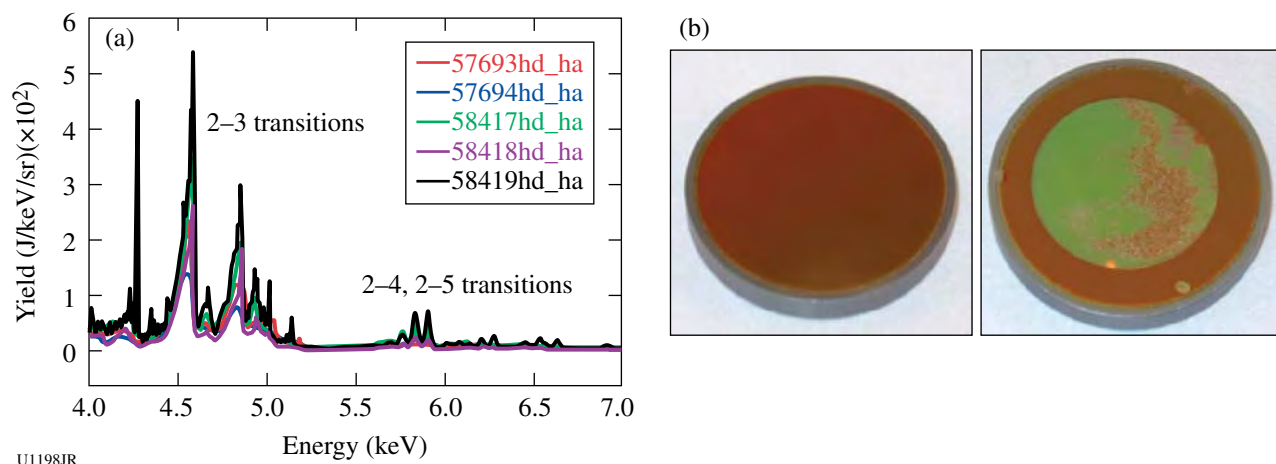


Figure 124.155

(a) The measured spectra from a series of Xe-filled targets shot during the x-ray source development and application campaigns in FY10. The x rays from the targets were used to study the response of radiation-hardened-by-design mirrors and photovoltaic solar cells. (b) Before and after images of a mirror specimen that was exposed to the unfiltered output of an Ar gas target on shot 57692.

raum drives.⁵¹ One of the NIF experiments (Rad-Transport) will apply this technique to characterize the drive inside a half-hohlraum. Because the VISAR is located along the equator on the NIF, characterization of the drive at the end of a half-hohlraum requires the use of a target-mounted turning mirror. A potential failure mode was the loss of reflectivity from the turning as a result of M-band x-ray preheat. An experiment was designed to empirically test the turning mirror's performance under an equivalent heat loading of the NIF radiation-transport experiment. A new configuration was designed that carefully followed constraints from the simulations and experiments, as shown in Fig. 124.156(a). Two types of mirrors were tested: Si and nanodiamond mirrors. The experiments were highly successful—no mirror blanking was observed in Fig. 124.156(b). One example of the VISAR image is shown in Fig. 124.156(c). From this data, the peak shock velocity was measured up to 50 km/s, or ~ 50 -Mbar pressure in quartz. This is the highest-pressure shock measured inside quartz to date. Both mirror types worked well and delivered high-quality meaningful data. From this data, it is expected that the mirrors will survive until the thinnest ablator section burns through and that the NIF experiment will deliver meaningful measurements.

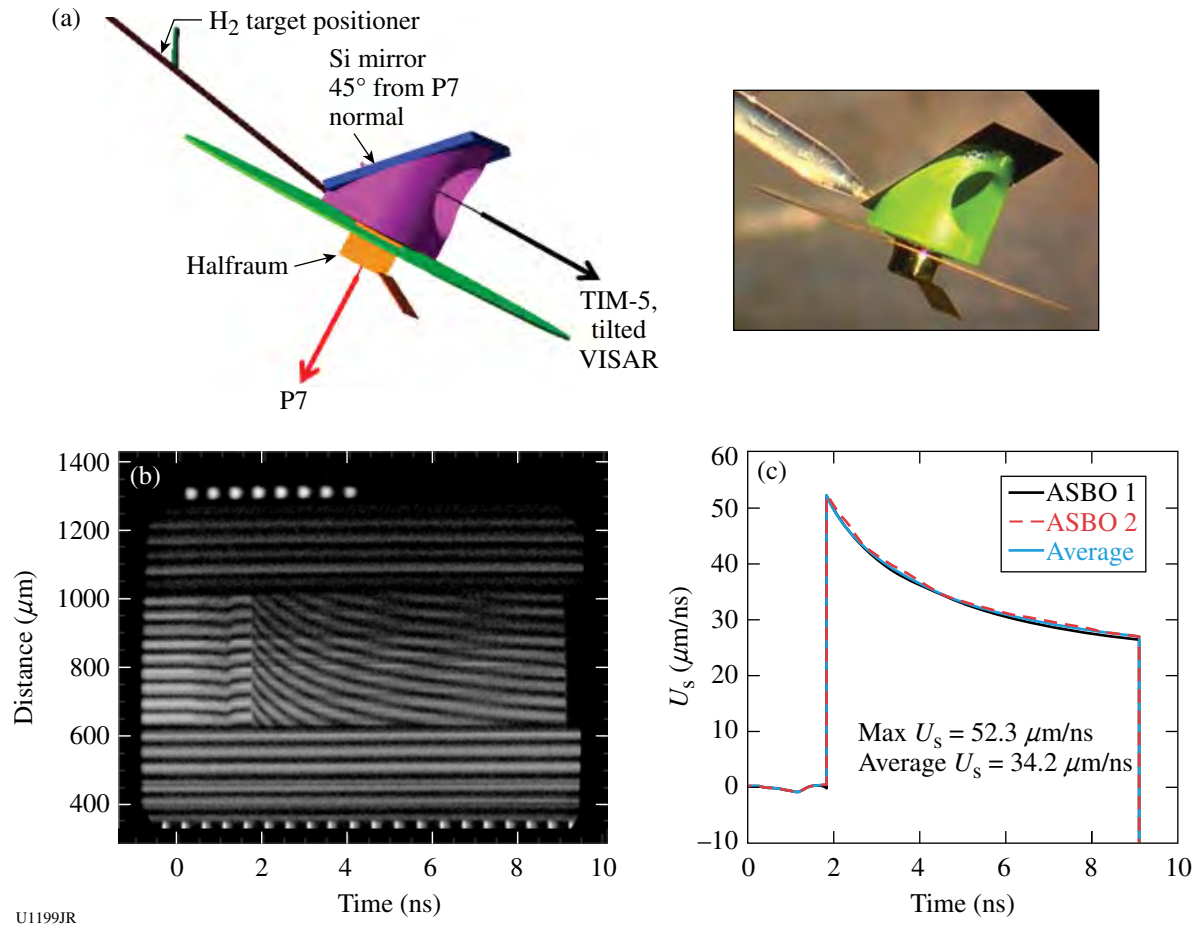
Beryllium x-ray Thomson scattering. The objective of the BeXRTS-10 campaign was to isochorically heat Be utilizing short-pulse-generated hot electrons and to measure the plasma temperature by means of noncollective x-ray Thomson scattering with high time resolution. Two OMEGA EP short-pulse beams were used with the backlighter beam heating a 250- μ m Be cube and the sidelighter beam creating a Zn K_{α} x-ray probe

at 8.6 keV. On this shot day, the sidelighter was delayed by 200 ps with an accuracy of ~ 25 ps, as observed by an ultrafast x-ray streak camera.

Zinc K_{α} x rays were scattered off the Be and collected by the Zinc von Hamos (ZVH) spectrometer, which uses a curved, highly efficient HOPG Bragg crystal for energy dispersion and focusing in the nondispersive direction. The spectrometer, specifically developed for the K_{α} scattering project, had to be rebuilt to meet new safety standards, and the new instrument was successfully fielded on this shot day.

A total of six shots were conducted including two low-energy activation shots. The latter ones were used to measure a high-resolution source spectrum and to record background signal levels. The facility had made a big effort to establish the beam timing, i.e., the delay between the backlighter and the sidelighter beams, on previous shot days. The single-photon-counting (SPC) camera was successfully used to observe the Zn K-shell source spectrum.

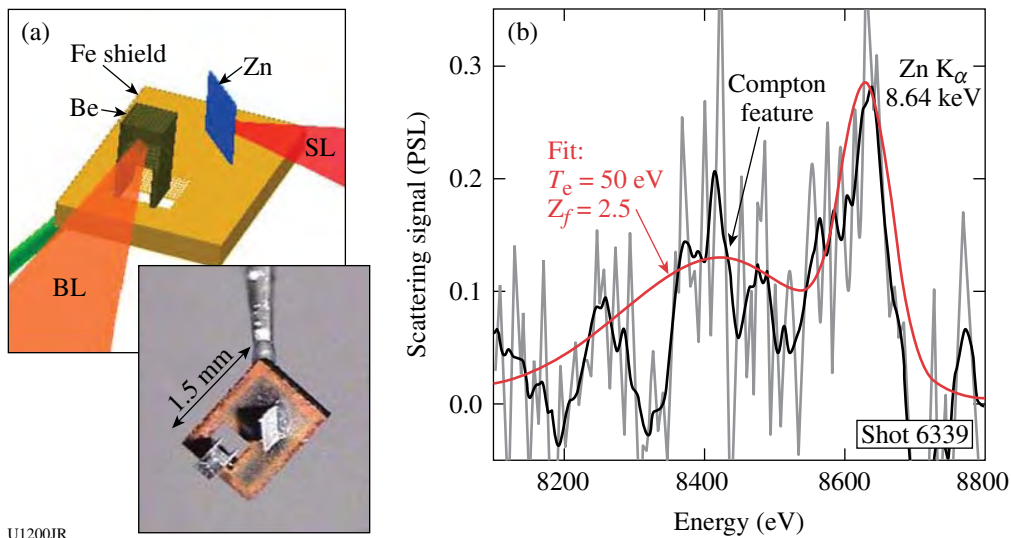
Compared to a previous shot campaign, the target size was significantly reduced and lower-Z shields were used in an effort to reduce bremsstrahlung levels. Different shield compositions were also tested. At the end of the shot day, an inelastically scattered Compton signal was successfully recorded from isochorically heated Be [cf. Fig. 124.157(b)], employing 62 J in the backlighter beam and 250 J in the sidelighter beam. These results represent significant progress compared to the previous shot campaign.



U1199JR

Figure 124.156

(a) VISAR mirror test experimental configuration. (b) An example of VISAR data measuring the shock speed in a SiO_2 window. No blanking is observed. (c) The measured shock speed is $52 \mu\text{m/ns}$, corresponding to an ~ 50 -Mbar ablation pressure.



U1200JR

Figure 124.157

(a) Experimental configuration and (b) x-ray Thomson-scattering spectrum from isochorically heated Be, utilizing a Zn K_α source line at 8.6 keV . The experimental data are fitted with $T_e = 50 \text{ eV}$ and ionization of $Z_f = 2.5$.

High-energy-backlighter development. The goal of this experiment was to compare the backlighter conversion efficiencies of high-Z materials driven by short- and long-pulse lasers. Short-pulse-generated x rays are believed to result from hot electrons that collide with K-shell electrons, causing K_{α} x-ray fluorescence. Long-pulse-generated x rays are believed to be created by thermal heating and ionization of the material. The goal was to perform systematic comparisons at high x-ray energies. The OMEGA EP Laser System is ideal for this type of test since both short- and long-pulse lasers are available to illuminate a target using the same diagnostics. In this set of experiments, three different types of materials were tested: Cu, Ag, and Sm. The initial analysis shows that the long pulse is much more efficient at generating the 8-keV Cu backlighter; whereas the 40-keV Sm x ray is much more efficiently generated with the short-pulse lasers. From these data, it was observed that the conversion efficiencies are approximately the same at ~ 17 keV, driven by either long- or short-pulse lasers (Fig. 124.158). At 8 keV, the long-pulse laser was more efficient by a factor of 10, whereas at 22 keV, the short-pulse laser was more efficient by a factor of 5.

Broadband x-ray Laue diffraction development. The lattice scattering campaign uses the broadband thermal x-ray emission from a direct-drive-implosion capsule to perform single-shot, *in-situ* white-light x-ray diffraction. This employs the classic Laue diffraction on a subnanosecond time scale

to investigate material behavior during shock or ramp compression. This technique will give insight into the material microstructure because lattice defects will cause nonuniform strain in the atomic structure, causing the diffraction spots to broaden and change shape. A directly driven implosion on the OMEGA laser is ideally suited for this technique, providing a short burst (~ 150 ps) of bright broadband x rays. The laser beams were pointed to five different pointing locations on the capsule to maintain implosion symmetry. Figure 124.159 shows gated framing camera images of the implosion capsule on a previous campaign that had 42 beams for the implosion, while Fig. 124.160 shows the improved symmetry by using the five different targeting locations. In principle, symmetry can be improved even further by adding more locations.

For these experiments the broadband x-ray diffraction (BBXRD) diagnostic was designed and qualified (Fig. 124.161). The diagnostic is designed with a tapered profile so that as many beams as possible can reach an implosion capsule placed 20 mm away from the single-crystal target that sits on the front plate of the BBXRD. The inside of the BBXRD has four trapezoidal image plate detectors on the tapered sides and a square piece on the back to record the transmitted diffraction. Simultaneous VISAR measurements can be made from the rear surface through a hole in the back plate. The diagnostics capability was successfully demonstrated on two campaigns

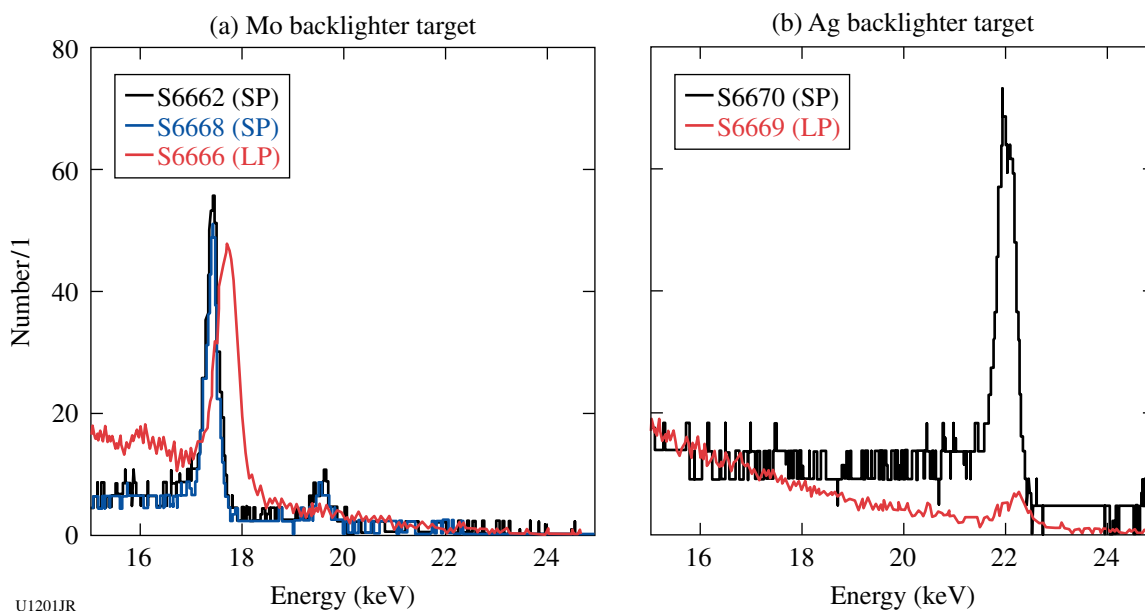


Figure 124.158

Comparison of high-energy backlighter yields driven by the 1-ns, 3ω long-pulse (LP) laser versus the 100-ps, 1ω short-pulse (SP) laser. The data were taken with the single-photon-counting camera. When normalized by the laser energies, we found that the Mo backlighter conversion efficiencies were about the same, whether driven by the short pulse or the long pulse.

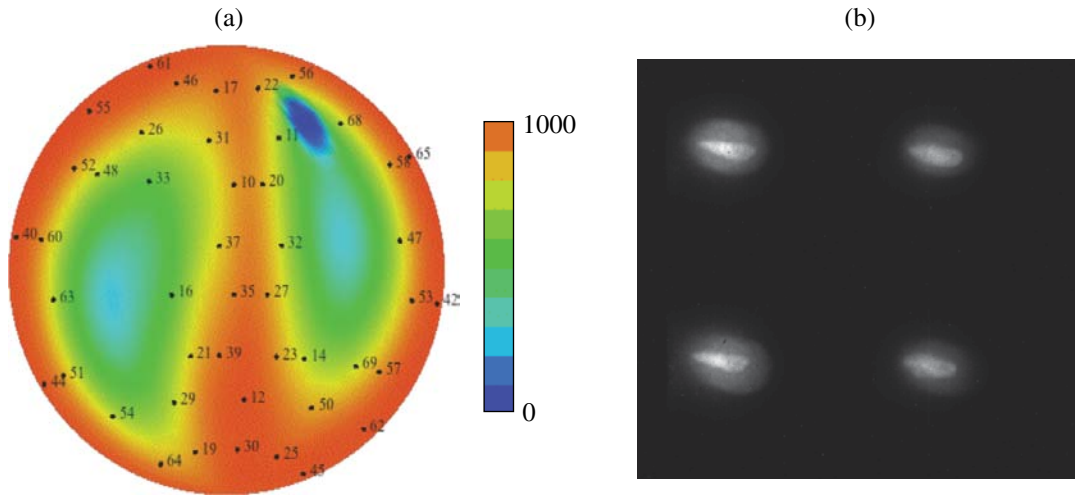
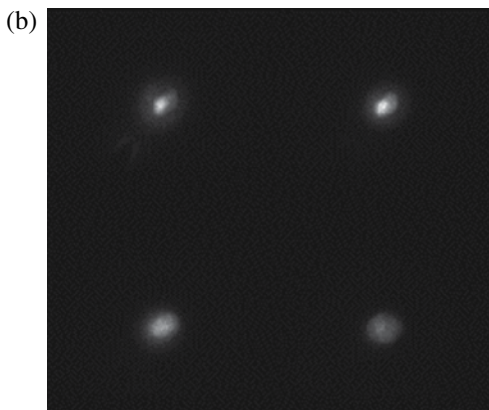
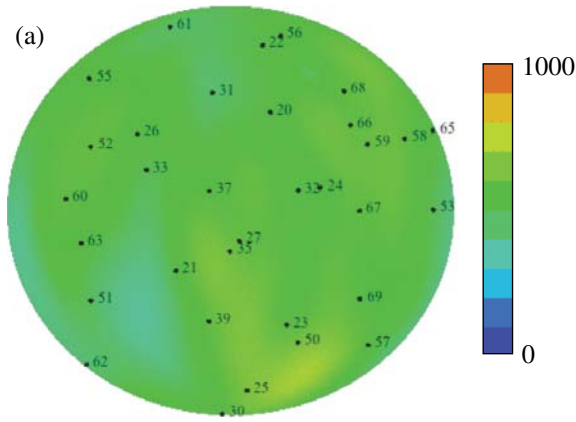


Figure 124.159

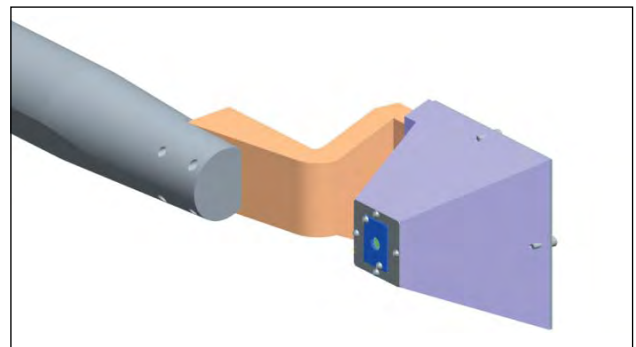
(a) The total laser power deposited and (b) gated framing camera images from the implosion capsule using 42 beams pointed to the center of the capsule.



U1203JR

Figure 124.160

(a) The total laser power deposited (TW/cm^2) and (b) gated framing camera images from the implosion capsule using 33 beams pointed to five different targeting locations on the capsule.



U1204JR

Figure 124.161

The BBXRD diagnostic in the VISRAD model showing the location of the implosion capsule and beams and CAD model.

of shock-compressed silicon (shown in Fig. 124.162) and copper. For the silicon images shown, it was estimated that the anisotropy in the compression by the shift in the spots was approximately 8% along the driven direction.

Powder x-ray diffraction development. The objective of this campaign is to demonstrate the use of powder x-ray diffraction

methods in the characterization of dynamically loaded (shocked and ramped) polycrystalline materials, particularly with a view to application on forthcoming NIF experiments. Such x-ray diffraction methods offer insight into processes occurring on the scale of the material lattice, which in turn determine the macroscopic response of the material to dynamic loads (e.g., its strength).

To date, the campaign has demonstrated x-ray diffraction from polycrystalline Ta foils using a quasi-monochromatic Mo backlighter source (see Fig. 124.163). Future campaigns will concentrate on improving the signal-to-noise ratio of the diffraction signal and will then aim to use this signal to characterize tantalum under a variety of shock and ramp-loaded conditions.

Powder x-ray diffraction measurements of solid Fe, Sn, and Ta to 500 GPa. An experimental platform was developed to measure powder x-ray diffraction on solid samples at pressures above Hugoniot melt. Fe, Sn, and Ta samples were sandwiched between a diamond pusher and window and ramp-compressed to high pressure and density using up to six OMEGA beams. VISAR velocity measurements were used to infer the pressure history in the sample, and the 8.37-keV Cu-He α x-ray source, driven by ten beams, was timed to coincide with the peak pressure. The diffraction signal was collimated through

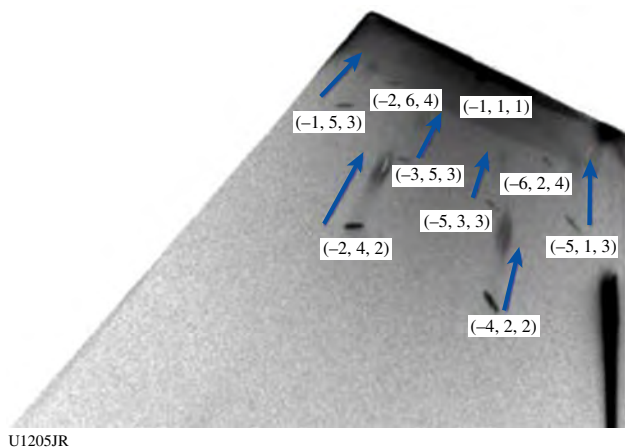


Figure 124.162
The tip of one of the trapezoidal image plates showing diffraction from uncompressed and shock-compressed silicon.

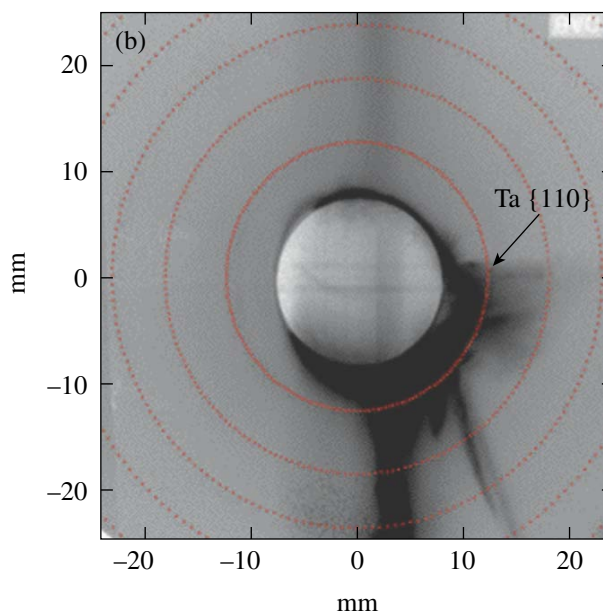
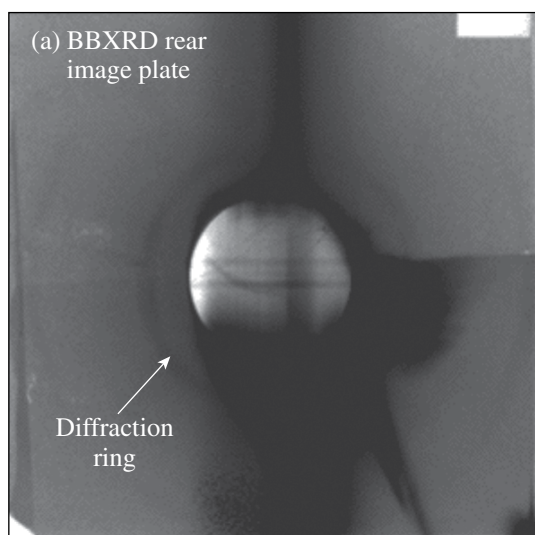


Figure 124.163
(a) Diffraction signature from polycrystalline Ta foil using a 17.5-keV x-ray source and LLNL broadband x-ray diffraction (BBXRD) diagnostics. Each crystallographic plane (hkl) generates a characteristic cone of x rays; the intersection of these cones with the image plate detectors results in a characteristic ring pattern. (b) Calculated pattern shown overlaid over data.

a 300- μm -diam aperture in a 150- μm -thick Ta substrate and captured on image-plate detectors. Density was inferred from the diffraction data by assuming a crystal structure, then verifying self-consistency with a best fit to density. Maximum diffraction pressures attained on Fe, Ta, and Sn samples were 480, 310, and 220 GPa, respectively, all above Hugoniot melt. Data from iron samples are shown in Fig. 124.164.

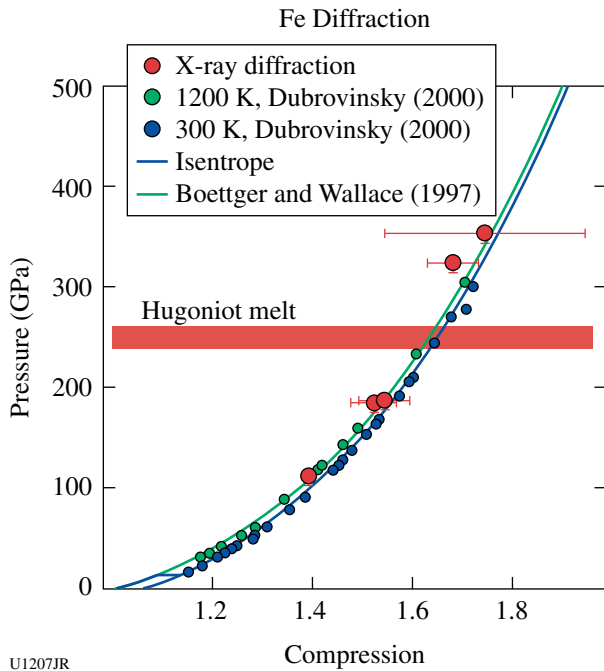


Figure 124.164
 In FY10, the OMEGA laser was used to obtain x-ray diffraction measurements of solid Fe (red circles) at pressures above the Hugoniot melt (red band at 250 GPa). The results are consistent with Fe remaining in an HCP structure up to the highest pressures observed (~480 GPa). Diffraction data from diamond anvil cells⁵² are also shown, along with a theoretical isentrope from Ref. 53.

ACKNOWLEDGMENT

This work was performed under the auspices of the U.S. Department of Energy by Lawrence Livermore National Laboratory under Contract DE-AC52-07NA27344.

FY10 LANL OMEGA Experimental Programs

In FY10, Los Alamos National Laboratory (LANL) executed 135 shots on the OMEGA Laser System and 24 shots on the OMEGA EP Laser System. LANL had three instruments qualified for use on OMEGA EP: the NIF5 spectrometer, the target-heating Verdi laser (THVL), and Thomson parabola ion energy (TPIE) diagnostic.

LANL experiments contributed to the National Ignition Campaign (NIC) in the following ways:

- Studies of the equation of state (EOS) of plastic ablators
- New experimental methods for determining the areal density of imploded ICF capsules using 4.44-MeV $^{12}\text{C}(n,n')\gamma$ rays
- Demonstration of NIF components of the neutron imaging system

High-energy-density (HED) campaigns included

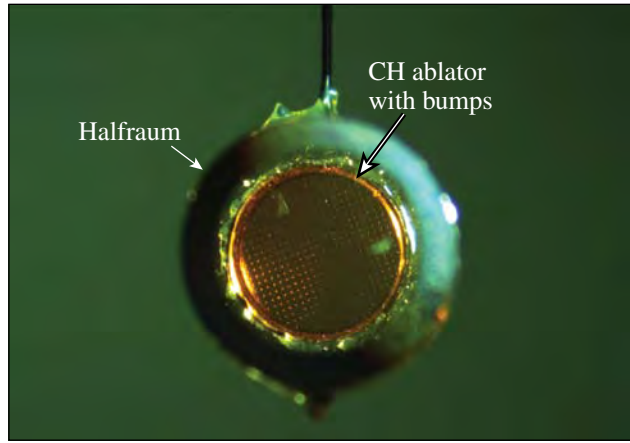
- Measurement of a supersonic radiation wave
- Measurement of capsule yield in the presence of high-Z dopants
- DT reaction product branching ratio measurements
- Energetic-ion generation from hemispherical targets
- Development of x-ray sources for phase-contrast imaging

Collaborations with AWE, LLE, LLNL, NRL, and National Security Technologies (NSTec) remain an important component of LANL's program on OMEGA.

CHaRM: Disagreement between EOS models is found in the prediction of bump evolution, which the CHaRM campaign hopes to resolve. This year a campaign began to measure the ablative Richtmyer–Meshkov (aRM) growth of isolated Gaussian-shaped bumps on plastic ablators. The ablative Richtmyer–Meshkov instability operates at the ablation front and is important because it controls the ablation surface perturbations present at the onset of Rayleigh–Taylor growth, which initiates once the shock has broken out and begins to accelerate the capsule.

General Atomics has sputtered 25- μm FWHM bumps, which are 4 to 8 μm tall, onto 120- μm -thick planar plastic ablators. The ablators are placed over one side of 0.9-scale gold halfraums (see Fig. 124.165), which are driven to 65-eV radiation temperatures corresponding to NIC foot levels. On-axis x-ray radiography using Saran backlighters (2.8 keV) allows one to measure bump areal density at successive times. Experiments this year have been hampered by low contrast from the combination of small areal-density variations from which to measure, as well as unwanted high-energy x rays in the system. An example of a measured low-contrast, 5- μm bump is shown in Fig. 124.166. The center of the bump (and lineout) shows a region of higher transmission, characteristic of a bump with a dip at its peak, which agrees with predictions at this time (4 ns after the start of the laser drive). Higher-contrast experiments are planned for FY11 along with shock-speed measurements to independently measure the drive conditions.

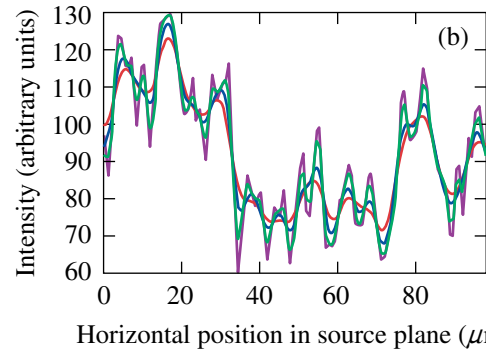
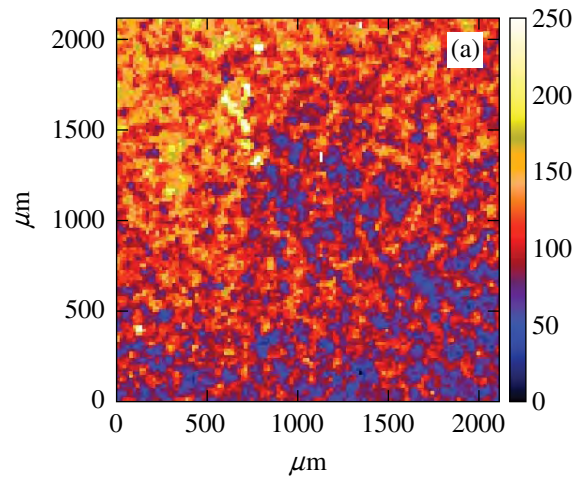
Gamma Reaction History: Gamma-ray measurements on fusion implosions were further developed for the NIC using



U1208JR

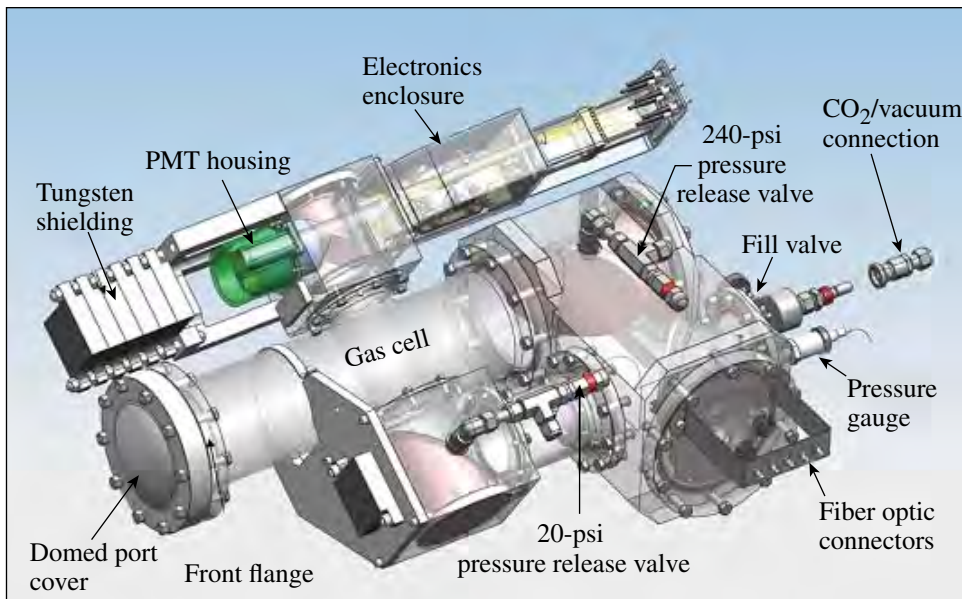
Figure 124.165
An optical image of a CHaRM target showing the perturbed plastic on the end of a 0.9-scale gold halfraum.

the gamma reaction history (GRH) diagnostic in FY10 (see Fig. 124.167). The GRH was first installed on the exterior of the OMEGA target chamber in 2009 (see Fig. 124.168). This instrument is a gas Cherenkov detector (GCD) designed for the NIF and being tested and used for nuclear studies on OMEGA. GCD's convert energetic γ rays to UV/visible Cherenkov photons for collection by fast optical recording systems. System impulse response better than 100-ps FWHM has been made possible by the combination of low-temporal-dispersion GCD's, ultrafast microchannel-plate photomultiplier tubes (PMT's),



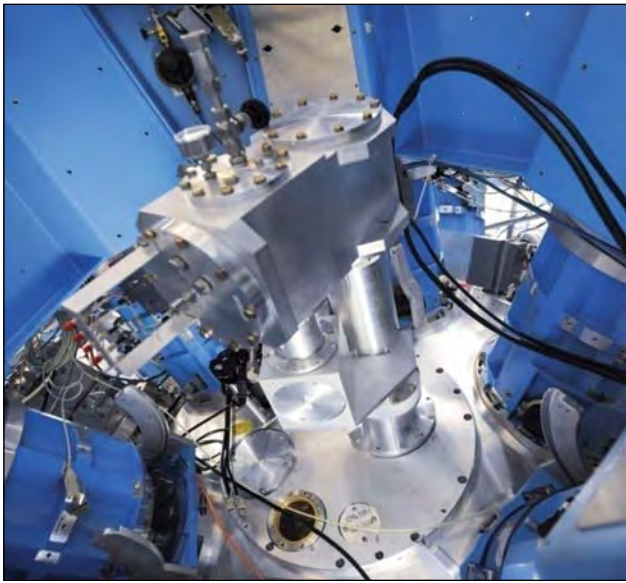
U1209JR

Figure 124.166
Image of the backlighter data obtained from radiography of a perturbed surface. The lineout indicates the presence of a bump.



U1210JR

Figure 124.167
Isometric view of the GRH diagnostic. After exiting the target chamber, energetic γ rays interact with a converter plate inside the domed port cover. The resulting relativistic electrons with energy above threshold generate UV/visible Cherenkov radiation inside the pressurized gas cell. A series of off-axis parabolic mirrors concentrate this light down to a 1-cm-diam active area of an ultrafast photomultiplier tube located inside the PMT housing. The electrical signal from the PMT is converted to infrared photons by a Mach-Zehnder modulator inside the electronics enclosure. This optical signal is then converted back to an electrical signal using high-speed photoreceivers connected directly to high-speed digitizers. The PMT is well shielded against direct-radiation effects by the tungsten shielding. Calibration and timing fiducial signals are injected into the optical path through the fiber-optic connectors.



U1211JR

Figure 124.168
Photograph of the GRH attached to the OMEGA target chamber.

and high-bandwidth Mach-Zehnder fiber-optic data links and digitizers, resulting in burnwidth measurement accuracy better than 10 ps.

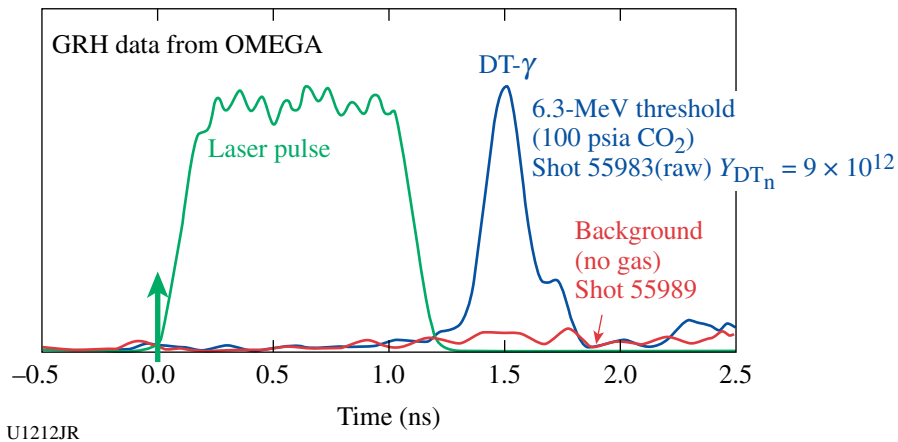
The GRH was absolutely timed using x rays from Au-ball shots on OMEGA. It has been shown that fusion bang times measured using the GCD-1 and the GRH agree to within 5 ps on average. Error budgets indicate that the GRH will be able

to meet the NIF requirement of measuring bang time to within 30 ps relative to the start of the laser pulse. Figure 124.169 shows raw GRH data placed on the laser time base along with the 1-ns laser pulse. Data with and without pressurized CO₂ demonstrate Cherenkov production and backgrounds, respectively.

Inherent variable energy-thresholding capability allows one to use GCD's as γ -ray spectrometers to explore fusion and other interesting nuclear processes. Recent GRH measurements of 4.44-MeV ¹²C(*n,n'*) γ rays produced as 14.1-MeV DT fusion neutrons pass through plastic capsules are paving the way for a new CH-ablator areal density measurement. This measurement is made possible by the use of SF₆ at high pressure (200 psia) resulting in a 3-MeV Cherenkov threshold.

The NIF GRH system consists of four individual gas cells, all essentially identical to the GRH on OMEGA. Located 6 m from target chamber center, the GRH-6m system began taking data on NIF in September 2010. OMEGA has provided an excellent platform to develop the detector technology and measurement techniques and will continue to provide a test bed for new physics investigations using GRH in the future.

The Neutron-Imaging System: In FY10, LANL successfully tested a major component of the NIF neutron-imaging system using the Omega Laser Facility. In order to record two images (14-MeV primary and 10- to 12-MeV down-scattered), a complex, multi-element lens (Fig. 124.170) must be used to view the front side of the neutron-to-light scintillator. Preliminary



U1212JR

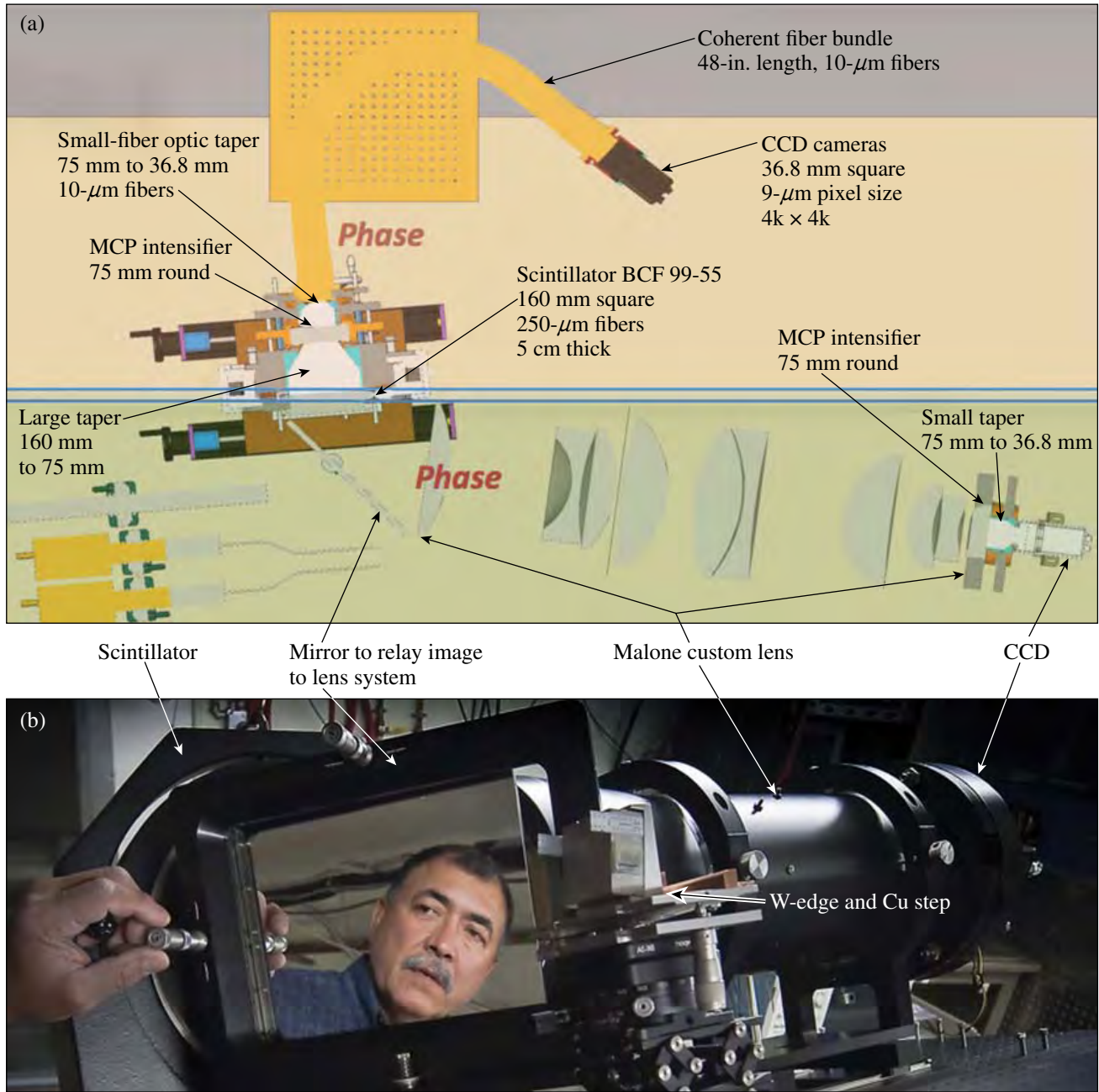
Figure 124.169
Raw GRH data shown on the laser time base along with the 1-ns laser pulse used to drive the fusion implosion. The GRH was pressurized with 100-psia CO₂ for shot 55983, resulting in a 6.3-MeV Cherenkov threshold. DT fusion γ rays at 16.75 MeV produced the signal shown. The small peak riding on the tail of the main peak is a result of ringing in the PMT. This feature is removed, and the main peak is sharpened by deconvolving the instrument response of the system. The GRH, evacuated for shot 55989, provided a background measurement of direct radiation interaction with the PMT and demonstrated gas is necessary to generate a real signal.

data analysis indicates that the lens channel obtains a source plane resolution close to $10\ \mu\text{m}$ and comparable to the fiber-coupled channel.

Flat-field images at prompt gamma time of flight and NIF down-scattered neutron time of flight were collected for important scintillator background and temporal response studies.

NIF-5

Radiation flow. The NIF-5 project obtained invaluable data on OMEGA for the development of a future NIF diagnostic to measure the propagation of a supersonic radiation front in a low-density foam. These data were obtained using two principal diagnostics: the NIF-5 spectrometer with the GXI-T detector and an x-ray backlighter to perform absorption spectroscopy of



U1213JR

Figure 124.170

(a) A schematic of the neutron imaging system; (b) a photograph of the neutron-imaging system while being aligned.

a tracer foil, and an x-ray framing camera and x-ray backlighter to measure the hydrodynamic expansion of the same foil. Together, these two diagnostics greatly constrain the models in an effort to better validate simulation codes.

The radiation flows from the hohlraum (top left, Fig. 124.171) and into a Be tube filled with a low-density (65-mg/cc) CH foam (bottom left, Fig. 124.171). A thin, square Ti foil (shown in blue but at an angle in the figure) is embedded in the target to diagnose the propagation of the radiation front down the tube. The hydrodynamic expansion of the foil (viewed edge-on) and the shock wave in the tube wall were imaged using an x-ray backlighter. The inset compares our data and a 2-D cylindrical RAGE simulation of the shock in the tube wall. The code is able

to qualitatively recreate the data. A more-detailed quantitative analysis is currently underway.

The absorption of CsI x rays by the foil in the orthogonal direction was also measured, providing a measurement of the charge state of the foil as a function of location along the radiation propagation direction. Figure 124.172 shows a schematic of the diagnostic: GXI-T with a Ge (111) crystal spectrometer snout. The absorption spectrum of the tracer was measured (along the detector strips) as a function of distance from the Au can bottom (orthogonal direction). Results are shown Fig. 124.173, along with a simulated Ti absorption spectrum, the latter showing the absorption lines expected given a certain foil temperature. The data show the Ti absorption lines

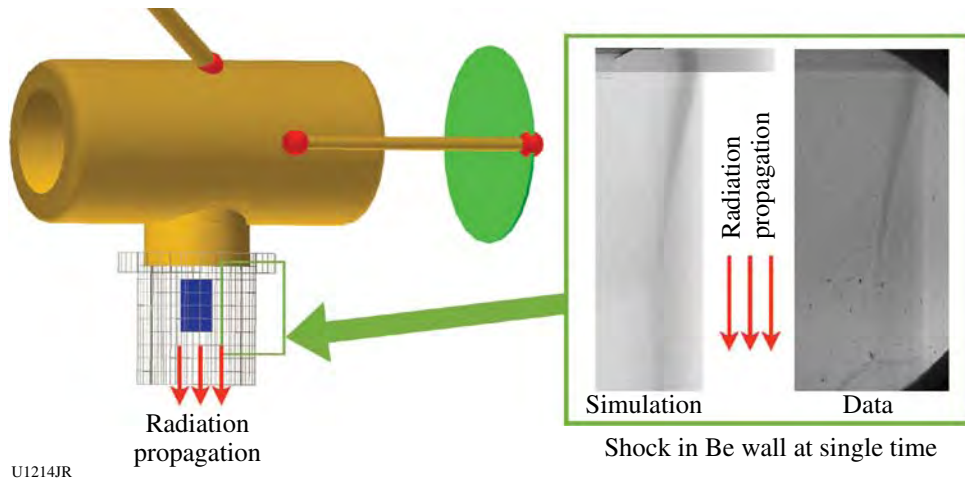
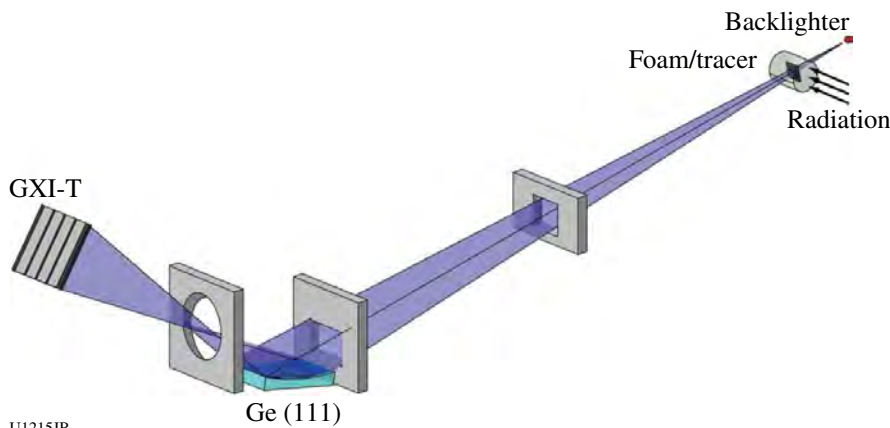
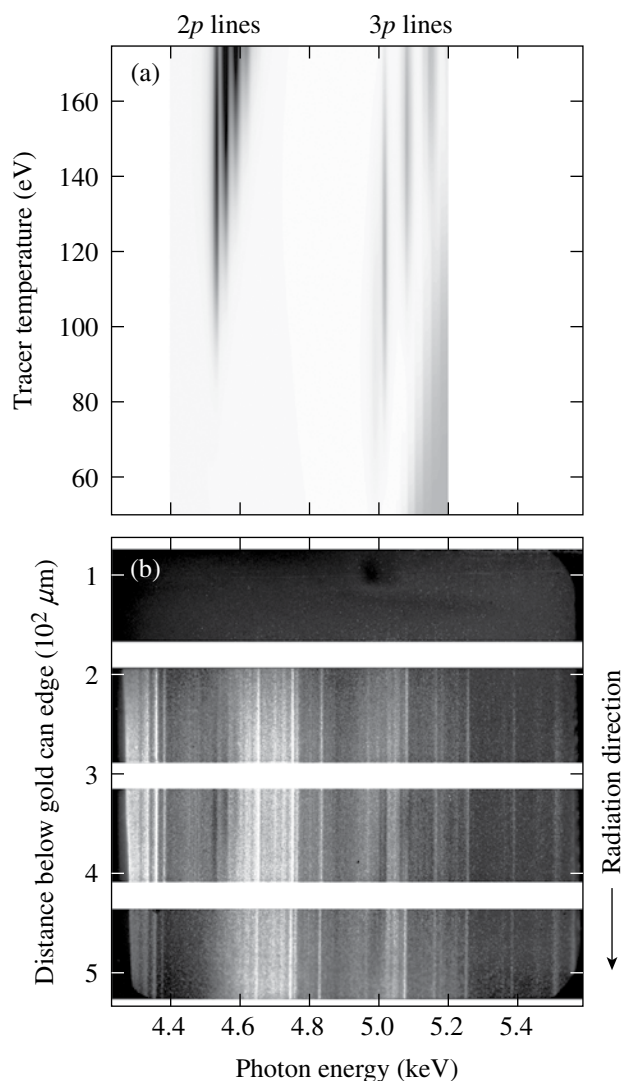


Figure 124.171
Radiation flows from the source, a hohlraum, into a foam cylinder (with an embedded tracer foil, in blue) enclosed in a Be tube (cross-hatched region). Inset: A comparison of simulation and data showing the shock in the tube wall.



U1215JR

Figure 124.172
Schematic of the diagnostic foam/tracer (target not to scale). A broadband x-ray backlighter illuminates a thin foil embedded in a low-density foam cylinder as a radiation front travels across it. The image of the foil is dispersed along one axis by a curved Ge crystal. The detector is composed of four separately gated strips.



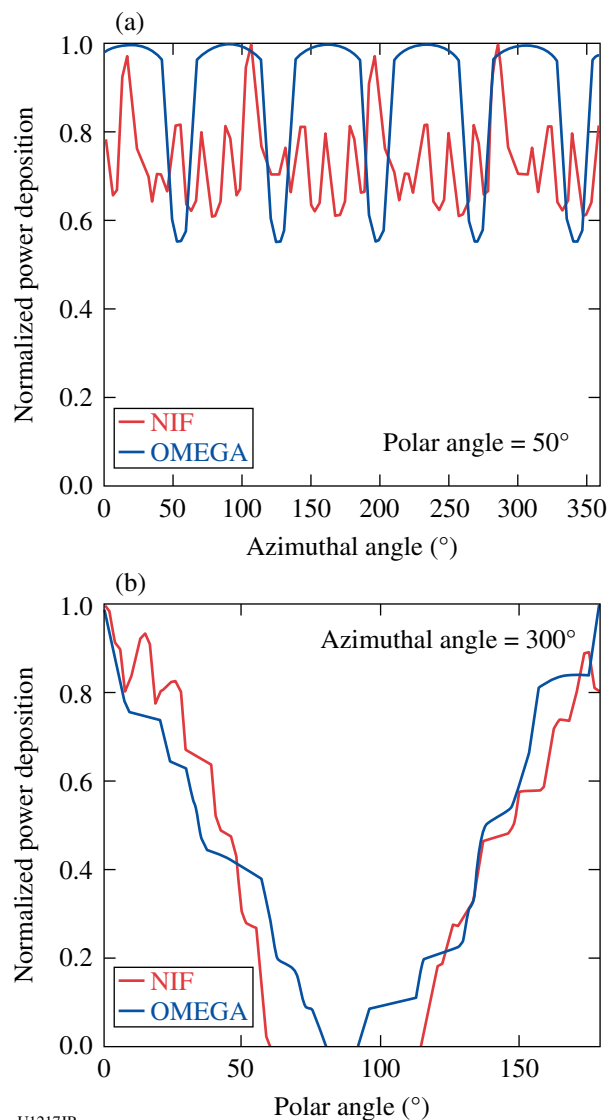
U1216JR

Figure 124.173
 (a) Simulated titanium absorption spectrum showing how the absorption lines can be used to determine the temperature of the tracer foil. (b) Data showing the titanium absorption lines overlaid onto our CsI backlighter-emission spectrum.

overlaid on the CsI backlighter emission spectrum. The initial analysis shows an ~200-mm-long radiation front with the tracer temperature ranging from ~130 eV midway down the foil to ~50 eV at the end of the foil.

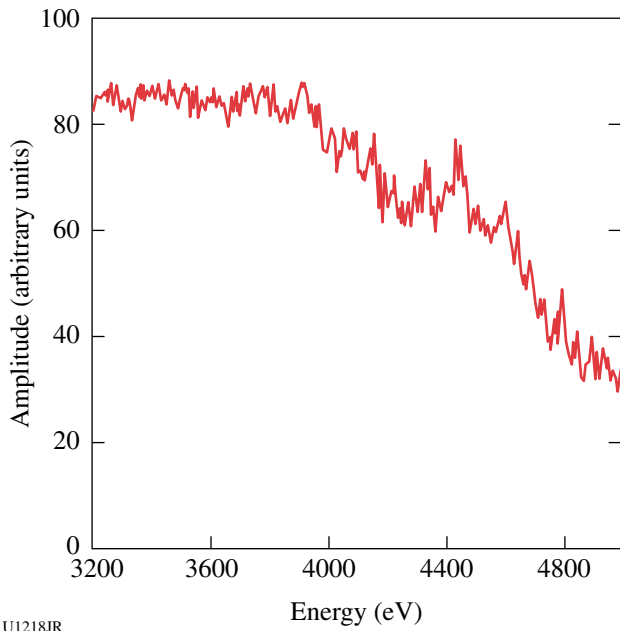
Short-duration backlighters. The NIF-5 campaign also executed a two-prong investigation into short-pulse quasi-continuum backlighters. This involved experiments on OMEGA EP using short-pulse lasers to irradiate a foil target and OMEGA experiments imploding Kr-fill capsules using a NIF-like irradiation pattern.

On the NIF, capsules must be polar driven because of the laser-beam geometry. Experiments were performed to determine what effect a polar-driven laser drive has on a capsule backlighter. Figure 124.174(a) shows the normalized laser power deposition in the azimuthal direction at the NIF and OMEGA. Although there are differences in the details, the peak-to-trough difference is nearly the same for both. Figure 124.174(b) shows the laser deposition as a function of polar angle for both the NIF and OMEGA configurations. Although there is some slight discrepancy, particularly at the equator, the profiles are very similar.



U1217JR

Figure 124.174
 Lineouts of the NIF and OMEGA laser power deposition profiles in the (a) azimuthal and (b) polar directions.



U1218JR

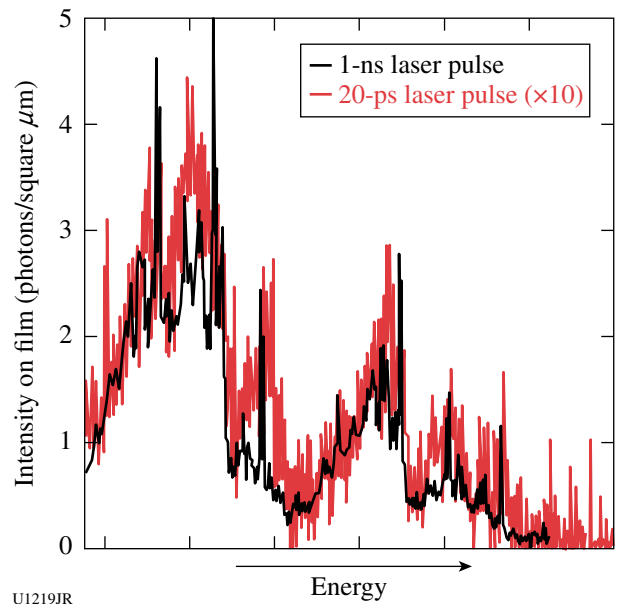
Figure 124.175
Signal amplitude versus photon energy for the bright core of a Kr capsule implosion.

Figure 124.175 shows the spectrum from a Kr capsule implosion. The spectrum is much more uniform than one would measure for a foil target, such as an L- or M-shell emitter, which is often chosen for spectroscopic measurements.

Experiments conducted on OMEGA EP studied both the K-shell and L-shell spectra of a CsI foil at three different laser pulse lengths (20 ps, 40 ps, and 1 ns). Figure 124.176 shows the L-shell spectrum of a CsI foil generated by a 1-ns and a 20-ps laser pulse. While the 1-ns spectrum has many narrow features, the 20-ps data show a broadening of the spectral lines.

The results of both of these backlighter experiments have provided invaluable data to evaluate their use for future LANL-led NIF experiments.

High-Z: The High-Z campaign had two main objectives: (1) to determine if the yield from plastic capsules would behave similarly to the yield of glass capsules when a high-Z dopant was added, and (2) to measure if the Ti x-ray emission from the Ti dopant in the shell was sufficiently high to use the multiframe monochromatic imager (MMI) in future experiments. The MMI diagnostic allows one to measure spatial and temporal profiles of the electron density and temperature in the plasma.



U1219JR

Figure 124.176
A comparison of the L-shell emission from a CsI foil resulting from irradiation from a 1-ns laser (black) and a 20-ps laser (red). The intensity of the 20-ps data has been multiplied by a factor of 10 to fit on the same scale as the 1-ns data.

To check the equivalency between plastic and glass capsules, a 900- μm -diam, 13.5- μm -thick plastic-shell target that contained 10 atm of D_2 gas was imploded and doped with varying amounts of Kr gas. The Kr gas-fill levels were designed to cover a range that produced significant degradation in the yield of the glass-shell capsules measured in previous experiments. In addition, some of the capsules contained Ti doped into the inner 1.5 μm of the plastic shell. The implosions were driven using the 60-beam OMEGA laser with full beam smoothing, resulting in a total laser energy of 23 kJ.

These experiments successfully demonstrated the equivalent behavior of the plastic capsules to the glass capsules as the Kr dopant level in the gas was increased. We also obtained Ti emission measurements from the capsule implosions. Based on these results, the second shot day was focused on enhancing the Ti emission from the capsules to improve the feasibility of using the MMI diagnostic.

Some examples of the spectrometer and imaging data are shown in Figs. 124.177 and 124.178. Figure 124.177 shows an image from the Henway time-integrated spectrometer for shot 56577. X-ray H-like and He-like Ti emission lines 2-1 transitions can be seen on channel C and 3-1 transitions on channel A. One can also see an absorption feature on channel C that comes from the colder Ti in the shell near the peak of

the implosion. The different horizontal strips in each image represent different filters that are used to provide a wavelength calibration. Figure 124.178 shows multiple images using the DDMMI spectrometer.

Good neutron data were also obtained from these shots. A comparison of the yield as a function of Kr dopant between the glass and plastic capsules is shown in Figure 124.179. The data indicate that the plastic capsules behave very similarly to the glass capsules with the yield dropping as the Kr concentration is increased, just as it did for the gas capsules. This indicates that the physics important for the observed degradation in yield

do not depend on the capsule material. In the future, we will use whichever type of capsule is appropriate for obtaining a better understanding of this physics.

The goal of additional experiments with these shots was to improve the Ti emission from the capsule implosions so that the DDMMI diagnostic could be used to measure temperature and density profiles in the gas. At present, the data for these shots are still being analyzed, and an evaluation will be made concerning the usefulness of these Ti-doped plastic capsules to enable one to measure the DDMMI of the plasma properties in the gas.

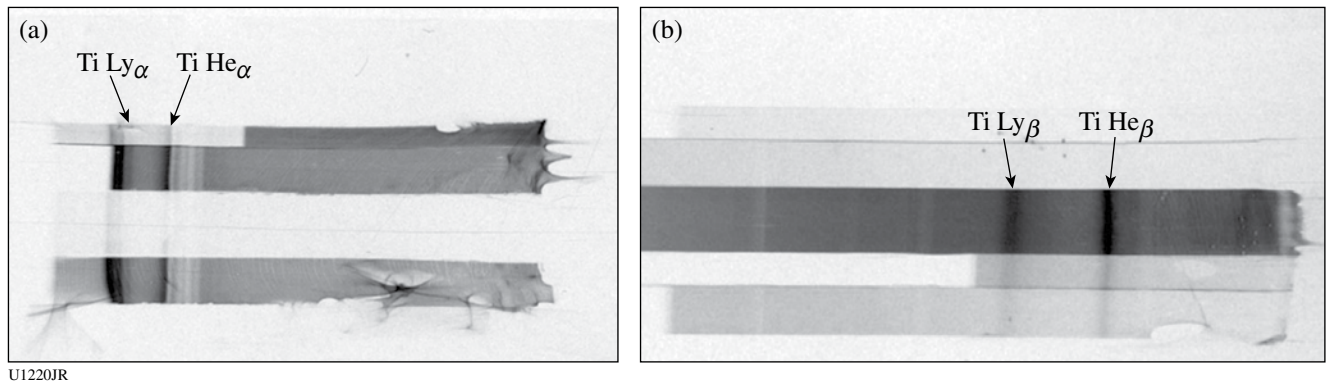


Figure 124.177 (a) Henway data showing the Ti He $_{\alpha}$ and Ti Ly $_{\alpha}$ lines; (b) Henway data showing the Ti He $_{\beta}$ and Ti Ly $_{\beta}$ lines.

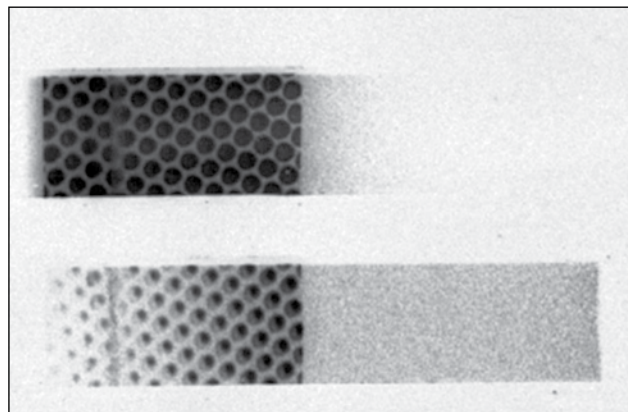


Figure 124.178 Image taken from one of the DDMMI spectrometers for shot 56568. Time goes from top to bottom for these images and the spectrum goes from lower to higher energy, right to left on each strip. The individual circles on these strips represent capsule images at a given photon energy and time. The lines that are just visible in the top strip are the He $_{\alpha}$ and Ly $_{\alpha}$ lines of Ti.

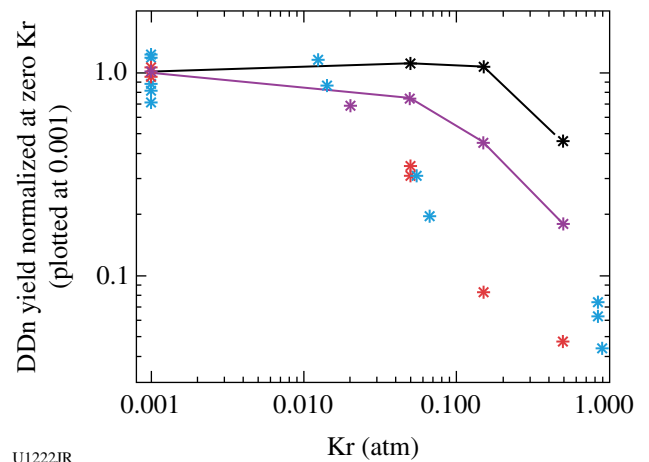


Figure 124.179 Comparison of normalized yields for glass and plastic capsules to simulations. The blue stars are data from glass-capsule implosions, while the red stars are data from the plastic-capsule shots. The purple curve represents calculations that include mix, while the black curve represents calculations without mix. The normalized yield levels for each set of capsules are 1.25×10^{11} for glass and 3.06×10^{11} for plastic, while the normalized simulation levels are 7.43×10^{11} for no mix and 2.85×10^{11} with mix.

DTRat: In addition to alphas and neutrons, the DT fusion reaction produces γ rays from the intermediate ${}^5\text{He}$ nucleus with a small branching ratio (BR) of several 10^{-5} γ/n . The excited ${}^5\text{He}$ can decay to the ground state, emitting a 16.75-MeV (width ~ 0.5 MeV) γ ray or to the broad first excited state emitting an ~ 13 -MeV (width ~ 4 MeV) γ ray. Knowledge of the BR between these two states is important to making absolutely calibrated measurements of the overall γ -ray spectrum on the NIF.

An energy-thresholding experiment was carried out for DT ICF implosions on OMEGA using a gas Cherenkov detector. After background subtraction, the fusion γ -ray Cherenkov peak was integrated for four different threshold energies (6.3, 8, 12, and 14 MeV). These integrated signals were then normalized to a specific threshold energy (for example, 12 MeV) and compared to the expected signal trends assuming a single γ -ray line at 16.75 MeV—assuming the two lines at 16.75 MeV and 13 MeV have nearly equal yield contributions (i.e., the “Hale” spectrum). Expected signal trends were calculated using the ACCEPT and Geant4 codes (Fig. 124.180).

In all of the intensity ratio graphs, a clear grouping of the experimental data around the theoretical values of the Hale spectra (double peak) was evident. This indicates that the DT reaction spectra are more like the Hale spectra and its mirror reaction D^3He than the previously assumed single-peak spectra. This study does not decisively conclude that the spectra are exactly like the Hale spectra but it confirms that there is a second peak in the spectra that has not been previously considered. This study is significant in that this is the first experimental evidence that clearly points to a double-peak spectra for D–T fusion in an ICF experiment. The refining of the exact spectra will be the subject of further studies.

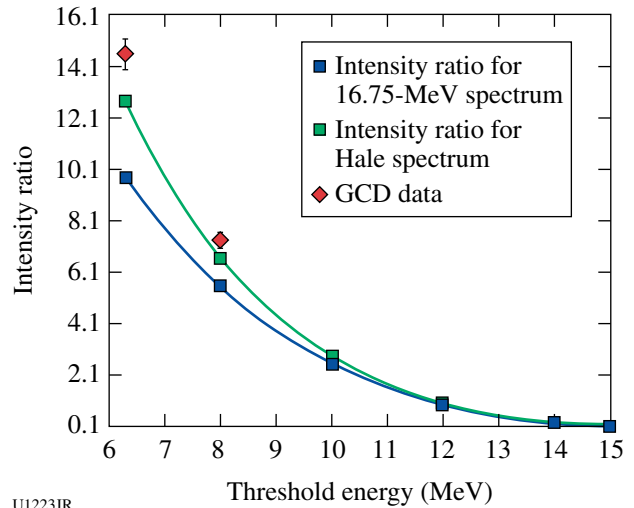


Figure 124.180

Ratio of GCD intensities as a function of threshold energy (MeV) normalized to 12-MeV threshold intensity ratio compared to Geant4 simulations. Red diamonds are experimental data. The green curve is obtained by folding the double-peak spectra⁵⁴ with a detector response of the GCD. The blue curve is assumed from a 16.75-MeV single-peak spectrum.

The DTRat campaign also performed experiments to examine the reduction of D–D yield attributable to the presence of ${}^3\text{He}$. These experiments not only measured the D^3He gamma signals but also observed D_2 gammas for the first time. This measurement provides new information to understand the nuclear reactions in an ICF capsule implosion.

OMEGA EP Ions: The LANL target-heating Verdi laser (THVL) was commissioned on OMEGA EP and was used to heat chemical-vapor-deposition (CVD) diamond hemispheres to greater than 1000 °C with the goal of producing nearly pure,

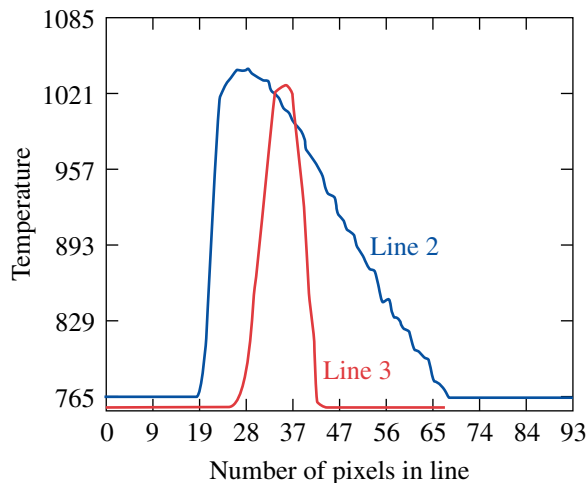


Figure 124.181

Temperature profile of a 500- μm -diam carbon rod heated at the tip by the THVL.

laser-accelerated carbon ion beams. Figure 124.181 shows a 500- μm -diam stand-in alignment target heated by the THVL to over 1000 °C as viewed through the system's pyrometer (left) and the software showing the lineout temperatures (right). Figure 124.182 shows similar data from the pyrometer, this time overlaid on a VisRAD representation of our CVD diamond Hemi target assembly for producing focused ions, showing the hemi heated to over 1000 °C in the center of the assembly.

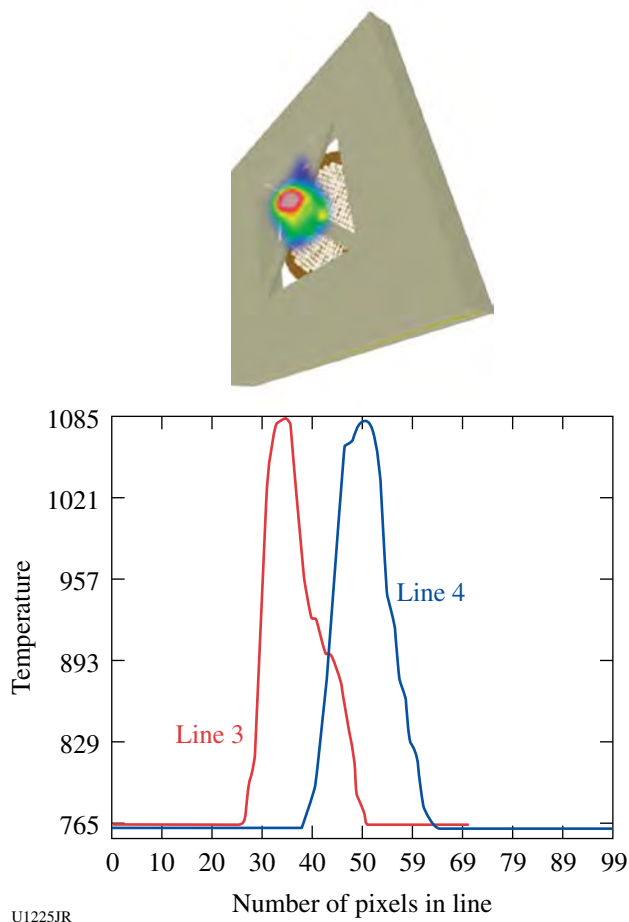


Figure 124.182
Temperature profile of a heated target overlaid with a VisRad image of target.

These heated targets were then shot using the short-pulse OMEGA EP Laser System with a 10-ps pulse at nearly a kilojoule, producing focused ion beams. The accelerated ions were diagnosed with the LANL-TPIE and LLNL-PFPII diagnostics. TPIE included a new cover plate that demonstrated an improved signal-to-noise ratio on the CR-39 solid-state nuclear track detector (SSNTD), and a LiF plate was added to the film-pack configuration to serve as a nuclear activation diagnostic of the carbon ion beam.

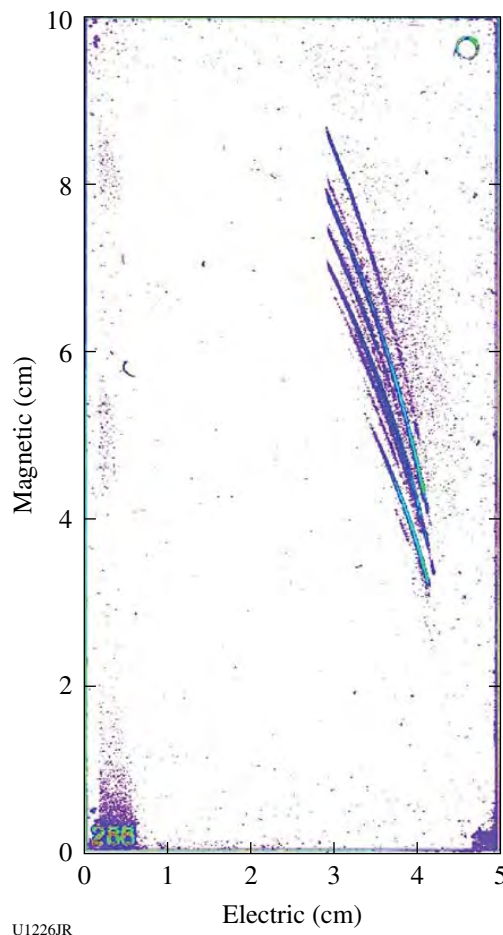


Figure 124.183
CR39 spectra from TPIE. The cutoff energies are for C5+ ~33 MeV (same as for C6+), C4+ ~28 MeV, and C3+ ~14 MeV.

TPIE recorded carbon and oxygen ions and an absence of protons on the SSNTD from the heated targets (Fig. 124.183). Energies of up to 2.75 MeV/nucleon for carbon were observed in large numbers, leading to preliminary conversion efficiencies of a few percent of laser energy into ion energy for each carbon species (depending on assumptions made about the beam size versus the solid angle of TPIE). This means that if all the carbon species could be focused to a 30- μm volume, energy densities of the order of 10^{14} J/m^2 could be achievable.

High-Energy X-Ray Generation (HEX): The high-energy x-ray campaign at LANL has shifted from x-ray production to application of high-energy x rays in phase-contrast imaging. The intent is to generate x rays of sufficient energy that the x-ray absorption is minimal through a Au-walled hohlraum. Given the correct geometric constraints, an interference pattern will be produced in the region of strong phase (or density) gradients. The relationship used to determine the optimal x-ray source to

target distance is $z = (2\lambda u^2)^{-1}$, where z is the propagation distance, λ is the x-ray wavelength, and u is the spatial frequency defined as the inverse of the x-ray source size, in this context. For example, using an x-ray energy of 17.48 keV and an x-ray source size, defined as wire diameter, of 5 μm , the optimal distance from source to target is 17.6 cm.

Experiments this year used K_α x-ray emission from Ag (22-keV) and Cu (8-keV) microfoils to investigate shocks produced in CH targets. As shown in Fig. 124.184, the backlighter beam drove a microfoil ($100 \times 100 \times 5 \mu\text{m}$) from the side using a 20-ps pulse at 1 kJ, and the edge was used to backlight the CH target driven by two 2-ns UV pulses with a total energy of 2 kJ.

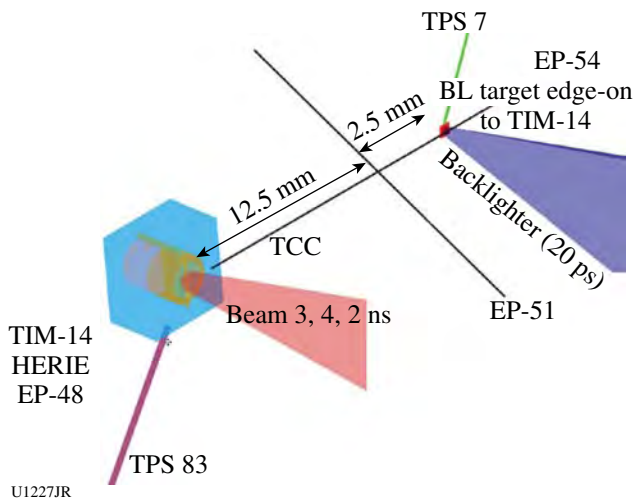


Figure 124.184 Configuration for HEX experiments on OMEGA EP. The primary diagnostic is the HERIE using image plates as the detector. A number of spectrometers were also employed including the TCS, DCS, ZVH, and DCHOPG.

Predicted shock behavior is shown in Fig. 124.185. Data were taken at 4, 6, and 8 ns. Image analysis is still ongoing. Figure 124.186 shows static data taken from gold grids illuminated by Cu emission on the left and Ag emission on the right. Both show high resolution and sufficient signal-to-noise ratio for the intended applications.

FY10 CEA Experiments on the Omega Facility

CEA-led teams conducted 62 shots on OMEGA during FY10. The experiments included ablator preheat characterization, Rayleigh–Taylor (RT) growth measurements, and rugby hohlraum characterization.

Ablator Preheat: Preheat and shock-breakout measurements were obtained in graded dopant targets on OMEGA on 14 June

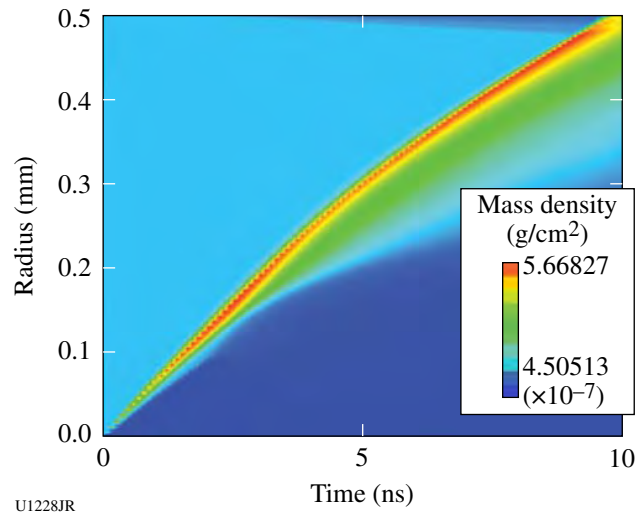


Figure 124.185 One-dimensional hydrodynamics calculation using HELIOS-CR predicting the shock structure as a function of time and position for a CH target driven by 2-kJ, 2-ns UV drive on OMEGA EP.

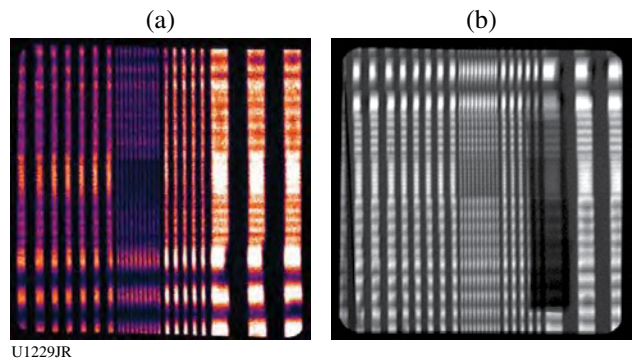


Figure 124.186 Static gold grids illuminated by Cu (left) and Ag (right) backlighters showing sufficient resolution and signal-to-noise ratio.

2010. CEA may use the graded dopant scheme for future ICF capsules. It consists of using several layers of Ge-doped plastic to protect the fuel from hard x rays; moreover, it must ensure hydrodynamic stability at the pusher/fuel interface. To this extent, the Ge-doped layers must be preheated by the M-band radiation so that the density profile across the shell will become nearly constant.

Two-dimensional transpositions of this design were shot on OMEGA. Preheat and shock breakouts were monitored using the ASBO diagnostic (Fig. 124.187). Extensive hohlraum energetics data were obtained using DMX and Dante broadband spectrometers. Detailed M-band radiation was measured using CEA μDMX and Henway spectrometers.

Rayleigh–Taylor Instability Experiments: We measured RT growths in indirectly driven rippled samples as function of Ge on OMEGA on 15 June 2010. These shots were intended to constrain physical models used in CEA hydrodynamic simulations.

These experiments will also provide us with a scaling between the length of RT spikes and corresponding optical-

depth variation measured on face-on radiography images. Differentiated behaviors as a function of dopant fraction were found, and as predicted, the highest growth factors were measured on highly doped samples (Fig. 124.188).

Additional data on face-on x-ray source characterization were obtained. For this purpose, a single Sc foil was shot in

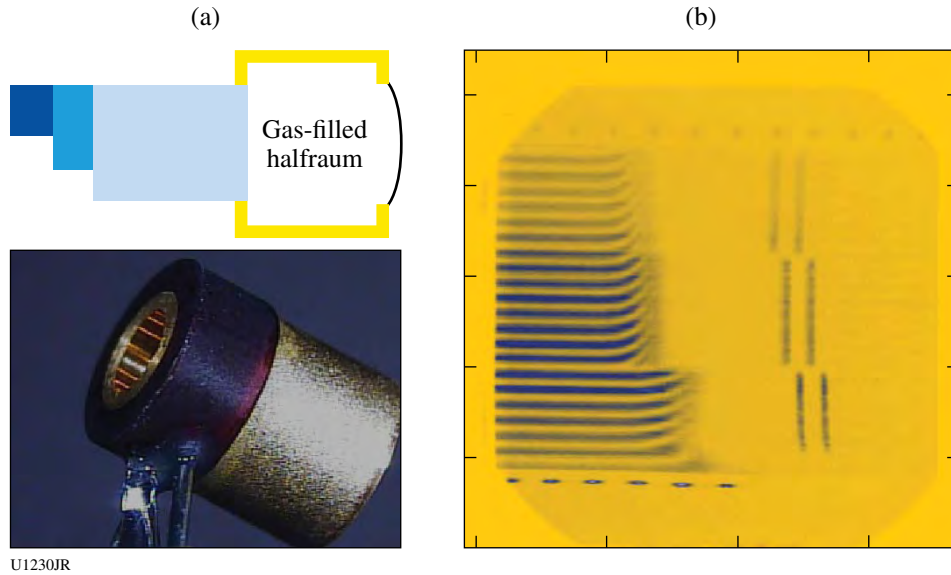


Figure 124.187
 (a) Schematic and real views of a target assembly. Samples were planar and comprised different steps of plastic doped with different atomic proportions of Ge. Steps were coated with Ta to be reflective. (b) Example of a VISAR image: fringe movement is due to preheat until the Ta coating stays reflective. Short flashes seen later in time are due to shock breakout.

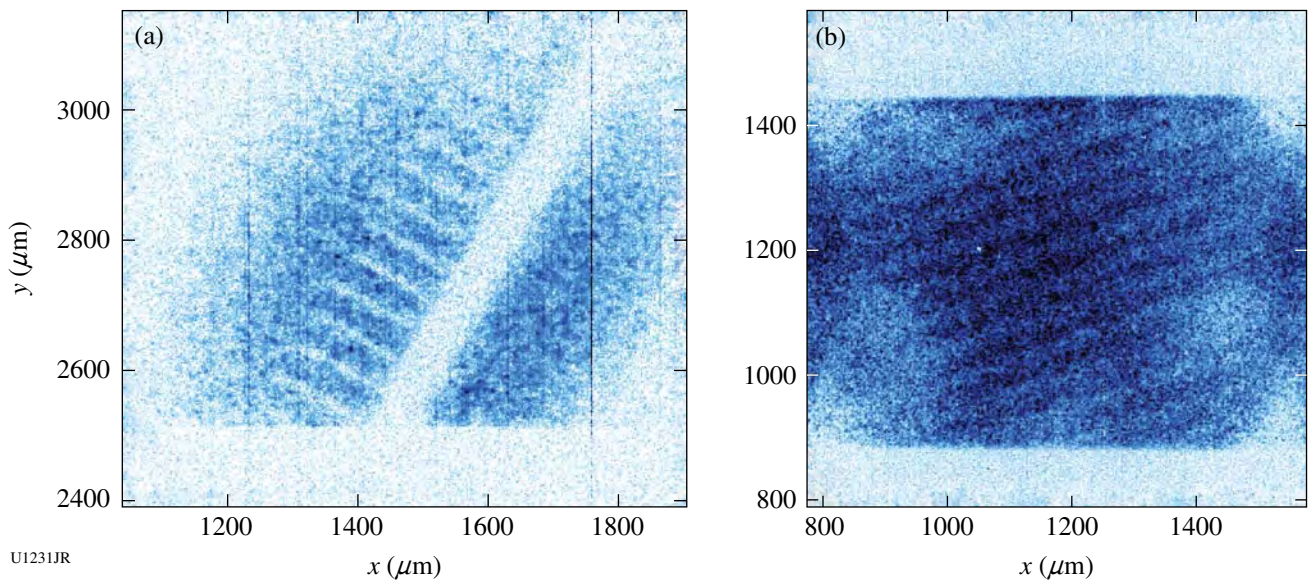


Figure 124.188
 (a) Side-on and (b) face-on radiography of a 20% atomic Ge plastic foil. Nonlinear RT growth spikes seen in (a) are approximately 200 μm long.

order to calibrate the radiography source routinely used in RT growth and in an implosion experiment. The influence of a gas-filled hohlraum plasma on the radiography signal was also studied using a Sc x-ray source placed behind a gas-filled hohlraum with no sample mounted on it (Fig. 124.189).

Implosions in Rugby Hohlräume: In the last few years, CEA has conducted extensive experimental investigations of the rugby hohlraum concept on OMEGA. Rugby hohlraums are part of an effort toward advanced, high-efficiency hohlraum designs, which could provide increased margin for ignition on LMJ and NIF and could also be suited for use in an IFE context because of their higher gains.

In 2009, in collaboration with LLNL (H. S. Park, H. F. Robey, and P. A. Amendt) and MIT (C. K. Li, F. H. Séguin, and R. D. Petrasso), a significant enhancement of x-ray drive in rugby hohlraums with respect to classical cylindrical hohlraums in a direct comparison (Fig. 124.190) was demonstrated. The improved capsule design led to the highest yields for indirect drive with noncryogenic deuterium fuel at the time, enabling researchers to use many nuclear diagnostics (neutron imaging, NTD, Fig. 124.191) for the first time in this configuration. These results were published in *Physical Review Letters* and *Science*.^{55,56} In 2010, the symmetry of implosion (Fig. 124.192) was successfully tuned with a calculated cone-balancing scheme based on the detailed simulations of a 2009

OMEGA experiment, therefore confirming the understanding of rugby hohlraum performance. The work this year was also extended to gas-filled rugby hohlraums with shaped pulses. Measurements have shown a relatively low level of backscatter (~5%), which could be further reduced by the use of polarization smoothing, and performance in good agreement with simulations. Direct comparison of gas-filled rugby and cylindrical hohlraums is planned on OMEGA at the end of 2010.

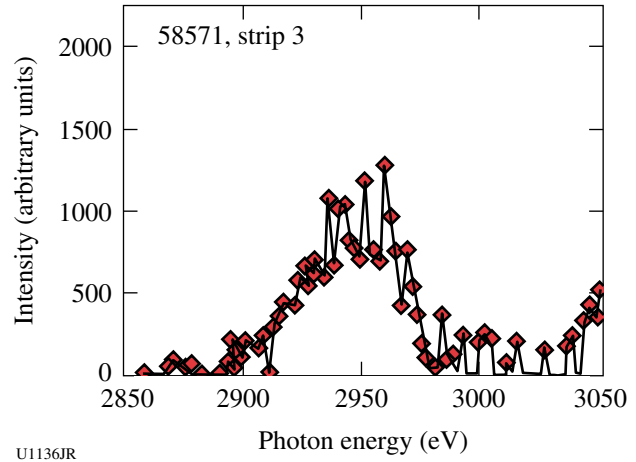


Figure 124.190
Evidence of 18% x-ray-drive enhancement with rugby hohlraums.

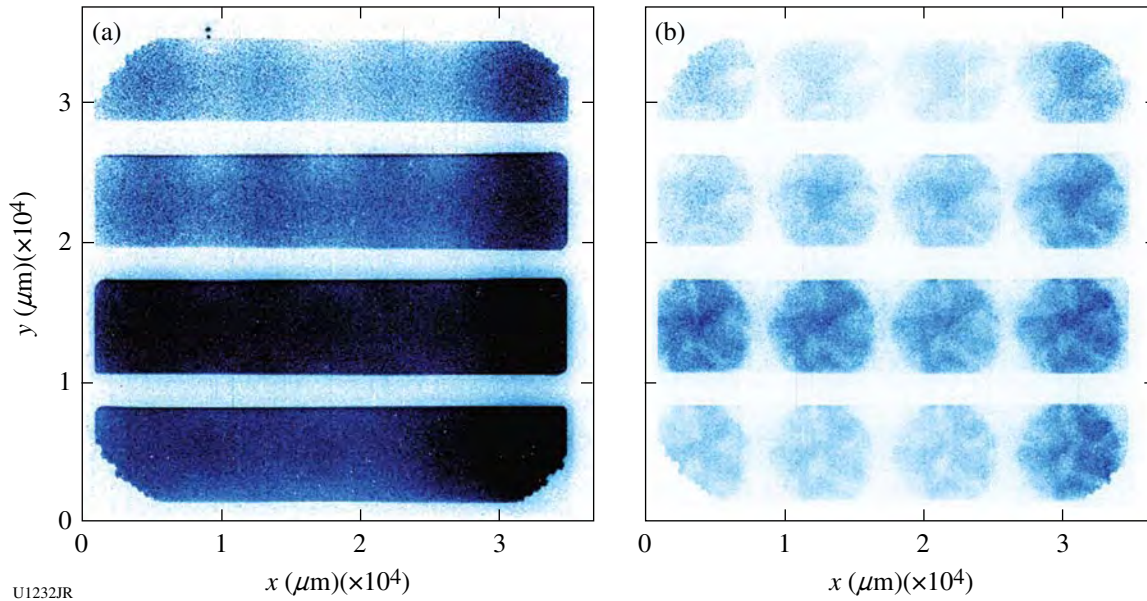
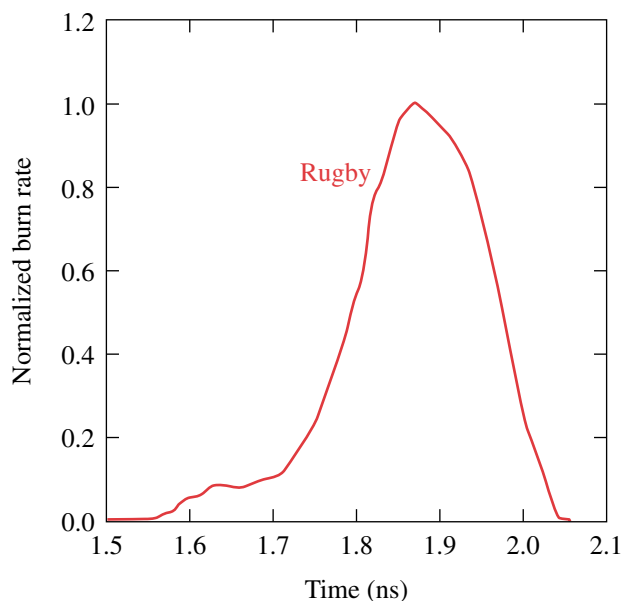
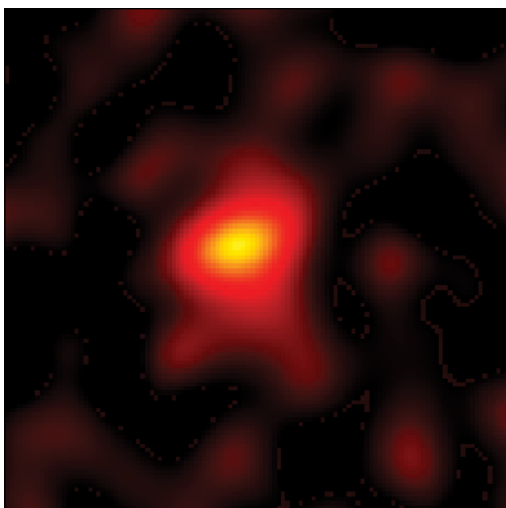
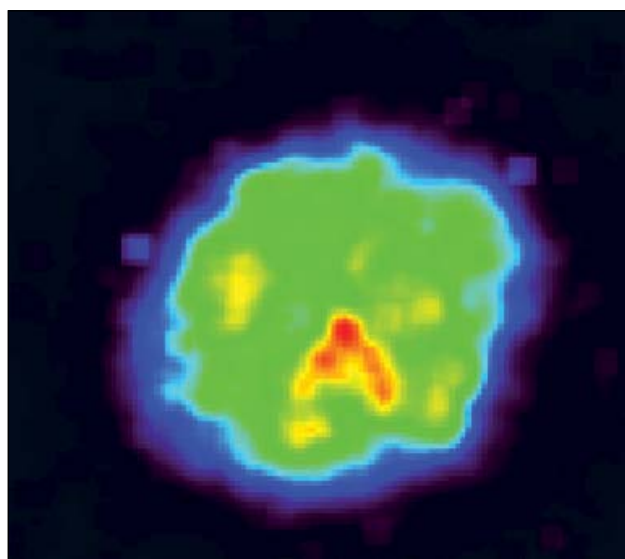


Figure 124.189
XRF images given by (a) a single Sc x-ray source and (b) a Sc source placed behind a gas-filled hohlraum with no sample mounted on it.



U1234JR

Figure 124.191
Neutron image and reaction history of deuterium-filled indirectly driven capsules.



U1235JR

Figure 124.192
Symmetric implosion obtained with calculated cone balance to compensate evaluated backscatter effects.

FY10 AWE OMEGA Experimental Programs

In FY10, AWE led three shot days on the OMEGA laser. This work encompassed an investigation of asymmetrically driven hohlraums (two days) and a Laue x-ray diffraction study of the dynamics of shocked tantalum crystals (one day).

Asymmetrically Driven Hohlraums: Work by AWE has continued to study the asymmetrically driven implosion of thin glass shells and aerogel-foam witness balls in hohlraum targets, as a sensitive test of radiation hydrodynamic modeling. Asymmetry of radiation drive is achieved by asymmetry of laser-beam energy and timing, by asymmetry of capsule position, and by introducing an annular restriction of diameter (baffle) within the hohlraum.

A 1.6-mm-diam, 2.7-mm-long hohlraum is heated by up to 30 OMEGA beams. X-ray backlighting of a thin-wall glass capsule (600- μm diameter, 3.5- μm wall thickness, 30- μm CH ablator) or silica aerogel sphere (600- μm diameter, 300- mg cm^{-3} density) provides the primary diagnostic of the angular distribution of radiation drive near the center of the hohlraum. The hydrodynamics are diagnosed by x-ray backlighting using an area-backlighting source together with a 16-image pinhole camera and a four-strip gated microchannel-plate (MCP) detector, or by point-projection x-ray backlighting together with a single-strip MCP detector. In the case of point backlighting (new to this campaign in FY10), just one single image is recorded but this is of higher spatial resolution (lower statistical “shot noise”) than in the case of multiple images, and this technique has the further advantage of potential sensitivity to refraction (phase-contrast enhancement) at the steep density gradients encountered at ablation and shock fronts within the capsule or foam witness ball.

In previous work⁵⁷ using hohlraums with end-to-end asymmetry of laser drive, a polar jet was recorded and was a particularly sensitive diagnostic of the angular distribution of early-time radiation drive. Many features of the hydrodynamics were successfully reproduced by hydrocode modeling, but modeling and experiment differed in one important respect: simulation showed a small “bump” of material at the most strongly driven pole of thin-shell capsules that was not observed in the experiment. Work during FY10 further investigated this feature of the hydrodynamics. The position of the capsule in the hohlraum was offset from hohlraum center (Fig. 124.193) to provide a further modulation of the angular distribution of the early-time drive at the hot pole. The polar bump was observed and demonstrated to be a genuine feature of the hydrodynamics (and not a near-axis artifact arising in the modeling). These

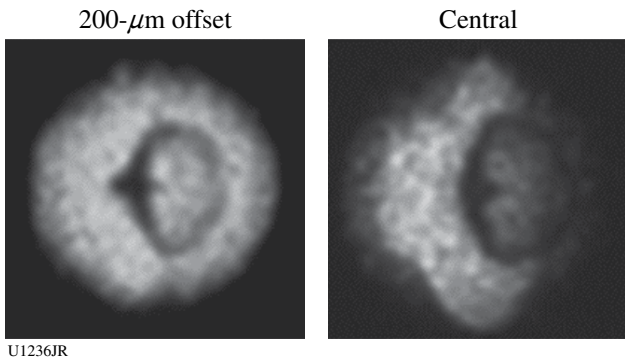
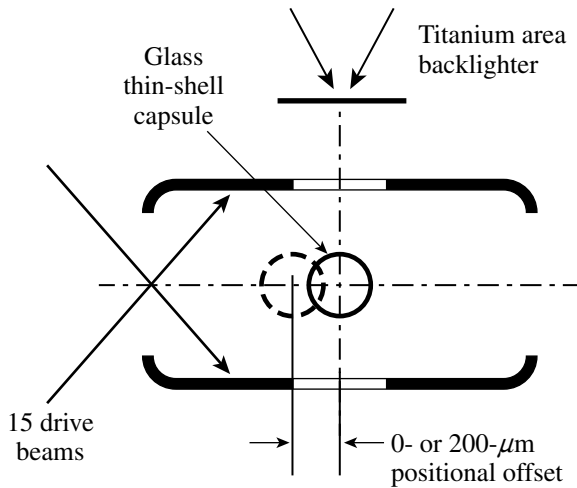


Figure 124.193 Experiment to investigate sensitivity of the polar “bump” to capsule position in an asymmetrically driven hohlraum. The hohlraum is aligned on the P6–P7 axis of the OMEGA target chamber and is driven by 15 beams of the OMEGA laser from one side only. A small displacement of position of the thin-wall glass capsule introduces a further modulation of the angular distribution of asymmetric drive, evident in the radiographs.

experimental data from OMEGA have been used to improve AWE’s hydrocode simulations, and detailed attention to pre-heat, near-axis resolution, and radiation-transport modeling has resulted in very much closer agreement with the experiment (Fig. 124.194).

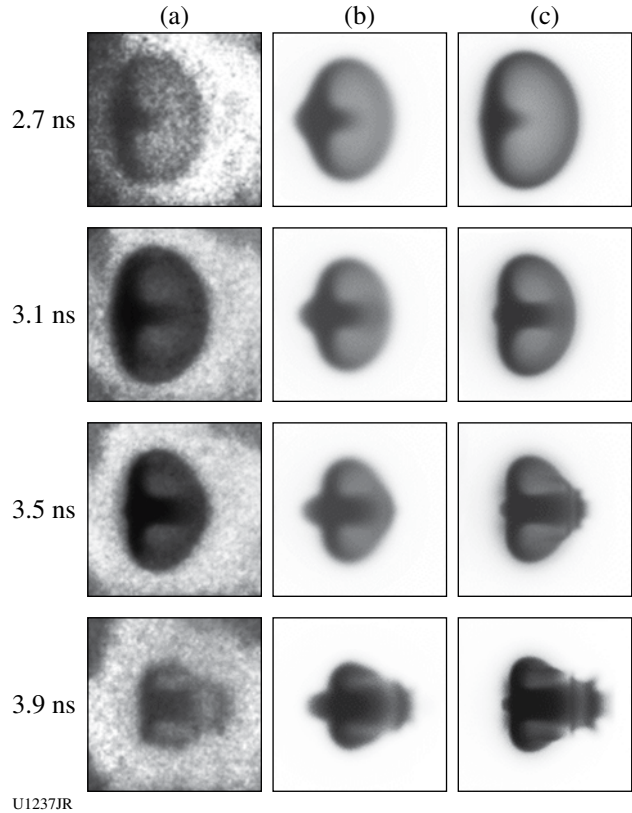
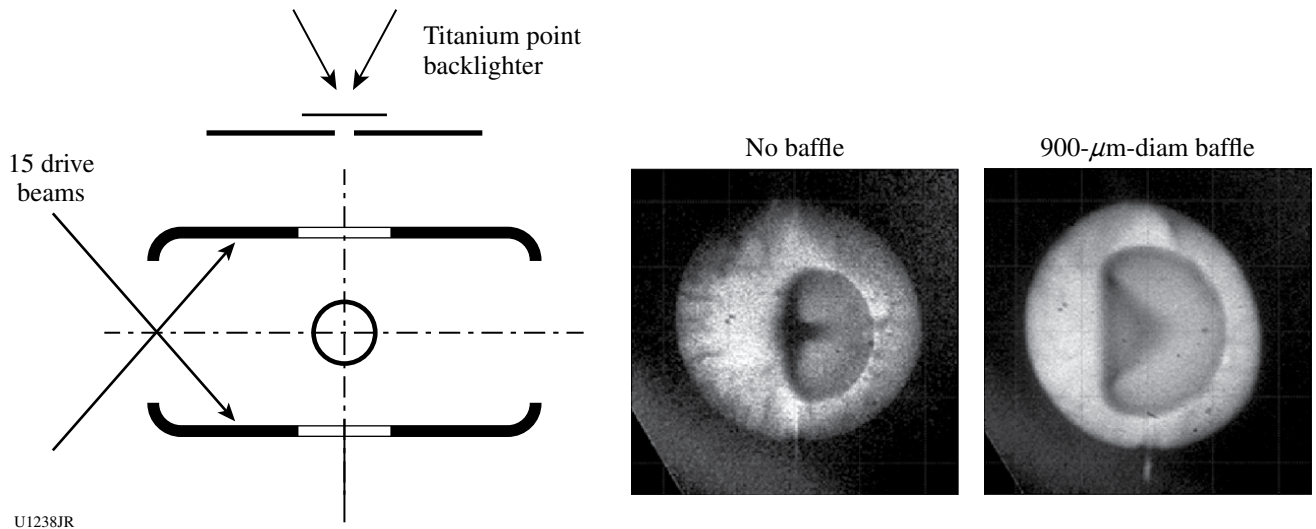


Figure 124.194 Sequence of experimental radiographs (a) of implosion of an asymmetrically driven thin-shell glass capsule compared with simulation before (b) and after (c) improvements to the modeling arising from experiments at OMEGA.

The use of internal, washer-shaped baffles (Fig. 124.195) in hohlraum targets provides a means of shielding an experimental assembly at hohlraum center from a direct view of the individual laser “hot spots” at the hohlraum wall (although at the expense of significant loss of symmetry of angular distribution of drive). X-ray backlighting measurements of capsule implosions in such targets have also been made during FY10 to provide a further benchmark test of hohlraum modeling. Figure 124.195 shows a comparison of 10- μm -resolution, point-projection-backlit images of capsule implosion in regular and baffled hohlraums. The improvement of spatial resolution in these images, in comparison with area-backlit images, is readily apparent (compare Figs. 124.193 and 124.195), as is the



U1238JR

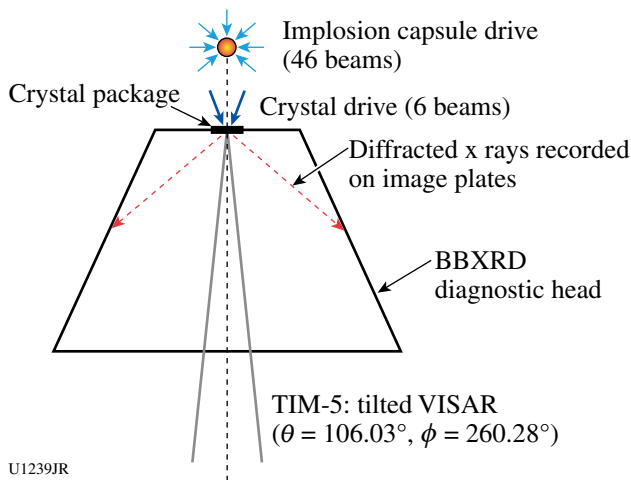
Figure 124.195
Point-backlit images of thin-shell implosions in regular and baffled hohlraums.

possible refraction-enhanced gradient of image intensity near the ablation front at the cold pole of the capsule.

Laue X-Ray Diffraction: The objective of this one-day campaign was to demonstrate the use of broadband x-ray (“white light”) Laue diffraction to probe the lattice dynamics of single-crystal tantalum under shock-loaded conditions, in conjunction with the newly commissioned LLNL BBXRD diagnostic (Fig. 124.196). This campaign complements work by

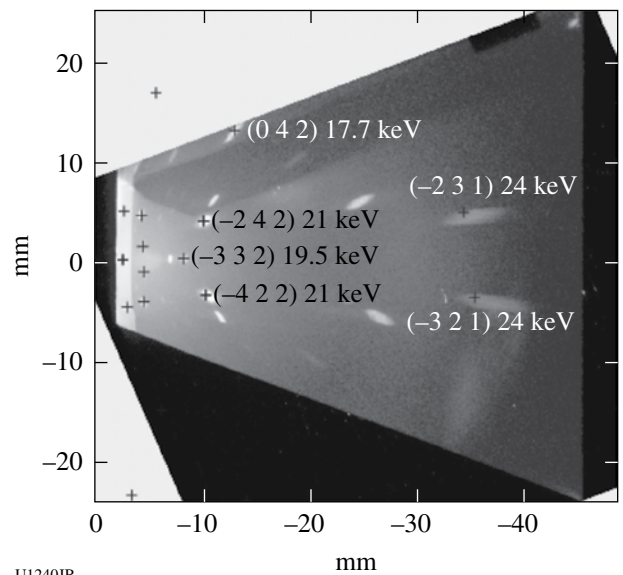
LLE and LLNL, which used the same developmental diffraction technique to investigate the lattice dynamics of shocked copper and silicon samples.

The white-light Laue technique produces a characteristic diffraction pattern (Fig. 124.197), in which each spot can be



U1239JR

Figure 124.196
Sketch of experimental setup showing an implosion capsule backlighter, a Ta crystal package mounted on BBXRD diagnostic, image plate detectors to record the diffraction pattern, and a VISAR diagnostic used to infer the state of the driven sample.



U1240JR

Figure 124.197
Diffraction pattern obtained from 5- μm -thick, single-crystal (100) Ta using an implosion capsule backlighter and LLNL broadband x-ray diffraction (BBXRD) diagnostic. Each crystallographic plane (hkl) generates a characteristic diffraction spot, some of which are labeled in the figure.

attributed to a crystallographic plane in the sample lattice. In principle, this pattern offers unique insight into changes in lattice structure generated under loaded conditions (be it ramp or shock loading), such as the formation and growth of defects and 1-D-to-3-D relaxation processes, by examining and interpreting the location and structure of the characteristic diffraction spots.

An implosion capsule backlighter (980- μm outer diameter with a 10- μm -thick CH wall) driven by 46 OMEGA beams (each beam contained 500 J in a 1-ns square pulse and was used with SG4 DPP) was employed to generate a smooth, broadband spectrum of x rays to produce the white-light diffraction pattern (Fig. 124.198). Such backlighters also have the advantage of a short temporal duration of emission, useful for probing lattice dynamics on an ~ 100 -ps time scale.

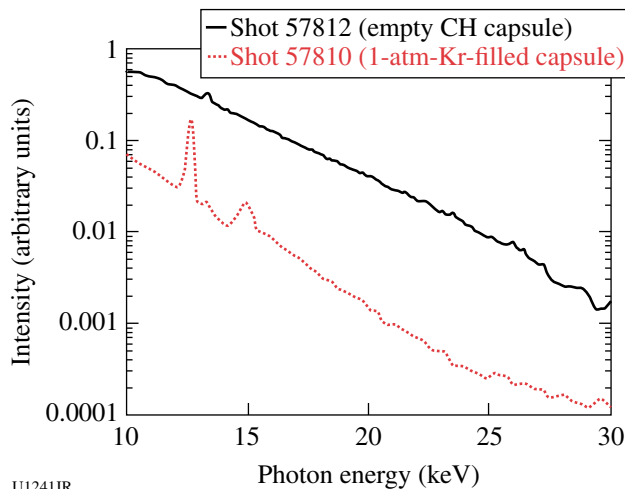


Figure 124.198
Time-integrated spectrum from an implosion capsule backlighter recorded using the double-crystal spectrometer (DCS).

Diffraction data were successfully recorded from both static and driven tantalum samples. Figure 124.197 illustrates the diffraction pattern from a static (i.e., undriven) Ta sample.

Several improvements will be employed in future campaigns. First, one of the most-challenging aspects of this experiment was the production of high-quality crystal samples that were flat and nominally free of crystallographic defects. Modifications will be made to the crystal package design, and improvements will be made to the assembly process in order to address this issue. Second, VISAR measurements indicated that the spatial uniformity of the drive on the crystal package should be improved in order to simplify the interpretation of the data. Changes in beam configuration are being examined to address this point.

REFERENCES

1. S. H. Glenzer *et al.*, *Phys. Rev. Lett.* **90**, 175002 (2003).
2. H. J. Lee, P. Neumayer, J. Castor, T. Döppner, R. W. Falcone, C. Fortmann, B. A. Hammel, A. L. Kritcher, O. L. Landen, R. W. Lee, D. D. Meyerhofer, D. H. Munro, R. Redmer, S. P. Regan, S. Weber, and S. H. Glenzer, *Phys. Rev. Lett.* **102**, 115001 (2009).
3. S. H. Glenzer *et al.*, *Phys. Rev. Lett.* **98**, 065002 (2007); A. L. Kritcher *et al.*, *Science* **322**, 69 (2008); A. García Saiz *et al.*, *Nat. Phys.* **4**, 940 (2008).
4. S. H. Glenzer *et al.*, *Phys. Plasmas* **10**, 2433 (2003); O. L. Landen *et al.*, *J. Quant. Spectrosc. Radiat. Transf.* **71**, 465 (2001); H. Sawada, S. P. Regan, D. D. Meyerhofer, I. V. Igumenschev, V. N. Goncharov, T. R. Boehly, R. Epstein, T. C. Sangster, V. A. Smalyuk, B. Yaakobi, G. Gregori, S. H. Glenzer, and O. L. Landen, *Phys. Plasmas* **14**, 122703 (2007).
5. L. M. Barker and R. E. Hollenbach, *J. Appl. Phys.* **43**, 4669 (1972).
6. G. W. Collins *et al.*, *Science* **281**, 1178 (1998); P. M. Celliers, D. K. Bradley, G. W. Collins, D. G. Hicks, T. R. Boehly, and W. J. Armstrong, *Rev. Sci. Instrum.* **75**, 4916 (2004); P. M. Celliers *et al.*, *J. Appl. Phys.* **98**, 113529 (2005); D. G. Hicks, T. R. Boehly, P. M. Celliers, J. H. Eggert, S. J. Moon, D. D. Meyerhofer, and G. W. Collins, *Phys. Rev. B* **79**, 014112 (2009); M. D. Knudson and M. P. Desjarlais, *Phys. Rev. Lett.* **103**, 225501 (2009).
7. J. Eggert, S. Brygoo, P. Loubeyre, R. S. McWilliams, P. M. Celliers, D. G. Hicks, T. R. Boehly, R. Jeanloz, and G. W. Collins, *Phys. Rev. Lett.* **100**, 124503 (2008).
8. Ya. B. Zel'dovich and Yu. P. Raizer, in *Physics of Shock Waves and High-Temperature Hydrodynamic Phenomena*, edited by W. D. Hayes and R. F. Probstein (Academic Press, New York, 1966), Vol. I, Chap. II, pp. 107–175.
9. R. P. Drake, *High-Energy-Density Physics: Fundamentals, Inertial Fusion, and Experimental Astrophysics*, Shock Wave and High Pressure Phenomena (Springer, Berlin, 2006).
10. J. J. Fortney *et al.*, *Phys. Plasmas* **16**, 041003 (2009).
11. B. A. Remington, R. P. Drake, and D. D. Ryutov, *Rev. Mod. Phys.* **78**, 755 (2006).
12. T. Guillot, *Science* **286**, 72 (1999).
13. W. J. Nellis, M. Ross, and N. C. Holmes, *Science* **269**, 1249 (1995).
14. W. J. Nellis, S. T. Weir, and A. C. Mitchell, *Science* **273**, 936 (1996).
15. N. Nettelmann *et al.*, *Astrophys. J.* **683**, 1217 (20085).
16. B. Militzer *et al.*, *Astrophys. J.* **688**, L45 (2008).
17. I. de Pater and J. J. Lissauer, *Planetary Sciences*, 5th ed. (Cambridge University Press, Cambridge, England, 2007), p. 544.
18. E. C. Stone and E. D. Miner, *Science* **246**, 1417 (1417).
19. S. Stanley and J. Bloxham, *Nature* **428**, 151 (2004).

20. P. Hartigan *et al.*, *Astrophys. J.* **705**, 1073 (2009).
21. J. M. Foster *et al.*, *Phys. Plasmas* **17**, 112704 (2010).
22. P. M. Celliers, P. Loubeyre, J. H. Eggert, S. Brygoo, R. S. McWilliams, D. G. Hicks, T. R. Boehly, R. Jeanloz, and G. W. Collins, *Phys. Rev. Lett.* **104**, 184503 (2010).
23. W. Lorenzen, B. Holst, and R. Redmer, *Phys. Rev. Lett.* **102**, 115701 (2009).
24. C. K. Li, F. H. Séguin, J. A. Frenje, J. R. Rygg, R. D. Petrasso, R. P. J. Town, P. A. Amendt, S. P. Hatchett, O. L. Landen, A. J. Mackinnon, P. K. Patel, V. Smalyuk, J. P. Knauer, T. C. Sangster, and C. Stoeckl, *Rev. Sci. Instrum.* **77**, 10E725 (2006).
25. T. R. Boehly, D. L. Brown, R. S. Craxton, R. L. Keck, J. P. Knauer, J. H. Kelly, T. J. Kessler, S. A. Kumpan, S. J. Loucks, S. A. Letzring, F. J. Marshall, R. L. McCrory, S. F. B. Morse, W. Seka, J. M. Soures, and C. P. Verdon, *Opt. Commun.* **133**, 495 (1997).
26. J. R. Rygg, F. H. Séguin, C. K. Li, J. A. Frenje, M. J.-E. Manuel, R. D. Petrasso, R. Betti, J. A. Delettrez, O. V. Gotchev, J. P. Knauer, D. D. Meyerhofer, F. J. Marshall, C. Stoeckl, and W. Theobald, *Science* **319**, 1223 (2008).
27. C. K. Li, F. H. Séguin, J. A. Frenje, M. Rosenberg, R. D. Petrasso, P. A. Amendt, J. A. Koch, O. L. Landen, H. S. Park, H. F. Robey, R. P. J. Town, A. Casner, F. Philippe, R. Betti, J. P. Knauer, D. D. Meyerhofer, C. A. Back, J. D. Kilkenny, and A. Nikroo, *Science* **327**, 1231 (2010).
28. C. K. Li, F. H. Séguin, J. A. Frenje, J. R. Rygg, R. D. Petrasso, R. P. J. Town, P. A. Amendt, S. P. Hatchett, O. L. Landen, A. J. Mackinnon, P. K. Patel, V. A. Smalyuk, T. C. Sangster, and J. P. Knauer, *Phys. Rev. Lett.* **97**, 135003 (2006).
29. C. K. Li, F. H. Séguin, J. A. Frenje, J. R. Rygg, R. D. Petrasso, R. P. J. Town, P. A. Amendt, S. P. Hatchett, O. L. Landen, A. J. Mackinnon, P. K. Patel, M. Tabak, J. P. Knauer, T. C. Sangster, and V. A. Smalyuk, *Phys. Rev. Lett.* **99**, 015001 (2007).
30. C. K. Li, F. H. Séguin, J. A. Frenje, J. R. Rygg, R. D. Petrasso, R. P. J. Town, O. L. Landen, J. P. Knauer, and V. A. Smalyuk, *Phys. Rev. Lett.* **99**, 055001 (2007).
31. C. K. Li, F. H. Séguin, J. R. Rygg, J. A. Frenje, M. Manuel, R. D. Petrasso, R. Betti, J. Delettrez, J. P. Knauer, F. Marshall, D. D. Meyerhofer, D. Shvarts, V. A. Smalyuk, C. Stoeckl, O. L. Landen, R. P. J. Town, C. A. Back, and J. D. Kilkenny, *Phys. Rev. Lett.* **100**, 225001 (2008).
32. C. K. Li, F. H. Séguin, J. A. Frenje, R. D. Petrasso, P. A. Amendt, R. P. J. Town, O. L. Landen, J. R. Rygg, R. Betti, J. P. Knauer, D. D. Meyerhofer, J. M. Soures, C. A. Back, J. D. Kilkenny, and A. Nikroo, *Phys. Rev. Lett.* **102**, 205001 (2009).
33. R. D. Petrasso, C. K. Li, F. H. Séguin, J. R. Rygg, J. A. Frenje, R. Betti, J. P. Knauer, D. D. Meyerhofer, P. A. Amendt, D. H. Froula, O. L. Landen, P. K. Patel, J. S. Ross, and R. P. J. Town, *Phys. Rev. Lett.* **103**, 085001 (2009).
34. O. V. Gotchev, P. Y. Chang, J. P. Knauer, D. D. Meyerhofer, O. Polomarov, J. Frenje, C. K. Li, M. J.-E. Manuel, R. D. Petrasso, J. R. Rygg, F. H. Séguin, and R. Betti, *Phys. Rev. Lett.* **103**, 215004 (2009).
35. G. Li, R. Yan, C. Ren, T.-L. Wang, J. Tonge, and W. B. Mori, *Phys. Rev. Lett.* **100**, 125002 (2008).
36. H. Chen, S. C. Wilks, D. D. Meyerhofer, J. Bonlie, C. D. Chen, S. N. Chen, C. Courtois, L. Elberson, G. Gregori, W. Kruer, O. Landoas, J. Mithen, J. Myatt, C. D. Murphy, P. Nilson, D. Price, M. Schneider, R. Shepherd, C. Stoeckl, M. Tabak, R. Tommasini, and P. Beiersdorfer, *Phys. Rev. Lett.* **105**, 015003 (2010).
37. S. H. Glenzer *et al.*, *Phys. Rev. Lett.* **88**, 235002 (2002).
38. University of Washington, Department of Physics, FEFF Project, 2004, <http://leonardo.phys.washington.edu/feff/> (24 June 2004).
39. W. Theobald, A. A. Solodov, C. Stoeckl, K. S. Anderson, R. Betti, T. R. Boehly, R. S. Craxton, J. A. Delettrez, C. Dorrer, J. A. Frenje, V. Yu. Glebov, H. Habara, K. A. Tanaka, J. P. Knauer, R. Lauck, F. J. Marshall, K. L. Marshall, D. D. Meyerhofer, P. M. Nilson, P. K. Patel, T. C. Sangster, W. Seka, N. Sinenian, T. Ma, F. N. Beg, and R. B. Stephens, *Bull. Am. Phys. Soc.* **55**, 291 (2010).
40. J. A. Halbleib *et al.*, *IEEE Trans. Nucl. Sci.* **39**, 1025 (1992).
41. N. Izumi, C. Hagmann, G. Stone, D. Hey, S. Glenn, A. Conder, A. Teruya, C. Sorce, R. Tommasini, W. Stoeffl, P. Springer, O. L. Landen, H. W. Herrmann, G. A. Kyrala, R. Bahukutumbi, V. Y. Glebov, T. C. Sangster, M. Eckart, A. J. Mackinnon, J. A. Koch, D. K. Bradley, and P. Bell, *Rev. Sci. Instrum.* **81**, 10E515 (2010).
42. T. Döppner, C. Fortmann, P. F. Davis, A. L. Kritcher, O. L. Landen, H. J. Lee, R. Redmer, S. P. Regan, and S. H. Glenzer, *J. Phys., Conf. Ser.* **244**, 032044 (2010).
43. H.-S. Park *et al.*, *Phys. Rev. Lett.* **104**, 135504 (2010); H.-S. Park *et al.*, *Phys. Plasmas* **17**, 056314 (2010).
44. N. R. Barton, private communication (2010).
45. D. L. Preston, D. L. Tonks, and D. C. Wallace, *J. Appl. Phys.* **93**, 211 (2003).
46. M. A. Meyers, A. Mishra, and D. J. Benson, *Prog. Mater. Sci.* **51**, 427 (2006).
47. D. G. Hicks, T. R. Boehly, P. M. Celliers, J. H. Eggert, E. Vianello, D. D. Meyerhofer, and G. W. Collins, *Phys. Plasmas* **12**, 082702 (2005).
48. O. A. Hurricane, *High Energy Density Phys.* **4**, 97 (2008).
49. E. C. Harding *et al.*, *Phys. Rev. Lett.* **103**, 045005 (2009).
50. O. A. Hurricane *et al.*, *Phys. Plasmas* **16**, 056305 (2009).
51. R. E. Olson *et al.*, *Rev. Sci. Instrum.* **77**, 10E523 (2006).
52. L. S. Dubrovinsky *et al.*, *Phys. Rev. Lett.* **84**, 1720 (2000).
53. J. C. Boettger and D. C. Wallace, *Phys. Rev. B* **55**, 2840 (1997).
54. G. M. Hale and D. C. Dodder, in *Nuclear Cross Sections for Technology*, edited by J. L. Fowler, C. H. Johnson, and C. D. Bowman, Natl. Bur. Stand. (U.S.), Spec. Publ. 594 (U.S. Government Printing Office, Washington, DC, 1980), pp. 650–658.

55. F. Philippe, A. Casner, T. Caillaud, O. Landoas, M. C. Monteil, S. Liberatore, H. S. Park, P. Amendt, H. Robey, C. Sorce, C. K. Li, F. Seguin, M. Rosenberg, R. Petrasso, V. Glebov, and C. Stoeckl, *Phys. Rev. Lett.* **104**, 035004 (2010).
56. C. K. Li, F. H. Séguin, J. A. Frenje, M. Rosenberg, R. D. Petrasso, P. A. Amendt, J. A. Koch, O. L. Landen, H. S. Park, H. F. Robey, R. P. J. Town, A. Casner, F. Philippe, R. Betti, J. P. Knauer, D. D. Meyerhofer, C. A. Back, J. D. Kilkenny, and A. Nikroo, *Science* **327**, 1231 (2010).
57. K. Vaughn *et al.*, *Phys. Plasmas* **17**, 056316 (2010).

Publications and Conference Presentations

Publications

- J. Bromage, C. Dorrer, and J. D. Zuegel, "Angular-Dispersion-Induced Spatiotemporal Aberrations in Noncollinear Optical Parametric Amplifiers," *Opt. Lett.* **35**, 2251 (2010).
- C. E. Clayton, J. E. Ralph, F. Albert, R. A. Fonseca, S. H. Glenzer, C. Joshi, W. Lu, K. A. Marsh, S. F. Martins, W. B. Mori, A. Pak, F. S. Tsung, B. B. Pollock, J. S. Ross, L. O. Silva, and D. H. Froula, "Self-Guided Laser Wakefield Acceleration beyond 1 GeV Using Ionization-Induced Injection," *Phys. Rev. Lett.* **105**, 105003 (2010).
- E. Głowacki, K. Horovitz, C. W. Tang, and K. L. Marshall, "Photoswitchable Gas Permeation Membranes Based on Liquid Crystals," *Adv. Funct. Mater.* **20**, 2778 (2010).
- E. Głowacki, K. Hunt, D. Abud, and K. L. Marshall, "Photo-switchable Gas Permeation Membranes Based on Azobenzene-Doped Liquid Crystals. II. Permeation-Switching Characterization Under Variable Volume and Variable Pressure Conditions," in *Liquid Crystals XIV*, edited by I. C. Khoo (SPIE, Bellingham, WA, 2010), Vol. 7775, p. 77750G (invited).
- J. C. Lambropoulos, C. Miao, and S. D. Jacobs, "Magnetic Field Effects on Shear and Normal Stresses in Magnetorheological Finishing," *Opt. Express* **18**, 19,713 (2010).
- M. Margala, P. Ampadu, Y. Shapir, and R. Sobolewski, "Ballistic Electronics: Breaking the Barrier in Terahertz Speed Processing," in *Terahertz Physics, Devices, and Systems IV: Advanced Applications in Industry and Defense*, edited by M. Anwar, N. K. Dhar, and T. W. Crowe (SPIE, Bellingham, WA, 2010), Vol. 7671, p. 76710I.
- N. Marrocco, G. P. Pepe, A. Capretti, L. Parlato, V. Pagliarulo, G. Peluso, A. Barone, R. Cristiano, M. Ejrnaes, A. Casaburi, N. Kashiwazaki, T. Taino, H. Myoren, and R. Sobolewski, "Strong Critical Current Density Enhancement in NiCu/NbN Superconducting Nanostripes for Optical Detection," *Appl. Phys. Lett.* **97**, 092504 (2010).
- R. L. McCrory, D. D. Meyerhofer, R. Betti, T. R. Boehly, R. S. Craxton, J. A. Delettrez, D. H. Edgell, V. Yu. Glebov, V. N. Goncharov, D. R. Harding, S. X. Hu, J. P. Knauer, F. J. Marshall, P. W. McKenty, P. B. Radha, S. P. Regan, T. C. Sangster, W. Seka, R. W. Short, D. Shvarts, S. Skupsky, V. A. Smalyuk, J. M. Soures, C. Stoeckl, W. Theobald, B. Yaakobi, J. A. Frenje, C. K. Li, R. D. Petrasso, F. H. Séguin, and D. T. Casey, "Progress in Cryogenic Target Implosions on OMEGA," *J. Phys.: Conf. Ser.* **244**, 012004 (2010).
- P. W. McKenty, R. S. Craxton, F. J. Marshall, T. C. Sangster, J. A. Marozas, A. M. Cok, M. J. Bonino, D. R. Harding, D. D. Meyerhofer, R. L. McCrory, J. D. Kilkenny, A. Nikroo, J. Fooks, M. L. Hoppe, J. M. Edwards, A. J. MacKinnon, D. H. Munro, and R. J. Wallace, "Design of High-Neutron-Yield, Polar-Drive Targets for Diagnostic Activation Experiments on the NIF," *J. Phys.: Conf. Ser.* **244**, 032054 (2010).
- D. D. Meyerhofer, J. Bromage, C. Dorrer, J. H. Kelly, B. E. Kruschwitz, S. J. Loucks, R. L. McCrory, S. F. B. Morse, J. F. Myatt, P. M. Nilson, J. Qiao, T. C. Sangster, C. Stoeckl, L. J. Waxer, and J. D. Zuegel, "Performance of and Initial Results from the OMEGA EP Laser System," *J. Phys.: Conf. Ser.* **244**, 032010 (2010).
- S. P. Regan, P. B. Radha, T. R. Boehly, T. Doeppner, K. Falk, S. H. Glenzer, V. N. Goncharov, G. Gregori, O. L. Landen, R. L. McCrory, D. D. Meyerhofer, P. Neumayer, T. C. Sangster, and V. A. Smalyuk, "Inferring the Electron Temperature and Density of Shocked Liquid Deuterium Using Inelastic X-Ray Scattering," *J. Phys.: Conf. Ser.* **244**, 042017 (2010).
- S. N. Shafir, C. D. Roll, and P. D. Funkenbusch, "Optimization of Deterministic Microgrinding (DMG) Conditions for Opti-

cal Glasses and Ceramics,” in *International Optical Design Conference (IODC)/Optical Fabrication and Testing (OF&T) Technical Digest on CD-ROM* (Optical Society of America, Washington, DC, 2010), Paper OWD4.

M. D. Skarlinski and S. D. Jacobs, “Modifying the Rheological Properties of Zirconia Coated Carbonyl Iron Suspensions through Acid-Base Titration and the Addition of Di-Ammonium Citrate,” in *International Optical Design Conference (IODC)/Optical Fabrication and Testing (OF&T) Technical Digest on CD-ROM* (Optical Society of America, Washington, DC, 2010), Paper JMB.

A. A. Solodov, M. Storm, J. F. Myatt, R. Betti, D. D. Meyerhofer, P. M. Nilson, W. Theobald, and C. Stoeckl, “Simulations of Electron-Beam Transport in Solid-Density Targets and the Role of Magnetic Collimation,” *J. Phys.: Conf. Ser.* **244**, 022063 (2010).

L. Sun, S. Jiang, and J. R. Marcianite, “All-Fiber Optical Faraday Mirror Using 56-wt%-Terbium-Doped Fiber,” *IEEE Photon. Technol. Lett.* **22**, 999 (2010).

H. X. Vu, D. F. DuBois, D. A. Russell, and J. F. Myatt, “The Reduced-Description Particle-in-Cell Model for the Two Plasmon Decay Instability,” *Phys. Plasmas* **17**, 072701 (2010).

L. Zeng, T. N. Blanton, and S. H. Chen, “Modulation of Phase Separation Between Spherical and Rodlike Molecules Using Geometric Surfactancy,” *Langmuir* **26**, 12,877 (2010).

L. Zeng, C. W. Tang, and S. H. Chen, “Effects of Active Layer Thickness and Thermal Annealing on Polythiophene: Fullerene Bulk Heterojunction Photovoltaic Devices,” *Appl. Phys. Lett.* **97**, 053305 (2010).

Forthcoming Publications

B. Ciftcioglu, J. Zhang, R. Sobolewski, and H. Wu, “An 850-nm Germanium Metal–Semiconductor–Metal Photodetector with 13-GHz Bandwidth and 8- μ A Dark Current,” to be published in the *Journal of Lightwave Technology*.

A. S. Cross, J. P. Knauer, A. Mycielski, D. Kochanowska, M. Wiktowska-Baran, R. Jakieła, J. Domagala, Y. Cui, R. James, and R. Sobolewski, “(Cd,Mn)Te Detectors for Characterization of X-Ray Emissions Generated During Laser-Driven Fusion Experiments,” to be published in *Nuclear Instruments and Methods in Physics Research, A*.

W. R. Donaldson, D. N. Maywar, J. H. Kelly, and R. E. Bahr, “Measurement of the Self-Phase-Modulation–Induced Bandwidth in a 30-kJ-Class Laser Amplifier Chain,” to be published in the *Journal of the Optical Society of America B*.

D. H. Froula, S. H. Glenzer, N. C. Luhmann, and J. Sheffield, “Plasma Scattering of Electromagnetic Radiation: Experiment, Theory and Measurement Techniques,” to be published by Elsevier.

V. Yu. Glebov, T. C. Sangster, C. Stoeckl, J. P. Knauer, W. Theobald, K. L. Marshall, M. J. Shoup III, T. Buczek, M. Cruz, T. Duffy, M. Romanofsky, M. Fox, A. Pruyne, M. J. Moran, R. A. Lerche, J. McNaney, J. D. Kilkenney, M. Eckart, D. Schneider, D. Munro, W. Stoeffl, R. A. Zacharias, J. J. Haslam, T. Clancy, M. Yeoman, D. Warwas, C. J. Horsfield,

J.-L. Bourgade, O. Landoas, L. Disdier, G. A. Chandler, and R. J. Leeper, “The National Ignition Facility Neutron Time-of-Flight System and Its Initial Performance,” to be published in *Review of Scientific Instruments*.

S. X. Hu, V. N. Goncharov, P. B. Radha, J. A. Marozas, S. Skupsky, T. R. Boehly, T. C. Sangster, D. D. Meyerhofer, and R. L. McCrory, “Two-Dimensional Simulations of the Neutron-Yield in Cryogenic Deuterium-Tritium Implosions on OMEGA,” to be published in *Physics of Plasmas*.

V. Kaushal, I. Iñiguez-de-la-Torre, H. Irie, G. Guarino, W. R. Donaldson, P. Ampadu, R. Sobolewski, and M. Margala, “A Study of Geometry Effects on the Performance of Ballistic Deflection Transistors,” to be published in *IEEE Transactions on Nanotechnology*.

F. J. Marshall, T. DeHaas, and V. Yu. Glebov, “Charge-Injection-Device Performance in the High-Energy-Neutron Environment of Laser-Fusion Experiments,” to be published in *Review of Scientific Instruments*.

J. B. Oliver, P. Kupinski, A. L. Rigatti, A. W. Schmid, J. C. Lambropoulos, S. Papernov, A. Kozlov, J. Spaulding, D. Sadowski, Z. Chrzan, R. D. Hand, D. R. Gibson, I. Brinkley, and F. Placido, “Large-Aperture Plasma-Assisted Deposition of ICF Laser Coatings,” to be published in *Applied Optics*.

J. S. Ross, S. H. Glenzer, J. P. Palastro, B. B. Pollock, D. Price, G. R. Tynan, and D. H. Froula, "Thomson-Scattering Measurements in the Collective and Noncollective Regimes in Laser Produced Plasmas," to be published in *Review of Scientific Instruments*.

C. Stoeckl, M. Cruz, V. Yu. Glebov, J. P. Knauer, R. Lauck, K. L. Marshall, C. Mileham, T. C. Sangster, and W. Theobald, "A Gated Liquid-Scintillator-Based Neutron Detector for Fast-Ignitor Experiments and Down-Scattered Neutron Measurements," to be published in *Review of Scientific Instruments*.

W. Theobald, V. Ovchinnikov, S. Ivancic, B. Eichman, P. M. Nilson, J. A. Delettrez, R. Yan, G. Li, F. J. Marshall, D. D. Meyerhofer, J. F. Myatt, C. Ren, T. C. Sangster, C. Stoeckl, J. D. Zuegel, L. Van Woerkom, R. R. Freeman, K. U. Akli, E. Giraldez, and R. B. Stephens, "High-Intensity Laser-Plasma Interactions with Wedge-Shaped Cavity Targets," to be published in *Physics of Plasmas*.

W. Wang, T. B. Jones, and D. R. Harding, "On-Chip Double Emulsion Droplet Assembly Using Electrowetting-on-Dielectric (EWOD) and Dielectrophoresis (DEP)," to be published in *Fusion Science and Technology*.

Conference Presentations

E. Głowacki, K. Hunt, D. Abud, and K. L. Marshall, "Photo-switchable Gas Permeation Membranes Based on Azobenzene-Doped Liquid Crystals. II. Permeation-Switching Characterization Under Variable Volume and Variable Pressure Conditions," *SPIE Optics and Photonics 2010*, San Diego, CA, 1–5 August 2010.

The following presentations were made at ICUIL, Watkins Glen, NY, 26 September–1 October 2010:

S.-W. Bahk, "A Simple Self-Referenced Piston Measurement for Characterizing a Segmented Wavefront from Tiled Gratings."

S.-W. Bahk, E. Fess, I. A. Begishev, and J. D. Zuegel, "High-Resolution, Adaptive Beam Shaping (HRABS) in a Multi-Terawatt Laser."

J. Bromage, C. Dorrer, and J. D. Zuegel, "A 160-nm-Bandwidth Front End for Ultra-Intense OPCPA."

C. Dorrer, "Temporal Characterization Diagnostics for High-Intensity Laser Systems."

C. Dorrer, D. Irwin, A. Consentino, and J. Qiao, "Contrast Measurements of Kilojoule Laser Pulses at the OMEGA EP Laser Facility."

C. Dorrer, P. Leung, M. Vargas, J. Boule, K. Wegman, Z. Zhao, and K. L. Marshall, "Development of High-Fluence Beam Shapers."

B. E. Kruschwitz, S.-W. Bahk, J. Bromage, D. Irwin, and M. D. Moore, "Improved On-Shot Focal-Spot Measurement Using Phase-Retrieval-Assisted Wavefront Measurements."

B. E. Kruschwitz, M. J. Guardalben, J. H. Kelly, J. Qiao, I. A. Begishev, J. Bromage, S.-W. Bahk, C. Dorrer, L. Folsbee, S. D. Jacobs, R. Jungquist, T. J. Kessler, R. W. Kidder, S. J. Loucks, J. R. Marciano, R. L. McCrory, D. D. Meyerhofer, S. F. B. Morse, A. V. Okishev, J. B. Oliver, G. Pien, J. Puth, A. L. Rigatti, A. W. Schmid, M. J. Shoup III, C. Stoeckl, K. A. Thorp, and J. D. Zuegel, "Current Performance of the OMEGA EP High-Energy Short-Pulse Laser System."

J. Qiao, A. W. Schmid, L. J. Waxer, T. Nguyen, J. Bunkenburg, C. Kingsley, A. Kozlov, and D. Weiner, "Real-Time Detection of Laser-Induced Damage on a 1.5-m Tiled-Grating Compressor During a 15-ps, 2.2-kJ Energy Ramp on OMEGA EP."

S. Papernov, A. Tait, W. Bittle, A. W. Schmid, J. B. Oliver, and P. Kupinski, "Submicrometer-Resolution Mapping of Ultraweak 355-nm Absorption in HfO₂ Monolayers Using Photothermal Heterodyne Imaging," *XLII Annual Symposium on Optical Materials for High Power Lasers*, Boulder, CO, 27–29 September 2010.

